# Availability assessment of AO corrected optical links by machine learning

Emile Klotz

Emile Klotz. Availability assessment of AO corrected optical links by machine learning. Instrumentation and Methods for Astrophysic [astro-ph.IM]. Laboratoire d'astrophysique de Marseille, 2023. English. NNT : 2023AIXM0477 . tel-04601901

# THÈSE DE DOCTORAT

Soutenue à Aix-Marseille Université
le 30 novembre 2023 par

## Emile KLOTZ

# Availability assessment of AO corrected optical links by machine learning

Discipline
Physique et Sciences de la Matière

Spécialité
Astrophysique et Cosmologie

École doctorale
ED 352 Physique et Sciences de la Matière

Laboratoire/Partenaires de recherche
Office national d'études et de recherches aérospatiales (ONERA)
Airbus Defence and Space (AIRBUS)
Laboratoire d'Astrophysique de Marseille (LAM)

Composition du jury

| | |
|---|---|
| Sukanta BASU<br>Professor, University at Albany | Rapporteur |
| James OSBORN<br>Associate Professor, Durham University | Rapporteur |
| Ghaya REKAYA<br>Professeure, Telecom ParisTech | Présidente du jury |
| Thomas OBERLIN<br>Maître de conférence, ISAE SUPAERO | Examinateur |
| Thierry FUSCO<br>Directeur de recherche, ONERA | Directeur de thèse |
| Christian MUSSO<br>Directeur de recherche, ONERA | Co-directeur de thèse |
| Sidonie LEFEBVRE<br>Maître de recherche, ONERA | Membre invitée |
| Nicolas VEDRENNE<br>Maître de recherche, ONERA | Membre invité |

# Affidavit

I, undersigned, Emile Klotz, hereby declare that the work presented in this manuscript is my own work, carried out under the scientific supervision of Thierry Fusco, in accordance with the principles of honesty, integrity and responsibility inherent to the research mission. The research work and the writing of this manuscript have been carried out in compliance with both the french national charter for Research Integrity and the Aix-Marseille University charter on the fight against plagiarism.

This work has not been submitted previously either in this country or in aother country in the same or in a similar version to any other examination body.

Palaiseau, 15/09/2023

Emile KLOTZ

# Acknowledgements

Me voici parvenu au terme de ces trois années de thèse. Cette aventure extraordinaire a été rendue possible grâce au soutien inestimable et aux contributions de nombreuses personnes, à qui je tiens à exprimer ma profonde gratitude.

Je tiens à remercier chaleureusement Sidonie Lefebvre et Nicolas Védrenne, qui ont été à la fois les piliers et les moteurs de mon travail. Un grand merci pour votre soutien quotidien. Vos conseils avisés, votre disponibilité constante et votre expertise ont été des atouts essentiels pour la réussite de ma thèse. Je suis reconnaissant de l'opportunité qui m'a été donnée de travailler à vos côtés. Un grand merci aussi à Christian Musso. Tu as toujours pris le temps de te pencher sur mes problèmes, et nos nombreuses discussions ont été véritablement enrichissantes.

Mes remerciements vont également au reste de l'équipe impliquée dans l'encadrement de cette thèse. En particulier Sylvain Poulenard, merci pour la confiance que tu m'as accordée à travers le cofinancement de cette thèse par Airbus, pour l'orientation que tu as donné à mes travaux et pour la vision critique dont tu as su faire part.

Je tiens à exprimer ma gratitude envers mon directeur de thèse, Thierry Fusco, tu as su rendre cette expérience plus facile tant sur le plan administratif que scientifique. Merci pour ta confiance.

Un merci particulier aux membres de mon jury, les deux rapporteurs S. Basu et J. Osborn, ainsi que G. Rekaya et T. Oberlin dont les échanges intellectuels ont enrichi mes idées et ont contribué à la qualité de ce manuscrit. La bienveillance dont vous avez fait part ont fait de ma soutenance un moment agréable qui me laissera à jamais un bon souvenir.

Enfin j'aimerais faire savoir ma reconnaissance envers toutes les personnes externes à l'équipe qui ont apporté leurs contributions scientifiques et sans qui cette thèse n'aurait surement pas la même valeur. Je pense en particulier à l'équipe de Miratlas, à F. Quatresooz , à G. Kermarrec et à B. Picinbono.

Lors de ces trois années passées à l'ONERA, j'ai eu l'occasion de partager mon temps entre deux équipes, la première MPSO, sur le site de Palaiseau, et la seconde HRA, basée à Châtillon. Cette particularité m'a amené à passer des moments avec grand nombre de collègues et je tiens à tous vous remercier. Mille mercis à Joris, Pierrick, Alina, Léa et Ewen avec qui j'ai partagé le meilleur bureau de Palaiseau, ainsi qu'à

Perrine, Pablo, Alix et Valentina, arrivés en même temps que moi au sein de HRA et avec qui j'ai passé d'innombrables moments merveilleusement drôles. Merci aussi au reste de l'équipe du bâtiment D1 et celle du 7ème étage, aussi bien doctorants que permanents, Valérie, Christophe, Laurie, Léa, Yann... et tant d'autres que je ne peux citer ici par peur d'en oublier. Vous m'avez fait passer trois années extraordinaires ! Merci pour tous ces bons moments et la superbe ambiance. Merci aussi pour votre soutien inconditionnel tout au long de la thèse.

Enfin, que serait cette thèse sans ma famille, en premier lieu Katrin, la femme que j'ai eu la chance d'épouser au cours de cette thèse. Tu as le pouvoir de me rendre heureux en toutes circonstances et de transformer chaque jour en un instant précieux. Grâce à toi la vie est facile et ces trois années se sont écoulées en un claquement de doigts. Merci aussi à Paul, Amédée, Siméon et Angèle mes frères et soeur ainsi qu'à mes parents et grands-parents. C'est toujours avec énormément de plaisir que j'échange avec vous. La curiosité dont vous avez fait part et l'intérêt que vous avez porté à mes sujets de recherches, pourtant loin de vos préoccupations, m'ont à la fois touché et encouragé à faire de mon mieux.

Grâce à l'ensemble des personnes citées ici, cette thèse a été une expérience à la fois enrichissante et gratifiante. Chacun de vous a contribué de manière significative à la réussite de ce projet, faisant de cette thèse une aventure non seulement possible, mais aussi agréable. Votre générosité, votre expertise et votre soutien constant ont été des éléments-clés pour rendre cette expérience aussi bien instructive sur le plan académique qu'humainement enrichissante.

À tous, je souhaite une excellente continuation dans vos projets respectifs. Que la chance accompagne chacun de vous dans vos futurs défis. Restez aussi généreux et passionnés dans vos activités, car c'est cette générosité qui fait de notre communauté académique un lieu d'apprentissage et de partage.

Je souhaite à chacun de pouvoir rencontrer des opportunités aussi stimulantes que celles que j'ai eu la chance de vivre grâce à votre collaboration.

Merci encore pour tout.

# List of publications and conference participation

## List of publications and/or patents produced in the framework of the thesis project:

E. Klotz, S. Lefebvre, N. Védrenne, C. Musso, S. Poulenard, and T. Fusco, “Assessment of adaptive optics-corrected optical links statistics from integrated turbulence parameters through a Gaussian process metamodel,” International Journal of Satellite Communications and Networking. Wiley, Sep. 04, 2023. doi: 10.1002/sat.1497. [Klo+23a]

## Participation in conferences during the thesis period:

1. E. Klotz, "Statistique de disponibilité d’un lien optique sol-espace à partir de mesures locales," in OPTIQUE Dijon 2021 / JRIOA
2. E. Klotz, S. Lefebvre, N. Védrenne, C. Musso, S. Poulenard, L. Coret, A. Louis, and T. Fusco, "Assessment of adaptive optics corrected optical links availability from integrated turbulence parameters by machine learning," in Imaging and Applied Optics Congress 2022 (3D, AOA, COSI, ISA, pcAOP), Technical Digest Series (Optica Publishing Group, 2022), paper JTu5D.4. [Klo+22]
3. Emile Klotz, Sidonie Lefebvre, Nicolas Védrenne, Christian Musso, Thierry Fusco, Sylvain Poulenard, Laurent Coret, Alexis Louis, "Forecasting of turbulence impact on optical link from geostationary satellite," Proc. SPIE 12777, International Conference on Space Optics — ICSO 2022, 1277758 (12 July 2023); https://doi.org/10.1117/12.2690991 [Klo+23b]

# Résumé

**Mots-clés** : *Communication optique en espace libre (FSO), Turbulence atmosphérique, Disponibilité de la liaison optique, Machine Learning*

Les liens optiques atmosphériques font figure de game-changer pour le futur des communications satellite-sol, que ce soit pour le rapatriement des données engrangées par les capteurs embarqués (télémesure) sur des satellites LEO ou pour le développement de l'internet globalisé et de l'internet des objets (IOT) en exploitant les satellites GEO comme relais.

L'influence de l'atmosphère reste un verrou essentiel qu'il convient de forcer pour pouvoir garantir la disponibilité très élevée attendue de systèmes de communication. La fiabilité de son évaluation conditionne les marges utilisées pour le dimensionnement des futurs systèmes, notamment dans le choix des emplacements des futures stations sols.

La performance d'un lien optique est notamment conditionnée par l'influence de la turbulence atmosphérique. Sur un lien optique entre un satellite géostationnaire et le sol des perturbations de l'onde optique en phase et en amplitude dégradent les propriétés du signal et compromettent la transmission d'informations. Différentes solutions de correction, optique adaptative à la réception, codes correcteurs, entrelacement, permettent de juguler ses effets. La forte variabilité spatiale et temporelle des conditions de turbulence, et la complexité de ces différentes méthodes de correction imposent une adaptation fine et conjointe de ces méthodes aux conditions atmosphériques locales.

L'objectif principal de cette thèse est d'améliorer notre compréhension de la disponibilité des liens optiques en présence de turbulences en utilisant des instruments de caractérisation simples combinés à de l'apprentissage machine. Nous avons proposé une méthodologie complète permettant de prédire la marge de puissance du système en l'absence de lien en utilisant seulement quatre paramètres intégrés facilement mesurables de la turbulence.

Ce travail représente une étape importante vers la reconfiguration intelligente et dynamique des réseaux de stations sols optiques. Nous avons introduit une méthodologie innovante pour l'évaluation des turbulences et la prédiction de la disponibilité d'un lien optique, en mettant l'accent sur une utilisation rationnelle de l'apprentissage machine combinée à une compréhension approfondie des phénomènes physiques. Tout en reconnaissant les limites et le besoin de mesures sur le terrain, ces travaux promettent des communications optiques satellite-sol plus fiables et plus efficaces.

# Abstract

**Keywords** : *Free-Space Optical (FSO) Communication, Atmospheric Turbulence, Optical Link Availability, Machine Learning*

This thesis addresses the pressing need for efficient and high-capacity data transmission between satellites and terrestrial infrastructure using Free-Space Optical (FSO) communication. However, the efficacy of optical links is heavily influenced by atmospheric turbulence, which causes signal fluctuations and wavefront distortions. In order to mitigate atmospheric channel impairments opto-mechanical methods, such as adaptive optics, and numerical methods such as error correcting codes and interleaving are considered. These methods are valuable but not foolproof and adverse weather conditions and strong turbulence can still disrupt communications, necessitating a network of ground stations in regions with favourable forecasts.

The core objective of this thesis is to enhance our understanding of optical link availability in the presence of turbulence using simple characterisation instruments combined with machine learning. We went as far as to propose a full methodology enabling the prediction of the system power margin in the absence of established link using only four easily measurable integrated parameters of the turbulence.

This work represents a significant step towards the smart and dynamic reconfiguration of a ground stations network. We introduce innovative methodologies for turbulence assessment and optical link prediction, emphasising a rational approach to machine learning combined with a profound understanding of physical phenomena. While recognising limitations and the need for field measurements, this research holds the promise of more reliable and efficient ground-based satellite optical communication systems.

# Résumé long

## Introduction et motivations

Ces dernières années, la demande de transmission de données haut débit entre satellites et infrastructures terrestres a connu un essor sans précédent, stimulée par le développement des réseaux de données haut débits spatialisés [Hau+19] et des constellations de télécommunication en cours de déploiement [Toy21].

Les limites actuelles des technologies radiofréquences (RF) sont devenues évidentes face aux demandes croissantes de communication sol-espace. Les technologies RF, bien que robustes et largement déployées, souffrent de certaines limitations. En premier lieu elles sont limitées par la bande passante disponible dans les gammes de fréquences allouées. Ainsi, la bande Ku (12 à 18 GHz), largement utilisée, offre un débit de données maximal d'environ 500 Mbps, tandis que la bande Ka (17,3 à 21,2 GHz) permet d'atteindre environ 1 Gbps. Ces chiffres ne permettent pas de répondre aux besoins des applications émergentes particulièrement gourmandes en débit telles que la diffusion de vidéos haute définition, la transmission de données d'observation de la terre et la diffusion pour un nombre croissant d'utilisateurs de l'internet par satellite pour pallier le déficit d'infrastructures fibrées au sol.

En outre, l'attribution du spectre pour les communications RF est fortement réglementée, ce qui entraîne une surcharge et un accroissement du risque d'interférences dans certaines bandes de fréquences.

Enfin, l'aspect non directionnel des liaisons RF traditionnelles, en plus de rendre les communications longue distance très énergivores, les rend vulnérables à l'interception et au brouillage de signaux. Ces vulnérabilités sont préoccupantes, en particulier pour les applications impliquant des informations sensibles telles qu'elles peuvent être échangées dans le domaine de la défense ou dans le domaine des transactions financières.

A contrario, les systèmes de communication optiques offrent une solution convaincante à ces limitations. Ces liaisons optiques ont été massivement adoptées dans les applications espace-espace, permettant des services inter-satellites à grande vitesse. Pour autant, l'émergence de liaisons optiques sol-espace et espace-sol pour des communications haut débit reste au stade de la démonstration. Elles permettraient de fournir un accès internet (jusqu'à 1 Tb/s) et faible latence aux régions éloignées et mal desservies. En outre, les caractéristiques de sécurité des communications optiques, qui permettent des liaisons directionnelles et l'exploitation de méthodes de cryptographie innovantes les rendent attractives pour les applications militaires.

Le besoin d'une large bande passante s'accompagne de la nécessité d'injecter le signal dans une fibre optique monomode (SMF) pour l'amplifier et/ou permettre une détection cohérente. Les fluctuations du signal injecté dues aux turbulences atmosphériques provoquent des variations d'amplitude (de la scintillation), et des distorsions du front d'onde.

Des méthodes physiques existent permettant d'atténuer les erreurs sur le lien, telles que l'optique adaptative (OA) utilisée pour corriger la phase déformée et maximiser l'injection. Des méthodes numériques (entrelacement et codage correcteur) sont également mises en œuvre pour compenser les pertes résiduelles d'information. Toutefois, en présence de conditions météorologiques défavorables, par exemple en présence de turbulences atmosphériques fortes ou d'occultation nuageuse, des interruptions peuvent toujours survenir. Dans cet optique le concept de diversité de site repose sur l'exploitation de stations sols disposées dans des zones géographiques suffisamment éloignées pour pouvoir considérer les conditions météorologiques décorrélées entre elles et pouvoir basculer d'une station à l'autre lorsque les conditions de transmission de données se dégradent sur la station courante. .

Pour gérer la bascule entre les stations, l'opérateur doit pouvoir anticiper les conditions de propagation sur l'ensemble des stations du réseau sol, ceci dans l'objectif de permettre la reconfiguration du réseau et la réorientation du terminal optique à bord du satellite dans un délai compatible de ces opérations (typiquement quelques dizaines de minutes).

Compte tenu de la variabilité importante des conditions de turbulence en fonction de l'emplacement des stations au sol, plusieurs initiatives ont été prises pour déployer des instruments de caractérisation de la turbulence atmosphérique permettant de récupérer à la fois des paramètres intégrés [Jab21] et des profils de turbulence à haute résolution verticale [Cha+20]. Si la relation entre la performance effective des communications et les profils de $C_n^2$ et de vent à haute résolution le long de la ligne de visée est actuellement bien documentée, une question se pose lorsqu'il s'agit de relier les paramètres intégrés, parfois mesurés sur une ligne de visée différente, à la performance effective d'une liaison optique. Cette question est d'autant plus pertinente que le lien optique étant corrigé par optique adaptative, le degré de correction affectera cette dépendance.

Il existe des indications en faveur d'une disponibilité de lien qui ne dépendrait que de quelques paramètres intégrés. Toutefois, une telle relation entre la performance du lien optique et les moments de la turbulence n'a jamais été clairement établie et l'expression exacte des résidus de correction fait intervenir une combinaison complexe de moments de turbulence et de profil de vent. Le manque de développement d'expressions analytiques ne permet pas de démontrer clairement que les paramètres intégrés sont suffisants pour caractériser la disponibilité. En revanche, des méthodes d'apprentissage automatique associées aux modèles de performance physique existants pourraient fournir des indications cruciales pour répondre à cette question sous réserve qu'une méthodologie appropriée soit proposée et mise en place pour ce faire.

C'est l'objectif principal du travail présenté dans cette thèse : étudier la possibilité d'évaluer les performances d'un lien optique corrigé par OA à partir d'un petit nombre de paramètres intégrés en s'appuyant sur une méthode d'apprentissage numérique.

# Résultats principaux

Le chapitre 1 donne un bref aperçu des percées historiques dans le domaine des communications optiques en espace libre, ainsi qu'une description des phénomènes atmosphériques qui ont un impact sur la liaison. L'accent est mis sur la compréhension de la turbulence optique et sur les principaux outils permettant de la modéliser.

Le chapitre 2 se concentre sur la compréhension des mécanismes de correction d'erreur, à la fois l'optique adaptative et les méthodes numériques. Il présente également Simplified Adaptive Optics Simulation Tool (SAOST), un modèle numérique permettant de générer des séries temporelles de puissance optique reçue après propagation dans l'atmosphère et correction par optique adaptative.

Le chapitre 3 introduit les outils d'apprentissage automatique qui seront utilisés tout au long de cette thèse, ainsi que la manière dont ils ont été utilisés pour résoudre des problèmes similaires dans le passé.

Les principaux résultats de ce travail sont présentés dans les chapitres 4 et 5. Dans le chapitre 4, en nous concentrant sur un lien GEO descendant, nous avons construit un métamodèle pour prédire à la fois la fonction de densité de probabilité et le temps de demi-corrélation de la puissance optique reçue en utilisant des techniques d'apprentissage automatique, en particulier la régression par processus gaussien (GP).

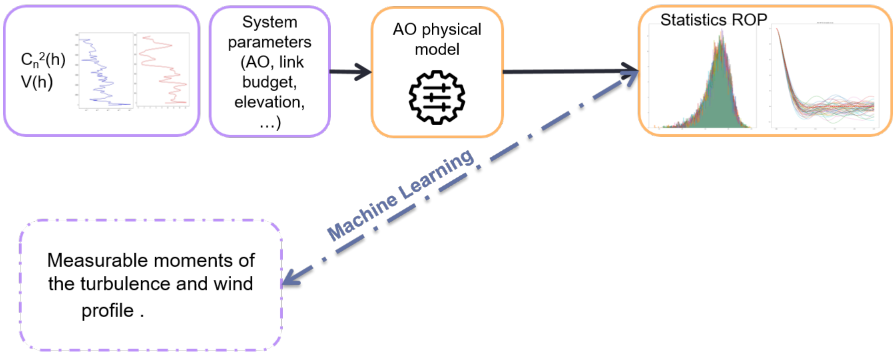

Figure 1.: Description schématique de la démarche

La démarche consiste, à l'aide de techniques usuelles de machine learning, en l'obtention de la densité de probabilité et de la fonction d'autocorrélation de l'erreur de phase et de la scintillation en utilisant uniquement les moments suivants :

- $r_0$ : le paramètre de Fried, défini comme le diamètre typique d'un télescope qui serait limité par la turbulence atmosphérique.
- $\bar{h}$ : une mesure de la dispersion verticale des couches atmosphériques, homogènes à une altitude.
- $\bar{v}$ : une évaluation de la vitesse moyenne du vent dans les couches turbulentes.
- $\sigma_\chi^2$ : la variance de log-amplitude.

Grâce à une base de données de plus de 35 000 profils de turbulence et de vent fournie par l'université de Durham (Profils calculés à partir du modèle ECMWF sur Tenerife pour l'année 2018. https://www.dur.ac.uk/cfai/sitecharacterisation/forecasts/), nous avons montré que la distribution de probabilité de l'atténuation en négligeant la scintillation ($L_\phi(t) == 10log10(\rho_\phi(t))$) suit une distribution de Gumbel :

$$f_{L_\phi}(x) = \frac{1}{\beta} e^{-(z+e^{-z})} \tag{0.1}$$

où $z = \frac{x-\mu}{\beta}$.

La densité de probabilité du terme de scintillation est connue [Can18a] et ne dépend que d'un paramètre : $\sigma_{\chi_{AP}}^2$.

En utilisant un processus Gaussien avec un noyau de Matérn $\frac{5}{2}$, nous sommes capables de prédire $\mu$, $\beta$ et $\sigma_{\chi_{AP}}^2$ en utilisant comme entrée uniquement les moments $r_0$, $\bar{h}$, $\bar{v}$ avec un coefficient de détermination supérieur à 0.99 dans chacun des cas (Figure **??**).

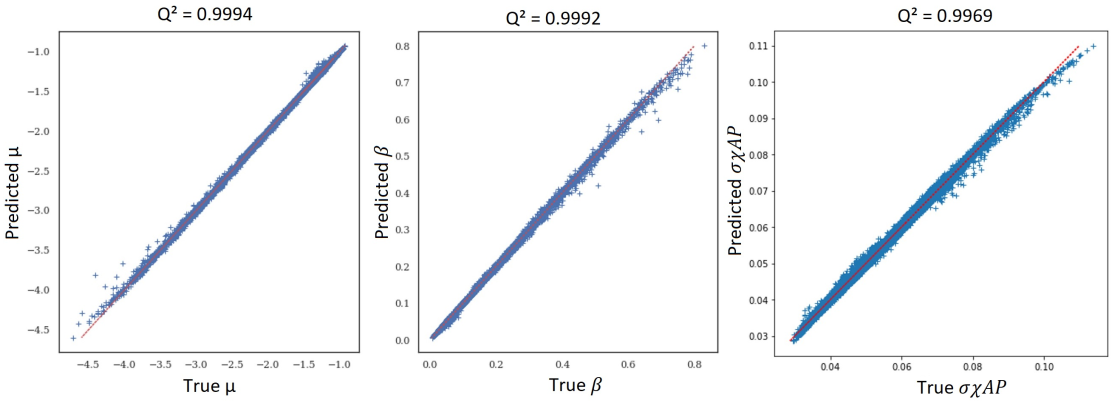

Figure 2.: Valeurs prédites avec un processus Gaussien utilisant $r_0$, $\bar{h}$ et $\bar{v}$ par rapport aux valeurs calculées de $\mu$, $\beta$ et $\sigma_{\chi_{AP}}$ / sur le jeu de test

Grâce à l'efficacité de la prédiction, et sous réserve de connaître $\sigma_\chi^2$ (par la mesure), nous sommes capables de reconstruire la distribution du flux couplé dans la fibre optique avec une erreur bien inférieure à toutes les marges systèmes qui sont habituellement prises dans ce cas d'application (erreur maximale de 0.5dB sur la reconstruction du quantile à 1% du flux couplé).

La même démarche a été entreprise sur la prédiction du temps de demi-corrélation de la phase et de la scintillation avec moins de succès. Pour garantir une bonne prédiction, des moments de la densité spectrale de puissance obtenus à l'aide d'un auto-encoder ont été ajoutés aux entrées du modèle et ont permis d'obtenir les résultats de la Figure 3 avec un coefficient de détermination de 0.99 pour la demi-corrélation de $\rho_\phi(t)$ et de 0.98 pour la demi-corrélation de $\rho_I(t)$.

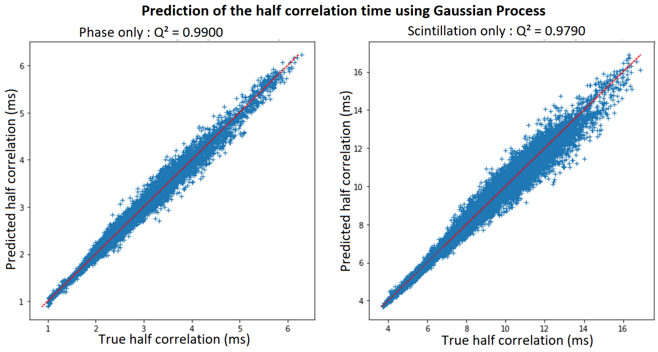

Figure 3.: Prédiction du temps de demi-corrélation en utilisant un processus Gaussien avec les entrées $r_0$, $\bar{h}$ et $\bar{v}$ et l'information sur la DSP de la scintillation mesurée sur une pupille de 5cm.

L'ensemble des résultats présentés dans ce résumé succinct a fait l'objet d'une analyse de sensibilité détaillée dans un article publié dans l'International Journal Communication and Networking.

L'utilisation d'un Forward Error Correction (FEC) et d'un entrelaceur dans la chaîne de détection introduit des non-linéarités, faisant de l'accès à la marge de puissance un problème complexe que nous avons résolu en utilisant deux outils différents pour générer des processus non gaussiens à l'aide des statistiques prédites plus tôt.

Nous avons présenté AnySim, une approche qui offre un moyen systématique de générer des séries temporelles non gaussiennes tout en préservant les propriétés statistiques souhaitées, en particulier la fonction d'autocorrélation.

Ensuite, nous avons exploré ARRC, une méthode basée sur les processus aléatoires conditionnels autorégressifs. Cette approche a été développée avec l'aide de Bernard Picinbono pour notre application et donne des résultats très prometteurs, tout en permettant de générer des séries à une vitesse de calcul inégalée, offrant ainsi une alternative intéressante à des approches plus complexes.

Ces techniques sont utilisées pour obtenir la marge de puissance de l'utilisateur final de la liaison optique, en tenant compte duFEC et de l'entrelaceur. La distribution de l'erreur absolue évaluée sur cette marge de puissance, visible Figure 4, est bien en dessous de la marge système prévue à 3dB.

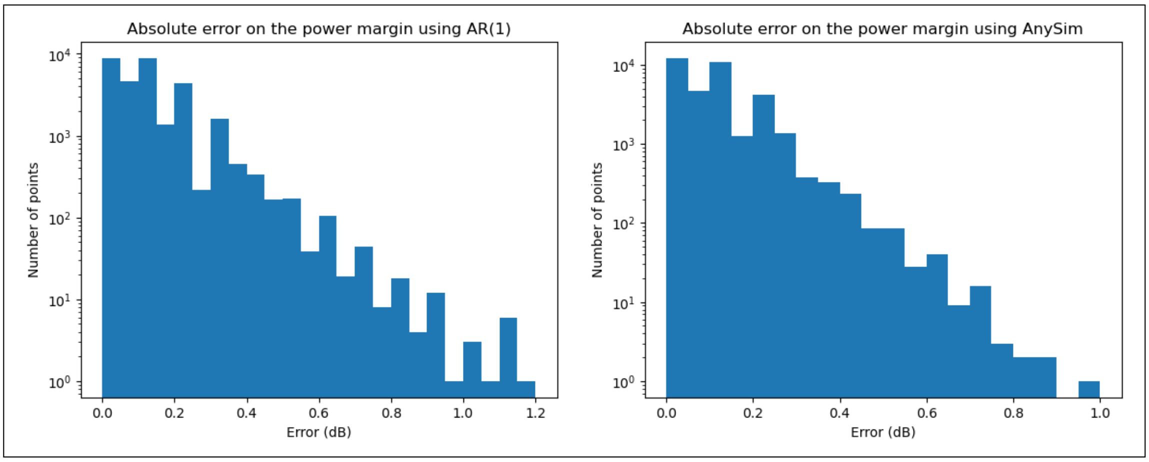

Figure 4.: Distribution de l'erreur absolue sur la marge de puissance. A gauche : **ARCA(1)** MODCOD 9/10 ; à droite : **AnySim** MODCOD 9/10

Tout au long des chapitres 4 et 5, des études de sensibilité systématiques ont été réalisées pour analyser l'impact de chacun des moments sur le modèle. Le chapitre 6 va plus loin en proposant l'étude d'une erreur systématique dans la mesure des moments due à un décalage entre la ligne de visée réelle et celle de l'instrument de caractérisation.

Enfin, le chapitre 7, plus exploratoire, s'est concentrée sur la capacité à prédire la valeur des moments et donc la disponibilité à des horizons temporels de quelques dizaines de minutes en utilisant des modèles de deep learning avancés.

Nous avons présenté un ensemble complet de résultats, en comparant différents modèles, y compris des méthodes basées sur ARIMA, NHITS et NBEAT. Les résultats indiquent clairement que NBEATS surpasse le modèle ARIMA + VMD correspondant à l'état de l'art actuel.

Nous avons ensuite introduit le concept de covariables. Ce sont des séries temporelles supplémentaires connues au moment de la prédiction et qui peuvent améliorer la précision de nos modèles. En particulier, nous avons discuté de l'inclusion de la température et de l'énergie cinétique turbulente au sol.

L'utilisation de ces covariables s'est avérée bénéfique, entraînant des améliorations significatives de la précision des prédictions. Ces covariables ont contribué à capturer les tendances sous-jacentes et à réduire le bruit, améliorant ainsi la capacité de nos modèles à faire des prédictions précises.

# Conclusions et perspectives

Les travaux présentés dans cette thèse représentent une étape importante dans la progression de notre compréhension de la prédiction de la disponibilité des liaisons optiques. Nous avons présenté une méthodologie permettant de passer de paramètres de turbulence intégrés à la marge de puissance en utilisant seulement des outils mathématiques simples.

En nous concentrant sur la liaison descendante GEO, nous avons démontré que, en supposant plusieurs hypothèses simplificatrices sur le modèle de performance du système d'OA, quatre paramètres intégrés de la turbulence semblent suffisants pour évaluer précisément la densité de probabilité du flux couplé. En outre, l'exploitation du spectre de puissance temporel de la scintillation enregistrée par un récepteur de petit diamètre permet d'évaluer le temps de corrélation de ce flux, ce qui rend la description statistique aussi complète que possible.

L'utilisation d'un code correcteur d'erreur et d'un entrelaceur dans la chaîne de détection introduit des non-linéarités, faisant de l'accès à la marge de puissance un problème complexe. Nous avons abordé ce problème en proposant deux méthodes pour générer des séries temporelles avec des statistiques non gaussiennes. L'une a déjà été publiée et démontrée et l'autre a été développée exclusivement pour notre application et donne des résultats très prometteurs. Avec des paramètres d'OA standard, nous avons démontré une prédiction de la marge de puissance avec une erreur absolue de moins de 1 dB sur l'ensemble de la base de données (mai 2021 Tenerife). En outre, le modèle est robuste aux éventuelles interruptions car il n'affiche aucun faux positif dans la prédiction de la disponibilité.

Les outils d'apprentissage automatique peuvent apporter une contribution décisive, à condition qu'ils soient abordés de manière rationnelle, par la compréhension des phénomènes physiques. Les outils créés ici sont intelligibles grâce à l'utilisation des processus gaussiens et aux nombreuses analyses de sensibilité réalisées. Au final, tout le travail a été effectué dans le but de réduire l'incertitude des résultats.

Enfin, au cours de ce travail, plusieurs bases de données ont été exploitées et les résultats de ces dernières ont été comparés à des mesures diurnes sur site, crédibilisant la portée de ce travail.

Nos simulations précédentes supposaient des mesures parfaites des paramètres de turbulence. Plus tard, une propagation de l'erreur de mesure a été étudiée. Nous avons supposé l'existence d'un instrument de caractérisation qui aurait un angle de visée différent de celui du satellite. Cela a conduit à la conclusion que, bien que tous les moments impactent également l'erreur commise sur la marge de puissance, une différence dans la ligne de visée en dessous de 60 degrés limite l'erreur maximale à 1 dB, ce qui est largement dans la marge du système.

Cependant, il convient de se concentrer davantage sur l'étude des erreurs potentielles introduites par les biais et le bruit des mesures instrumentales. La comparaison entre les mesures fournies par des instruments de caractérisation tels que celui proposé par Miratlas et des mesures effectuées à l'aide de l'analyseur de front d'onde sur une liaison optique réelle est essentielle. Cela permettra de compléter l'approche de l'erreur d'angle de visée qui a été réalisée discrètement sur une grille à mailles larges et aidera à établir et à quantifier tous les phénomènes susceptibles d'influencer les mesures des paramètres intégrés.

Nous pouvons également constater que l'analyse de sensibilité à l'aide des indices Sobol ou Shapley ne tient pas compte des queues des distributions. Cependant, ce sont ces événements rares qui provoquent des interruptions de liaison, et une attention particulière devrait être consacrée à leur compréhension. À cet égard, des techniques telles que celles présentées dans [MAG21] seraient probablement plus appropriées.

Il convient également de noter que tous les résultats sont basés sur un modèle pseudo-analytique validé expérimentalement (SAOST). Cela implique une plage de validité et des hypothèses sous-jacentes. Les plus restrictives sont sans aucun doute l'hypothèse d'indépendance phase-amplitude, la propagation limitée aux faibles perturbations et la description purement monochromatique des processus en jeu. De plus, le modèle ne contient que ce qu'on y met, et des paramètres codés en dur tels que l'échelle externe deviennent des variables dans des conditions réelles.

Toutes ces préoccupations concernant les limitations inhérentes à ces hypothèses bénéficieront grandement de campagnes de mesure sur le terrain. L'ONERA développe actuellement une station sol de démonstration GEO-feeder (FEELINGS [Cyr+22]). Son objectif principal est de valider les modèles de propagation optique à travers l'atmosphère, y compris celui développé dans ce travail. Le télescope de 60 cm sera mis en service sur le site de Fauga-Mauzac et sera accompagné d'une station Miratlas pour mesurer les paramètres intégrés. La mesure simultanée de ces paramètres intégrés, de la puissance optique injectée lors du fonctionnement de la liaison et des profils de $C_n^2$ reconstruits à partir des données de l'analyseur de front d'onde [Véd08] permettra de constituer une base de données complète sans biais de modèle. Cette base de données sera comparée à la fois avec des profils simulés issues de modèles météorologiques et avec les sorties SAOST pour justifier les statistiques établies dans cette thèse. Cette base de données permettra également de ré-entraîner les méta-modèles, soit à partir de zéro, soit à l'aide de techniques d'apprentissage par transfert, afin de les adapter au site d'exploitation et aux conditions réelles.

Enfin, les résultats initiaux obtenus avec les techniques de deep learning pour la prédiction des paramètres intégrés sur de longues périodes doivent être considérablement développés. Malgré des résultats prometteurs, il existe plusieurs pistes d'amélioration. Les travaux futurs consisteront à explorer l'utilisation de covariables différentes et futures. La capacité prédictive s'est concentrée sur le paramètre de Fried, d'autres paramètres devraient être étudiés. Enfin, étant donné que la variabilité de la couche au sol n'est pas finement représentée par Weather Research and Forecasting Model (WRF), il convient d'étudier l'impact des variations à haute fréquence du paramètre de Fried lors de démonstrations en conditions réelles. L'utilisation de modèles composites pour tenir compte de ces variations pourrait apporter des solutions. Des études visant à améliorer les données obtenues par les prévisions WRF devraient être envisagées, en utilisant par exemple le travail réalisé dans [Raf+22] où des méthodes d'apprentissage sont proposées pour tenir compte de mesures locales dans les modèles de turbulence, en prenant ainsi en compte la spécificité d'un site donné.

# Contents

**Contents** xvii

**List of Figures** xx

**List of Tables** xxvi

**Acronymes** xxvii

**Introduction** 1

**1. Free Space Optical Communications** 4
- 1.1. Overview of free-space optical communications breakthroughs . . . . 6
- 1.2. Atmospheric impairment . . . . . . . . . . . . . . . . . . . . . . . . 7
  - 1.2.1. Absorption and scattering . . . . . . . . . . . . . . . . . . . . 8
  - 1.2.2. Scope of work . . . . . . . . . . . . . . . . . . . . . . . . . . 10
- 1.3. Atmospheric optical turbulence . . . . . . . . . . . . . . . . . . . . 11
  - 1.3.1. Kolmogorov theory . . . . . . . . . . . . . . . . . . . . . . . 11
  - 1.3.2. The refractive-index fluctuation profile: $C_n^2(h)$ . . . . . . . . . . 13
  - 1.3.3. $C_n^2$ in the boundary layer and in the free atmosphere . . . . . . 14
- 1.4. Modelling of the atmospheric turbulence channel . . . . . . . . . . . 16
  - 1.4.1. Parametric modelling for average behaviour . . . . . . . . . . . 16
  - 1.4.2. Non parametric/ profile based modelling . . . . . . . . . . . . . 18
  - 1.4.3. Experimental considerations . . . . . . . . . . . . . . . . . . . 20

**2. Power Margin Calculation From $C_n^2$ and Wind Profiles** 22
- 2.1. Wave propagation and adaptive optics correction . . . . . . . . . . . . 23
  - 2.1.1. Optical propagation and injection . . . . . . . . . . . . . . . . 23
  - 2.1.2. Adaptive optics . . . . . . . . . . . . . . . . . . . . . . . . . 25
- 2.2. Modelling received optical power after AO correction . . . . . . . . . 28
  - 2.2.1. SAOST: The Simplified Adaptive Optics Simulation Tool . . . . . 28
- 2.3. Data reliability mechanisms . . . . . . . . . . . . . . . . . . . . . . 30
  - 2.3.1. Modulation . . . . . . . . . . . . . . . . . . . . . . . . . . . 30
  - 2.3.2. Forward error correction . . . . . . . . . . . . . . . . . . . . . 31
  - 2.3.3. Interleaver . . . . . . . . . . . . . . . . . . . . . . . . . . . 32
- 2.4. Downlink static link budget . . . . . . . . . . . . . . . . . . . . . . 35

**3. Machine Learning for Link Availability Assessment** 37
- 3.1. State of the art of the use of Machine learning for link availability assessment . . . . . . . . . . . . . . . . . . . . . . . . . . . . . . 38

3.2. Usual supervised machine learning techniques . . . . . . . . . . . . . . . 39
3.3. Machine learning for time series prediction . . . . . . . . . . . . . . . . 43
    3.3.1. ARIMA . . . . . . . . . . . . . . . . . . . . . . . . . . . . . . . . . . 43
    3.3.2. LSTM . . . . . . . . . . . . . . . . . . . . . . . . . . . . . . . . . . 45
    3.3.3. Advanced time series forecasting . . . . . . . . . . . . . . . . . . . 45
3.4. Sensitivity analysis . . . . . . . . . . . . . . . . . . . . . . . . . . . . 47

**4. ROP's Statistics Assessment 50**
4.1. Integrated parameters estimation . . . . . . . . . . . . . . . . . . . . . 51
4.2. Creating a database . . . . . . . . . . . . . . . . . . . . . . . . . . . . 53
    4.2.1. ERA5 and Durham University's model . . . . . . . . . . . . . . . . 53
    4.2.2. Statistical description of the database of profiles . . . . . . . . . 56
    4.2.3. The associated database of ROP . . . . . . . . . . . . . . . . . . . 58
4.3. Estimating the PDF of ROP . . . . . . . . . . . . . . . . . . . . . . . . . 58
    4.3.1. Methodology . . . . . . . . . . . . . . . . . . . . . . . . . . . . . . 61
    4.3.2. Linear regression . . . . . . . . . . . . . . . . . . . . . . . . . . . 62
    4.3.3. MLP . . . . . . . . . . . . . . . . . . . . . . . . . . . . . . . . . . 64
    4.3.4. Gaussian process . . . . . . . . . . . . . . . . . . . . . . . . . . . 66
    4.3.5. Influence of the AO design . . . . . . . . . . . . . . . . . . . . . . 78
4.4. Results on the half-correlation time . . . . . . . . . . . . . . . . . . . . 84
    4.4.1. Metamodel construction . . . . . . . . . . . . . . . . . . . . . . . . 84
    4.4.2. Sensitivity analysis . . . . . . . . . . . . . . . . . . . . . . . . . . 87
    4.4.3. Influence of the AO design . . . . . . . . . . . . . . . . . . . . . . 88
4.5. Discussions . . . . . . . . . . . . . . . . . . . . . . . . . . . . . . . . . 90

**5. Predicting the Link Availability 92**
5.1. Methods for the generation of stochastic processes with arbitrary marginal distributions . . . . . . . . . . . . . . . . . . . . . . . . . . . . . . . . 93
    5.1.1. System . . . . . . . . . . . . . . . . . . . . . . . . . . . . . . . . . 97
    5.1.2. AnySim . . . . . . . . . . . . . . . . . . . . . . . . . . . . . . . . . 97
    5.1.3. Extended ARMA: ARRC . . . . . . . . . . . . . . . . . . . . . . . . 104
5.2. Results . . . . . . . . . . . . . . . . . . . . . . . . . . . . . . . . . . . 112
    5.2.1. Impact of the half-correlation time . . . . . . . . . . . . . . . . . 112
    5.2.2. Comparison between **AnySim** and ARRC(1) . . . . . . . . . . . . 114
    5.2.3. Sensitivity analysis . . . . . . . . . . . . . . . . . . . . . . . . . . 117

**6. Instrumental Considerations 120**
6.1. Impact of deviation in the line of sight . . . . . . . . . . . . . . . . . . 121
6.2. Error on the moments . . . . . . . . . . . . . . . . . . . . . . . . . . . . 122
6.3. Error on the associated power margin . . . . . . . . . . . . . . . . . . . 124

**7. From Minutes to Hours Availability Forecasting 128**
7.1. Database construction . . . . . . . . . . . . . . . . . . . . . . . . . . . 129
    7.1.1. Geographical location . . . . . . . . . . . . . . . . . . . . . . . . 129
    7.1.2. WRF simulations . . . . . . . . . . . . . . . . . . . . . . . . . . . 130

7.1.3. $C_n^2$ modelling . . . . . . 130
7.2. Comparison to on site measurements . . . . . . 135
7.3. Use of machine learning for temporal prediction . . . . . . 141
7.3.1. Method . . . . . . 141
7.3.2. Results . . . . . . 143
7.3.3. Arima . . . . . . 143
7.3.4. Deep neural network for temporal prediction . . . . . . 144
7.4. Introduction of covariates in the deep learning models . . . . . . 148
7.5. Results . . . . . . 150
7.6. Potential improvements in temporal prediction of moments . . . . . . 151

**Conclusion** **153**

**A. $C_n^2$ profile decimation method suited to the study of turbulence** **157**
A.1. Database . . . . . . 157
A.2. Gauss-Legendre quadrature . . . . . . 158
A.3. Results . . . . . . 159

**B. Statistical description without the use of moments** **162**
B.1. Impact of the half-correlation on the minimum of an interleaved MI time series for a poorly corrected signal . . . . . . 164
B.1.1. Autocorrelation fit . . . . . . 164
B.2. Comparison with uncorrelated time series . . . . . . 164
B.3. Results . . . . . . 167
B.3.1. Results on the database using a 900ms time series as input . . . 167
B.3.2. Impact of the half correlation time on the prediction . . . . . . 168
B.4. Limitations . . . . . . 169

**Bibliography** **190**

# List of Figures

1. Description schématique de la démarche . . . . . . . . . . . . . . . . . . . . x
2. Valeurs prédites avec un processus Gaussien utilisant $r_0$, $\bar{h}$ et $\bar{v}$ par rapport aux valeurs calculées de $\mu$, $\beta$ et $\sigma_{\chi_{AP}}$ / sur le jeu de test . . . . . xi
3. Prédiction du temps de demi-corrélation en utilisant un processus Gaussien avec les entrées $r_0$, $\bar{h}$ et $\bar{v}$ et l'information sur la DSP de la scintillation mesurée sur une pupille de 5cm. . . . . . . . . . . . . . . . . xii
4. Distribution de l'erreur absolue sur la marge de puissance. A gauche : **ARCA(1)** MODCOD 9/10 ; à droite : **AnySim** MODCOD 9/10 . . . . . . xiii

1.1. Example of what could be an optimal European ground station network 7
1.2. An early atmospheric transmission curve published in "Remote Sensing: A Survey Report" in 1967. . . . . . . . . . . . . . . . . . . . . . . . . . . . 8
1.3. Atmospheric transmittance around the C-band -©Geek3 - Own work, CC BY-SA 4.0 . . . . . . . . . . . . . . . . . . . . . . . . . . . . . . . . . . . 9
1.4. Difference between Rayleigh and Mie scattering (Figure from [Bar20]) . 10
1.5. Comparison between the Von Karman Spectrum and the Kolmogorov spectrum . . . . . . . . . . . . . . . . . . . . . . . . . . . . . . . . . . . . 12
1.6. The boundary layer over a diurnal period - *Source: COMET/METED* . . 15

2.1. Detection channel of the optical link . . . . . . . . . . . . . . . . . . . . . 23
2.2. Simplistic example of a 3 bit repetition, R = 3 and T = 1 . . . . . . . . . . 31
2.3. Visualisation of the effect of an interleaver on a turbulent channel . . . 32
2.4. Architecture of a convolutional interleaver and deinterleaver . . . . . . 33

3.1. Architecture de N-BEATS, figure issue de [Ore+19] . . . . . . . . . . . . 46

4.1. Sampling of the 113 pressure levels of the ERA5 model used, given in altitude above ground. Zoom on the right represents the first vertical 5 kilometres. . . . . . . . . . . . . . . . . . . . . . . . . . . . . . . . . . . 54
4.2. Tenerife with OGS-Rx accurately localized by red dot. The purple line indicate Teleo's operational line of sight at 33,2° . Each coloured squared is a point of the grid at a given time. The value is the ground altitude seen by ERA5 for each of the points. . . . . . . . . . . . . . . . . . . . . . . . 55
4.3. Example of $C_n^2$ (left) and wind (right) profiles from the database. Given for a 30° elevation in meters above ground. . . . . . . . . . . . . . . . . . . 56
4.4. Statistics of the selected integrated parameters of the turbulence for the database presented in section 4.2.1. . . . . . . . . . . . . . . . . . . . . . . 57

4.5. Gumbel fit on the distribution of $L_\phi$ in three cases: first one in blue corresponds to the minimum of coupling efficiency, second one in orange is an average coupling efficiency and last one in green is obtained for the profile with the highest coupling efficiency. . . . . . . . . . . . . . . . . 61
4.6. Linear regression on $r_0$, $\bar{h}$ and $\bar{v}$ to assess the values of $\mu$ (left) and $\beta$ (right). Simulated value (SAOST) in abscissa, output of the model in ordinate. Only for the test set. . . . . . . . . . . . . . . . . . . . . . . . . . . . 62
4.7. Linear regression on $r_0$, $\bar{h}$ and $\bar{v}$ to assess the values of $\sigma_\chi^2$. Simulated value (SAOST) in abscissa, output of the model in ordinate. Only for the test set. . . . . . . . . . . . . . . . . . . . . . . . . . . . . . . . . . . . . 63
4.8. Linear regression on $\frac{1}{r_0}^{5/3}$, $\bar{h}^{5/3}$ and $\bar{v}^{5/3}$ to assess the values of $\mu$ (left) and $\beta$ (right). . . . . . . . . . . . . . . . . . . . . . . . . . . . . . . . . . 63
4.9. Linear regression on $\frac{1}{r_0}^{5/3}$, $\bar{h}^{5/3}$ and $\bar{v}^{5/3}$ to assess the values of $\sigma_\chi^2$ . . . 64
4.10. MLP metamodel on $r_0$, $\bar{h}$ and $\bar{v}$ to assess the values of $\mu$ (left) and $\beta$ (right). Simulated value (SAOST) in abscissa, output of the model in ordinate. Only for the test set. . . . . . . . . . . . . . . . . . . . . . . . . . . . 65
4.11. MLP metamodel on $\frac{1}{r_0}^{5/3}$, $\bar{h}^{5/3}$ and $\bar{v}^{5/3}$ to assess the values of $\mu$ (left) and $\beta$ (right). Simulated value (SAOST) in abscissa, output of the model in ordinate. Only for the test set. . . . . . . . . . . . . . . . . . . . . . . . . 65
4.12. Results of the Gaussian Process (GP) to assess the values of $\mu$ and $\beta$ using $r_0$, $\bar{h}$ and $\bar{v}$ as inputs . . . . . . . . . . . . . . . . . . . . . . . . . . . 67
4.13. Sensitivity analysis on the prediction of $\mu$ and $\beta$ using $r_0$, $\bar{h}$ and $\bar{v}$ . . . 68
4.14. Results of the Gaussian Process (GP) to assess the values of $\mu$ and $\beta$ using $r_0$ and $\bar{v}$ as inputs . . . . . . . . . . . . . . . . . . . . . . . . . . . . . . . 68
4.15. Results of the GP to assess the values of the mean and the variance of the coupled flux distribution using $r_0$ and $\bar{v}$ as inputs . . . . . . . . . . . 69
4.16. Results of the GP to assess the values the mean and the variance of the coupled flux distribution using adaptive learning with $r_0$ and $\bar{v}$ as inputs. 70
4.17. Results of the GP metamodel to assess the value of $\sigma_{\chi_{AP}}$ using $r_0$, $\bar{h}$ and $\bar{v}$. 71
4.18. Sensitivity analysis on the prediction of $\sigma_{\chi_{AP}}$ using $r_0$, $\bar{h}$ and $\bar{v}$ . . . . . 71
4.19. Results of the GP metamodel to assess the value of $\sigma_{\chi_{AP}}$ using $r_0$ and $\bar{h}$. 72
4.20. Results of the GP to assess the value of $\sigma^2_{\chi_{AP}}$ using as a single input $\frac{r_0}{\bar{h}}$. . 72
4.21. $\sigma^2_{\chi_{AP}}$ as a function of $\theta_0$ ($\mu rad$). In red a curve fit with the law $\sigma^2_{\chi_{AP}} = a \times \theta_0^b$. 73
4.22. $\sigma^2_{\chi_{AP}}$ as a function of $\theta_0$ for different values of the pupil diameter. In red a curve fit with the law $\sigma^2_{\chi_{AP}} = a \times \theta_0^b$. . . . . . . . . . . . . . . . . . . . . . 75
4.23. Coefficient of determination of the fit of $\sigma^2_{\chi_{AP}}$ as a power law of $\theta_0$, according to the pupil diameter. . . . . . . . . . . . . . . . . . . . . . . . . 76
4.24. PDF computed from SAOST time series and PDF computed from our metamodel with, from left to right: $L_\phi(t)$, $\rho_I$ and the received optical power. . . . . . . . . . . . . . . . . . . . . . . . . . . . . . . . . . . . . . 77
4.25. Histogram and Cumulative Distribution Function (CDF) of the absolute error on prediction of the mean, the standard deviation and the 1% quantile. . . . . . . . . . . . . . . . . . . . . . . . . . . . . . . . . . . . . . 78

4.26. Fitting, temporal and total residual error's variance for each of the Adaptive Optics (AO) cases considered. . . . . . . . . . . . . . . . . . . . . . . . . 80
4.27. Distribution of the parameters of the Probability density function (PDF) of $f_{smf}$ depending on the AO cases. . . . . . . . . . . . . . . . . . . . . . . . 81
4.28. Prediction of the parameters of the PDF of $f_{smf}$ depending on the AO cases. . . . . . . . . . . . . . . . . . . . . . . . . . . . . . . . . . . . . . . 82
4.29. Sensitivity analysis on the prediction of $\mu$ and $\beta$ depending on the AO cases. . . . . . . . . . . . . . . . . . . . . . . . . . . . . . . . . . . . . . . 83
4.30. Prediction of the half-correlation time using GP on inputs $r_0$, $\bar{h}$ and $\bar{v}$; x axis shows the real value and y the predicted one. On the left the half-correlation neglecting scintillation effects and on the right . . . . . 84
4.31. Architecture of the autoencoder used to encode the power spectral density. 85
4.32. Comparison of the computed Power spectral density;: (PSD) and the one reconstructed using the autoencoder. . . . . . . . . . . . . . . . . . 86
4.33. Prediction of the half-correlation time using GP on inputs $r_0$, $\bar{h}$ and $\bar{v}$ and information on the PSD of scintillation for a 5cm pupil. The same other parameters as in figure 4.30. . . . . . . . . . . . . . . . . . . . . . . . . 86
4.34. Sensitivity analysis of the model described in Figure 4.30. . . . . . . . . 87
4.35. Sensitivity analysis of the model described in Figure 4.33. . . . . . . . . 87
4.36. Half-correlation of the coupling rate neglecting the scintillation for the 2 other cases of AO . . . . . . . . . . . . . . . . . . . . . . . . . . . . . . . 88
4.37. Assessment of the half-correlation using 3 moments (left) and the 3 moments plus the 5 parameters of the PSD (right) for AO case 2 . . . . 89
4.38. Assessment of the half-correlation using 3 moments (left) and the 3 moments plus the 5 parameters of the PSD (right) for AO case 3 . . . . 89
4.39. Sensitivity analysis of the half-correlation assessment using 3 moments plus the 5 parameters of the PSD (right) for AO case 2 (left) and 3 (right) 90

5.1. The two sets of profiles, one in green for a good case of correction and one in red for a poor correction case. . . . . . . . . . . . . . . . . . . . . 96
5.2. The integrated parameters of the two previous sets of profiles (same colours) compared to the whole database. . . . . . . . . . . . . . . . . . 96
5.3. The values of coupling efficiency of the two previous sets of profiles (same colours) compared to the whole database for our standard case of AO. . . . . . . . . . . . . . . . . . . . . . . . . . . . . . . . . . . . . . . 96
5.4. Mutual Information vs received optical power, in red a zoom on the saturation zone . . . . . . . . . . . . . . . . . . . . . . . . . . . . . . . . 97
5.5. Generated time series of coupling efficiency using **AnySim** compared to the targets for the two profiles described in Figure 5.1. . . . . . . . . . . 99
5.6. Generated distribution and autocorrelation of coupled flux using **AnySim** compared to the target. . . . . . . . . . . . . . . . . . . . . . . . . . . . 100
5.7. Generated time series of scintillation using **AnySim** compared to the target series . . . . . . . . . . . . . . . . . . . . . . . . . . . . . . . . . 101

5.8. Generated distribution and autocorrelation of scintillation using **AnySim** compared to the target series. . . . . . . . . . . . . . . . . . . . . . . . . . 102
5.9. Generated time series of coupled flux using **AnySim** compared to the target series . . . . . . . . . . . . . . . . . . . . . . . . . . . . . . . 103
5.10. Generated distribution and autocorrelation of scintillation using **AnySim** compared to the target series. . . . . . . . . . . . . . . . . . . . . . . . . . 103
5.11. Estimated power margin using **AnySim** and machine learning meta-models compared to target one. . . . . . . . . . . . . . . . . . . . . . . . . 104
5.12. Partial autocorrelation function of the target (SAOST) time series for the poor correction case. . . . . . . . . . . . . . . . . . . . . . . . . . . . . . 105
5.13. The roots of $D(z)$ with the coefficients calculated in Table 5.2. . . . . . . 107
5.14. Time series of coupling efficiency generated using ARRC(4) method compared to the target series for the poor correction case. . . . . . . . . 108
5.15. Statistics of the time series of coupling efficiency generated using ARRC(4) method compared to the target series for the poor correction case. . . . 108
5.16. Time series of coupling efficiency generated using ARRC(1) method compared to the target series for the poor correction case. . . . . . . . . 110
5.17. Statistics of the time series of coupling efficiency generated using ARRC(1) method compared to the target series for the poor correction case. . . . 110
5.18. Generated distribution and autocorrelation of scintillation using ARRC(1) compared to the target one. . . . . . . . . . . . . . . . . . . . . . . . . . 111
5.19. Power margin depending on the interleaver size calculated with ARRC(1) compared to the ground truth. . . . . . . . . . . . . . . . . . . . . . . . . 112
5.20. Distribution of power margin error using **AnySim** for MODCOD 3/10 (top) and 9/10 (bottom) - interleaver 100ms. In blue using the model with $r_0$, $\bar{h}$, $\bar{v}$ and $\sigma_\chi^2$ in yellow when the PSD of scintillation is added. . 113
5.21. Distribution of the estimated power margin with time series generation versus the distribution of the target power margin.
**Upper left:** ARRC(1) MODCOD 9/10; **Upper right:** **AnySim** MODCOD 9/10; **Lower left:** ARRC(1) MODCOD 3/10; **Lower right:** **AnySim** MODCOD 3/10 . . . . . . . . . . . . . . . . . . . . . . . . . . . . . . . 115
5.22. Generated vs real power margin with $R^2$ score for each case
Upper left: ARRC(1) MODCOD 9/10; Upper right: **AnySim** MODCOD 9/10; Lower left: ARRC(1) MODCOD 3/10; Lower right: **AnySim** MODCOD 3/10 . . . . . . . . . . . . . . . . . . . . . . . . . . . . . . . . . . 116
5.23. Distribution of the absolute error on the power margin.
Upper left: ARRC(1) MODCOD 9/10; Upper right: **AnySim** MODCOD 9/10; Lower left: ARRC(1) MODCOD 3/10; Lower right: **AnySim** MODCOD 3/10 . . . . . . . . . . . . . . . . . . . . . . . . . . . . . . . . . . 117
5.24. Sensitivity analysis for each of the studied cases . . . . . . . . . . . . . . 118

6.1. Method for the creation of composite profiles . . . . . . . . . . . . . . . 121
6.2. Composite profile creation for a 30° elevation . . . . . . . . . . . . . . . 122

6.3. Distribution of the error on each of the moments for different elevations (in °) . . . 123
6.4. Absolute error on the power margin for the true positive cases for the different elevation angles . . . 125
6.5. Sensitivity analysis on the absolute error on the power margin as a function of the relative error on the moments for different elevations . . . . 126

7.1. Comparison between the temperature profile extracted from the dataset using TKE (orange) and from the one using Dewan's (blue) for 4 random occurences . . . 131
7.2. Comparison between the wind profiles extracted from from the dataset using TKE (orange) and from the one using Dewan's (blue) for 4 random occurrences. Full line zonal and dashed line meridional . . . 131
7.3. Comparison between zenital $C_n^2$ profile extracted from TKE and from Dewan approach for 4 random occurences . . . 133
7.4. Comparison between the averaged moments profile extracted from the TKE approach (orange) and from Dewan's (bleu) for an zenith angle measurement at 550 nm . . . 134
7.5. Miratlas Integrated Sky Monitor. . . . 135
7.6. Comparison of the temperature and humidity on the ground level obtained through WRF (orange) and measured through the local meteorological station (blue) . . . 136
7.7. Comparison of the $r_0$ obtained through WRF (orange) and measured through the local meteorological station (blue) . . . 137
7.8. Comparison of the $r_0$ obtained through WRF (orange) and the average value over 20 minutes of $r_0$ measured through the local meteorological station (blue) . . . 138
7.9. $r_0$ Miratlas after subtraction of a 20 min width sliding average (Trend) . 139
7.10. Distribution and autocorrelation of the noise in the $r_0$ Miratlas without the trend (20 minutes averaged) . . . 140
7.11. Prediction of an ARIMA model for $r_0$ prediction, trained on the first 12 days of April WRF data and validated on the next 2 days . . . 143
7.12. ARIMA model on each mode of the decomposition proposed by [Li+23] for $r_0$ prediction trained on the first 12 days of April WRF data and validated on the next 2 days . . . 143
7.13. Scores on the prediction of $r_0$ as a function of time with associated error (April) . . . 144
7.14. Two examples of prediction of $r_0$ over one day using Neural Basis Expansion Analysis for Time Series Forecasting (N-BEATS) for July . . . . 146
7.15. Two examples of prediction of $r_0$ over one day using N-BEATS for April 147
7.16. Comparison of N-BEATS with (yellow) and without (purple) TKE as a past covariate for a prediction of a few hours the $22^{nd}$ of April. . . . . 149

7.17. Comparison of N-BEATS with TKE (purple) as a past covariate and with T° + TKE (yellow) as past covariates for a prediction of a few hours the $22^{nd}$ of October. . . . . . . . . . . . . . . . . . . . . . . . . . . . . . 150

A.1. GRUAN is envisaged as a global network of eventually 30-40 radiosonding stations. . . . . . . . . . . . . . . . . . . . . . . . . . . . . . . 157
A.2. Gauss-Legendre interpolation of the $C_n^2$ profile and associated wind profile 160
A.3. Moments from the 50 layers interpolated profiles compared to moments from the 6000+ layers profiles . . . . . . . . . . . . . . . . . . . . . . . . . 161

B.1. Temporal serie of ROP (blue) vs MI (red) on an average case of turbulence (top) and a case of weak turbulence (bottom). . . . . . . . . . . . . . . . 163
B.2. Autocorrelation of ROP (blue) vs MI (orange) on an average case of turbulence (left) and a case of weak turbulence (right). . . . . . . . . . . 163
B.3. Exponential approximation of the autocorrelation of MI. . . . . . . . . 164
B.4. Minimum of MI time series vs interleaver size (in log scale on the right). In blue for the correlated time series and in red for an uncorrelated time series with the same distribution. . . . . . . . . . . . . . . . . . . . . . . 165
B.5. Evolution of the variance with the interleaving time, computed from the time series and evaluated from the above equations. 1ms = 4points so for 100ms, n=400 . . . . . . . . . . . . . . . . . . . . . . . . . . . . . . 166
B.6. Law of the min vs $\mu - 3\sigma$ and $\mu - 5\sigma$. 1ms = 4points so for 100ms n=400 167
B.7. Assessment of the minimum of the interleaved series of Mutual Information (MI) using the statistical method. . . . . . . . . . . . . . . . . . . . 168
B.8. Absolute and relative error(in %) on the assessment of the minimum of the interleaved MI series (when the link is not available (min<0.94)) . . 168

# List of Tables

2.1. Onboard terminal link budget contribution . . . . . . . . . . . . . . . . . 36
2.2. Optical Ground Station (OGS) link budget contribution . . . . . . . . . 36

4.1. Relative errors on quantiles with the Gumbel fit over the 37059 power attenuation's series. . . . . . . . . . . . . . . . . . . . . . . . . . . . . 60
4.2. Score on the assessment of $\mu$ and $\beta$ for different kernels . . . . . . . . . 66

5.1. AR(5) coefficients calculated on the of the target (SAOST) time series for the poor correction case. . . . . . . . . . . . . . . . . . . . . . . . . . . 106
5.2. AR(4) coefficients calculated on the of the target (SAOST) time series for the poor correction case. . . . . . . . . . . . . . . . . . . . . . . . . . . 106

6.1. Error in % made on the moments for different elevations . . . . . . . . 122
6.2. Main elements of the confusion matrix given in % at different elevations 124

7.1. Grid parameters from WRF simulations. . . . . . . . . . . . . . . . . . . 130
7.2. Prediction score for the different models and different moments of interest. The left score is the Root Mean Square Error (RMSE) and the right one the Mean Absolute Error (MAE) . . . . . . . . . . . . . . . . . . . . . . 151

# Acronymes

**AO** Adaptive Optics. xxii, 2, 3, 25–30, 51, 52, 58, 63, 68, 78–83, 88–90, 95, 101, 104, 114, 118, 125, 153, 154

**CDF** Cumulative Distribution Function. xxi, 78

**ECMWF** European Centre for Medium range Weather Forecasts. 53, 55, 122, 129

**FEC** Forward Error Correction. xii, 3, 31–34, 101, 154

**FSO** Free Space Optics. 2, 5, 6, 8, 9, 14, 16

**GEO** Geostationary Orbit. 1, 6, 11, 35, 90, 118, 121

**GP** Gaussian Process. xxi, xxii, 41–43, 50, 66–72, 81, 84, 86

**LEO** Low Earth Orbit. 1, 6

**LES** Large Eddy Simulation. 127

**MAE** Mean Absolute Error. xxvi, 142, 151

**MI** Mutual Information. xxv, 34, 35, 93, 97, 101, 164, 168, 169

**N-BEATS** Neural Basis Expansion Analysis for Time Series Forecasting. xxiv, 145–147, 151

**N-HITS** Neural Hierarchical Interpolation for Time Series Forecasting. 145, 151

**OGS** Optical Ground Station. xxvi, 7, 35, 36, 121, 122

**PACF** Partial Autocorrelation Function. 105, 106

**PDF** Probability density function. xxii, 58, 59, 61, 72, 78, 81, 82, 93, 105

**PSD** Power spectral density;:. xxii, xxiii, 85–90, 113

**RMSE** Root Mean Square Error. xxvi, 142, 151

**ROP** Reicived Optical Power. 3, 11, 35, 52, 57, 93, 97, 112, 118, 154, 162, 164

**SAOST** Simplified Adaptive Optics Simulation Tool. x, xv, xxi, xxiii, xxvi, 3, 28, 30, 52, 57, 58, 61–63, 65, 79, 80, 99–101, 105, 106, 110, 111, 113, 156, 158

**SMF** Single Mode Fiber. 1, 24, 25, 27, 51, 105, 154

**TKE** Turbulent Kinetic Energy. 132, 135, 148, 151

**WFS** Wave Front Sensor. 26, 27, 155, 156

**WRF** Weather Research and Forecasting Model. xv, 129, 130, 135, 156

# Introduction

In recent years, the demand for efficient and high capacity data transmission between space assets and terrestrial infrastructure has experienced an unprecedented surge driven by the development of space data highways [Hau+19] and upcoming communication mega-constellations [Toy21].

The limitations of current radiofrequency (RF) technologies have become evident in the face of the escalating demands for space-to-ground communication. RF systems, although robust and widely deployed, face critical challenges. They are constrained by limited available bandwidth within allocated frequency bands. For instance, the widely used Ku-band (12 to 18 GHz) offers a maximum downlink data rate of approximately 500 Mbps, while the Ka-band (17.3 to 21.2 GHz) provides around 1 Gbps. These figures, though remarkable in their own right, fall significantly short of the requirements for emerging applications such as high-definition video streaming from space, earth observation data transmission, and the ever-increasing field of internet delivery via satellite.

In addition, spectrum allocation for RF communication is heavily regulated, leading to overcrowding and increased interference in certain frequency bands.

Finally, the non-directional aspect of traditional RF links, on top of making long-distance communications high energy consumption, expose them to eavesdropping and optical jamming. These vulnerabilities are concerning, particularly for applications involving sensitive information, defense, and financial transactions.

In contrast, optical communication systems offer an interesting solution to these RF limitations. These optical links have been massively adopted in space-to-space applications, enabling high-speed inter-satellites and efficient space data relay services, where satellites in Low Earth Orbit (LEO) can quickly transmit data to Geostationary Orbit (GEO) or other LEO satellites equipped with optical terminals.

However, the emergence of ground-based satellite optical links remains a relatively new field, but one which is bound to develop further. It would enable the delivery of high-speed (up to 1 Tb/s), low latency internet access to remote and under-served areas, which are not benefitting from a complete and robust fibre-optic network. Furthermore, the security features of optical communications, which enable directional links and quantum cryptography, make them crucial for military applications.

With the need for high bandwidth comes the necessity to inject the signal into a Single Mode Fiber (SMF) for amplification and/or to enable coherent detection. Deep fluctuations in the injected signal happen due to atmospheric turbulence that causes amplitude variations, i.e. scintillation, and wavefront distortions in the receiver aperture plane.

When it comes to high data rate optical links, most promising mitigation techniques rely on the joint exploitation of aperture averaging associated to AO correction to mitigate injected power fluctuations and the use of numerical interleaving associated to an adequately chosen forward error correction to compensate for remaining signal impairments.

However, no matter how good these methods are, there will always be cases where the weather is unfavourable (cloud cover, absorption) or the turbulence is too strong to hope for a low-latency communication channel without interruptions. The complexity and cost associated with implementing advanced optical correction methods to ensure high-quality corrections are substantial.

In practice,Free Space Optics (FSO) communications projects often rely on extensive networks of ground stations. This strategic approach enables satellites to continually target regions of the globe where favourable weather conditions are predicted. Managing atmospheric transmission and turbulence conditions is indeed a critical factor, and it is addressed through diverse site selection, as discussed in [Pou+14]. However, it's worth noting that, until now, the impact of turbulence on the handover process has not been adequately addressed.

One of the primary goals of this thesis is to provide an assessment of performance, and even predictions, regarding how turbulence influences the handover process. To accurately predict data transmission capacity for network optimisation several tens of minutes ahead is of critical importance as it will enable to manage relatively time consuming operations (optical terminal reorientation, network reconfiguration) without loss of information while accurately predicting data transmission capacity.

Considering the significant variability of turbulence conditions with the location of ground stations, several initiatives has been taken to deploy atmospheric turbulence characterisation instruments of different types, enabling the retrieval of both integrated parameters [Jab21] and high vertical resolution turbulence profiles [Cha+20]. If the relationship between effective communication performance and high resolution $C_n^2$ and wind profiles along the line of sight is well documented at the time, a question arises when it comes to relating integrated turbulence parameters, sometimes measured on a different line of sight, to the effective performance of an optical link. This question is all the more relevant that the optical link being corrected by AO the degree of correction will affect this dependence.

Considering the importance of integrated turbulence parameters in the assessment of AO corrected error budgets, indications exist in favour of a link performance that would depend only on a few integrated parameters. But a relationship between corrected optical link performance and moments of the turbulence has never been clearly established. The exact expression of the correction residuals involves a complex combination of moments of turbulence and wind profile, whose weightings strongly depend on the system parameters. The tractability of analytical expressions raises real challenges for a clear-cut demonstration that integrated parameters are sufficient to characterise optical link availability. Machine learning methods associated with physical performance models might provide crucial indications to answer this question.

It is the major prospect of the work presented in this thesis.

Chapter 1 provides a brief overview of historical free-space optical communications breakthroughs, as well as a description of atmospheric phenomena that impact the link. A focus is set on understanding optical atmospheric turbulence and the main tools for modelling it.

Chapter 2 offers an overview of error correction mechanisms, both adaptive optics and numerical methods. It also introduces SAOST, a numerical model for generating time series of Reicived Optical Power (ROP) after propagation through the atmosphere and correction by AO.

Chapter 3 introduces the state of the art of the machine learning tools that will be used throughout this thesis.

The main results of this work are presented in chapters 4 and 5. Chapter 4 presents how, after identification of 4 turbulence and wind profile moments, we are able, through the use of Gaussian processes, to assess integrally the statistics of a coupled flux time series in the case of a corrected GEO-downlink.

Chapter 5 introduces two non-Gaussian stochastic process generation techniques. These techniques are then used to recover the end user power link margin of the optical link, taking into account FEC and the interleaver.

Throughout Chapters 4 and 5, systematic sensitivity studies were carried out to see the impact of each of the moments on the model. Chapter 6 goes further by investigating the influence of a difference line of sights between atmospheric turbulence characterisation and the optical link performance assessment.

Finally, Chapter 7 presents a preliminary study of the ability to predict the state of turbulence in advance. This is done by using deep neural networks to predict moments at different time horizons. Addition of covariate in the learning process to improve these predictions has also been carried out.

# 1. Free Space Optical Communications

## Contents

1.1. Overview of free-space optical communications breakthroughs . . . . 6
1.2. Atmospheric impairment . . . . . . . . . . . . . . . . . . . . . . . . . . . . 7
  1.2.1. Absorption and scattering . . . . . . . . . . . . . . . . . . . . . . . . . . 8
  1.2.2. Scope of work . . . . . . . . . . . . . . . . . . . . . . . . . . . . . . . 10
1.3. Atmospheric optical turbulence . . . . . . . . . . . . . . . . . . . . . . . . 11
  1.3.1. Kolmogorov theory . . . . . . . . . . . . . . . . . . . . . . . . . . . . . 11
  1.3.2. The refractive-index fluctuation profile: $C_n^2(h)$ . . . . . . . . . . . 13
    1.3.2.1. Structure function . . . . . . . . . . . . . . . . . . . . . . . . 13
  1.3.3. $C_n^2$ in the boundary layer and in the free atmosphere . . . . . . . 14
    1.3.3.1. The boundary Layer . . . . . . . . . . . . . . . . . . . . . . . . 14
1.4. Modelling of the atmospheric turbulence channel . . . . . . . . . . . . . . 16
  1.4.1. Parametric modelling for average behaviour . . . . . . . . . . . . . . 16
    1.4.1.1. Hufnagel-Valley . . . . . . . . . . . . . . . . . . . . . . . . . . 17
    1.4.1.2. Hufnagel-Andrews-Philips . . . . . . . . . . . . . . . . . . . . . 17
  1.4.2. Non parametric/ profile based modelling . . . . . . . . . . . . . . . . 18
    1.4.2.1. Thrope's scale . . . . . . . . . . . . . . . . . . . . . . . . . . . 19
    1.4.2.2. Gladstone . . . . . . . . . . . . . . . . . . . . . . . . . . . . . 19
    1.4.2.3. Tatarski . . . . . . . . . . . . . . . . . . . . . . . . . . . . . . 20
  1.4.3. Experimental considerations . . . . . . . . . . . . . . . . . . . . . . 20

Optical atmospheric turbulence has been of interest in astronomy for centuries and was quite soon identified as a key limiting factor for the optical resolution of astronomical observations.

In his *Opticks* treatise of 1704 [New04], Isaac Newton gives an accurate description of atmospheric turbulence and its impact on space observation, insightful observations at the time:

> *'If the theory of making telescopes could at length be fully brought into practise, yet there would be certain bounds beyond which telescopes could not perform. For the air through which we look upon the stars is in a perpetual tremor, as may be seen by the tremulous motion of shadows cast from high towers and by the twinkling of the fixed stars. The only remedy is a serene and quiet air, as may perhaps be found on the tops of the highest mountains above the grosser clouds.'* (Opticks p.107 (2nd ed, 1719))

Since Newton, nearly every major astronomer has observed the impact of the atmospheric turbulence and contributed to its understanding. Observation site selection became one of the major issues in astronomical research. During the 19th century, astronomers began to conduct mountaintop expeditions to make ever more precise observations. Early researchers, such as Lord Rayleigh (1842-1919) and Vilhelm Bjerknes (1862-1951), developed theoretical models of turbulence that were based on the assumption of small-scale, isotropic, and homogeneous turbulence.

Technological advancements in optics, electronics, and computing at the beginning of the 20th century enabled researchers to better understand the complex physical processes that govern atmospheric turbulence. While a formalism was born with the work of Karl Strehl [Str95] and Fritz Zernike [Zer38], Andrei Kolmogorov proposed his turbulent cascade model [Kol41] in 1941 which is still used today as a basis for all modern models.

The second half of the 20th century was marked by the development of more advanced measurement techniques, including adaptive optics by Horace Babcock [Bab53] and wavefront sensing by Roland Shack [Sha70]. These two methods have significantly improved our ability to characterise and mitigate the effects of atmospheric turbulence on optical systems. The theory of light propagation through a turbulent medium becomes better established during this period with the work of Tatarski [Tat61], Fried [Fri66], Greenwood [Gre77], and Roddier [Rod81].

Despite the fact that understanding atmospheric turbulence remains a significant challenge for physicists, in recent years, with the growing popularity of FSO communications, accurate models of atmospheric turbulence have become necessary to design robust systems and ensure reliable high-speed data transmission through the atmosphere. The challenge is even more demanding as it differs in many ways from what astronomers have been interested in. Turbulence models used by astronomers are often based on average behaviour over relatively long periods of time, on sites selected for their ideal conditions and studied exclusively during night time (apart from solar imaging, for which the observation time slots are carefully selected to limit the impact of turbulence). FSO communications systems, on the other hand, must be designed to operate continuously, day and night, on sites close to network nodes and therefore to densely populated areas.

## 1.1. Overview of free-space optical communications breakthroughs

The first occurrence of FSO communication dates back to 1880 when Alexander Graham Bell and Sumner Tainter invented what they called the optical phone, also known as the photophone [Bel80]. This invention consisted of an optical modulator and a demodulator that enabled the wireless transmission of a wireless voice telephone message at a distance of up to 213 metres. Having anticipated the mass adoption of fibre optics, Bell went so far as to say that the invention was his "greatest achievement [...] greater than the telephone".

Innovations slowly kept pace for 100 years until NASA achieved a breakthrough, in 1992 with the Ground/Orbiter Lasercomm Demonstration (GOLD) demonstrating the first uplink optical communication between a telescopes located at NASA's TMF and the Japanese Engineering Test Satellite (ETS-VI) [WL93]. This feasibility demonstration was quickly followed by Japan's ETS-VI demonstration in 1994, which served as a testament to the viability of GEO downlink optical communication channel achieving 1Mbit/s. This milestone truly underscored the growing interest and investment in lasercom technologies across the global space community[Ara+96].

The early 2000 saw the arrival of the world's first laser inter-satellite link achieved by the European Space Agency (ESA) between the ARTEMIS geostationary satellite and the french LEO observation satellite SPOT 4[FHL91]. The LOLA experiment, funded by DGA, was the first demonstration of a link between a highaltitude aircraft and a geostationary platform reaching 50 Mbp/s links across 40,000 km [Caz+17]. First LEO to ground FSO links appeared later in 2006 with the Japanese space agency OICETS LEO sattelite[Toy+12].

The second decade of the 21st century saw a tremendous amount of space optical links mostly led by NASA and the JAXA. One of the important breakthrough that can be noted is the 385,000 km optical link between ground and the *Lunar Atmosphere and Dust Environment Explorer* done by NASA in October 2013 achieving a 622 Mbit/s downlink and 20 Mbit/s uplink between earth and the moon orbit[Bor+09].

Today, ground-to-space optical links are becoming increasingly available, with the emergence of numerous ground stations operated by institutions as well as the private sector. Tesat's TAOGS, for example, has several hundred links to its credit, testifying to the quality of its optical payload[Sau+16; Ric+17; Hei+18].

Finally, more recently, OA precompensation has been demonstrated with a GEO satellite on Alphasat [Sod+21].

## 1.2. Atmospheric impairment

Due to it's optical nature, the optical link is severely degraded as it propagates through the atmosphere. In this section we will cover the atmospheric phenomena that disrupt the link: cloud cover and the presence of aerosols, absorption, diffraction and diffusion, and atmospheric optical turbulence.

The first and foremost troublesome phenomenon is cloud cover-induced blockage. To overcome this problem, the feasibility of handover on a ground station network has been demonstrated [Pou+14; PCR15]. The location of these stations should ideally be close to the nodes of the network, i.e. close to high population densities. Several studies have investigated the optimal location of these stations by studying the spatial and temporal correlation of cloud cover [Erd+21; Gon+20; FM15]. The existence of sets of meteorologically anti-correlated locations was highlighted, guaranteeing almost systematically that at least one ground station has a clear sky to enable an efficient optical link. In [Fuc+17] and in [Hau+19], it was concluded that an OGS network with 10 OGS was necessary but sufficient to have an annual availability of 99.9%. The proposed network is very similar to the one given as an example in Figure 1.1.

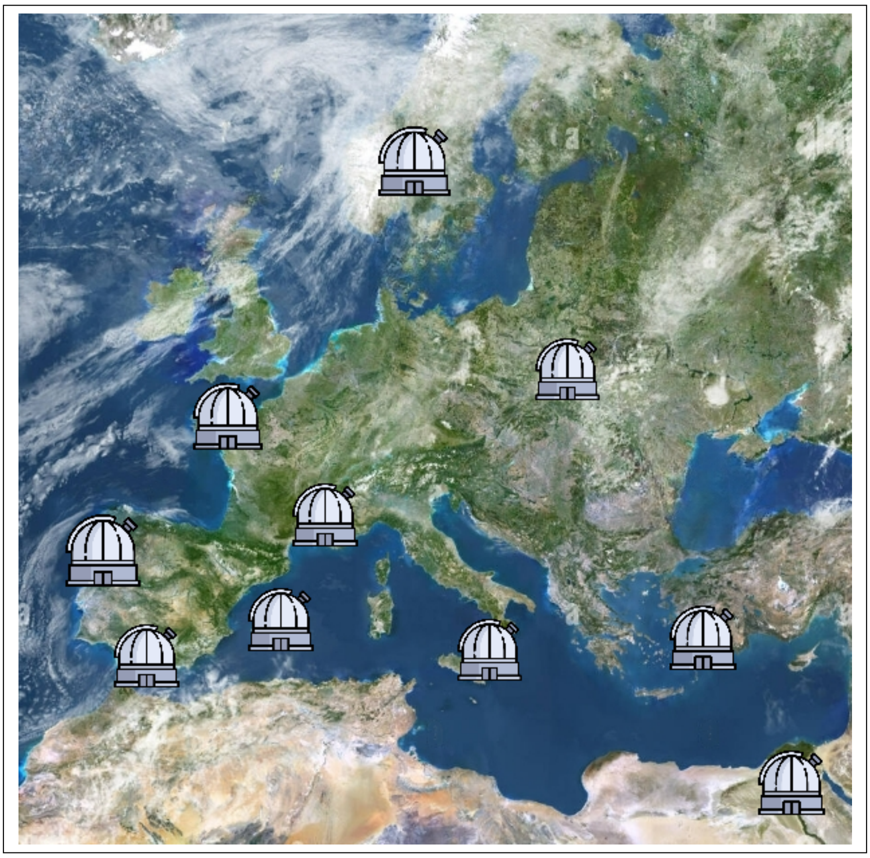

Figure 1.1.: Example of what could be an optimal European ground station network

Up to recently, these studies are limited to estimating clear-sky propagation conditions, with all clouds considered to be totally opaque. In [PCR15] and in [GC19], a more realistic estimate of the availability of the optical link is achieved by taking into account optically thin clouds in the link budgets, as they do not completely attenuate the optical link. The presence of tropospheric aerosols and their impact on the link is also being studied. To this point there are very few attempts in the open literature to validate experimentally the contribution of atmospheric transmission to the link budget, whereas this is currently one of the major question marks remaining in the link budget.

### 1.2.1. Absorption and scattering

Another key phenomenon is the atmospheric absorption of certain wavelengths of electromagnetic radiation. Depending on the molecules and particles present in Earth's atmosphere, some wavelength are more impacted than others as is shown in Figure 1.2.

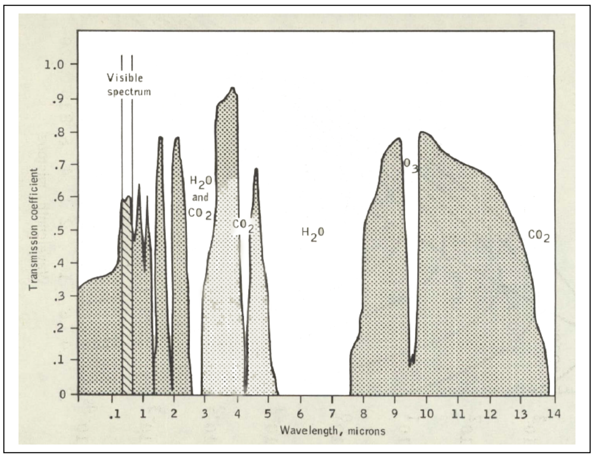

Figure 1.2.: An early atmospheric transmission curve published in "Remote Sensing: A Survey Report" in 1967.

In the rest of this work we consider the usual wavelength used for FSO links: 1550 nanometers. This wavelength is chosen for two main reasons. The first one being that numerous optical components have been developed for this wavelength widely used in land-based optical fibre communication. This availability of low cost, of the shelf, optical transceivers, amplifiers, multiplexers, etc. and the use of existing protocols enables economies of scale and wide compatibility with existing infrastructure. The second reason is that the 1550 nm wavelength falls within a low atmospheric absorption windows in the near-infrared spectrum. This makes it an attractive choice for optical communication because signals at this wavelength can propagate through the atmosphere with higher transmittance and reduced dispersion. On top of that, wavelengths in the 1550 nm range are generally considered eye safe at higher power compared to shorter wavelengths, like those in the visible spectrum.

The region in the near-infrared around 1550 nm corresponds to what is usually called the C band. It ranges from approximately 1530 to 1565 nm. The C band was historically selected for fibre telecommunications because it is conveniently located around the minimum absorption of standard optical fibre (0.2dB / km).

Various molecules and particles in the atmosphere can interact with and absorb specific wavelengths of light. The primary contributors to atmospheric absorption in the C band region include water vapour ($H_2O$), carbon dioxide ($CO_2$), and oxygen ($O_2$).

Absorption of light by these molecules results in vibration of their bonds, and the conversion of the photon electromagnetic energy into internal energy of the absorber. The vibrational modes correspond to energy levels of the molecules allowing them to absorb light at characteristic wavelengths. As a result, one can see massive decline in atmospheric transmission around this given wavelength. (Figure 1.2).

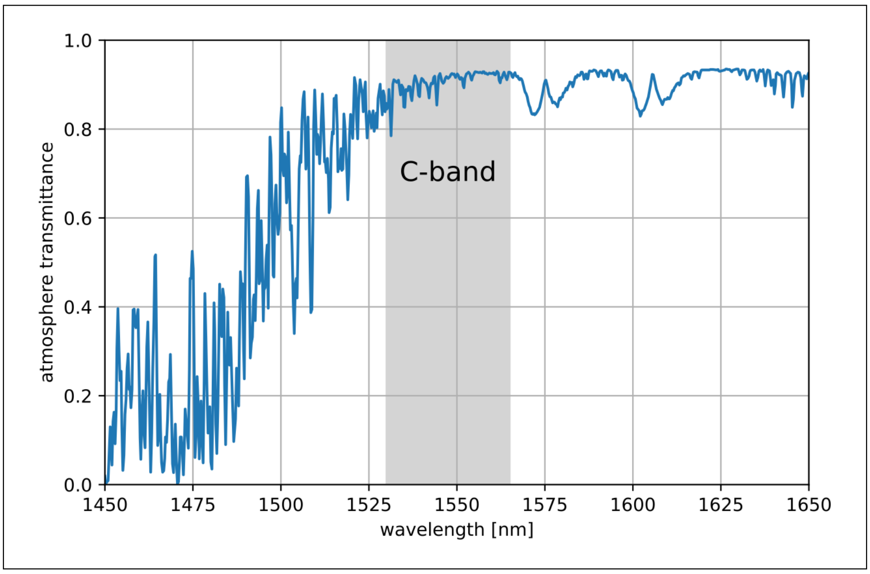

Figure 1.3.: Atmospheric transmittance around the C-band -©Geek3 - Own work, CC BY-SA 4.0

Figure 1.3 shows the atmospheric transmittance for the selected region around the C band, justifying the use of a 1550 nm signal in the case of FSO links operation. The transmittance of 92.4% is given for a vertical transmission of 99 km at mid-latitude for a clear summer day. Reality is a little more complex, with the existence of very fine absorption bands that depend on the elevation. A complete study of the case of optical links can be found in [Art+19].

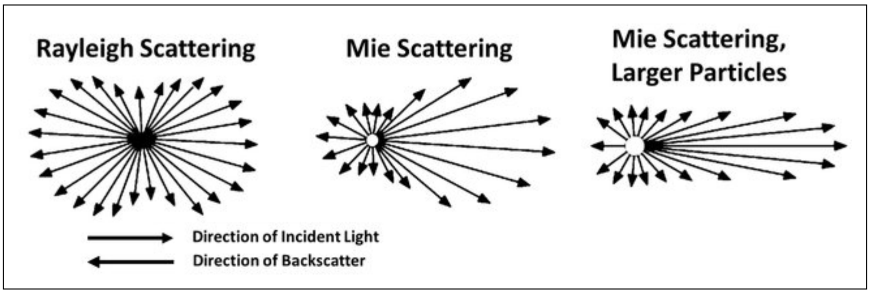

Figure 1.4.: Difference between Rayleigh and Mie scattering (Figure from [Bar20])

In addition to absorption, scattering effects occur due to light interaction with atmospheric particles, leading to changes in its direction and intensity. Figure 1.4, shows the two main types of scattering. The Rayleigh scattering is caused by particles that are significantly smaller than the wavelength, mostly caused by air molecules and mist. The intensity of Rayleigh scattering is proportional to $I \propto \frac{1}{\lambda^4}$. Consequently, in the C band (where the wavelength is large compared to the visible wavelength), the energy dissipated in Rayleigh scattering is almost negligible [AA12].

Mie scattering, on the other hand, is the dominant form of scattering in clear skies conditions [AA12; Sha+15]. It is caused by particles comparable in size to the wavelength, such as aerosols, ice crystals, or volcanic ash.

The value of Mie scattering is according to [Sha+15]:

$$\beta_{\text{scat}} = 1.4244 \times 10^{-9} \frac{1}{\lambda^{1.3}} \tag{1.1}$$

and the atmospheric attenuation roughly equal to $\tau = \mathrm{e}^{-\beta \mathrm{L}}$ according to Beer's law[Bee52], L being the propagation distance. In this case, the scattering is closely proportional to the inverse of the wavelength, which again encourages the use of larger wavelengths.

## 1.2.2. Scope of work

In the rest of this PhD we consider the cloud mitigation techniques to be fully operational, we can for example site the work of Sylvain Poulenard [Pou+14; Fuc+17] that focuses on macro phenomenons and the cloud coverage to manage the handover between stations. We also make the assumption that the attenuation due to absorption and scattering is fully understood.

The following will focus exclusively on the description, modelling and understanding of the atmospheric optical turbulence, the most limiting phenomenon when it comes to high data rate optical link in clear sky conditions.

## 1.3. Atmospheric optical turbulence

Turbulence is a complex three-dimensional phenomenon that occurs when fluid flows, in this case the air, becomes highly irregular and unpredictable.

The study of chaotic fluid flow (turbulence) is, to date, *"the most important unsolved problem of classical physics"* according to Nobel Laureate and theoretical physicist Richard Feynman, a thought shared by Werner Heinzenberg, who was rumoured as having replied to the question what he would ask to God if given the opportunity:

> When I meet God, I am going to ask him two questions: why relativity? And why turbulence? I really believe he will have an answer for the first.

Despite decades of research, there is no universal theory capable of describing accurately the evolution of turbulence. Most of the industrial work is based on computational fluid dynamics simulations (CFD), which are among the most demanding simulations in terms of calculation capacity.

Atmospheric optical turbulence is no exception. It depends on the topography of the ground and its nature, on the wind speed associated with the different layers of the atmosphere, and on fluctuations in temperature and humidity. In short, it depends on all the phenomena that can cause random variations of air density and humidity, quantities on which the refractive index of the air depends.

When the wave propagates through the atmosphere it encounters regions of fluid, of varying sizes, with slightly different refractive index. The incident wavefront, considered to be flat due to the distance from the satellite (at least for GEO), becomes deformed as it passes through the turbulent eddies. The wavefront is so degraded as it approaches the ground that it becomes almost impossible to inject the remaining light into a single-mode optical fibre without massive losses. Therefore, the study of ROP and link availability necessarily requires understanding and simulating the impact of atmospheric turbulence on optical propagation.

### 1.3.1. Kolmogorov theory

Kolmogorov's work on turbulence [Kol41] was motivated by a desire to understand the statistical properties of this complex phenomenon. Base on Lewis Fry Richardson work, he proposed a theory of turbulent cascades that describes how energy is transferred from large scales to small scales in a turbulent flow.

The idea behind the theory of turbulent cascades is that when energy is injected into a fluid flow at a large scale, it dissipates into smaller and smaller scales through a series of eddies or vortexes. This process continues until the eddies are too small to drive new ones and energy is dissipated into heat through viscous forces at the smallest scales. The range of scales over which this energy transfer occurs is known as the inertial range. Within this inertial range, the turbulence is fully developed, meaning that the energy is dissipated primarily through non-linear interactions between different scales of motion.

Kolmogorov proposed that within this range the statistical properties of the turbulence are scale invariant. This means that the statistical properties of turbulence on one scale are similar to those on another scale.

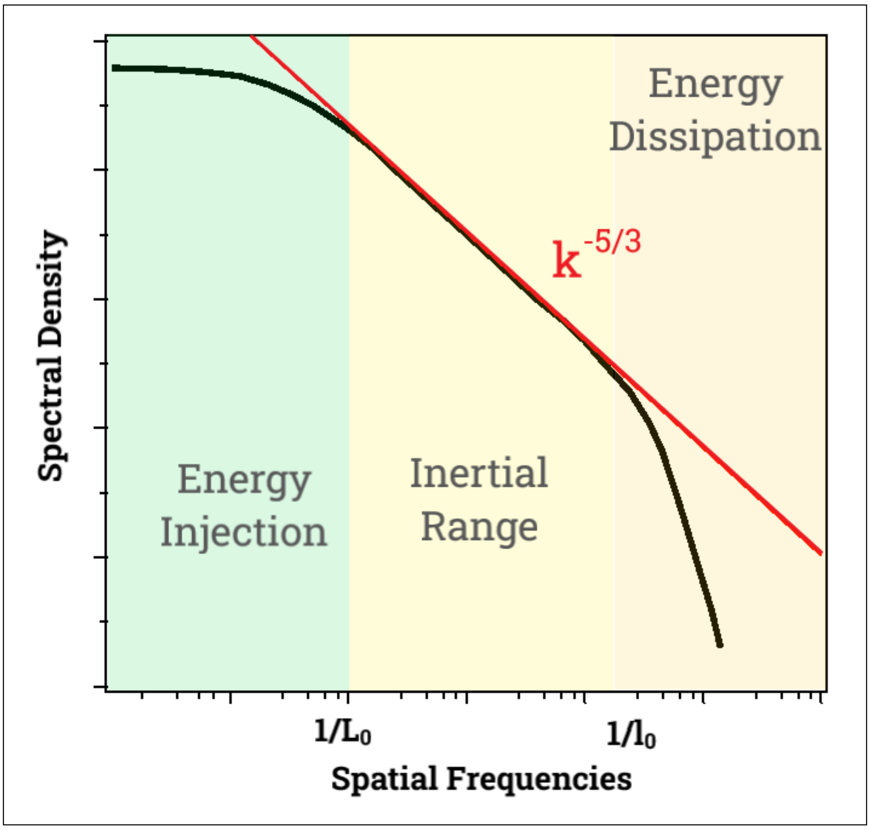

Figure 1.5.: Comparison between the Von Karman Spectrum and the Kolmogorov spectrum

This key result of Kolmogorov's theory is translated in the form of the energy spectrum of turbulence. The energy spectrum describes how the energy is distributed across different scales in the flow. According to Kolmogorov, it should follow a power law of the form $E(k) \propto k^{-5/3}$, where $E(k)$ is the energy spectrum at a given wavenumber k (cf. Figure 1.5). This prediction has since been confirmed through observations and is known as the Kolmogorov -5/3 law.

From this modelling, two quantities emerge. The parameter $L_0$ known as the outer scale corresponds to the characteristic size of the largest eddies. It can also be seen as the size of the phenomenons (meteorological perturbations) allowing for the creation of these first eddies.

The inner scale $l_0$ corresponds to the physical size of the viscosity regime, the eddies below this size contain little energy and enter the dissipation regime of Figure 1.5.

Bellow this length, all the kinetic energy is dissipated to heat because of friction.

Typical size of $L_0$ ranges from meter to tens of meters depending on the distance from ground while $l_0$ ranges from millimetre near ground to the centimetre at higher altitudes.

## 1.3.2. The refractive-index fluctuation profile: $C_n^2(h)$

### 1.3.2.1. Structure function

The impact of atmospheric turbulence on the availability of a free space optical communications link relies in the local fluctuations of pressure and temperature (relative humidity fluctuation do not impact meaningfully the refractive index at optical wavelengths [Rod81]).

This variations are usually described using the second order structure function:

$$D_T(\delta) = \langle (T(\mathbf{r}) - T(\mathbf{r}+\delta))^2 \rangle \tag{1.2}$$

where $T(\mathbf{r})$ is the temperature at a position given by the vector $r$ whereas $\delta$ is a distance in the 3 dimensional space.

This ensemble average can be seen as analogue to a correlation measurement of the temperature over a distance $|\delta|$. The cascade theory limits the measurement of this correlation structure to the inertial range (Figure 1.5) making this description relevant only when $l_0 < |\delta| < L_0$.

In 1949, Alexander Mikhailovich Obukhov showed, based on the work of Kolmogorov, that the temperature structure function follows a power law [Obu+49]:

$$D_T(\delta,\mathbf{r}) = C_T^2(\mathbf{r})|\delta|^{2/3} \text{ ,with } l_0 < |\delta| < L_0 \tag{1.3}$$

where $C_T^2$ is called the temperature structure constant measured in $K.m^{-2/3}$ .

Following this work, Valerian Ilich Tatarski showed in 1961 that the refractive index structure function behaves accordingly [Tat61]:

$$D_n(\delta,\mathbf{r}) = \langle (n(\mathbf{r}) - n(\mathbf{r}+\delta))^2 \rangle \tag{1.4}$$

$$= C_n^2(\mathbf{r})|\delta|^{2/3} \text{ ,with } l_0 < |\delta| < L_0 \tag{1.5}$$

where $C_n^2$ is the refractive index structure constant measured in $m^{-2/3}$.

As we will see in the rest of this work, knowledge of $C_n^2(h)$ for altitude h ranging from the ground level to the end of the stratosphere is crucial in the study of optical link. The sole knowledge of this refractive index constant profile and the associated wind profile enables end-to-end accurate simulation of the effects of the atmosphere on the propagation of an optical wave. One of these models will be discussed in Section 2.2.

### 1.3.3. $C_n^2$ in the boundary layer and in the free atmosphere

Classic description of earth's atmosphere is usually done using five layers even though much more complex descriptions can be found. These layers are the troposphere, the stratosphere, the mesosphere, the thermosphere, and the exosphere ending at the Kármán line set at 100 km above sea level and arbitrary chosen as the limit to outer space. 90% of the mass of the atmosphere in other hands is contained below 16 km (one should note that the exact height of the tropopause vary based on latitude). Even though atmospheric activity remains at higher altitude with, for example, the formation of noctilucent clouds in the mesosphere (between 50 and 80 km), the concentration is so low that relevant $C_n^2$ profiles in the case of FSO communications do not exceed heights of 20 km for a zenith sighting from the ground.

Bellow this height of 30 km are two layers, the troposphere and the stratosphere. The troposphere is the layer ranging from ground level to about 12 kilometers. The higher one goes in the troposphere the lower the temperature gets. It is the layer where most of the meteorological phenomena that we are familiar with occur, with more than 99% of the atmosphere water contained in this range.

The next layer, the stratosphere, is located between 12 and about 50 kilometres. The limit between the troposphere and the stratosphere is characterised by an inversion in temperature because, from this altitude, the higher up one goes, the warmer the temperatures become. This is due to the massive absorption of ultraviolet rays from the sun in the ozone layer that it contains.

#### 1.3.3.1. The boundary Layer

To better describe all turbulent phenomena, another zone should be introduced that differs greatly from the free atmosphere layers described above in the turbulence structures it contains.

The boundary layer is the lowest portion of the Earth's atmosphere; it differs from the so-called free atmosphere, as it is strongly influenced by Earth surface over short time scales.

During the day, the heating of the ground results in convective instability leading to rise of thermal plumes, which behave differently depending on the nature of the terrain. Whereas vegetation absorbs energy (heat) during the day for photosynthesis and re-emits it in the evening, a tarmac surface will tend to radiate heat instantaneously.

The topography also has a major impact because of its influence on air flow speeds and directions, causing for example wind shears.

This boundary layer typically ranges from 100 m above the sea at night to 3 km above a desert at noon. Typical height is given for 1.5 km over land.

To limit the impact of optical turbulence, astronomical observatories are usually installed at high altitudes, the boundary layer on top of a high mountain will be thin and standing above the boundary layer of surrounding areas.

The formation and behaviour of the boundary layer are primarily driven by diurnal (daily) variations in solar heating and longwave radiational cooling. A description of the boundary layer over a diurnal period is visible in Figure 1.6 then described in the following.

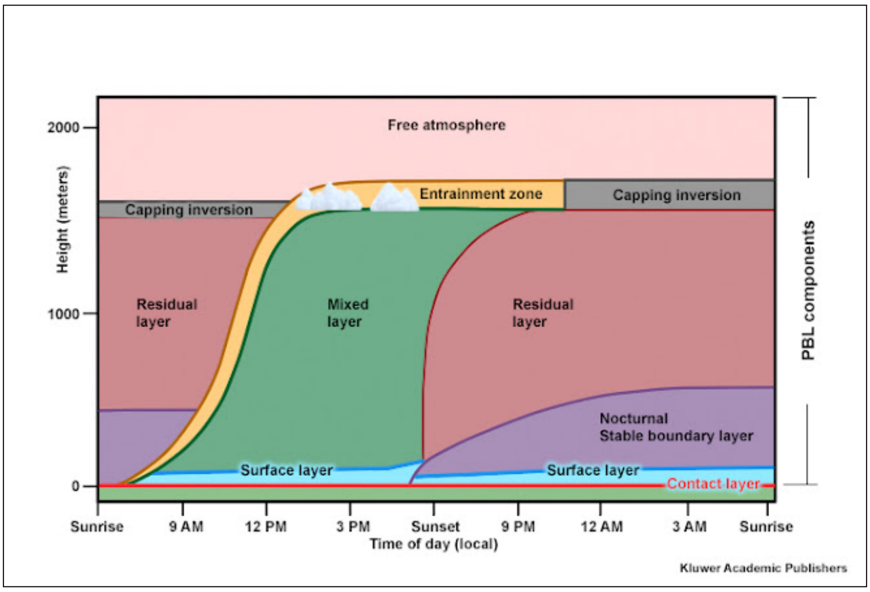

Figure 1.6.: The boundary layer over a diurnal period - *Source: COMET/METED*

The main boundary layer phenomenon is called the convection. It is when the turbulent kinetic energy is converted into potential energy due to warm air moving upward and cooler air downward.

In the first metres, the turbulent kinetic energy generation due to the air-to-ground difference in atmospheric parameters exceeds the convection. The vertical air buoyant motion is limited, it is called the surface layer.

This surface layer is followed during the day by the mixed layer, where strong turbulence occurs due to high wind speed and great thermal activity causing large convection structures (buoyant turbulence).

The rest of the layers has less impact on the $C_n^2$ profiles but for the curious reader definitions can be found in the Glossary of Meteorology of the American Meteorological society.

With typical values found to be around 3 to 4 orders of magnitude larger than in the free atmosphere, modelling the $C_n^2$ in the boundary layer is and will remain one of the main challenge for FSO link assessment. The behaviour of the turbulence in the boundary layer is extremely site dependant. And while the canonical description in Figure 1.6 helps us understand the phenomena involved, there exists no easy exhaustive models to describe the chaotic behaviours that take place. Large-eddy simulation (LES) models can reproduce many traits of observed turbulent flows and are a rapidly growing topic in boundary layer meteorology, however they are extremely computational intensive and hard to parameterize.

High resolution $C_n^2$ measurement can be performed thanks to rather complex instrumentation such as Moon Limb Profiler by night [Ari+20], Sun Limb Profiler [Ari+20], SLODAR (SLOpe Detection And Ranging), SL-SLODAR (surface-layer SLODAR) [Osb+10], SHIMM(Shack-Hartmann Image Motion Monitor) [Per+23], FMCW radars, thermosondes, etc. Such instruments are being deployed to demonstrate high-resolution turbulence characterisation capacity on several sites throughout Europe [Zia+22].

Still many limitations remain. On top of the cost and complexity of such instruments, high resolution $C_n^2$ profile characterisation along the line of sight of the target used (moon, sun or star) differs from the optical links direction.

## 1.4. Modelling of the atmospheric turbulence channel

Over the last three decades, many powerful models have emerged to describe the atmosphere as accurately as possible, especially for meteorological purposes. These models are based on a wide range of data, including local measurements taken by weather stations, satellite or radar images, sounding balloon launches, etc.. These models and instruments though are for meteorological purpose only and do not focus on optical quantities.

This, combined with the difficulty of getting a refractive index measurement over tens of kilometres, led to the creation of multiple models that try to describe the $C_n^2$ accurately using meteorological data.

### 1.4.1. Parametric modelling for average behaviour

The advantage of using parametric models is that it is possible to describe the entire turbulent profile ($C_n^2$) using only the altitude and a small number of parameters. In the literature, two of these parametric models are commonly found. The first is the Hufnagel-Valley model [Huf74; Val80] (HV), a very simple but widely used two-parameter model. The second, derived from it, is the Hufnagel-Andrew-Philips model [And+12a; And+12b] (HAP).

### 1.4.1.1. Hufnagel-Valley

In his 1974 paper [Huf74], Hufnagel introduced the quantity

$$v^2 = \left(\frac{1}{15 \times 10^3}\right) \int_{5\times 10^3}^{20\times 10^3} w^2(h)dh \tag{1.6}$$

where $w$ is the wind speed often chosen using a Bufton wind profile. This quantity was shown to be highly correlated to scintillation index measurement. By transitivity, he showed that the integrated wind profile between 5 and 20km controls the strength of turbulence in the upper layers.

Assuming an exponential decay of the turbulence through the troposphere, the following empirical model was proposed as a description of the $C_n^2$ profile.

$$C_n^2(h) = 2.2 \times 10^{-53} \times h^{10} \left(\frac{v}{27}\right)^2 e^{\frac{-h}{100}} + 10^{-16} e^{\frac{-h}{1500}} \tag{1.7}$$

This two layers model with a single parameter (v) was found to be suitable only for the free atmosphere as the strength of the $C_n^2$ in the boundary layer (below 1 to 3 km) was not accounted for.

This was supposedly solved by the physician Ulrich following the recommendations of Valley [Val80].

The newly introduced Hufnagel-Valley model became a three layer model with two parameters:

$$C_n^2(h) = 0.00594(\frac{v}{27})^2(10^{-5} \times h)^{10} e^{\frac{-h}{100}} + 2.7 \times 10^{-16} e^{\frac{-h}{1500}} + C_n^2(0) e^{\frac{-h}{1000}} \tag{1.8}$$

Where $v$ is according to Hufnagel's definition and the new parameter $C_n^2(0)$ is nothing other than $C_n^2$ at the ground-level.

### 1.4.1.2. Hufnagel-Andrews-Philips

Numerous experiments such as that of Kaimal [Kai+76] show that, in the convective boundary layer, the $C_n^2$ decrease is not exponential but on average in $h^{-4/3}$ during the day and $h^{-2/3}$ at night. This led to the creation of a more realistic model by Andrews and Philips giving their names to the Hufnagel-Andrews-Phillips HAP model [And+12b]:

$$C_n^2(h) = \left(0.00594\left(\frac{v}{27}\right)^2 (10^{-5}h)^{10} e^{\frac{-h}{100}} + 2.7 \times 10^{-16} e^{\frac{-h}{1500}}\right) + C_n^2(0)\left(\frac{1}{h}\right)^{4/3} \tag{1.9}$$

The power law describing the decrease in $C_n^2$ in the boundary layer as a function of the time of day has been later described as follows:

$$p = \begin{cases} -0.11(12-TH)^2 + 1.83(12-TH) - 6.22, & 0.75 < TH < 3.5 \\ 1.45 - 0.02(TH-6)^2, & 3.5 < TH < 8.5 \\ -0.048TH^2 + 0.68TH - 1.06, & 8.5 < TH < 11.25 \end{cases} \tag{1.10}$$

where the temporal hour TH is defined as:

$$TH = \frac{TIME - SUNRISE}{TP} \text{ where } TP = \frac{SUNSET - SUNRISE}{\alpha} \tag{1.11}$$

where $\alpha$ is a parameter of the latitude; leading to a more complete HAP model which remains the reference today:

$$C_n^2(h) = M[0.00594(\frac{v}{27})^2(10^{-5}h)^{10}e^{\frac{-h}{100}} + 2.7\times10^{-16}e^{\frac{-h}{1500}}] + C_n^2(0)(\frac{1}{h})^p \tag{1.12}$$

M being a newly introduced parameter accounting for the background turbulence in the free atmosphere.

More advanced parametric models exist, especially developed in the scope of defence application to describe the ground turbulence and its impact on horizontal communications systems. Some of them, such as PAMELA [Oh+04], go so far as to account for terrain roughness and outer scale length, but require a particularly large set of input parameters to give accurate results.

It should be noted that whatever the parametric model, they will be suitable for describing the average value of the turbulence over a given site, but will not give an instantaneous and accurate turbulence profile description.

It also appears that simpler models such as HAP have often been developed for specific sites at given time of the year and it is not clear to what extent they would be suitable to describe other sites or meteorological conditions.

### 1.4.2. Non parametric/ profile based modelling

As our work aims at characterising the statistics of the instantaneous received optical power and, especially the distribution's tail to describe the probability of interruption, we need to work with a non parametric model based on real world meteorological profile measurements. It will be more suitable to describe any small variation in the turbulence induced by different meteorological conditions and should, in theory, work for any location and any hour of the day.

Such a description can be achieved using Thrope's method, Gladstone's formula, or Tatarskii's theory, among others. In these approaches, the $C_n^2$ profile is calculated from precise vertical profiles of meteorological parameters (temperature, pressure, and often wind speed and wind direction).

#### 1.4.2.1. Thrope's scale

Thrope [Thr77] and Basu [Bas15] proposed a simple approach that relies only on knowing the temperature and pressure profile. Or, to be more accurate, the profile of potential temperature $\theta$ given by:

$$\theta(h) = T(h)\left(\frac{P_0}{P(h)}\right)^{R/c_p} \tag{1.13}$$

Where $P_0$ is the reference pressure (1000 hPa), $R$ is the specific gas constant of dry air (approximately 287 J kg$^{-1}$ K$^{-1}$ and $c_p$ is the heat capacity of dry air at constant pressure (approximately 1005 J kg$^{-1}$ K$^{-1}$.

In an ideal case, without turbulence, the potential temperature is a strictly increasing function with height.

The Thrope length $L_T$ is defined as the length of temperature inversion measured in relation to a strictly ascending profile. In practical terms, it is the distance between a measurement point in the actual profile and the same point in the profile sorted in ascending order. The sorted profile can be seen as a temporal average profile and the Thrope length as the deviations from this average profile. We then have:

$$C_T^2(h) = c_1 L_T(h)^{4/3}\left(\frac{\delta\theta_s(h)}{\delta h}\right)^2 \tag{1.14}$$

Where $c_1$ was obtained by Basu [Bas15] through fitting to experimental measurements and $\theta_s$ the sorted potential temperature.

#### 1.4.2.2. Gladstone

All models such as Ziad's [Zia16], Trinquet's [TV07] and Masciadri's [MVB99] describe the $C_T^2$ are based on the Gladstone formula to recover the $C_n^2$:

$$C_n^2(h) = \frac{80\times10^{-6}P(h)}{T(h)^2}\,C_T^2(h) \tag{1.15}$$

This formula, originally developed for astronomical observations, is powerful as it links the refractive index structure constant to the temperature structure function. Doing so allows a straightforward determination of $C_n^2$. $P(h)$ and $T(h)$, which are the atmospheric pressure and temperature at altitude $h$, are easily measurable as macro-meteorological parameters. The $C_T^2$ can be measured using a differential temperature sensor on board a meteorological balloon, but can also be modelled quite accurately as temperature variations are more predictable than refractive-index ones.

This Gladstone formula relies on the assumption that in the free atmosphere the pressure variations are slow and large as opposed to the temperature variations, making the pressure structure parameter negligible and thus not present in the model. The atmosphere water content has little impact on propagation in the infrared domain, and so any information on humidity is also absent.

We give here a short introduction to Masciadri's $C_T^2$ model, as it will be of use in Chapter 7. Presented in [MVB99], the chosen $C_T^2$ model is:

$$C_T^2(h) = 0.45L(h)^{4/3}\left(\frac{\partial\theta(h)}{\partial h}\right)^2 \tag{1.16}$$

here $\theta(h)$ is the potential temperature introduced previously and $L(h)$ is the Deardoff length, analogous to an outer scale profile. It's parametric form that is derived from a profile of turbulent kinetic energy will be detailed in equation 7.2.

### 1.4.2.3. Tatarski

This outer scale based description of the $C_n^2$ is commonly used and referred to as the Tatarski model from the name of the physicist who introduced it in [Tat71]. The $C_n^2$ profile is computed using:

$$C_n^2(h) = 2.8M(h)^2L_0(h)^{\frac{4}{3}} \tag{1.17}$$

where $M(h)^2 = \left[\left(\frac{79\times10^{-6}P(h)}{T(h)^2}\right)\left(\frac{dT(h)}{dh}+\gamma\right)\right]^2$, $\gamma$ the adiabatic gradient $\approx 9.8\times10^{-3}$ K m$^{-1}$ and $L_0$ is the outer scale profile of the Kolmogorov cascade theory.

An outer scale model that seems particularly promising is the Dewan model[Dew+93]. Based on empirical consideration, this model makes the distinction between the troposphere and the stratosphere as followed:

$$\begin{aligned} L_0(h)^{4/3} &= 10^{1.64+42.0S(h)}\text{(Troposphere)} \\ L_0(h)^{4/3} &= 10^{0.506+50.0S(h)}\text{(Stratosphere)} \end{aligned} \tag{1.18}$$

where S(h) the wind shear can be calculated using the wind speed along both directions in the 2D plane $S(h) = \sqrt{\left(\frac{dV_x}{dh}\right)^2 + \left(\frac{dV_y}{dh}\right)^2}$.

The simplicity of this model lies in the fact that, with only pressure, temperature and wind profiles, we can obtain a full description of the $C_n^2$ profile. It makes it suitable for use with radiosounding data, as they most often do not contain more information (except for the relative humidity).

## 1.4.3. Experimental considerations

Comparison between the different methods of $C_n^2$ profile generation was conducted at the beginning of my PhD using radiosounding data obtained at Tenerife. Even though several papers have found the Thorpe approach and its analog (called the Ellison approach) to be superior than other approaches [Wu+20; Hu+23], best results where, in our case, obtained using Masciadri's or Dewan's model. The little success for the Thrope's scale approach coming from the lack of available sounding resolution. However, this comparison was carried out in more detail and compared to real data in a published proceeding of the Instituto de Astrofsica de Canarias [Mon17], leading to similar conclusions. Therefore, we invite the reader to refer to these results.

However, during this exploratory phase, we used radiosound data operated by the GGCOS Reference Upper Air Network (GRUAN) [Tho+13]. In the measurement process, the balloon goes up to 33 kilometres above ground where it explodes. It makes a measurement of various meteorological quantities every given time period, providing extremely resolved profiles of between six and seven thousand points leading to the modelling of extremely resolved $C_n^2$ profile.

The physical models for calculating the optical power received after propagation of the optical wave through the atmosphere and correction by adaptive optics have a calculation time proportional to the number of layers. The number of layers that allows a simulation to be carried out in a reasonable time is more in the region of one hundred than ten thousands. When trying standard decimation methods to reduce the size of these profiles, it was shown that they led to significant errors in the measurement of the turbulence moments ($r_0$, $\tau_0$ and $\theta_0$ introduced in Chapter 2).

However, in Chapters 4, 5, and 6 it will be shown that, under certain conditions, these moments contain all the information required to describe the power margin of the optical link. These considerations led us to develop a method for decimating the profiles, constructed in such a way as to preserve the moments. This method is fully described in Appendix A.

# 2. Power Margin Calculation From $C_n^2$ and Wind Profiles

## Contents

2.1. Wave propagation and adaptive optics correction . . . . . . . . . . . . . . 23
  2.1.1. Optical propagation and injection . . . . . . . . . . . . . . . . . . . . 23
    2.1.1.1. Single mode fiber coupling . . . . . . . . . . . . . . . . . . . 24
  2.1.2. Adaptive optics . . . . . . . . . . . . . . . . . . . . . . . . . . . . . . 25
    2.1.2.1. The fitting error . . . . . . . . . . . . . . . . . . . . . . . . . 25
    2.1.2.2. The temporal error . . . . . . . . . . . . . . . . . . . . . . . . 26
    2.1.2.3. Aliasing error . . . . . . . . . . . . . . . . . . . . . . . . . . 26
    2.1.2.4. Noise . . . . . . . . . . . . . . . . . . . . . . . . . . . . . . . 27
    2.1.2.5. Non-common path errors . . . . . . . . . . . . . . . . . . . . . 27
    2.1.2.6. Scintillation error . . . . . . . . . . . . . . . . . . . . . . . . 27
    2.1.2.7. Integrated parameters and error budget . . . . . . . . . . . 27
2.2. Modelling received optical power after AO correction . . . . . . . . . . . 28
  2.2.1. SAOST: The Simplified Adaptive Optics Simulation Tool . . . . . 28
2.3. Data reliability mechanisms . . . . . . . . . . . . . . . . . . . . . . . . . . 30
  2.3.1. Modulation . . . . . . . . . . . . . . . . . . . . . . . . . . . . . . . . 30
  2.3.2. Forward error correction . . . . . . . . . . . . . . . . . . . . . . . . 31
  2.3.3. Interleaver . . . . . . . . . . . . . . . . . . . . . . . . . . . . . . . . 32
    2.3.3.1. Mutual information . . . . . . . . . . . . . . . . . . . . . . . 33
2.4. Downlink static link budget . . . . . . . . . . . . . . . . . . . . . . . . . . 35

## 2.1. Wave propagation and adaptive optics correction

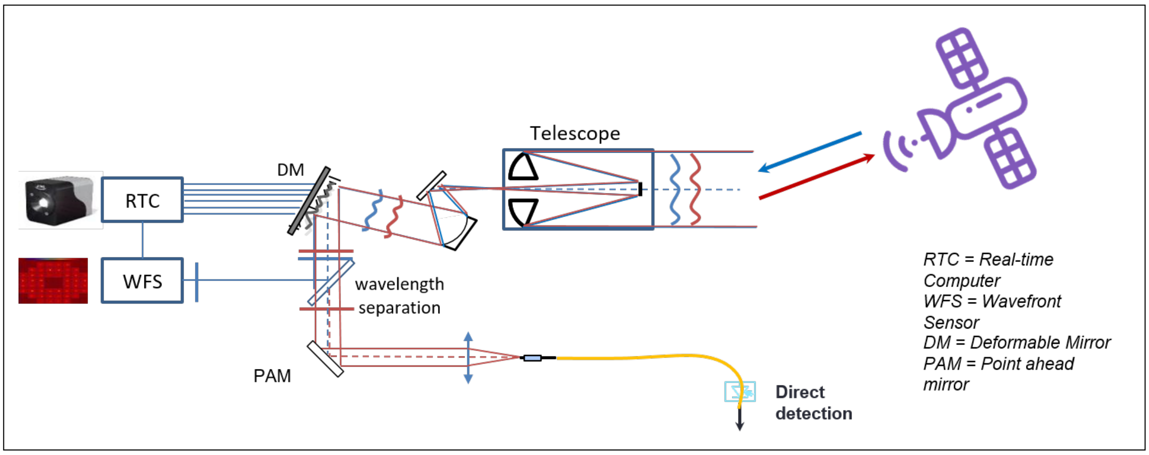

Figure 2.1.: Detection channel of the optical link

### 2.1.1. Optical propagation and injection

In the following we assume the optical field to be a monochromatic plane wave. We consider an optical wave emitted by the optical antenna of a GEO satellite located close to 36,000 km from Earth surface. At this distance, the optical signal received on ground from the satellite is in the far-field region (Fraunhofer region) of the satellite. The received wavefront can thus be approximated by a monochromatic plane wave.

Under this assumption, as any other electromagnetic wave, the optical field obeys Maxwell's laws. The optical signal frequency being much higher than the frequency of the refractive index temporal fluctuation, and the interaction between the different polarization components of the wave being negligible at the considered wavelength, the propagation can be described using the reduced Helmholtz propagation equations:

$$\Delta\Psi(\boldsymbol{r},t)+k^2n^2(\boldsymbol{r},t)\Psi(\boldsymbol{r},t) \tag{2.1}$$

Where $\Delta$ is the Laplacian operator ($\nabla^2$), $\Psi$ is the scalar electric field, $k=\frac{2\pi}{\lambda}$ with $\lambda$ the wavelength is the wave number and $n(\boldsymbol{r},t)$ is the refractive index fluctuation (with respect to its statistical average) at the point represented by its coordinates in space $\boldsymbol{r}$.

This partial differential equation has no analytical solution in the general case, however, one can be found assuming small phase perturbations. The approach consists in solving the scalar Helmholtz propagation equation by a perturbative approach with a perturbation described by the argument of an exponential function:

$$\Psi(\boldsymbol{r},t)=\exp\big(\psi_0(\boldsymbol{r})+\psi(\boldsymbol{r})\big) \tag{2.2}$$

where $\exp\big(\psi_0(\boldsymbol{r})\big)$ is the amplitude of the unperturbed field in an homogeneous media. The analytical expression of $\psi(\boldsymbol{r})$ is given in [Fan75]:

$$\psi(\boldsymbol{r}) = \frac{k^2}{2\pi \exp\big(\psi_0(\boldsymbol{r})\big)} \int_y d\boldsymbol{r}' \delta n\left(\boldsymbol{r}'\right) \exp\big(\psi_0(\boldsymbol{r}')\big) \frac{\exp\left(ik\left|\boldsymbol{r}-\boldsymbol{r}'\right|\right)}{|\boldsymbol{r}-\boldsymbol{r}'|} \tag{2.3}$$

The perturbation regime in which this perturbative approach remains valid is called the Rytov regime. This assumption is supposed to be valid all over the work presented in this thesis. The relevance of this assumption is put into perspective with respect to encountered turbulence conditions at the beginning of Section 4.2.2.

The perturbation term $\psi(\boldsymbol{r},t)$ can be decomposed in:

$$\psi(\boldsymbol{r},t) = \chi(\mathbf{r},t) + j\phi(\mathbf{r},t) \tag{2.4}$$

with $\chi(\mathbf{r},t)$ is the log-amplitude variation caused by the turbulence and $\phi(\mathbf{r},t)$ is the turbulence induced phase variations.

After propagation through the turbulent atmosphere, the perturbed wavefront before the telescope is thus written:

$$\Psi'(\mathbf{r},t) = A_0 \exp\big(\chi(\mathbf{r},t) + j\phi(\mathbf{r},t)\big) \tag{2.5}$$

where $A_0 = \exp\big(\psi_0(\boldsymbol{r})\big)$ is the unperturbed complex field amplitude.

#### 2.1.1.1. Single mode fiber coupling

The complex field focused by the telescope is injected in a SMF to be amplified and detected (see Figure 2.1). The instantaneous coupling efficiency $\rho(t)$ is given by the overlap integral $\Omega(t)$ between the unique Gaussian mode $M_0(\boldsymbol{r})$ of the SMF and the complex wavefront [SR88]:

$$\rho(t) = |\Omega(t)|^2 \tag{2.6}$$

With:

$$\Omega(t) = \frac{\iint P(\boldsymbol{r}) \cdot \Psi'(\boldsymbol{r},t) \cdot M_0^*(\boldsymbol{r}) d^2\boldsymbol{r}}{\left(\iint P(\boldsymbol{r}) \cdot \Psi'(\boldsymbol{r},t) \cdot \Psi'^*(\boldsymbol{r},t) d^2\boldsymbol{r} \iint P(\boldsymbol{r}) \cdot M_0(\boldsymbol{r}) \cdot M_0^*(\boldsymbol{r}) d^2\boldsymbol{r}\right)^{\frac{1}{2}}}, \tag{2.7}$$

and the pupil transmittance $P(\boldsymbol{r})$ given as:

$$P(\boldsymbol{r}) = \begin{cases} 1 & \text{if } 0 \leq \frac{2|r|}{D} \leq 1 \\ 0 & \text{otherwise} \end{cases} \tag{2.8}$$

## 2.1.2. Adaptive optics

An AO system can be used between the telescope and the SMF (see Figure 2.1) to correct the turbulence induced phase variation and thus maximise the coupling efficiency.

The purpose of this part is to give a general understanding of an AO system and to give a sense to the contributors to its error budget, which sometimes involves making gross approximations in their descriptions.

AO is a powerful but imperfect technique and residual phase variation $\phi_{res}(\boldsymbol{r},t)$ remains.

In the Rytov regime, Canuet demonstrated that the mean coupling efficiency $\bar{\rho}$, in a single mode fiber of a corrected optical downlink is [Can+18]:

$$\bar{\rho} \approx \rho_0 exp(-\sigma^2_{\Phi_{res}} - \sigma^2_{\chi}) \tag{2.9}$$

where $\rho_0$ is the instantaneous coupling efficiency in the absence of turbulence and calculated as the overlapping integral of the plane wavefront of the incident beam and the SMF Gaussian mode. $\sigma^2_{\chi}$ is the log-amplitude variance and accounts for the amplitude variations in the receiver aperture (scintillation) not corrected by the AO. $\sigma^2_{\phi_{res}}$ is the residual variance of the phase after correction .

If the errors are assumed to be uncorrelated, the error budget of the AO system is the sum of the following contributors [Fus+06]:

### 2.1.2.1. The fitting error

The fitting error is due to intrinsic limitation of the AO system. The perturbed wavefront is often decomposed on a basis of orthogonal polynomials, called the Zernike polynomials. This basis presents the significant advantage to be described analytically and since the work of Noll a tractable description of the statistical main properties of the atmospheric turbulence projected on the Zernike polynomials has been proposed [Nol76]. Based on this description the uncorrected modes contribution residual variance $\sigma^2_{fitting}$ can be approximated by:

$$\sigma^2_{fitting} \approx 0.458\,(N_{corr}+1)^{-\frac{5}{3}}\left(\frac{D}{r_0}\right)^{\frac{5}{3}} \tag{2.10}$$

where $N_{corr}$ stands for the maximum corrected radial order, that depends on the number of actuators of the mirror, D is the diameter of the receiving aperture and $r_0$ is the Fried parameter. Fried's parameter [Fri66] is defined as the maximum diameter of a telescope whose resolution would be limited by atmospheric turbulence. In the case of a plane wave considering a Kolmogorov spectrum the Fried parameter can be calculated according to:

$$r_0 = \left[0.423\left(\frac{2\pi}{\lambda}\right)^2 \int_0^\infty C_n^2(z)dz\right]^{-\frac{3}{5}} \tag{2.11}$$

where $\lambda$ is the optical wavelength and $C_n^2$ corresponds to the $C_n^2$ along the line of sight.

### 2.1.2.2. The temporal error

AO relies on a close loop operation. If the computing time of the control is none zero, the delay between the measurement and the correction introduces a residual error that affects the controlled modes. This temporal error $\sigma^2_{tempo}$ will increase with the speed of evolution of the turbulence relative to the sampling frequency of the servo-control.

A gross description of this error can be given under the hypothesis of frozen flow where the turbulent wave-fronts are described as frozen and translate across the pupil at the wind speed V, we can write $\sigma^2_{tempo}$ for a turbulent atmosphere composed of a single layer at altitude z as:

$$\sigma^2_{tempo}(\tau, z) = 6.88\left(\frac{V(z)\tau}{r_0(z)}\right)^{\frac{5}{3}} \tag{2.12}$$

In this equation $V(z)$ is the wind speed at altitude $z$ and $\tau$ is the period of the AO servo loop. Looking at the full profile integrated over $z$, $\sigma^2_{tempo}$ becomes

$$\sigma^2_{tempo}(\tau) = \left(\frac{\tau}{\tau_0}\right)^{\frac{5}{3}} \tag{2.13}$$

allowing for the introduction of parameter $\tau_0$:

$$\tau_0 = \left[2.91\left(\frac{2\pi}{\lambda}\right)^2 \int_0^\infty V(z)^{\frac{5}{3}} C_n^2(z)dz\right]^{-\frac{3}{5}} \tag{2.14}$$

when $V(z)$ and $C_n^2(z)$ are given along the line of sight.

$\tau_0$ is known as the turbulence coherence time. It is a fundamental parameter that characterises how quickly the phase of an optical wave changes due to turbulence in the atmosphere.

### 2.1.2.3. Aliasing error

The aliasing error, $\sigma^2_{alias}$ is due to the finite dimensions of the wavefront sensor (Wave Front Sensor (WFS)). The resolution of the spatial sampling of the phase in the pupil is indeed conditioned by the number of micro-lenses in the WFS. Consequently, the high spatial frequencies of the turbulence are poorly sampled and a phenomenon of aliasing occurs.

#### 2.1.2.4. Noise

The noise error, $\sigma_n^2$, comes from the photon noise that disturbs the readings of the WFS and propagates into an additional variance in the AO loop correction.

#### 2.1.2.5. Non-common path errors

Other source of errors are always present in a real system, they can come from vibrations, calibration bias or any other phenomenon that could have an impact on the quality of the correction. In the interest of keeping models simple and presenting a general method, these sources of error are not represented. However, it is important to carry out field experiments to ensure that the system is reliable and that its errors are negligible.

#### 2.1.2.6. Scintillation error

The log amplitude variance $\sigma_\chi^2$ plays a double role in the global coupling efficiency of the system. First, the scintillation leads to a variation of the wavefront amplitude that is not corrected by the AO and directly affects the coupled power into the SMF, the AO correcting only the phase fluctuation. Second, this variation of amplitude deteriorates the readings of the WFS as it assumes a homogeneity of amplitude. Therefore, the scintillation adds measurement noise on the WFS.

The Rytov approximation is valid for weak turbulence, where the fluctuations are small. Under this regime $\sigma_\chi^2$ can be approximated in the following way [Tat61; Fan75]:

$$\sigma_\chi^2 = 0.563 \left(\frac{2\pi}{\lambda}\right)^{\frac{7}{6}} \int_0^\infty z^{\frac{5}{6}} C_n^2(z)\, dz \tag{2.15}$$

According to [GG65; Fan75], $\sigma_\chi^2$ value is accurate when it is less than 0.3, which corresponds to the experimental limit of validity of the small perturbation approximation for horizontal propagation, The case of vertical propagation was not addressed and should be further investigated for an exhaustive study. This formula highlights that the scintillation is a high-order moment and thus influenced by the turbulent layers further away from the receiver.

#### 2.1.2.7. Integrated parameters and error budget

On top of $r_0$, $\tau_0$ and $\sigma_\chi^2$, another integrated parameters of the turbulence will be at use in the following. It is the anisoplanatic angle $\theta_0$ that characterises the angular separation between two points in a field of view where the wavefront distortions induced by atmospheric turbulence become significantly different.

$$\theta_0 = \left[2.914\left(\frac{2\pi}{\lambda}\right)^2 \int_0^\infty z^{\frac{5}{3}} C_n^2(z)dz\right]^{-\frac{3}{5}} \tag{2.16}$$

These four integrated parameters are derived from the calculation of the integral of $C_n^2$ and wind, with different weightings. Similarly, the main contributors to the AO error budget can generally also be expressed using power laws that depend on these same profiles.

A link between the error budget and the integrated parameters may therefore exist, and it is this consideration that has led us, in the remainder of the thesis, to use machine learning to try find a link between the two.

## 2.2. Modelling received optical power after AO correction

Although the Helmholtz equation cannot be resolved analytically along the line of sight, the statistical properties of the field can be resolved locally using a Monte-Carlo approach [MF88]. This allows for end-to-end mobilisations of the propagation and of of closed AO loop but at the expense of computing time, which is prohibitively long for resolved profiles. This does not allow such models to be used on databases with a substantial number of profiles.

### 2.2.1. SAOST: The Simplified Adaptive Optics Simulation Tool

An alternative approach to end-to-end modelling is the use of simplified pseudo-analytical models to represent at least part of the data formation process. When it comes to the simulation of the coupling efficiency, a class of simulation tools, relying on the description of the wavefront perturbations by random draws of appropriately filtered coefficients, gives access to realistic estimations in at least hundred times faster timescales as it would be with end-to-end simulation tools. Such a tool has been developed for the generation of correlated time series of received optical power attenuation due to the telescope aperture truncation and injection into the single mode fiber. Among these tools, we can cite the open source *Fourier domain adaptive optics simulation tool* (FAST) [FTO22] or the ONERA in-house tool called SAOST whose mechanism is described in [Con+19; Véd+16; Can18a].

We call $\rho_\phi$ the coupling efficiency related to residual phase defects and $\rho_I$ the coupling efficiency of the scintillation. Time series of $\rho_\phi$ and $\rho_I$ are supposed to be fully uncorrelated and are generated independently.

The parametric form of $\rho_I$ can be obtained using the following approximation [Can+18, Appendix B]

$$\rho_I \approx \exp\left(-\sigma_\chi^2\right)\exp\left(2\chi_{AP}(t)\right) \tag{2.17}$$

in the weak fluctuation regime (verified in section 4.2.2) of the log amplitude of the electric field in the pupil plane $\chi(r,t)$ where $\sigma_\chi^2$ is the variance of the punctual log amplitude and $\chi_{AP}(t)$ the aperture averaged log-amplitude fluctuations of variance $\sigma_{\chi_{AP}}^2$. The analytic model of $\sigma_{\chi_{AP}}^2$ can be found in [Rob+08].

It has been experimentally verified that the statistics of aperture averaged irradiance is log-normal when the aperture size is bigger than the typical coherence scale of the perturbed field[Tat71; Vet+07], which is the case here. We assume here that the normalised irradiance fluctuations $I(t) = \exp\left(2\chi_{AP}(t)\right)$can therefore be described by the exponent of a normally distributed random variable $\chi_{AP}$ of parameters $\chi_{AP}(t) \sim \mathcal{N}(-\sigma_{\chi_{AP}}^2, \sigma_{\chi_{AP}}^2)$, the average of this normal law being fixed to $-\sigma_{\chi_{AP}}^2$ to ensure energy conservation.

The normalised irradiance distribution, $I(t)$, can then be described as the following log-normal distribution:

$$f_{\rho_I}(x) = \frac{1}{2x\sigma_{\chi_{AP}}\sqrt{2\pi}} \exp\left[-\frac{\left[\ln(x) + 2\sigma_{\chi_{AP}}^2\right]^2}{2(2\sigma_{\chi_{AP}})^2}\right], \quad x > 0 \tag{2.18}$$

$\sigma_{\chi_{AP}}^2$ being computed from the $C_n^2$ and wind profiles in the small perturbations approximation.

The description of $\rho_\phi$ yields a more complex process. The corrected turbulence phase $\phi(\boldsymbol{r},t)$ is decomposed on the Zernike's polynomial basis up to a certain order index $N$ with the Zernike coefficient being $a_i$ for $i = 2, 3, \cdots, N$.

These coefficients $a_i$ are obtained through random draws considering a Gaussian distribution of variance $\sigma_{a_i}^2$. Let $n$ be the number of corrected modes by the AO. If $N \geq i > n$, the modal variance is the one of the uncorrected mode given by Noll's equation [Nol76]. The sum of the modal variance of the uncorrected mode is the fitting error. The number of corrected modes (piston excluded) up to a given radial order $N_{corr}$ can be computed according to:

$$n = \frac{(N_{coor}+1)(N_{coor}+2)}{2} - 1 \tag{2.19}$$

For the corrected modes, the modal variance is obtained by adding the contribution of the aliasing error according to the modal distribution given in [RVL98; Nei08] and the temporal error term whose modal expression is found in [CRM95].

The generation of correlated temporal series is simply done by drawing the random coefficients according to the temporal spectra of the Zernike coefficients given in [CRM95] and the temporal characteristics of scintillation described in [Rob+08].

On the duration of a single time series turbulence conditions are assumed to be stationary. The temporal characteristics of turbulence residuals rely on the frozen flow approximation (temporal evolution of the turbulence is approximated by a lateral translation of a phase screen with spatial statistics described by Kolmogorov's power law). This process neglects by construction the impact of turbulence induced boiling.

SAOST also neglects the influence of non-common path aberrations between the wavefront sensor and the injection path, assumes a perfect wavefront sensor (not sensitive to scintillation), a Zernike description of the correction phase and an infinitely fast deformable mirror (the delay in the loop mostly comes from integration time of the wavefront sensor and calculation of the control voltages sent to the mirror).

Comparison between SAOST and end-to-end models can be found in [Can+18]. Experimental validation has been conducted under relevant conditions for a GEO feeder link and can be found in [Bon+22].

## 2.3. Data reliability mechanisms

Due to cost and technological limitations, AO systems are still imperfect. Furthermore, they only impact the phase error and do not correct scintillation induced fadings. For this reason, numerical methods have to be used allowing for a robust system that would not be impacted by strong fading and loss of bits of data.

On the transceiver part, the signal is coded and modulated. This step is referred to as MODCOD for Modulation and Coding. On top, an interleaver is usually used to introduce randomness in the signal and uncorrelate error bursts.

### 2.3.1. Modulation

The first part of the MODCOD, the modulation, is the process of varying one or more properties of a carrier signal (usually its amplitude, frequency, or phase) in accordance with the information being transmitted. To put it simply, this is the transformation that enables to go from a digital signal in bits to a physical signal that can be sent (electrically or optically).

We can cite two types of modulations that are often used for optical communications, the first is called On-Off Keying (OOK) and the second, Quadrature Phase Shift Keying (QPSK).

In OOK modulation, the bits in the numerical signal (0s and 1s) directly map to the presence or absence of the carrier signal.

- When you want to transmit a "1," you send a signal with a high amplitude.
- When you want to transmit a "0," you send a signal with low amplitude.

In QPSK modulation, the link between the bits of the numerical signal and the modulated optical signal is a bit more complex because QPSK encodes two bits of binary data in each symbol by using different phases of the carrier signal.

- With QPSK, binary data are group into pairs (e.g., 00, 01, 10, 11), and each pair corresponds to a different phase of the carrier signal.
- The carrier signal is then modulated by shifting its phase to one of four possible values (0, $\frac{\pi}{2}$, $\pi$, or $\frac{3\pi}{4}$) based on the binary pair.

This allows to transmit multiple bits simultaneously, making QPSK more bandwidth-efficient than OOK, which transmits one bit per symbol by turning the carrier on or off. On the other hand, the detector must be able to discriminate between the four phase states, which makes it more sensitive to noise than a simple OOK modulation. In the following, only OOK modulation is considered.

### 2.3.2. Forward error correction

In the literature, we find, for the coding, the term FEC for "Forward error correction"[KS10]. This error-correcting code adds redundancy bits to the signal that the receiver uses to correct any transmission errors.

One can define the coding rate as a measurement of the redundancy added to the signal:

$$R = \frac{k}{n} \tag{2.20}$$

where k is the number of information bits which constitute the message and n the number of transmitted bits including the redundancy.

The parameter T is given as the maximum number of errors acceptable for reconstructing the information.

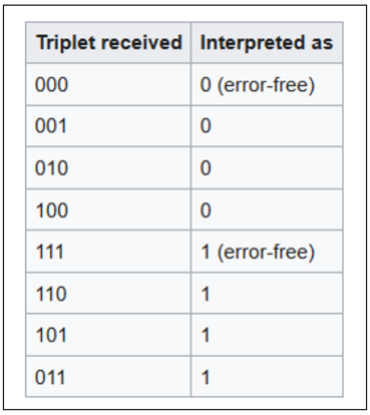

| Triplet received | Interpreted as |
|---|---|
| 000 | 0 (error-free) |
| 001 | 0 |
| 010 | 0 |
| 100 | 0 |
| 111 | 1 (error-free) |
| 110 | 1 |
| 101 | 1 |
| 011 | 1 |

Figure 2.2.: Simplistic example of a 3 bit repetition, R = 3 and T = 1

In the simplistic example of Figure 2.2, the FEC consists of repeating the same bit of information 3 times. In these circumstances, R is equal to three but T is only equal to one.

Throughout the scope of this thesis, two FEC will be studied, one with a lot of redundancy, $R = \frac{3}{10}$, and the other less so, $R = \frac{9}{10}$.

### 2.3.3. Interleaver

The errors in the signal detection are not only errors due to measurement noise but also errors due to propagation through the turbulent atmosphere. The properties of the turbulent channel lead to deep fadings over characteristic times much longer than the period of the carrier signal (duration of a bit). As **R** is generally chosen to be close to one to keep bandwidth high, we are susceptible to attenuations that impede the detection of most or all of a data word, as can be seen in the first line of the bottom of the Figure 2.3. As illustrated on the Figure the bits underlined in red are lost.

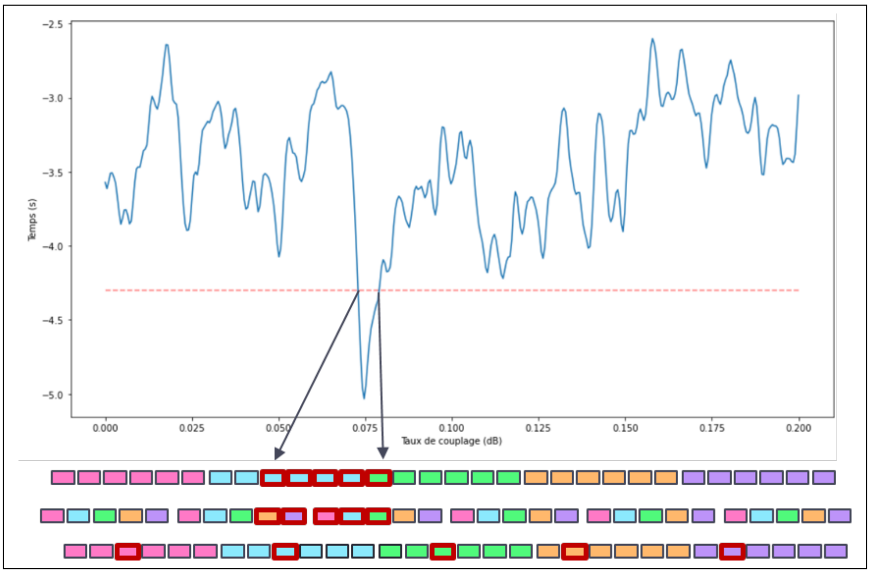

Figure 2.3.: Visualisation of the effect of an interleaver on a turbulent channel

The solution lies in the application of an interleaver, which consists of sending the bits of the same word non-consecutively and therefore interleaved with other words as can be seen in the second line of Figure 2.3.

In doing so, we randomise the error and find ourselves in a case analogous to an uncorrelated channel, with random detection noise. The third line of Figure 2.3 illustrates the reconstruction where the error is distributed over all words and fully rectified by the FEC.

The application of an interleaver introduces latency into the signal, since all bits of information must be received before the word can be reconstructed. All the information corresponding to the interleaving duration shall be buffered to be processed simultaneously. Therefore, a compromise must be chosen between the loss of bandwidth due to the redundancy introduced by the FEC and the latency brought be the interleaver. The characteristics of the channel are at the heart of this compromise.

Several types of interleaver exist but in the following we will only consider a convolutional interleaver, a brief explanation of which is given here.

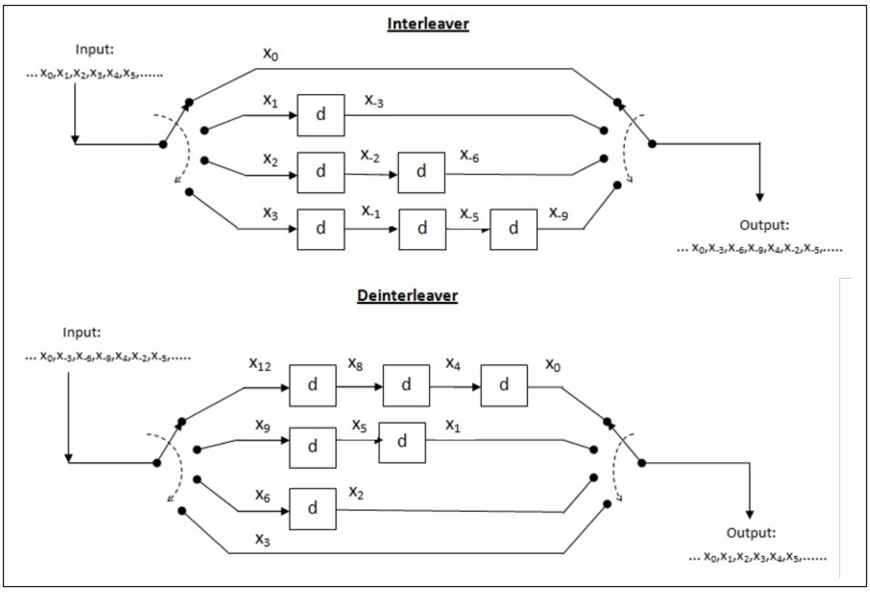

Figure 2.4.: Architecture of a convolutional interleaver and deinterleaver

A convolutional interleaver consists of $n$ delay lines, which are essentially memory elements or buffers. Each delay line can store $d$ symbols. The stream of data bits is distributed across these $n$ delay lines, filling the first delay line first with $d$ symbols, then the next one with $d$ symbols, and so on until the $n$ delay lines are filled.

In the detection part, the data are stored in the same $n \times d$ matrix but this time the output is obtained by reading one symbol of each of the $n$ delay lines in a systematic way until all the interleaved data are generated.

#### 2.3.3.1. Mutual information

Mutual information quantifies the amount of information that can be reliably transmitted. It is a direct measure of how much of the original data's information can be preserved and correctly received at the destination. It is typically denoted as $MI$ and is measured in bits per channel.

Lets assume the following channel

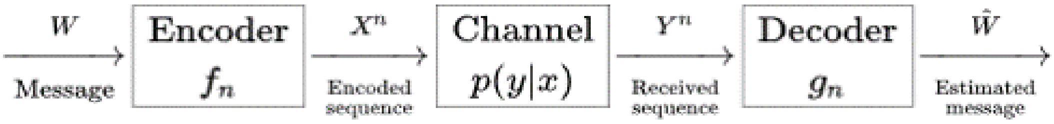

where:

- $W$ is the message to be transmitted;
- $X$ is the channel input symbol ( $X^n$ is a sequence of $n$ symbols) taken in an alphabet $\mathcal{X}$;
- $Y$ is the channel output symbol ( $Y^n$ is a sequence of $n$ symbols) taken in an alphabet $\mathcal{Y}$;
- $\hat{W}$ is the estimate of the transmitted message;
- $f_n$ is the encoding function for a block of length $n$;
- $p(y \mid x) = p_{Y|X}(y \mid x)$ is the noisy channel, which is modeled by a conditional probability distribution of receiving the symbol $y$ knowing that the symbol $x$ was sent.
- $g_r$ is the decoding function for a block of length $n$.

$\boldsymbol{X}$ and $\boldsymbol{Y}$ are random variables.

The mutual information is defined as:

$$I(X;Y) = \sum_{x,y} \mathbb{P}(x,y) \log \frac{\mathbb{P}(x,y)}{\mathbb{P}(x)\mathbb{P}(y)} \tag{2.21}$$

where $\mathbb{P}(x)$ and $\mathbb{P}(y)$ are the marginal distributions.

The choice of MODCOD directly impacts the mutual information of the communication system. Higher-order modulation schemes can transmit more information per symbol, but will be more susceptible to noise and errors resulting in lower MI. In the same way, a more robust MODCOD FEC increases MI by adding redundancy to the transmitted data, but at the cost of lower data rates. Finally the interleaver improves the mutual information by reducing the susceptibility to burst errors but at the cost of latency in the signal.

The required mutual information represents the minimum amount of mutual information that needs to be maintained between the emitter and the receiver to ensure reliable communication. It is determined by the atmospheric conditions, the detection channel (level of noise and interference), and the desired bit error rate. Designing an effective communication system is always a tradeoff between achieving the required MI while keeping the best bandwidth and the lowest latency.

In our study, MI will not be calculated from the analytical expressions and thus we do not make assumptions on the detection channel. Airbus provided the equivalent between the instantaneous ROP and the associated MI from an experimental setup that incorporates the characteristics of the modulation/demodulation chain measured in the laboratory. The optical downlink signal between the on-board terminal described in [Ber+23] and the ESA OGS is considered. The communication chain equipment (Laser Communication Electronic, Modems and Laser Power Electronics) considered are described in [Pou+23] where one can find the equivalence between the ROP and the bit error ratio.

Having access to this information, the determination of the link power margin from a time series of ROP is a straightforward process:

- a correlated temporal series of ROP is generated,
- the corresponding mutual information time series is obtained as a function of ROP,
- the effect of the convolutional interleaver is emulated by applying a moving averaging window over the time series of MI whose size corresponds to the depth of the simulated interleaver,
- if the minimum of the interleaved series of mutual information is higher than the required mutual information, the process is repeated on the time series of ROP with an artificially poorer link budget until the required mutual information is reached.
- The power margin of the link is obtained as the difference between the original link budget and the worst one.

## 2.4. Downlink static link budget

In this thesis, we focus on a high bandwidth (10 Gbps) GEO-downlink telecommunication link. We report here the static losses link budget obtained while considering other losses that those due to atmospheric turbulence.

The downlink link budget in the absence of turbulence is defined as follows.

For the onboard terminal we used the downlink link budget from the paper [Roy+15] and consequently considered a contribution of 110.4 dBW = 0 dBW + 114.1 dB - 3 dB - 0.7 dB to the transmission as presented in Table 2.1.

The channel static losses considered are those proposed in [Pou+14] including fine cirrus clouds and absorption losses with a line-of-sight contribution of -5.4 dB. The free space propagation losses were computed according to [KD74] for a GEO satellite and are -289.85 dB.

| **Parameter** | **Downlink** |
|---|---:|
| Tx diameter [cm] | 25.0 |
| Tx power [W] | 1.0 |
| Tx power [dBW] | 0.0 |
| Tx antenna gain [dB] | 114.1 |
| Tx optical loss [dB] | −3.0 |
| Tx pointing loss [dB] | −0.7 |

Table 2.1.: Onboard terminal link budget contribution

| **Parameter** | **Downlink** |
|---|---:|
| Rx Optical Antenna Gain [dB] | 121.63 |
| Rx Optical Transmission [dB] | −3.6 |
| Rx Static aberration losses [dB] | −0.5 |
| Rx Optical Transmission margin [dB] | −1.0 |

Table 2.2.: OGS link budget contribution

Finally, the ground station budget is the one of the upcoming ONERA's OGS FEELINGS [Cyr+22] given in Table 2.2.

The addition of all this contributors leads to a 15 $\mu$W link budget or −38.33 dBm. This is the value used throughout the remainder of this work.

# 3. Machine Learning for Link Availability Assessment

## Contents

3.1. State of the art of the use of Machine learning for link availability assessment . . . 38
3.2. Usual supervised machine learning techniques . . . 39
3.3. Machine learning for time series prediction . . . 43
  3.3.1. ARIMA . . . 43
  3.3.2. LSTM . . . 45
  3.3.3. Advanced time series forecasting . . . 45
    3.3.3.1. N-BEATS . . . 45
    3.3.3.2. N-HITS . . . 46
    3.3.3.3. Probabilistic forecasting . . . 47
3.4. Sensitivity analysis . . . 47

In this chapter, we aim at providing a brief overview of the machine learning tools that will be used throughout this thesis: metamodels, deep learning models for time series prediction and global sensitivity indices, starting by describing how they have been used on similar problems in the past.

## 3.1. State of the art of the use of Machine learning for link availability assessment

Over the past ten years, some studies have taken advantage of machine learning to estimate atmospheric turbulence or predict temporal changes. Most focus on evaluating $C_n^2$ near the land surface, such as [Bas+20] and [WB16], which propose to use a multilayer perceptron (MLP) trained, respectively, on seven measured meteorological input variables: wind speed, temperature and temperature gradient, soil temperature, relative humidity, net radiation and sol water content, or only five input variables: wind speed, relative humidity, pressure, wind shear and potential temperature gradient. In [Su+20], only four meteorological variables are used: surface temperature, temperature, wind speed, and relative humidity measured at 0.5 m and 2 m. The prediction results are generally accurate but associated with a particular scenario. In addition to these multilayer perceptron metamodels, [Jel+21] compared three other metamodels: polynomial regression, random forest and boosted regression trees with six input variables: air temperature, air-water temperature difference, pressure, relative humidity, wind speed and solar radiation. Best results were obtained with random forest but the predictions were not always accurate.

Some deep neural networks have also been used more recently: in [Lam+20] a ResNet residual network is proposed to retrieve the refractive index structure parameter from the height above sea level and the corresponding wind speed, instead of relying on analytical formulae. The performances are promising, but it would require to collect training data from many different places on earth in order to deliver accurate results. A recent Ph.D. work aimed at forecasting future daytime $C_n^2$ conditions from prior meteorological data: wind speed, pressure, temperature, relative humidity, and solar irradiance and $C_n^2$ measurements [Gro21]. Neural networks (multilayer perceptron and recurrent neural network) are used to create a low-altitude model capable of forecasting $C_n^2$ up to four hours later using sixteen hours of prior measurements. The forecast quality is not always sufficient, best in the middle of the day, moderate in the morning, and generally worst in the evening.
Finally, some recent approaches [Vor+20] use a deep neural network to infer the atmospheric turbulence refractive index structure parameter $C_n^2$ from short-exposure images of turbulence-induced laser beam intensity scintillation.

Other studies focus instead on temporal prediction of the integrated turbulence parameters. Among these we can cite [Mil+19], where turbulence nowcasting, i.e. the ability to forecast the turbulence conditions over the next two hours, is investigated at Paranal Observatory. MLP performed best among the three metamodels tested: random forest, MLP and long short-term memory (LSTM) deep network trained on one or two hours history of meteorological and integrated turbulence parameters such as seeing, coherence time, temperature, pressure, wind speed, and direction. In [Gio+20], a random forest metamodel is trained to predict seeing over the next two hours on a large atmospheric database measured by the Calern Atmospheric Turbulence Station, including ground meteorological conditions, vertical profiles of the $C_n^2$ and integrated parameters characterising the optical turbulence: seeing, isoplanetic angle, and coherence time.

As far as FSO are concerned, machine and deep learning methodology mostly focus on compensating the effects of atmospheric turbulence on the performance of the whole single input single output (or SISO) and multiple input multiple output (or MIMO) FSO system [AKN22] or on predicting parameters of the FSO channel [Esm+21], such as optical signal-to-noise ratio. Closer to the methodology we propose in this paper, two publications aim to predict the RSSI (Received Signal Strength Indicator) of the FSO. In [Tót+18], pressure, air temperature, particle concentration, visibility, relative humidity, and wind speed in different past time horizons are used as input variables for the metamodels. The best results were obtained with the random forest and enabled to retrieve some behavioural patterns of the atmosphere that influence RSSI. [Lio+21] compared different metamodels: k-nearest neighbors, tree-based methods-decision trees, random forest, gradient boosting and MLP trained on seven local atmospheric parameters: wind speed, pressure, temperature, humidity, dew point, solar flux and air-sea temperature difference. Best determination coefficient $R_2$ is 0.949, and is obtained with the MLP metamodel.

## 3.2. Usual supervised machine learning techniques

- KNN

  The k-nearest neighbors algorithm (k-NN) is a non-parametric supervised learning method that can be used both for classification and regression. The concept is quite simple: the class of an input is the most common class among its k nearest neighbors (k is a small integer, typically 3 or 5). In the regression case, its output value is the average of the values of its k nearest neighbors. The best choice of k depends upon the data and must be tuned thanks to hyperparameter optimization. Generally, the distance metric for continuous variables is the Euclidean distance and thus the algorithm is not robust to outliers or noisy features.

- Gradient Boosting

  Gradient boosting is a supervised learning method, and consists in creating multiple weak models, which are typically simple decision trees , and combining them in an ensemble to get a strong metamodel [HTF09]. Starting from a first simple metamodel, it then iteratively improves the prediction by focusing at each new step on the residuals (i.e. prediction errors) from the previous stage and minimizing the loss function by adding weak learners using gradient descent. It can be used either for classification or for regression, using different loss functions, like mean squared error (MSE) for regression and log-likelihood for classification. This method is quite popular for its prediction speed and accuracy, particularly with large and complex datasets.

- MLP

  A neural network can be described as an oriented graph built up from a set of neurons, which are non-linear parametric functions organized in successive layers. These layers exchange informations, but all the neurons of a layer work in parallel. The most used network is the multi hidden layer back-propagation network, or multi-layer perceptron (MLP): the unknown parameters, or weights, are associated to the neurons inputs. The neurons thus simply consist in a non-linear function $F$, the activation function, applied to a potential $\psi$ : $\psi = w_0 + \sum_{i=1}^{N} w_i x_i$ where the $n$ $x_i$ are the input data and the $w_i$ the weights. It can be used for regression and for classification.

  [HSW89] and [Bar93] theorems state that a single hidden layer MLP set up of a finite number of neurons, with the same non-linear activation function, like the hyperbolic tangent, and a linear output neuron, is a parsimonious universal approximator. If we choose the hyperbolic tangent as $n_c$ hidden neurons activation function, the MLP $\varphi$ has the following form:

$$\varphi(x, w) = \sum_{i=1}^{n_c} w_{n_c+1,i} \tanh\left(\sum_{j=1}^{n} w_{ij} x_j + w_{i0}\right) + w_{n_c+1,0} \tag{3.1}$$

  which is not explicit, but parsimonious: there are $q = (n+2)n_c + 1$ weights.

  These $q$ weights $w_j$ are estimated by supervised training: a cost function $J$ with a weight decay penalisation, to prevent large parameters values and thus instabilities, is minimised.

$$J(w) = \frac{1}{2} \sum_{i=1}^{N} \left\| y_i - \varphi(x_i, w) \right\|^2 + \frac{\alpha}{2} \sum_{j=1}^{q} w_j^2 \tag{3.2}$$

  Finding the optimal weights is very difficult in practice, and algorithms only provide local minima of the error function. The generic approach to minimizing $J$ is by gradient descent. In this work, the minimization is done with the L-BFGS algorithm (limited memory Broyden-Fletcher-Goldfarb-Shanno algorithm), described in [LN89], which, at each iteration, makes a variation of the parameter that depends on the gradient and on an approximation of the Hessian of the total squares error.

The framework of the MLP leads to an easy computation of the gradient: it can be computed by a forward and backward sweep over the network, and only the quantities local to each unit have to be kept track of. This algorithm is called backpropagation. In this work, we use the scikit-learn python package to build the MLP metamodel.

- Gaussian Process

  In the field of machine learning, a Gaussian process (GP) is a powerful statistical model that treats functions as random variables. It provides a flexible framework for modeling complex data patterns and making predictions. A GP is defined by the following distribution:

$$f(\mathbf{x}) \sim \mathcal{GP}(m(\mathbf{x}), R(\theta, \mathbf{x}, \mathbf{x}')) \tag{3.3}$$

  Here, $f(\mathbf{x})$ represents a function drawn from a Gaussian process, $m(\mathbf{x})$ is the mean function that captures the expected value of the function at each input $\mathbf{x}$, and $R(\theta, \mathbf{x}, \mathbf{x}')$ is the covariance function (kernel) that captures the pairwise relationships and similarity between input points $\mathbf{x}$ and $\mathbf{x}'$, $\theta$ being the hyper-parameter.

  By utilizing observed data, a GP allows us to compute the posterior distribution over functions that are consistent with the data. This distribution can be used to make predictions at new, unseen input points. The predictive distribution is obtained by conditioning on the observed data, providing estimates of both the expected value and uncertainty of the predictions.

  In this study, we focus on a stationary process $Z$, which means that, for new points, the prediction consists of a linear combination of the observed values, with weights that depend on the distance between the new input point and the training data. The assumption is that, the closer the inputs are, the more correlated the outputs are. The kernel is thus a similarity function.

  **The Radial Basis Function (RBF)** kernel [Buh03] is the most widely used kernel and is nothing more than a squared exponential distance between two given points:

$$R\left(x - x'\right) = \exp\left(-\left\|\mathbf{x} - \mathbf{x}'\right\|^2 / 2\sigma^2\right) \tag{3.4}$$

  with $\sigma$ the kernel length scale. The value of the RBF kernel decreases with distance from one when $x = x'$ to 0 for an infinite distance.

Sums of radial basis functions find use in approximating given functions, this approximation process can be seen as a rudimentary form of neural networks. Recently RBFs started playing a crucial role in GP modeling where they are commonly used as covariance functions. RBF kernel can capture both short-range and long-range dependencies in the data, making it suitable for handling different types of input spaces and complex functions.

**The Matérn** 5/2 **kernel** [RW05, Chapter 4] is a specific form of the Matérn kernel and an extension of the radial basis function kernel. Like the RBF kernel, the Matérn kernel is used to define the similarity or correlation between different input points in the dataset. It computes the similarity of two given points $x$ and $x'$ in dimension $d$ as follows:

$$\begin{aligned} R\left(x-x'\right) = \sigma^2 \Bigg( & 1+\sqrt{5}\sum_{j=1}^{d}\frac{\left|x_j-x'_j\right|}{\theta_j} \\ & +\frac{5}{3}\sum_{j=1}^{d}\frac{\left(x_j-x'_j\right)^2}{\theta_j^2}\Bigg)\exp\left(-\sqrt{5}\sum_{j=1}^{d}\frac{\left|x_j-x'_j\right|}{\theta_j}\right) \end{aligned} \tag{3.5}$$

where the $\theta_j$ (length scales) are the hyperparameters and should be optimized in addition to $\sigma^2$ (variance). It combines a polynomial term and an exponential term to model the correlation between data points. It is known for its smoothness and differentiability up to two times. It is often preferred when there is a need to capture both short-range and long-range dependencies in the data. The kernel function decays rapidly as the distance between points increases, but still allows for some correlation even at larger distances. This property makes it suitable for modeling processes with moderate smoothness and irregularities.

**The constant kernel** is equivalent to a constant value:

$$R\left(x-x'\right) = k\,. \tag{3.6}$$

It is often used as part of a product-kernel where it scales the magnitude of the other kernel or as part of a sum-kernel, where it modifies the mean of the GP. Here we use it only in a product kernel. All the features are standardised by removing the mean and scaling to unit variance before the training of the GP, thus the mean is always 0. By incorporating the constant kernel in the product-kernel, it allows for controlling the overall amplitude or scaling factor of the covariance structure. This can be particularly useful when dealing with data that exhibit different scales or when fine-tuning the influence of different kernel components.

**The white kernel**[RW05, Chapter 4], also known as the white noise kernel, is a covariance function commonly used in GP regression to model measurement errors or uncertainties in the data. It introduces uncorrelated white Gaussian noise to the covariance structure.

Mathematically, the white kernel is defined as follows:

$$R(x - x') = \sigma^2 \cdot \delta(x - x') \tag{3.7}$$

where $\delta$ is the Kronecker delta function, which returns 1 when $x$ equals $x'$ and 0 otherwise. The parameter $\sigma^2$ represents the variance of the white Gaussian noise. This means that the white kernel assigns a non-zero covariance only when the input points $x$ and $x'$ are identical, indicating that there is noise associated with that specific point.

The versatility of GP models lies in their ability to capture a wide range of patterns without imposing specific parametric forms. The choice of covariance function enables the modeling of various types of relationships and dependencies in the data.

This probabilistic model enables the estimation of predictive distributions, providing not only point predictions but also a measure of uncertainty associated with each prediction. This is particularly valuable in situations where having a quantification of the uncertainty is important for decision-making and risk assessment in many real-world applications or further analysis.

## 3.3. Machine learning for time series prediction

### 3.3.1. ARIMA

While ARIMA is not a machine learning algorithm per se, it is commonly used alongside machine learning methods in time series forecasting and analysis. In recent years, there has been a growing overlap between traditional statistical methods like ARIMA and modern machine learning techniques, with practitioners often combining them to achieve more accurate and robust predictions.

ARIMA is a time series forecasting model that combines autoregressive, differencing and moving average components to predict future values based on past observations and patterns. ARIMA, which stands for Autoregressive Integrated Moving Average, is a powerful time-series forecasting model commonly used in various fields to predict future values based on historical observations and patterns. It combines three key components to capture and model the underlying time series data.

The autoregressive component of ARIMA models the relationship between the current value of the time series and its past values. It is mathematically expressed as:

$$X_t = c + \phi_1 X_{t-1} + \phi_2 X_{t-2} + \ldots + \phi_p X_{t-p} + \varepsilon_t \tag{3.8}$$

where,

- $X_t$ represents the current value of the time series at time $t$.
- $c$ is a constant.
- $\phi_1, \phi_2, \ldots, \phi_p$ are autoregressive parameters accounting for the influence of past values on the current value.
- $X_{t-1}, X_{t-2}, \ldots, X_{t-p}$ are lagged values of the time series.
- $\varepsilon_t$ is a white noise error term.

When the time series is non stationnary in the sense of mean (but not variance) the integrated component acts as a differencing step, that can be applied as many time as nescessary to eliminate the non-stationarity. It can be be expressed as:

$$Y_t = (1-B)^d X_t \tag{3.9}$$

where,

- $Y_t$ represents the differenced series at time $t$.
- $B$ is the backshift operator (a delay operator).
- $d$ is the order of differencing required to make the time series stationary.
- $X_t$ is the original time series.

The differenced series $Y_t$ is obtained by applying the difference operator $(1-B)^d$ to the original time series $X_t$. This differencing helps remove trends and make the time series stationary, which is a fundamental requirement for ARIMA modeling.

The moving average component models the relationship between the current value of the time series and past white noise error terms. Mathematically, the MA component can be expressed as:

$$X_t = \mu + \varepsilon_t - \theta_1 \varepsilon_{t-1} - \theta_2 \varepsilon_{t-2} - \ldots - \theta_q \varepsilon_{t-q} \tag{3.10}$$

where,

- $\mu$ is the mean of the time series.
- $\varepsilon_t$ is the white noise error term at time $t$.
- $\varepsilon_{t-1}, \varepsilon_{t-2}, \ldots, \varepsilon_{t-q}$ are lagged error terms.
- $\theta_1, \theta_2, \ldots, \theta_q$ are moving average parameters representing the influence of past error terms on the current value.

In summary, ARIMA combines these three components (AR, I, and MA) to model time series data and make future predictions. The parameters $\phi_i$, $d$, and $\theta_j$ are estimated from the historical data, and the model is used to forecast future values based on the identified patterns and relationships within the time series.

### 3.3.2. LSTM

Long Short-Term Memory (LSTM) [HS97; Lin+21] is a type of recurrent neural network designed for sequence modeling, making it well-suited for time series forecasting and natural language processing.

They work with three main components. The first is called a memory cell, and it allows the LSTM to store and access information over long sequences. The second, the input gate, controls what information is stored in the memory cell. Finally, the output gate determines which information from the memory cell is passed on to the output. It uses a sigmoid activation function in combination with the current input and previous hidden state to decide what to output.

LSTMs process input sequences step by step, updating their memory cell and hidden state at each time step. This allows them to capture patterns and dependencies in sequential data. They are known for their ability to handle both short-term and long-term dependencies, making them a powerful tool.

### 3.3.3. Advanced time series forecasting

Some deep neural network have been specifically designed for time series forecasting. In this area, N-BEATS (Neural Basis Expansion Analysis for Time Series) and N-HITS (Neural Hierarchical Time Series) represent two innovative deep learning architectures that have garnered attention for their ability to capture intricate temporal patterns and dependencies within chronological data. Deep learning methods dedicated to time series are developing fast, our aim here was not to benchmark all the latest methods, but to assess the added value of a high-performance deep method (N-BEATS is ranked 3rd for time series few-shot learning on paperwithcode for the TimeHetNet dataset) compared with more traditional methods such as ARIMA. Our method's choice was guided by available implementation in a widely used python toolbox, such as DARTS.

#### 3.3.3.1. N-BEATS

N-BEATS [Ore+19], characterised by its stack of fully connected layers organised into blocks, stands out for its adaptability in capturing diverse temporal patterns. based on backward and forward residual links Each block consists of a multilayer perceptron and encompasses multiple fully connected sub-layers, each containing learnable basis functions. Another important feature of these blocks is that they are based on backwar and forward residual links, meaning that they learn to predict not only the future data points in the form of a forecast but also to predict the input data as well in the form of a backcast.The backcast output is used to clean the inputs of subsequent blocks, while the forecasts are summed up to compose the final prediction.

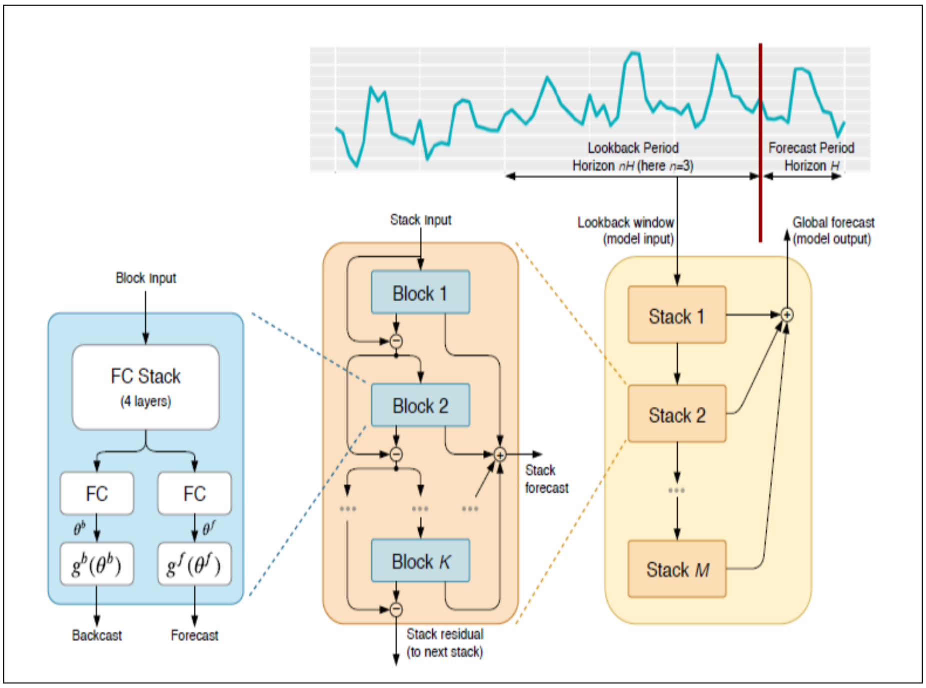

Figure 3.1.: Architecture de N-BEATS, figure issue de [Ore+19]

These basis functions are capable of learning the complex nuances present in the time series, allowing N-BEATS to flexibly use these functions to capture a wide spectrum of temporal behaviours. The blocks are grouped in stacks, and each stack is devoted to learn a different characteristic of the time series. N-BEATS also gives a measurement of uncertainty in its predictions and thus offer a more comprehensive approach.

### 3.3.3.2. N-HITS

Long-horizon forecasting still remains a big challenge for N-BEATS due to prediction volatility and computational complexity. To address this challenge , the Neural Hierarchical Interpolation for Time Series (N-HITS) was created [Cha+22] 3 years later. Built on the foundation of N-BEATS, it introduced innovations oriented towards long-horizon forecasting. N-HITS introduces a hierarchical interpolation and multi-rate input processing approach to specialize its partial outputs across diverse frequencies within the time series. This specialisation, not only enables the accurate prediction of different signal bands, it also lowers significantly memory consumption and computational time.

#### 3.3.3.3. Probabilistic forecasting

In order to increase the confidence in the prediction results obtained, a probabilistic prediction can be performed. Indeed, being able to construct a confidence interval around the prediction value is a crucial issue in the analysis and interpretation of future temporal predictions. The main probabilistic forecasting methods include:

- estimating the parameters of a selected distribution, such as Gaussian. The neural network is trained by minimizing the negative log-likelihood of the training samples. In cases where prior information is accessible, the training process also includes regularization through a Kullback-Leibler divergence term. This regularization helps align the predicted distribution with the one defined by the prior parameters.

- performing quantile regression with chosen quantile values. The neural network is then trained with the pinball loss. This produces an empirical non-parametric distribution. If $\alpha$ is the quantile of interest, $y$ the output and $z$ the quantile forecast, the pinball loss function can be written as:

$$
\begin{aligned}
L_\alpha(y,z) &= \quad (y-z)\alpha \text{ if } y \geq z & (3.11)\\
&= \quad (z-y)(1-\alpha) \text{ if } z > y & (3.12)
\end{aligned}
$$

- using Monte Carlo dropout, which can also be used as a way to capture model uncertainty. Dropout was first used at training time, as a regularisation method to prevent overfitting. The main idea is quite simple: it boils down to randomly removing nodes or neurons during training, thus simplifying the model and preventing it from memorising the training data. Monte Carlo Dropout consists in applying dropout during inference time, in order to produce multiple predictions for a single input.

- using conformal predictions methods adapted to time series. Conformal prediction is a very general method to build predictive intervals for any black-box predictive model, including neural networks, which are valid in the meaning of achieving nominal marginal coverage, built using finite sample, and do not request specific distributional assumptions except that the data are exchangeable. It is a quite popular method on the rise. Of course, as far as time series are concerned, the exchangeability assumption is not met, and different solutions have been proposed to tackle distribution shifts [Zaf+22][XX21][JBA22].

## 3.4. Sensitivity analysis

In this study, we utilise the Sobol' indices [Sob01], also known as variance-based sensitivity analysis, to assess the importance of input variables in the uncertainty of the output. The Sobol' indices, thanks to functional analysis of variance (FANOVA), allow us to decompose the variance of the output of interest, denoted as $Y$, into fractions that can be attributed to each input variable or subsets of variables used in our metamodel. Sobol indices sum to one and are positive and thus can be used to assess the effects of the variables on the output. However, they assume mutual independence between the input variables. In the following, this will not always be verified; nevertheless, some other indices derived from these Sobol' indices and will enable us to rank the input variables based on their contribution to the output uncertainty.

The first-order Sobol' indices, denoted as $S_i$ with $i \in D = \{1, ..d\}$ and $d$ is the number of uncertain inputs, quantify the individual contribution of a specific input variable $X_i$ to the output variance. On the other hand, the total Sobol' indices, denoted as $S_{T_i}$, measure the contribution of the studied input variable $X_i$ to the output variance, accounting for all its interactions with other input variables of any order. Estimating the Sobol' indices is achieved using a Monte Carlo method, and they can be expressed as follows:

$$S_i = \frac{\mathrm{Var}(\mathbb{E}[Y|X_i])}{\mathrm{Var}(Y)} \tag{3.13}$$

$$S_{T_i} = 1 - \frac{\mathrm{Var}(\mathbb{E}[Y|X_{\sim i}])}{\mathrm{Var}(Y)} \tag{3.14}$$

Here, $\mathbb{E}$ represents the expectation (or mean) of the random variables. First-order indices range from 0 to 1, and the difference between 1 and their sum reflects the overall influence of interaction effects. If the total index associated with an input variable is close to zero, it implies that the input has a negligible impact on the output variability and can be set at a constant value. Conversely, Sobol' indices close to one indicate a significant influence of the input variable on the output.

Although Sobol' indices are commonly used to assess the sensitivity of simulation codes to specific inputs, it is important to note that their interpretation becomes challenging when dealing with correlated inputs. In our case, the integrated parameters of the turbulence considered in the following are most likely strongly correlated as they all relate to the moments of the same profiles. To address correlated inputs, methods based on Shapley values from cooperative game theory have been developed [Owe14; SNS16; IP19]. The associated Shapley indices always sum to one, are non-negative, and provide a straightforward and intuitive way to interpret the effects of interactions and contributions of dependencies between the involved inputs on the total output variance. The idea is to redistribute a value $v$ between all players (here the input variables) of a coalition thanks to some allocation scheme. The Shapley effects can be written as:

$$Sh_i = \sum_{A \in P(D); i \in A} \frac{\sum_{B \in P(A)} (-1)^{|A|-|B|} S_B^T}{|A|} \tag{3.15}$$

where $P(D)$ is the power-set of $D$, that is to say the set of subsets of $D$.

However, Shapley effects may sometimes attribute a non-zero part of the output variance to some input that does not contribute at all to the deterministic model, only because it is correlated with influential other inputs [Ioo+21]. In order to address this issue, [Her+22] have proposed to make use of another allocation system, the proportional values [Ort00], and obtained new sensitivity indices called the proportional marginal effects (PME). The PME indices lead to a proportional redistribution of the Sobol' indices: the greater the marginal contribution of the variable, the greater its share of the variance. Moreover, they allow to allocate a null indice to variables that have no link with the output of interest (exogeneous variables), but are correlated to influential variables.

By considering both the Sobol' indices and the Shapley and PME indices, we gain valuable insights into the sensitivity and interplay of input variables, allowing us to understand their influence on the variability of the output in the presence of correlations.

# 4. ROP's Statistics Assessment

## Contents

4.1. Integrated parameters estimation . . . . . 51
4.2. Creating a database . . . . . 53
  4.2.1. ERA5 and Durham University's model . . . . . 53
  4.2.2. Statistical description of the database of profiles . . . . . 56
  4.2.3. The associated database of ROP . . . . . 58
4.3. Estimating the PDF of ROP . . . . . 58
  4.3.1. Methodology . . . . . 61
  4.3.2. Linear regression . . . . . 62
  4.3.3. MLP . . . . . 64
  4.3.4. Gaussian process . . . . . 66
    4.3.4.1. Results: GP on the determination of $\mu$ and $\beta$ . . . . . 66
    4.3.4.2. Analyzing central moments: mean and variance assessment . . . . . 69
    4.3.4.3. Results: Gaussian process combined with adaptive learning . . . . . 69
    4.3.4.4. Results: Gaussian process on the determination of $\sigma^2_{\chi_{AP}}$ 70
    4.3.4.5. Impact of the receiver aperture in the evaluation of the variance term of the integrated intensity on the pupil from $\theta_0$. . . . . . 73
    4.3.4.6. PDF reconstruction . . . . . 77
  4.3.5. Influence of the AO design . . . . . 78
4.4. Results on the half-correlation time . . . . . 84
  4.4.1. Metamodel construction . . . . . 84
  4.4.2. Sensitivity analysis . . . . . 87
  4.4.3. Influence of the AO design . . . . . 88
4.5. Discussions . . . . . 90

Knowledge of turbulence and wind profiles at kilometre vertical resolution along the line of sight guarantees a precise assessment of fading statistics [Can+18] hence an accurate evaluation of optical link performance. However, as discussed in 1.4, measuring accurate $C_n^2$ and wind profiles requires instruments that are both expensive and complex to operate. Despite these challenges, emerging initiatives seek to systematically document integrated turbulence parameters using simpler instruments [Jab21]. Observatories have long been deploying integrated parameter characterisation facilities.

Considering the importance of integrated turbulence parameters in the assessment of AO corrected error budgets, there are indications in favour of a link performance that would depend only on a few integrated parameters, but such a relation between corrected optical link performance and integrated turbulence parameters has never been clearly established. The exact expression of the correction residuals involves a complex combination of the $C_n^2$ profile and the wind moments (Section 2.1.2). Their weightings depend on the AO loop parameters, including the number of corrected Zernike modes, the correction frequency, and the loop delay, among others. Sources of noise for the wave front sensor and the detection channel are also impacted by the values of these integrated parameters.

However, the tractability of analytical expressions raises real challenges for a clear-cut demonstration that integrated parameters are sufficient to characterise optical link availability. Machine learning methods associated with physical performance models might provide crucial indications to answer this question. In the following, we will expose a methodology enabling the user to assess the statistics of the error residuals and the coupled flux in the ground station. This methodology will be tested on different AO cases to assess the dependence of the dimensioning parameters on certain integrated parameters.

## 4.1. Integrated parameters estimation

Our work focusses on the assessment of injected power statistics. It appears that, under certain conditions, the average coupled power into the SMF may be described with a few sets of integrated parameters of the $C_n^2$ and wind profiles. Intuitively we are led to look at the same parameters $r_0$, $\tau_0$, $\theta_0$ and $\sigma_\chi^2$, the most commonly used integrated parameters in asronomical observations. Fried parameter ($r_0$), atmospheric coherence time ($\tau_0$), and isoplanatic angle ($\theta_0$) are leveraged to optimize and dimension AO systems for ground-based telescopes[Har98]. The Fried parameter, representing the scale of turbulence-induced variations in the atmosphere, guides the design of deformable mirrors and the wavelength selection, while a shorter atmospheric coherence time prompts quicker adjustments of the deformable mirror to track turbulence changes. The isoplanatic angle, indicating the angular region with consistent turbulence effects, influences the selection of the field of view. Utilising this information, astronomers can calibrate AO systems for optimal compensation of atmospheric turbulence, resulting in sharper and higher-resolution images of celestial objects.

We aim at showing how these parameters contribute to the error budget of a classic detection channel with an AO system and determine how they could play a role in the prediction of the distribution and the autocorrelation function of the ROP.

These parameters can be estimated using the AO loop information themselves [Fus+04]. In the case of a ground station, however, where the link has not yet been established, they can be provided by easily deployable instruments and give relevant information on the link power margin.

- Experimentally, Fried's parameter can be estimated either from the jitter of a star at the focal plane of an imager or more robustly thanks to differential imaging, such as performed with a DIMM [Tok02].
- The estimation of $\theta_0$ can be derived, for instance, from limited aperture averaged scintillation by night-time [LH79] or thanks to a Shabar measurement by day-time [Bec01].
- The turbulence coherence time $\tau_0$ can be extracted from the temporal analysis of the jitter of a bright enough point source image [Con94].
- Finally, the point source log-amplitude variance $\sigma_\chi^2$ can also be measured. In [Rod81, Chapter 8], it is demonstrated that stellar irradiance fluctuations can be measured through an aperture smaller than their typical scale. During day time, we could consider using the Shabar of [Bec01] to estimate $\sigma_\chi^2$ on the sun.

A study of how a measurement error on the moments impacts the prediction of the link availability will be conducted in 6.

As shown in equation 2.12 and equation 2.16, in the plane wave approximation (used in SAOST), $\tau_0$ and $\theta_0$ are both defined using Fried's parameter $r_0$: we can instead use parameters $\bar{v}$ and $\bar{h}$ that are decoupled from $r_0$, independent of the wavelength and independent of the line of sight:

$$\bar{v} = \left[ \frac{\int_0^\infty v(z)^{\frac{5}{3}} C_n^2(z) dz}{\int_0^\infty C_n^2(z) dz} \right]^{\frac{3}{5}}, \tag{4.1}$$

and

$$\bar{h} = \left[ \frac{\int_0^\infty z^{\frac{5}{3}} C_n^2(z) dz}{\int_0^\infty C_n^2(z) dz} \right]^{\frac{3}{5}} \tag{4.2}$$

where $\bar{v}$ and $\bar{h}$ are related to $\tau_0$ and $\theta_0$ with:

$$\tau_0 = 0.314 \frac{r_0}{\bar{v}} \tag{4.3}$$

and

$$\theta_0 = 0.314 \frac{r_0}{\bar{h}} \tag{4.4}$$

These two parameters have a physical meaning (see Section 2.1.2), while $\bar{v}$ [RGL82], homogeneous to a speed, describes an average wind speed over turbulent layers, $\bar{h}$ [Rod81] is a measure of the height dispersion of atmospheric layers, homogeneous to an altitude. It provides an assessment of the physical origin for the angular decorrelation of the phase perturbations while being independent from the turbulence strength.

## 4.2. Creating a database

In order to describe the received optical power statistics using the previously defined set of integrated parameters from the $C_n^2$ and wind profiles, the best approach is to build a large database of such profiles.

To our knowledge, there is no experimental database available that would be representative of the various atmospheric conditions. Databases such as the one presented in [Osb+18] at Paranal are targeted towards astronomical usage and thus mostly cover night periods in very good turbulence cases in regards of what could be encountered by an optical telecommunication ground station. This leads us to use a database from an atmospheric reanalysis model. Indeed, data provided by numerical models present the advantage of precisely controlling the underlying hypothesis and input parameters at the expense of more questionable relevance.

Our work aims at characterising the statistics of the instantaneous received optical power and especially the distribution's tail, to describe the probability of interruption, we thus need to work with a theoretical model that would describe any small variation in the turbulence induced by different meteorological conditions and would work for any location and any hour of the day.

### 4.2.1. ERA5 and Durham University's model

The database of profiles we exploited was provided by Durham University. Wind and $C_n^2$ profiles were obtained through a global turbulence model, capable of converting meteorological data from a general circulation model into 3-dimensional optical turbulence maps. This model based on Tatarskii's is developed in [OS18][1] and was confronted successfully to on site integrated parameters measurements in Tenerife. It was improved to include a separate boundary layer and enable stronger turbulence strength near the ground to be modelled [OCJ23].

The general circulation model used is ERA5 [Ser19] from European Centre for Medium range Weather Forecasts (ECMWF). This model, from which the turbulence is calculated, has a spatial resolution of 0.3° along latitude and longitude and provides a forecast for every hour. We chose a grid of 11 by 11 points around Tenerife's island (with a spatial resolution of $\approx 30km$), which is a site of interest for a potential future ground station, and focused on the first 19 days of march 2018. It leaves us with 121

---

[1] The equation used by Osborn and Sarazin is dimensionally incorrect, the turbulent kinetic energy is defined as the wind shear in $s^{-1}$. This was pointed out by S. Basu.

simultaneous measurements for each hour, with some missing values. On the overall 19 days considered, we thus have 37059 profiles on 113 pressure levels each. The pressure levels sampling is non-linear such as the resolution is better near ground, as it can be seen in the Figure 4.1.

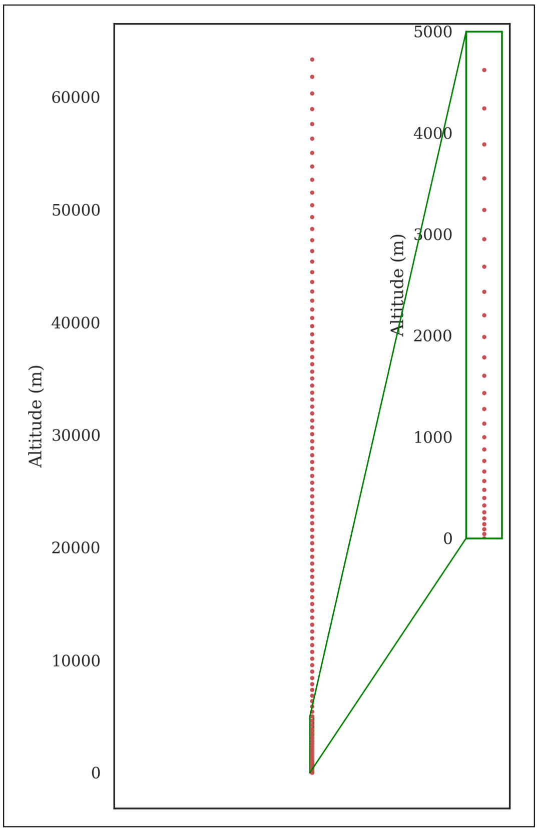

Figure 4.1.: Sampling of the 113 pressure levels of the ERA5 model used, given in altitude above ground. Zoom on the right represents the first vertical 5 kilometres.

The spatial mesh is sufficiently loose to justify the independence between these profiles. In addition, some profiles correspond to a location above the ocean, others above the island, giving access to different environments (see Figure 4.2).

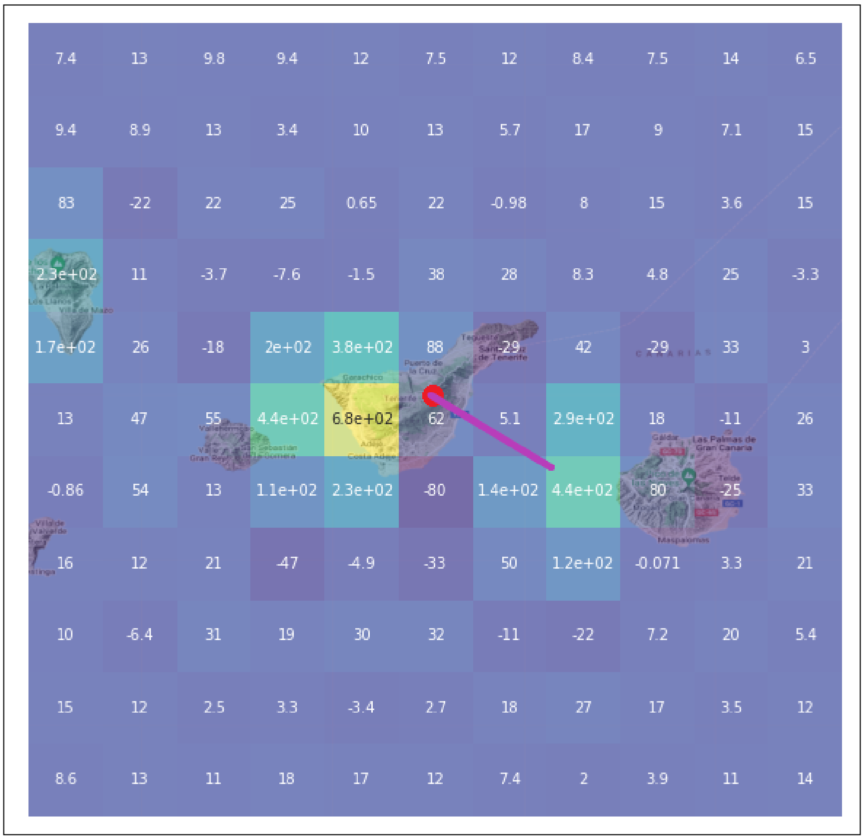

| | | | | | | | | | | |
|---|---|---|---|---|---|---|---|---|---|---|
| 7.4 | 13 | 9.8 | 9.4 | 12 | 7.5 | 12 | 8.4 | 7.5 | 14 | 6.5 |
| 9.4 | 8.9 | 13 | 3.4 | 10 | 13 | 5.7 | 17 | 9 | 7.1 | 15 |
| 83 | -22 | 22 | 25 | 0.65 | 22 | -0.98 | 8 | 15 | 3.6 | 15 |
| 2.3e+02 | 11 | -3.7 | -7.6 | -1.5 | 38 | 28 | 8.3 | 4.8 | 25 | -3.3 |
| 1.7e+02 | 26 | -18 | 2e+02 | 3.8e+02 | 88 | -29 | 42 | -29 | 33 | 3 |
| 13 | 47 | 55 | 4.4e+02 | 6.8e+02 | 62 | 5.1 | 2.9e+02 | 18 | -11 | 26 |
| -0.86 | 54 | 13 | 1.1e+02 | 2.3e+02 | -80 | 1.4e+02 | 4.4e+02 | 80 | -25 | 33 |
| 16 | 12 | 21 | -47 | -4.9 | -33 | 50 | 1.2e+02 | -0.071 | 3.3 | 21 |
| 10 | -6.4 | 31 | 19 | 30 | 32 | -11 | -22 | 7.2 | 20 | 5.4 |
| 15 | 12 | 2.5 | 3.3 | -3.4 | 2.7 | 18 | 27 | 17 | 3.5 | 12 |
| 8.6 | 13 | 11 | 18 | 17 | 12 | 7.4 | 2 | 3.9 | 11 | 14 |

Figure 4.2.: Tenerife with OGS-Rx accurately localized by red dot. The purple line indicate Teleo's operational line of sight at 33,2° . Each coloured squared is a point of the grid at a given time. The value is the ground altitude seen by ERA5 for each of the points.

Past weather observations and model output that the center has gathered and archived over the years is freely available directly on ECMWF website.

In the following, we consider that these profiles are representative of measured data and could be obtained with instruments directly measuring turbulence along the line of sight.

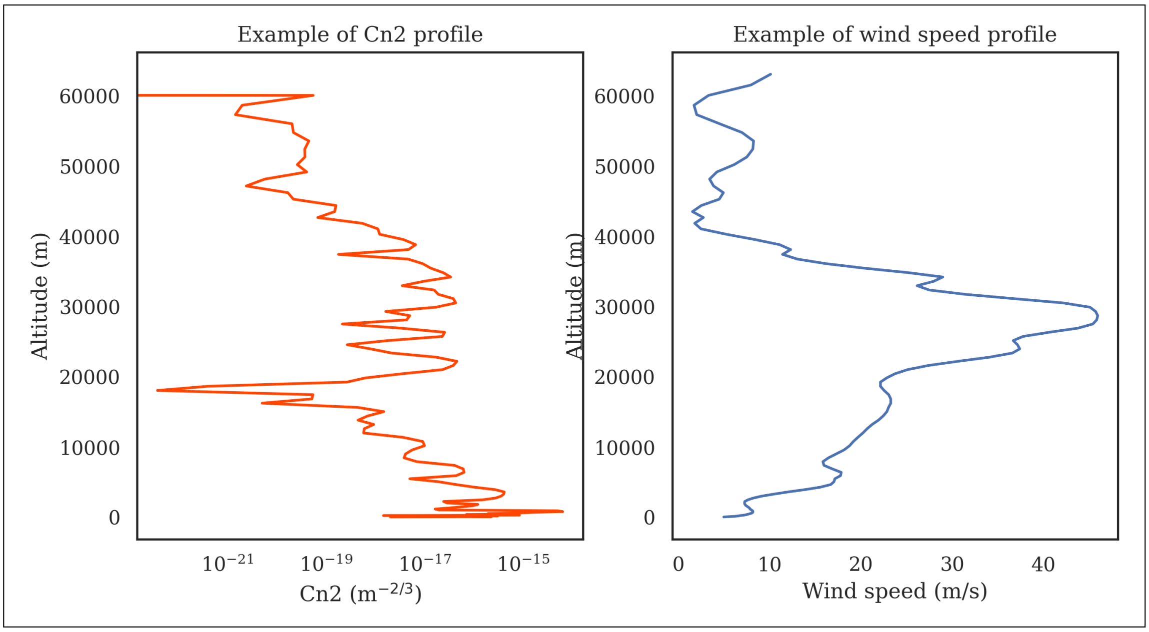

Figure 4.3.: Example of $C_n^2$ (left) and wind (right) profiles from the database. Given for a 30° elevation in meters above ground.

### 4.2.2. Statistical description of the database of profiles

We report in Figure 4.4 the distribution and cumulative distribution of Fried's parameter, $\bar{h}$, $\bar{v}$ and $\sigma_\chi^2$ for all profiles of the database. All evaluations in this section and in the following are done at a 1.55 µm wavelength for a 30° elevation unless stated otherwise.

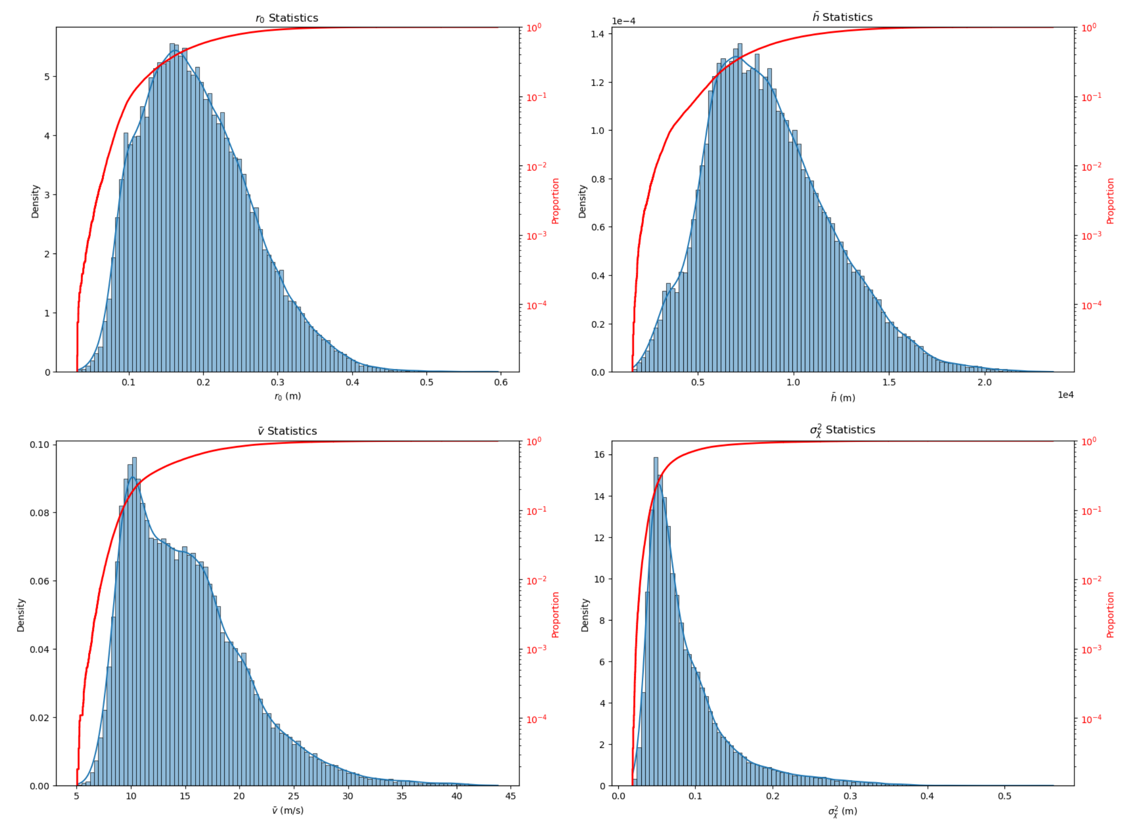

Figure 4.4.: Statistics of the selected integrated parameters of the turbulence for the database presented in section 4.2.1.

The quality of the dataset can be inferred from the variability of the integrated parameters. Even though the selected profiles all belong to the first 19 days of the same month, the range of the integrated parameters is conform to what we could expect from a dataset representative of the diversity of conditions that can be encountered in a real life scenario (see some measurements done at Teide Observatory [Per+06; Sol+13; Gar+09]). With a $r_0$ ranging from a few centimetres up to 60 centimetres, we have profiles considered as representative of very challenging turbulence conditions while the larger values are the one expected from an astronomical site during night time. $\bar{h}$, $\bar{v}$ also show great variability over the whole range of expected values and reinsure us about our ability to have a generalist approach despite the use of a finite dataset.

As one can see in Figure 4.4, point source log-amplitude variance is very rarely above 0.3, which tends to consolidate the Rytov regime hypothesis that is necessary to use SAOST to simulate time series of ROP. Less than 0.05% of our 37059 profiles have a $\sigma_\chi^2 \geq 0.3$. The limit of the Rytov regime has been experimentally fixed for horizontal propagation [GG65] to $\sigma_\chi^2 \approx 0.3$. Horizontal propagation corresponds to a particular configuration where the $C_n^2$ can be considered constant. Vertical path propagation differs from close-to-ground propagation. Several characteristics of the propagation medium, such as the inner and outer scale, might be different to what is experienced few meters from ground and over short distances. Meanwhile, the horizontal propagation case being to some extent a worst case scenario for the slant path, $\sigma_\chi^2 \approx 0.3$ might be considered as a lower bound for the limit of the Rytov regime. This analysis could be consolidated by numerical simulations, however considering the significant ambition of such a study with respect to the small number of cases involved, it should be kept as a perspective work.

### 4.2.3. The associated database of ROP

All the generations of power attenuation's time series have been done with the same parameters of a state of the commercial off-the-shelf AO components. We assume an AO system that corrects the first 10 radial orders with a frequency of 2 kHz. The simulation is done with a time sampling of 4 kHz for a duration of 10 seconds, which gives us 40.000 points per time series. The telescope has a 60 cm diameter.

We adopt in this part the same approach as in SAOST [Can18b], i.e. to consider independently the effects due to the phase error and those due to the scintillation; the benefit of this dissociation is to be able to interpret the results more easily. The same notation as in chapter 2 is chosen with $\rho_\phi$ the coupling efficiency neglecting the impact of scintillation, and $\rho_I$ the term of scintillation. $f_{smf}$, the coupled flux in a single mode fiber, is the product of both.

## 4.3. Estimating the PDF of ROP

We aim to train a machine-learning algorithm that would give us the Probability Density Function (PDF) of $\rho_\phi$ and of $\rho_I$. In a second step, we will also want to estimate the half-correlation time of those quantities. One usual and effective way to describe a distribution using machine learning is to parameterise the PDF and then use a model to estimate the parameters.

From the parametric form of $\rho_I$ detailed in equation 2.18 and 2.17 we can easily deduce that the parametric expression of the $\rho_I$' distribution depends only on the two parameters $\sigma_\chi^2$ and $\sigma_{\chi_{AP}}^2$.

While measuring the punctual log amplitude requires choosing a collector that is small enough to limit the impact of pupil averaging but large enough to provide sufficient flux, measuring the full pupil poses greater implementation difficulties because of the need for a large collector. Since this variance is not easily measurable, we investigate in which extend the assessment of $\sigma_{\chi_{AP}}^2$ is possible using the selected moments $r_0$, $\bar{h}$ and $\bar{v}$.

Regarding the distribution of $\rho_\phi$, we choose to study

$$L_\phi(t) = 10\log_{10}\left(\rho_\phi(t)\right) \tag{4.5}$$

the loss in power induced by the phase fluctuation in dB, as it enables to emphasize the impact of the smaller values of $\rho_\phi(t)$, that are the critical values for the application.

Studying the distribution of $\rho_\phi(t)$ on our 37 k profiles, we highlighted that it has an exponential decay, which is consistent with the closed form of the distribution already proposed by Canuet [Can18b].

If **X** has an exponential decay then $-\log(\mathbf{X})$ follows a standard Gumbel distribution.

We assume that **X** follows a distribution from an exponential family

$$f_X(x|\theta) = h(x)g(\theta)\exp\left[\eta(\theta)T(x)\right] \tag{4.6}$$

with $\theta$ called the parameter of the family, $g(\theta)$ and $\eta(\theta)$ defined functions, $h(x) = x^\gamma$, $T(x) = x^\alpha$ and $\alpha \geq 0$.

Remark:

if $h(x)g(\theta) = \lambda\delta(x > 0)$, $\eta(\theta) = -\lambda$ and $T(x) = x$ with $\lambda > 0$ then $f_X(x|\theta)$ is an exponential distribution.

The PDF of $\mathbf{Y} = -\log(\mathbf{X})$ is expressed as follows:

$$f_Y(y|\theta) = e^{-y}\, h\left(e^{-y}\right) g(\theta)\exp\left[\eta(\theta)T(e^{-y})\right] \tag{4.7}$$

which leads to

$$f_Y(y|\theta) = e^{-(1+\gamma)y} g(\theta)\exp\left[\eta(\theta)e^{-\alpha y}\right] \tag{4.8}$$

It can be reformulated (up to a scale factor) as a Gumbel distribution:

$$f_Y(y|\theta) = \frac{1}{\beta}e^{-(z+e^{-z})} \tag{4.9}$$

with $z = \frac{x-\mu}{\beta}$

We verified numerically that the distribution that best fit the distribution of $L_\phi(t)$, with respect to the Bayesian information criterion (model simplicity vs. data fit) and sum of square error, is a Gumbel distribution of the following form:

$$\frac{1}{\beta}e^{-(z+e^{-z})} \tag{4.10}$$

where $z = \frac{x-\mu}{\beta}$.

This result is particularly interesting as, with the Gumbel distribution being a good enough approximation of the PDF of power attenuation, we can describe the PDF with only two parameters, $\mu$ and $\beta$, that contain all the information on the statistic of power attenuation.

The quality of the fit can be seen by looking at the relative error measured between

| Quantile<br>Relative error | 0.001 | 0.003 | 0.01 | 0.03 | 0.1 |
|---|---|---|---|---|---|
| Mean | 1.43% | 0.91% | 0.57% | 0.37% | 0.19% |
| 1% | 0.02% | 0.01% | 0.01% | 0.01% | 0.01% |
| 50% | 1.17% | 0.75% | 0.48% | 0.33% | 0.17% |
| 99% | 5.36% | 3.28% | 1.92% | 1.14% | 0.54% |

Table 4.1.: Relative errors on quantiles with the Gumbel fit over the 37059 power attenuation's series.

the quantiles of the experimental distribution and those of the theoretical distribution. We show in table 4.1 the statistics of relative error made on some relevant quantiles. The statistics are given for the whole database. Such small relative errors emphasize to which extent our fit is appropriate. It is to be noticed that, the number of data of our simulations being finite, the error on the smallest quantiles can be due to a lack of data to precisely estimate the latest, as much as a non ability of the Gumbel distribution to describe precisely the smallest quantiles. Further work in this regard was not conducted but this is a very encouraging intermediate result that will need to be confirmed in the field. This will require access to a large volume of experimental data, which will be possible by 2024 with the operation of the FEELINGS ground station as part of the first satellite-ground links, for which we will have access to all the hypotheses, conditions, and data.

Figure 4.5 aims at visually illustrating the goodness of the fit in the diversity of conditions encountered. We computed an average value of power attenuation as well as the two extrema.

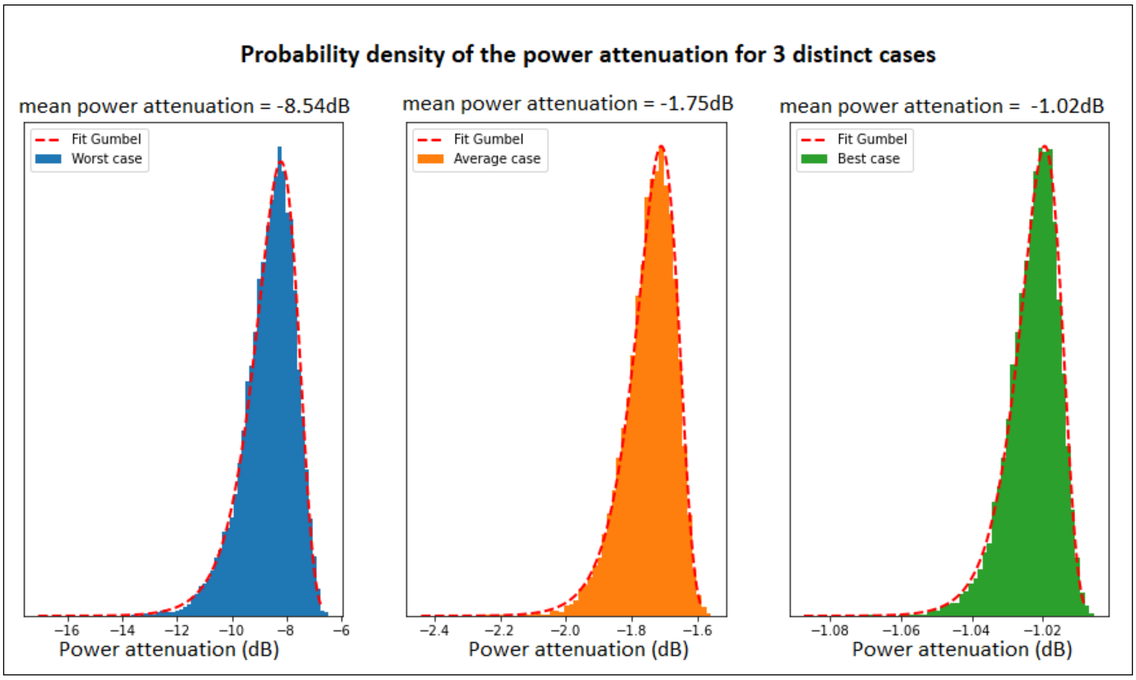

Figure 4.5.: Gumbel fit on the distribution of $L_\phi$ in three cases: first one in blue corresponds to the minimum of coupling efficiency, second one in orange is an average coupling efficiency and last one in green is obtained for the profile with the highest coupling efficiency.

In this section we demonstrated that knowledge of $\mu$, $\beta$ and $\sigma^2_{\chi AP}$, associated with the measured values of $\sigma^2_\chi$, are sufficient and necessary to describe the PDF of the received optical power. As a result, the next sections will focus on the assessment of the 3 unknown parameters $\mu$, $\beta$ and $\sigma^2_{\chi AP}$ using usual machine learning techniques and the set of measured moments as inputs.

### 4.3.1. Methodology

Our database was split in two datasets: one training set containing 10% of the randomly selected profiles and a test set containing the remaining 90%. The results of the regression is presented in figure 4.6 for the assessment of $\mu$ and $\beta$ and in figure 4.7 for the assessment of $\sigma^2_{\chi AP}$. The formalism used for the figure is the same one that will be used for any future model. It contains only the points from the test set, the abscissa corresponds to the value obtained with the numerical direct model SAOST and the ordinates gives the output of the machine learning metamodel. When the ordinate is equal to the abscissa, the prediction of the metamodel is nearly perfect and all points are on the diagonal (red dashed line). The deviation from the diagonal is related to the prediction error of the metamodel. To compute it we rely on the coefficient of determination $R_2$, which stands for the percentage of the output variance explained by the metamodel, but computed on $n$ test data $Y_i$ instead of training ones (it is traditionally named $Q_2$ in machine learning papers):

$$R_2 = 1 - \frac{\sum_{i=1}^{n}(Y_i - \hat{Y}_i)^2}{\sum_{i=1}^{n}(Y_i - \bar{Y})^2} \tag{4.11}$$

where $\bar{Y}$ is the mean of the test data and $\hat{Y}_i$ stands for the output of the metamodel for the same input values as $Y_i$. $R_2$ is between 0 and 1, and should be close to 1 for an accurate metamodel prediction.

## 4.3.2. Linear regression

Figure 4.6 to figure 4.9 are here to present a baseline and validate our prior intuitions. Figure 4.6 and 4.7 show the results of the simplest model one can think of, the linear regression. Inputs of the linear regression are $r_0$, $\bar{h}$ and $\bar{v}$ and the output is either an assessment of $\mu$, $\beta$ or $\sigma$. Visually and through the $R_2$ score, one can see that the results are unsatisfactory, even though a trend exists for small values of $\mu$ and large values of $\beta$, which correspond to a case of strong turbulence (low average coupled flux with a high variance).

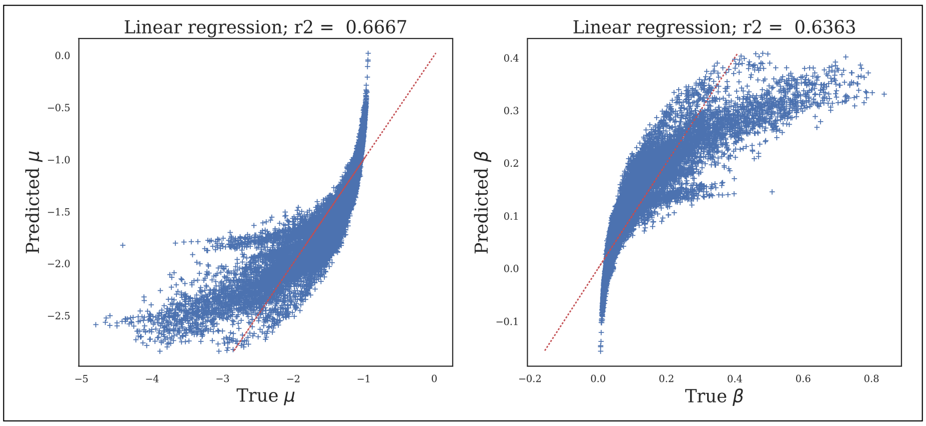

Figure 4.6.: Linear regression on $r_0$, $\bar{h}$ and $\bar{v}$ to assess the values of $\mu$ (left) and $\beta$ (right). Simulated value (SAOST) in abscissa, output of the model in ordinate. Only for the test set.

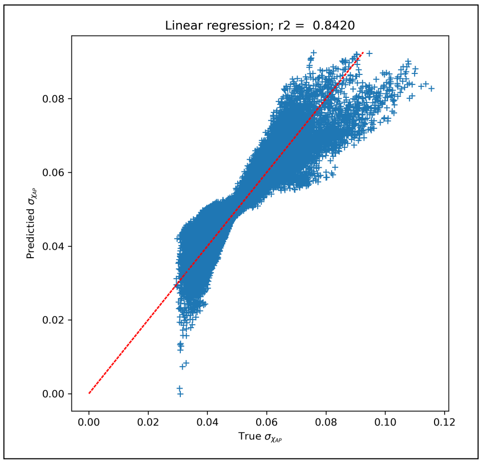

Figure 4.7.: Linear regression on $r_0$, $\bar{h}$ and $\bar{v}$ to assess the values of $\sigma_\chi^2$. Simulated value (SAOST) in abscissa, output of the model in ordinate. Only for the test set.

The first test to improve this prediction was to make the linear regression on $\frac{1}{r_0}^{5/3}$, $\bar{h}^{5/3}$ and $\bar{v}^{5/3}$ instead of $r_0$, $\bar{h}$ and $\bar{v}$ (Figure 4.8 and 4.9). We expect the results to be better as the error budget of the AO depends linearly on $\frac{1}{r_0}^{5/3}$, $\bar{h}^{5/3}$ and $\bar{v}^{5/3}$ under strong simplification (see the section about the error budget of an AO 2.1.2). As expected, the $R_2$ score on $\mu$ and $\beta$ which fully describes the turbulent phase is increased by almost 25% in each case (Figure 4.8). The change in the input variables does not have a positive impact on the prediction of the scintillation, but there was no indication in this sense either.

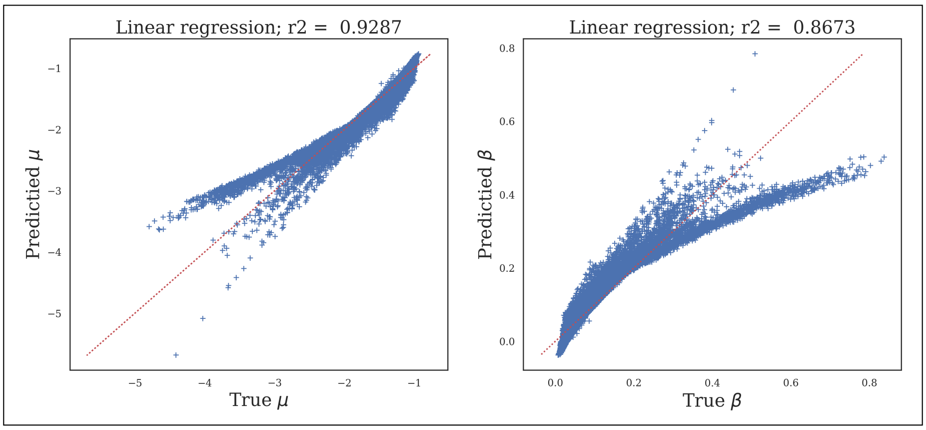

Figure 4.8.: Linear regression on $\frac{1}{r_0}^{5/3}$, $\bar{h}^{5/3}$ and $\bar{v}^{5/3}$ to assess the values of $\mu$ (left) and $\beta$ (right).

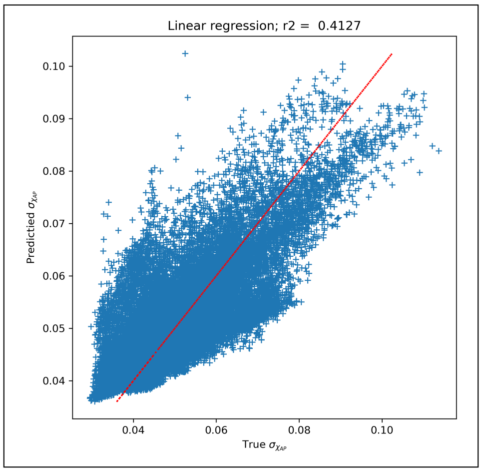

Figure 4.9.: Linear regression on $\frac{1}{r_0}^{5/3}$, $\bar{h}^{5/3}$ and $\bar{v}^{5/3}$ to assess the values of $\sigma^2_\chi$

### 4.3.3. MLP

In order to improve the prediction quality, we focused on non-linear metamodels, and first on a Multi-layer Perceptron regressor (MLP). Different configurations where tested with 1 to 3 hidden layers and either 20, 50 or 100 neurons per layer. In each of the cases 3 functions were tested as the activation layer:

- A logistic sigmoid function: f(x) = 1 / (1 + exp(-x))
- A tanh (or hyperbolic tan) function: f(x) = tanh(x)
- A rectified linear unit function (relu): f(x) = max(0, x)

Starting with the normalised values of $r_0$, $\bar{h}$ and $\bar{v}$ as inputs, we found that the best prediction score is obtain for a 3 hidden layers model with 50 neurons per layer and a tanh activation function resulting in the prediction of figure 4.10.

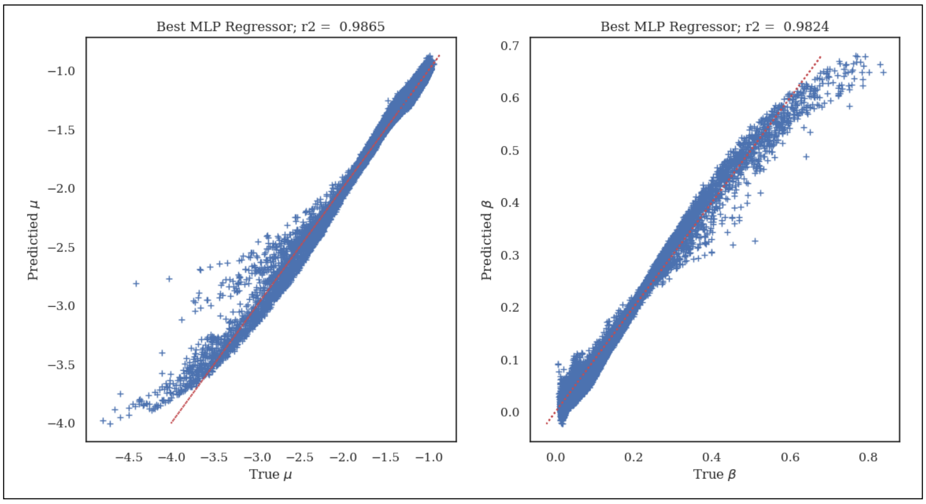

Figure 4.10.: MLP metamodel on $r_0$, $\bar{h}$ and $\bar{v}$ to assess the values of $\mu$ (left) and $\beta$ (right). Simulated value (SAOST) in abscissa, output of the model in ordinate. Only for the test set.

Better predictions start to emerge with the use of this non-linear metamodel.

Doing the same data pre-processing as for the linear regression and using this time $\frac{1}{r_0}^{5/3}$, $\bar{h}^{5/3}$ and $\bar{v}^{5/3}$ as inputs, we find that the bestfitting model still has 3 layers but this time with repectively 50, 100 an 50 layers. The best activation function is now the relu function and the results can be seen in Figure 4.11

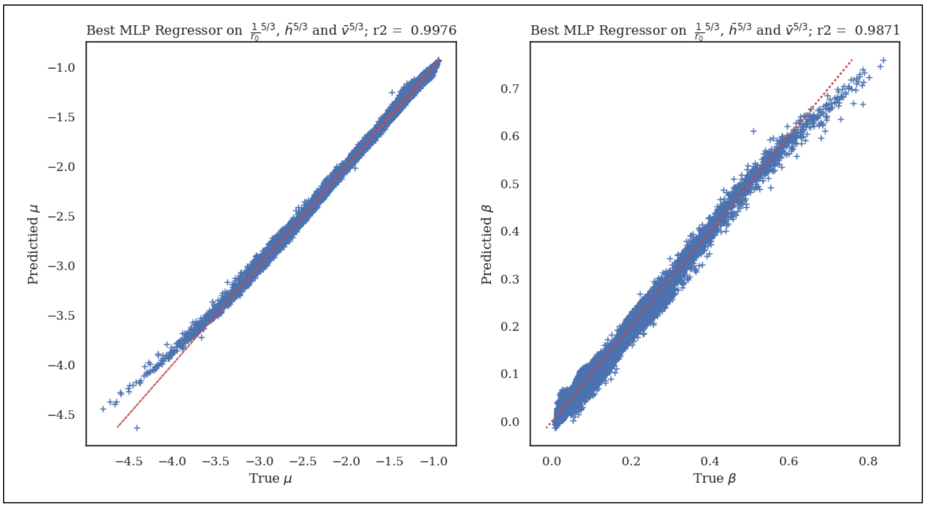

Figure 4.11.: MLP metamodel on $\frac{1}{r_0}^{5/3}$, $\bar{h}^{5/3}$ and $\bar{v}^{5/3}$ to assess the values of $\mu$ (left) and $\beta$ (right). Simulated value (SAOST) in abscissa, output of the model in ordinate. Only for the test set.

This change produces much better results and shows once again that moments do indeed come into play to the 5/3 power in the definition of $\mu$ and $\beta$.

| **Kernel** | **Score $\mu$** | **Score $\beta$** |
|---|---|---|
| RBF | -6.776 | -0.814 |
| Matern | 0.994 | 0.994 |
| Constant*RBF+White | 0.946 | 0.685 |
| Constant*Matern+White | 0.999 | 0.999 |

Table 4.2.: Score on the assessment of $\mu$ and $\beta$ for different kernels

## 4.3.4. Gaussian process

As seen in chapter 3, a GP writes the output of interest as the sum of a regression part, a constant term in this study, and a centered stochastic process $Z$:

$$\gamma(x) = \beta_0 + Z(x) \tag{4.12}$$

where the stochastic part $Z(x)$ is a Gaussian centered process fully characterized by its covariance function $Cov(Z(x), Z(u)) = \sigma^2 R(\theta, x, u)$ with $\sigma^2$ the variance of $Z$ and $R$ the correlation function, or kernel, that accounts for spatial correlation effects and $\theta$ the hyper-parameter.
In this study, we focus on a stationary process $Z$, which means that, for new points, the prediction consists of a linear combination of the observed values, with weights that depend on the distance between the new input point and the training data. The assumption is that, the closer the inputs are, the more correlated the outputs are. The kernel is thus a similarity function.

In a first step, we focused on the assessment of $\mu$ and $\beta$, the parameters that describe the coupled flux, while neglecting the impact of scintillation, in order to ease the analysis of the results.

We were led to test different kernels to determine which one best fits with our problematic. To do so and reduce the computational cost, we trained four different GP with different kernels for the prediction of $\mu$ and $\beta$ using the training set (10% of the database). The $R_2$ score given in table 4.2 is calculated on the test set (the remaining 90% of the database).

This probabilistic model enables the estimation of predictive distributions, providing not only point predictions but also a measure of uncertainty associated with each prediction. This is particularly valuable in situations where having a quantification of the uncertainty is important for decision-making or further analysis.

### 4.3.4.1. Results: GP on the determination of $\mu$ and $\beta$

Judging at the $R_2$ scores presented in table 4.2 it appears clear that the best kernel one can use to determine the statistics of coupled flux is a Matérn kernel. The addition of a constant product-kernel and a white sum-kernel brings real benefit on the points on which the prediction error was large, which has the effect of slightly improving the overall score to an outstanding value superior to 0.999 in both cases. Figure 4.12 illustrate the goodness of the fit with such a kernel. On the left, we can see the predicted values of $\mu$ as a function of their true values (as given by the physical model) for each point of the test set.

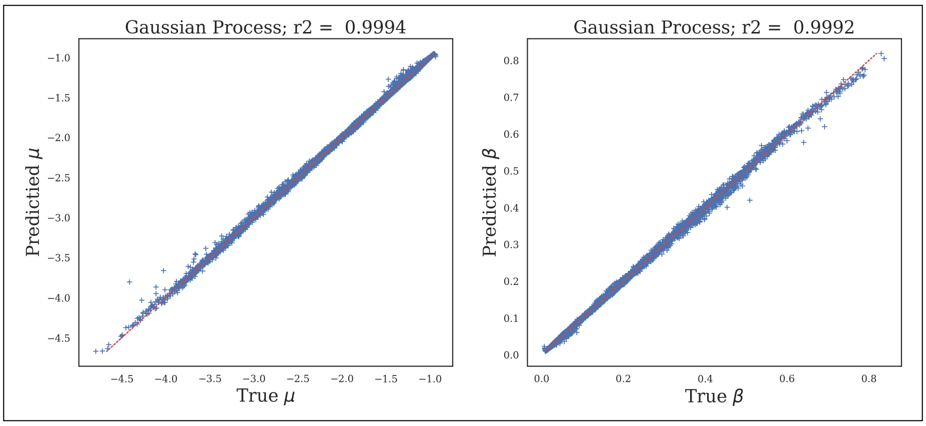

Figure 4.12.: Results of the GP to assess the values of $\mu$ and $\beta$ using $r_0$, $\bar{h}$ and $\bar{v}$ as inputs

After finding satisfactory results with this GP metamodel, a sensitivity analysis conducted according to section 3.4 gave us informative input on the impact of $r_0$, $\bar{h}$ and $\bar{v}$ on the final results of this GP (Figure 4.13). Sensitivity indices were estimated using "Sensitivity: Global Sensitivity Analysis of Model Outputs" [Ioo+21], an open source, GPL-2 licensed, **R** library developed for the treatment of uncertainties. Due to the correlations among the 3 input variables, we focused on the first order sobol indices, Shapley indices and PME indices (presented in section 3.4).

As expected, $r_0$ has the strongest impact on the final variance and, according to Sobol' indices, accounts for approximately 80% of the total variance in both cases. $\bar{v}$ accounts for the rest of the variance while $\bar{h}$ as very little effect: its Sobol' and PME indices are indeed almost equal to zero. It is interesting to compare Shapley and PME indices for $\bar{v}$ and $\bar{h}$: $\bar{v}$ has an effect on the GP predicted output and, thanks to its correlations and interactions with the 2 other input variables, its Shapley and PME effects are larger than its first order Sobol indice.

On the contrary, $\bar{h}$ has a non negligible Shapley effect due to correlations with the 2 other input variables, but its PME indice is very small, and this variable is thus non influential.

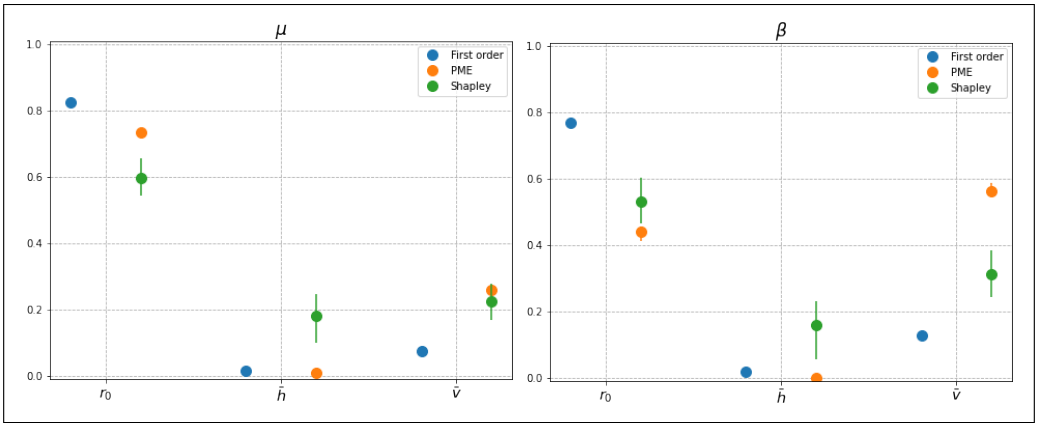

Figure 4.13.: Sensitivity analysis on the prediction of $\mu$ and $\beta$ using $r_0$, $\bar{h}$ and $\bar{v}$

This conclusion is not surprising, as the downlink AO error budget described in section 2.1.2 involves the terms $r_0$ (equation 2.10) and $\bar{v}$ (equation 2.13). $\bar{h}$ signs for the sensitivity of the injection efficiency to the vertical distribution of the turbulence. As the residual error variance in the error budget is, in the current considered case, the result of an integral over the overall turbulence profile, this very little sensitivity to $\bar{h}$ was expected.

The lower impact of the term $\bar{h}$ brought us to consider another GP taking as inputs only the two parameters $r_0$ and $\bar{v}$. The error made by this GP can be seen on figure 4.14 and shows very high $R_2$ scores comparable to the ones of figure 4.12, underlying the irrelevance of the input $\bar{h}$.

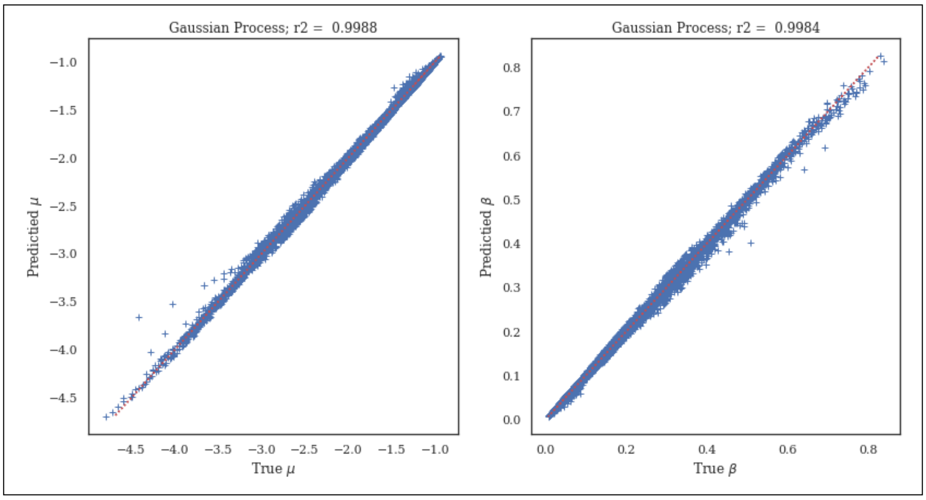

Figure 4.14.: Results of the GP to assess the values of $\mu$ and $\beta$ using $r_0$ and $\bar{v}$ as inputs

One can notice that, on a small number of points for low values of $\mu$, the error is noticeably greater than in the previous case. These small values of $\mu$ correspond to low values of the mean of the Gumbel law, and thus worst case scenario with a low average coupled flux.

#### 4.3.4.2. Analyzing central moments: mean and variance assessment

Talking in term of $\mu$ and $\beta$ is not necessarily the most intuitive and results would happen to be a lot more readable on the mean and the variance of the distribution. That is what is done in this section.

The mean of the Gumbel law depends on $\mu$ and $\beta$ in the following way:

$$Mean = \mu + \gamma\beta \tag{4.13}$$

where $\gamma$ is the Euler constant and the variance $\sigma^2$ is given by:

$$\sigma^2 = \frac{\pi^2}{6}\beta^2 \tag{4.14}$$

#### 4.3.4.3. Results: Gaussian process combined with adaptive learning

In figure 4.15, one can see the results of the training process in terms of mean and variance instead of $\mu$ and $\beta$ with respectively a $R_2$ score of 0.999 and 0.997. Even though these scores are very high, we can visually see that variance in the prediction error is higher for low values of the mean of the Gumbel law and high variance.

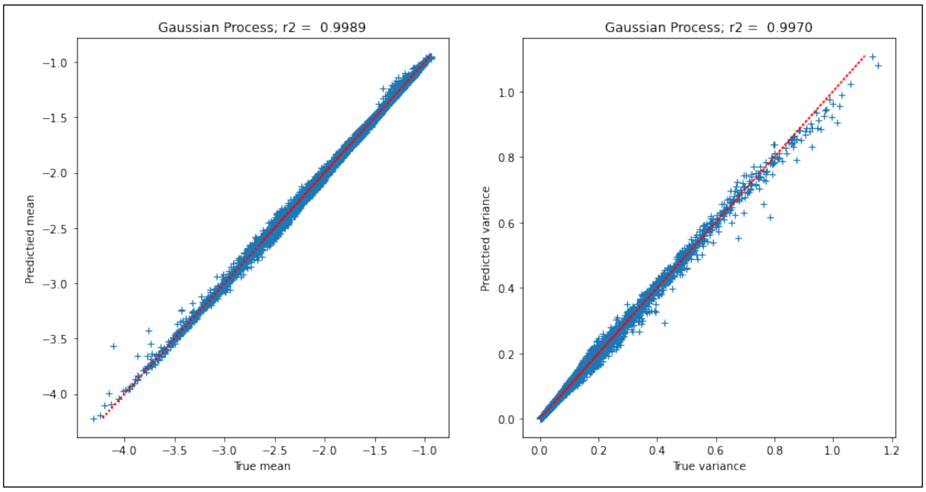

Figure 4.15.: Results of the GP to assess the values of the mean and the variance of the coupled flux distribution using $r_0$ and $\bar{v}$ as inputs

Adaptive learning can be used to overcome this problem. It consists of training the model $n$ times with the inclusion of new training points after each iteration, from the remaining 90% data. The new train data that is added to the train database is the data for which the prediction error is the highest. It is then removed from the test database. This dynamic approach enables to continuously update the model's performance. Instead of solely relying on an initial training set that might not cover the worst cases, this method allows the model to adapt and learn from the worst examples encountered during validation, making it more robust to handle all scenarios.

After 10 iterations, we obtain the results of figure 4.16, where the $R_2$ score did not evolve much but where the error is minimal on all points considered in the test set.

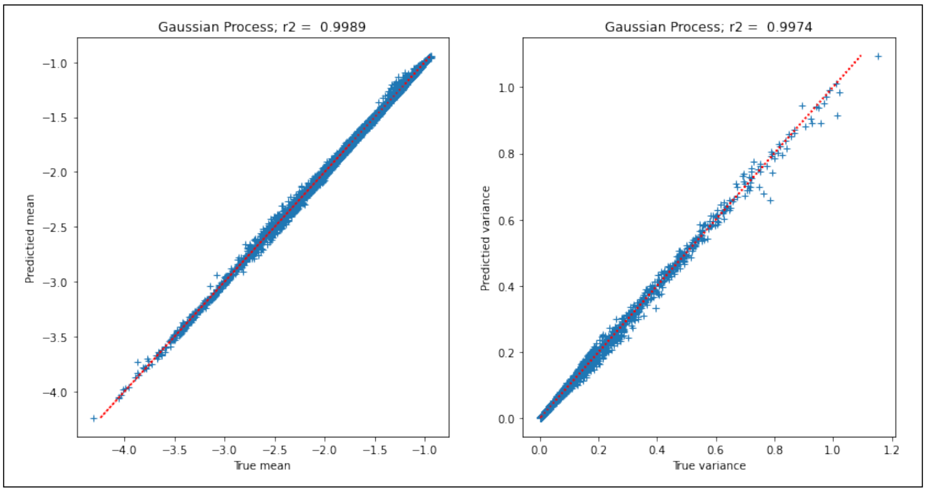

Figure 4.16.: Results of the GP to assess the values the mean and the variance of the coupled flux distribution using adaptive learning with $r_0$ and $\bar{v}$ as inputs.

#### 4.3.4.4. Results: Gaussian process on the determination of $\sigma^2_{\chi_{AP}}$

Doing the same steps as before to assess the scintillation distribution and using a similar Gaussian process, with the same kind of kernel, gives a score of 0.996. This is a remarkable result, as it enables us to estimate the scintillation rate averaged over a pupil of substantial diameter without having to deploy a disproportionately large instrument.

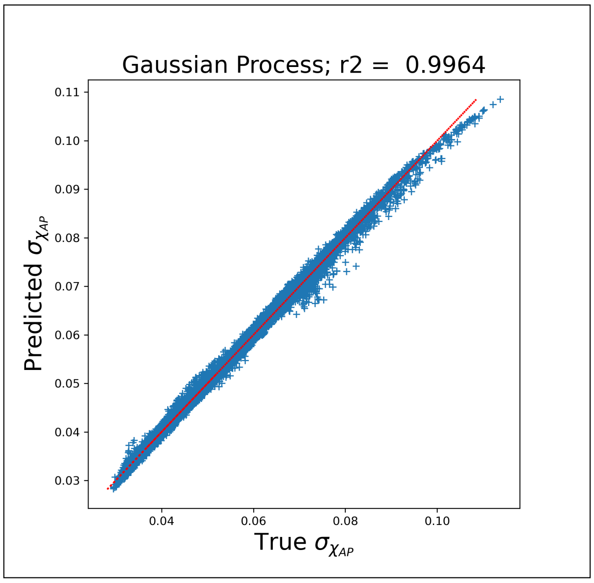

Figure 4.17.: Results of the GP metamodel to assess the value of $\sigma_{\chi_{AP}}$ using $r_0$, $\bar{h}$ and $\bar{v}$.

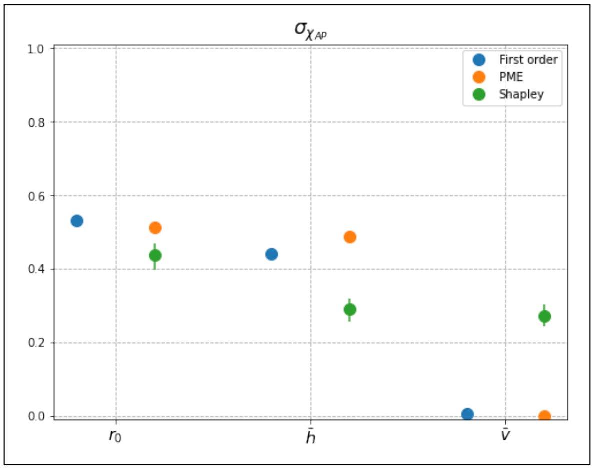

Figure 4.18.: Sensitivity analysis on the prediction of $\sigma_{\chi_{AP}}$ using $r_0$, $\bar{h}$ and $\bar{v}$

Sensitivity analysis can also be conducted for the prediction of $\sigma^2_{\chi_{AP}}$ where, according to figure 4.18, the impact of $\bar{v}$ seems very low: its first order Sobol' and PME indices are almost equal to zero, and its Shapley indice is larger, but also accounts for its correlation with the two other input variables. We remind here that both Shapley and PME indices account for both correlations and interactions among input variables, but that PME indices can enable to identify exogeneous variables and associate them very small sensitivity indices. Removing $\bar{v}$ from the input parameters of our metamodel leads us to a prediction score of 0.995 (Figure 4.19), very close to the 0.996 obtained with $\bar{v}$. This result was to be expected, as expressions of the variance of log-amplitude averaged on a pupil that can be found in the literature are independent of the wind speed profile [Zia+00].

Figure 4.19.: Results of the GP metamodel to assess the value of $\sigma_{\chi_{AP}}$ using $r_0$ and $\bar{h}$.

The input reduction can be pushed even further by choosing as the only input of the model the ratio $\frac{r_0}{\bar{h}} \propto \theta_0$. The results of this univariate model can be seen on figure 4.20: there is no significant change in the $R_2$ score and one can say that, at least under the weak fluctuation approximation, the PDF of the scintillation only depends on $\theta_0$.

Figure 4.20.: Results of the GP to assess the value of $\sigma^2_{\chi_{AP}}$ using as a single input $\frac{r_0}{\bar{h}}$.

This implies that one can find a power law between $\sigma^2_{\chi AP}$ and $\theta_0$ such as:

$$\sigma^2_{\chi AP} = a \times \theta_0^b \tag{4.15}$$

Experimentally, using results of figure 4.20 for a pupil diameter of 60 cm, we get $a = 0.06$ an $b = -1.62$. The power law describes $\sigma^2_{\chi AP}$ with a coefficient of determination of 0.99 (figure 4.21).

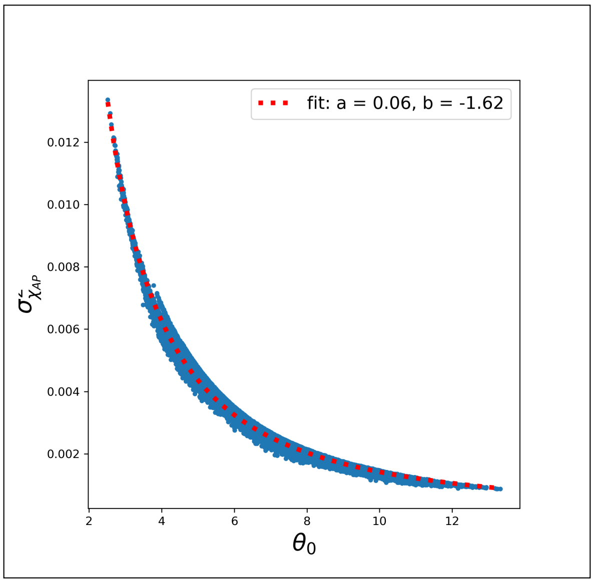

Figure 4.21.: $\sigma^2_{\chi AP}$ as a function of $\theta_0$ ($\mu rad$). In red a curve fit with the law $\sigma^2_{\chi AP} = a \times \theta_0^b$.

#### 4.3.4.5. Impact of the receiver aperture in the evaluation of the variance term of the integrated intensity on the pupil from $\theta_0$.

The amount of scintillation affecting a system can be defined using the scintillation index $\sigma_I^2$, the normalized variance of the field intensity. It is related to the variance of the log-amplitude by [Mah00, Equation 3.31]

$$\sigma_I^2 = \frac{\langle I^2 \rangle}{\langle I \rangle^2} - 1 = \exp\left(4\sigma^2_{\chi AP}\right) - 1 \tag{4.16}$$

The analytical description of $\sigma_I^2$ given in [Véd08] follows:

$$\sigma_I^2 = 9.62\lambda^{-2} \int \mathrm{d}h C_N^2(h) P(h), \tag{4.17}$$

where for a circular pupil of diameter D:

$$P(h) = \int_0^\infty f^{-8/3} \sin^2\left(\pi\lambda h f^2\right) \times \left(\frac{2J_1(\pi D f)}{\pi D f}\right)^2 \mathrm{d}f, \tag{4.18}$$

with $f$ the spatial frequency and $J_1$ the first order Bessel function. Note that this expression is provided assuming a Kolmogorov power spectral density for index of refraction fluctuations. No outer scale parameter is taken into account.

This equation of the log-amplitude variance takes into account the diameter over which it is averaged. It raises the question to know how the relationship between $\theta_0$ and $\sigma^2_{\chi AP}$ is impacted by the value of $D$ and to what extend the scintillation impact can be assessed using only this input. Figure 4.22 shows the same as figure 4.21 for different sizes of the averaging pupil at $1.5\mu m$.

One can see that, for small pupils values, $\theta_0$ and $\sigma^2_{\chi AP}$ are uncorrelated but, with pupils higher than 10 cm, these two quantities become highly correlated with the values of $\sigma^2_{\chi AP}$ that can be described as power laws of $\theta_0$, with coefficient of determination higher than 0.98. Figure 4.23 shows this coefficient of determination as a function of the pupil diameter.

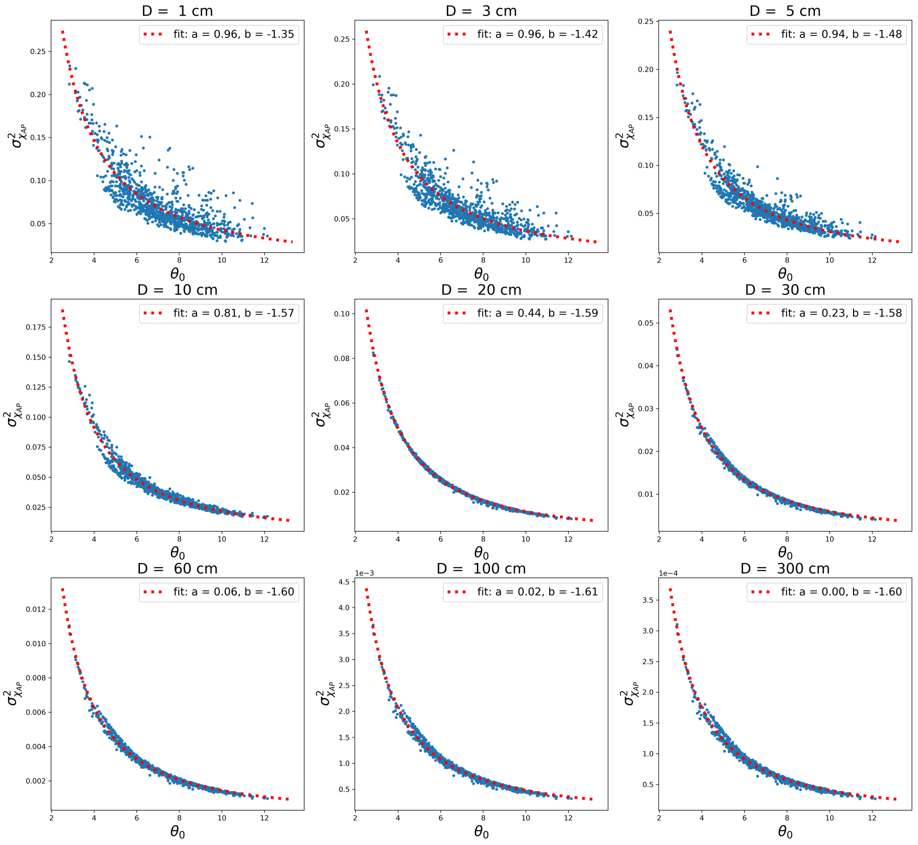

Figure 4.22.: $\sigma^2_{\chi AP}$ as a function of $\theta_0$ for different values of the pupil diameter. In red a curve fit with the law $\sigma^2_{\chi AP} = a \times \theta_0^b$.

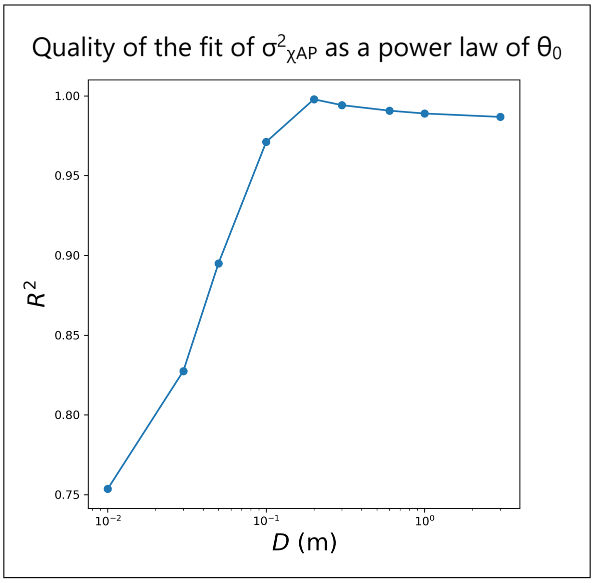

Figure 4.23.: Coefficient of determination of the fit of $\sigma^2_{\chi AP}$ as a power law of $\theta_0$, according to the pupil diameter.

As a reminder

$$\theta_0^{-5/3}(z) = 114.7\lambda^{-2}\int_0^L \mathrm{d}z C_N^2(z) z^{5/3}, \tag{4.19}$$

along the line of sight. Using the formula of $P(h)$ for a central obscuration ratio $\epsilon$,

$$\begin{aligned} P(h) = & \frac{1}{\left(1-\epsilon^2\right)^2}\int_0^\infty f^{-8/3}\sin^2\left(\pi\lambda h f^2\right) \\ & \times\left[\frac{2J_1(\pi D f)}{\pi D f} - \epsilon^2\left(\frac{2J_1(\epsilon\pi D f)}{\epsilon\pi D f}\right)\right]^2 \mathrm{d}f, \end{aligned} \tag{4.20}$$

Aziz Ziad et al [Zia+00] showed that $P(h) \approx P(h_0)(h/h_0)^{5/3}$ for a pupil diameter $D = 10cm$ and a central obscuration $\epsilon = 0.4$ at a wavelength $\lambda = 0.5\mu m$. This leads to $\theta_0^{-5/3} = K\sigma_I^2$ and thus, an accurate way to measure the isoplanatic angle using an instrument with a 10 cm pupil.

In our case with no central obscuration and a wavelength $\lambda = 1.5\mu m$, one can see that the error is minimal for a pupil around 20 cm in diameter. However, the relation between $\theta_0$ and the scintillation index is not linear, thus making analytical development more complex, and this point was not investigated further in this study.

The conclusion of this study is that the isoplanatic angle can be infered by an instrument such as the one developed in [Zia+00]. From the isoplanatic angle, the scintillation index and thus the log-amplitude variance can be calculated as soon as the pupil diameter is above 10 cm. The ideal case for determining precisely the log-amplitude statistics using $\theta_0$ would be when the ground station telescope diameter is close to 20 cm, however with a telescope of 60 cm, the prediction error remains small.

This result strongly depends on the impact of the outer scale and the wavelength considered. These conclusions would also have to be weighted by the elevation of the satellite that plays a major role. These considerations have not been studied in the context of this thesis, the aim of which is to lay the foundations of a methodology that remains to be refined.

#### 4.3.4.6. PDF reconstruction

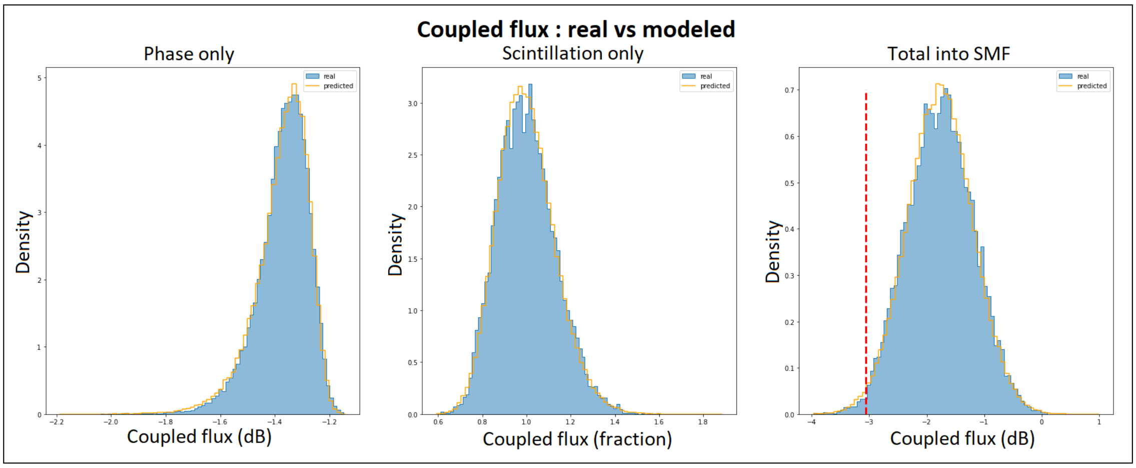

Figure 4.24.: PDF computed from SAOST time series and PDF computed from our metamodel with, from left to right: $L_{\phi}(t)$, $\rho_I$ and the received optical power.

As we are able to predict $\mu$, $\beta$ and $\sigma_{\chi_{AP}}$ from the moments, the next step is to reconstruct the probability density of the received optical power using the parametric descriptions of $L_{\phi}(t)$ (equation 4.5) and $\rho_I$ (equation 2.17). An example is given in figure 4.24 where, for one randomly selected profile, we can see, from left to right, the statistical reconstruction of $L_{\phi}(t)$, $\rho_I$ and the received optical power.

In order to characterize the relevance of our estimation on the received optical power's statistic, we can compute the absolute error made on the mean and standard deviation of the reconstructed PDF of the received optical power.

The *absolute error* is a measure of the difference between the *approximate value* and the *exact or true value* of a quantity. Mathematically, the absolute error ($\Delta x$) for a given quantity $x$ is calculated as:

$$\Delta x = |x_{\text{approx}} - x_{\text{true}}| \tag{4.21}$$

where:

$x_{\text{approx}}$ is the approximate value of $x$,
$x_{\text{true}}$ is the true or exact value of $x$.

We also look at the absolute error on the 1% quantile of the received optical power (see red dashed line on figure 4.24) as we want a faithful reproduction of the tail of the distribution. Statistics on the absolute error associated to our 37 k profiles can be seen in figure 4.25.

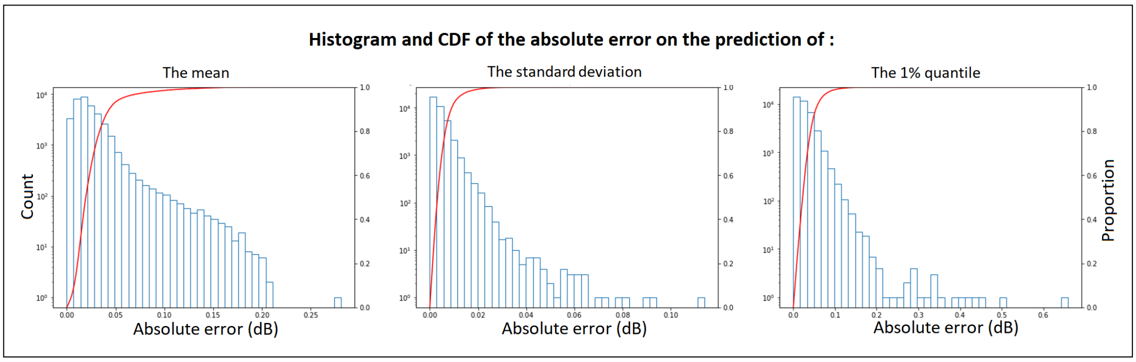

Figure 4.25.: Histogram and CDF of the absolute error on prediction of the mean, the standard deviation and the 1% quantile.

In all profiles, the prediction error on the value of the quantile 1% is inferior to 0.7 dB, which is consistent with the current assumptions made in the commonly used link budgets (margins are typically 3 dB).

We have to put into perspective this value with the fact that the temporal series of ROP generated with SAOST are finite and thus part of the error is due to the non perfect convergence of the random variable. The weight of this error due to convergence in the overall error has yet to be determined.

### 4.3.5. Influence of the AO design

Our model to predict the PDF of the $f_{smf}$ was validated on other AO cases. We settle on two other AO cases that where chosen to give more weight either to the spatial error term or to the temporal error one.

This new dimensioning has led to the fitting error being divided by 2 and the time error multiplied by 2.

In practice we took the asymptomatic evaluation of the fitting error proposed by Conan in [Con94]:

$$\sigma^2_{fitting} \approx 0.458\,(N_{corr}+1)^{-\frac{5}{3}}\left(\frac{D}{r_0}\right)^{\frac{5}{3}} \tag{4.22}$$

and the approximated expression of the temporal error given in [RF23]:

$$\sigma^2_{tempo} = 0.243 f_{bw}^{-\frac{5}{3}}\left(\frac{\bar{v}}{r_0}\right)^{\frac{5}{3}} \tag{4.23}$$

where $f_{b\omega}$ the servoing bandpass is given by:

$$f_{b\omega} = \frac{1}{2\pi T}\sqrt{\frac{g}{1+2\tau T}} \tag{4.24}$$

$\tau$, the loop delay, is chosen constant as 2 in our case, $g$ , the gain of the loop, is chosen such as $g \approx \frac{1}{1+\tau/T}$ and $T$ is the sensor integrating time given as $T = \frac{1}{f_{samp}}$ with $f_{samp}$ the loop sampling frequency.

Lets write $\sigma^{2^{(1)}}_{fitting}$ and $\sigma^{2^{(1)}}_{tempo}$, respectively the average fitting and temporal error of our main AO dimensioning of 10 radial orders and a sampling frequency of $2kHz$, for a given case of turbulence and wind profile. We want to find two other designs $^{(2)}$ and $^{(3)}$ such as:

$$\begin{aligned} \sigma^{2^{(1)}}_{fitting} &= 2\sigma^{2^{(2)}}_{fitting} = \frac{1}{2}\sigma^{2^{(3)}}_{fitting} \\ \sigma^{2^{(1)}}_{tempo} &= \frac{1}{2}\sigma^{2^{(2)}}_{tempo} = 2\sigma^{2^{(3)}}_{tempo} \qquad \forall r_0, \bar{v} \end{aligned} \tag{4.25}$$

This gives us:

$$\begin{aligned} N^{(1)}_{corr} &= 10 \\ N^{(2)}_{corr} &= 15.67 \approx 15 \\ N^{(3)}_{corr} &= 6.26 \approx 6 \end{aligned}$$

and:

$$\begin{aligned} f^{(1)}_{samp} &= 2000Hz \\ f^{(2)}_{samp} &= 1318.5Hz \approx 1300Hz \\ f^{(3)}_{samp} &= 3033Hz \approx 3000Hz \end{aligned}$$

SAOST simulations were run for these two AO cases on 5000 profiles to reduce computational time. These 5000 profiles where chosen such as they cover uniformly the space of averaged coupled flux obtained with the main AO dimensioning. In other words, we started by sorting the 37059 profiles based on the averaged coupled flux obtained with SAOST with a correction of 10 radial order with a 2kHz sampling frequency. Then, on this sorted database, we drew 5000 evenly distributed pairs of $C_n^2$ and wind profiles.

Results of these 5000 simulations can be seen on figure 4.26 that displays the distribution of fitting error, temporal error as well as total error for each of the AO cases. Figure 4.27 displays the distribution of of $\mu$ in $dB$, $\beta$ and $\sigma^2_{\chi_{AP}}$ for the same AO cases.

From figure 4.26, one can see that the error terms behave overall as anticipated, with a factor of 2 in the distributions sizes between each AO cases. The total error, on the other hand, stays quite well approximated by the sum of the fitting and the total error no matter the case, meaning than no other term of the AO error budget becomes predominant or has a significant impact, even the aliasing error, which we might have thought would have had a bigger impact.

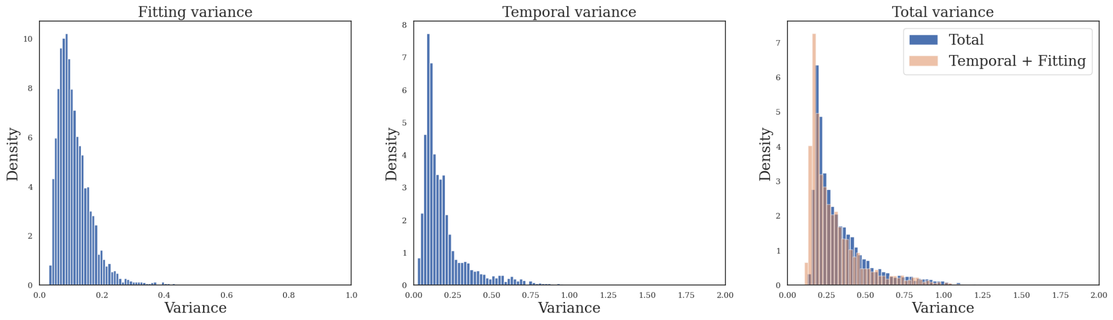

(a) AO case 1: 10 $N_{corr}$; 2kHz

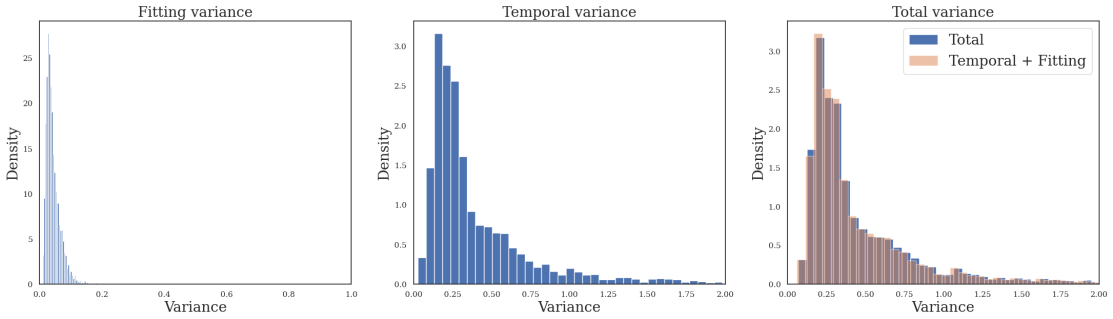

(b) AO case 2: 15 $N_{corr}$; 1.3kHz

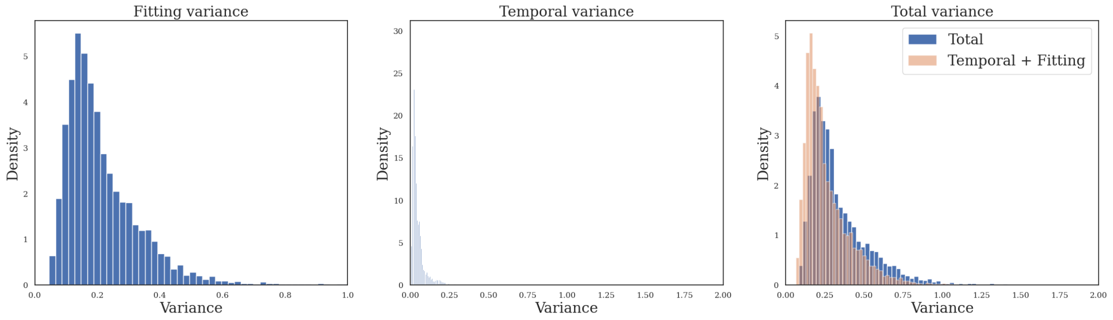

(c) AO case 3: 6 $N_{corr}$; 3kHz

Figure 4.26.: Fitting, temporal and total residual error's variance for each of the AO cases considered.

On figure 4.27, the (a) panel shows the distribution of $\mu$ in $dB$, $\beta$ and $\sigma^2_{\chi AP}$ for the 37059 profiles and serves as a reference for the AO cases (b) and (c) displayed in the middle and bottom panel. First thing to consider is the lack of variations in the $\sigma^2_{\chi AP}$'s distribution over the different cases (the top panel distribution is smoother only because it's estimated on a larger amount of points). It is an experimental validation of Chapter 2 claim, i.e. AO only corrects the phase distortion but does not impact the scintillation, thus the scintillation is, under our initial assumptions (SAOST) completely independent from the residual error's variance.

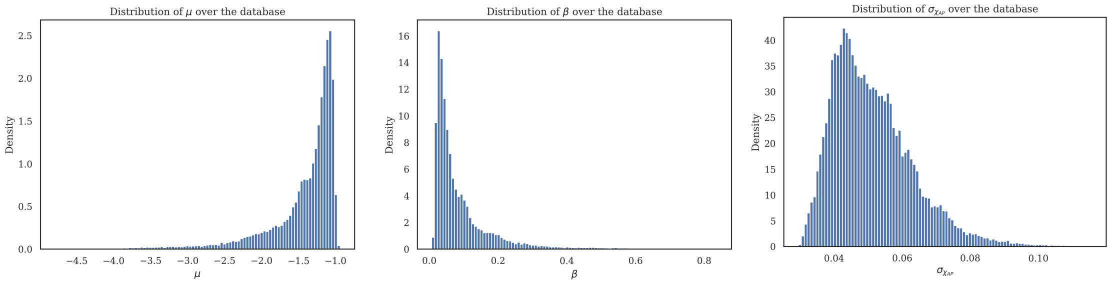
Distribution of $\mu$ over the database
Distribution of $\beta$ over the database
Distribution of $\sigma_{\chi_{AP}}$ over the database

(a) AO case 1: 10 $N_{corr}$; 2kHz

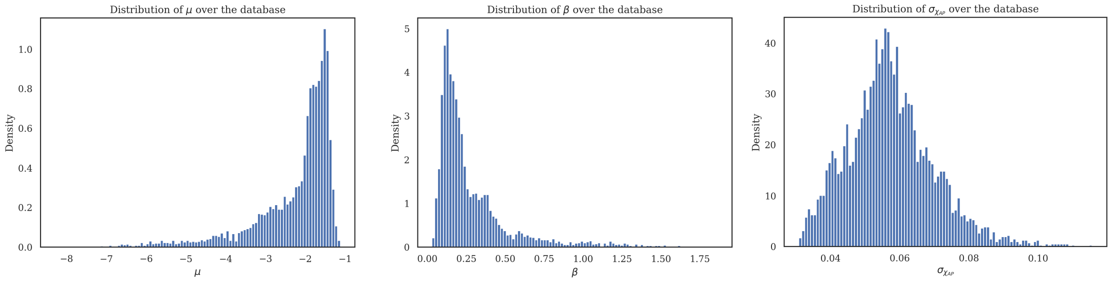
Distribution of $\mu$ over the database
Distribution of $\beta$ over the database
Distribution of $\sigma_{\chi_{AP}}$ over the database

(b) AO case 2: 15 $N_{corr}$; 1.3kHz

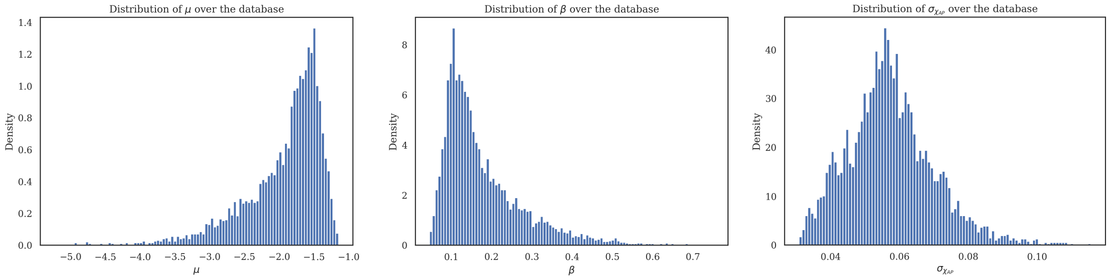
Distribution of $\mu$ over the database
Distribution of $\beta$ over the database
Distribution of $\sigma_{\chi_{AP}}$ over the database

(c) AO case 3: 6 $N_{corr}$; 3kHz

Figure 4.27.: Distribution of the parameters of the PDF of $f_{smf}$ depending on the AO cases.

The distributions of $\mu$ and $\beta$, on the other hand, behave differently depending on the AO case. Case (b) emphasizes best this phenomenon where $\mu$ and $\beta$ distributions have much heavier tails than in the base case (a). This is simply explained by the total residual error distribution (figure 4.26 (b)) that takes more extreme values due to a very strong temporal error on some profiles. More residual error on the phase induces automatically a decrease of the average coupling efficiency and a higher variance in the coupling efficiency time series. The same phenomenon can be noted for case (c), but on a smaller scale.

We ran the GP to predict $\mu$, $\beta$ and $\sigma^2_{\chi AP}$ using $r_0$, $\bar{h}$ and $\bar{v}$ as input. The training set was this time composed of 70% of the data to keep approximately the same number of training profiles as in the previous section. Figure 4.28 illustrates the results of the prediction on the test set (30% of the 5000 profiles). As expected, the prediction score is the same no matter the AO for $\sigma^2_{\chi AP}$. We can also see that the $R_2$ score stays approximately the same for the prediction of the coupled efficiency PDF parameters, no matter the number of corrected radial orders and the sampling frequency (as long as one stays in the range of these studied common values).

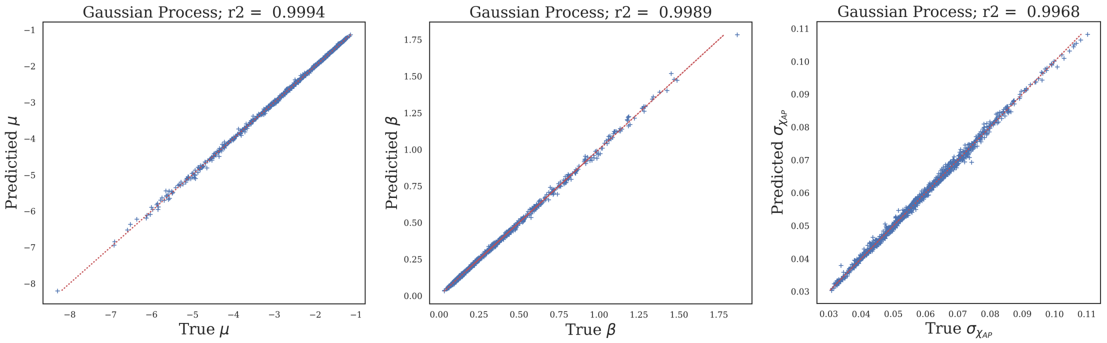

(a) AO case 2: 15 $N_{corr}$; 1.3kHz

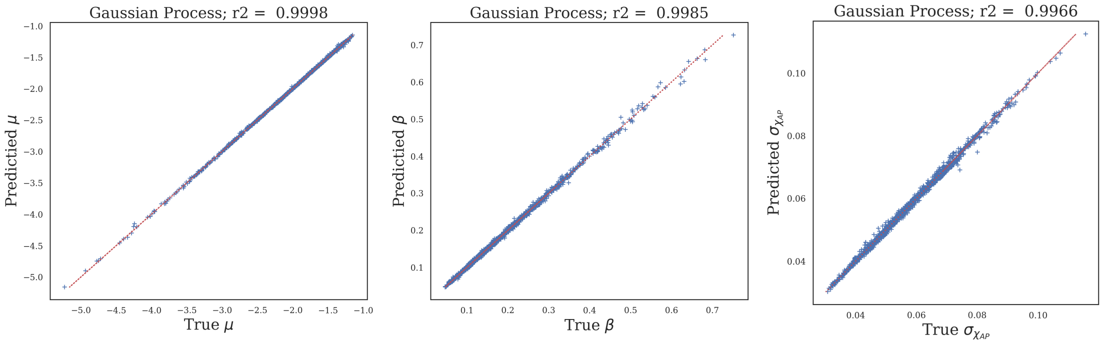

(b) AO case 3: 6 $N_{corr}$; 3kHz

Figure 4.28.: Prediction of the parameters of the PDF of $f_{smf}$ depending on the AO cases.

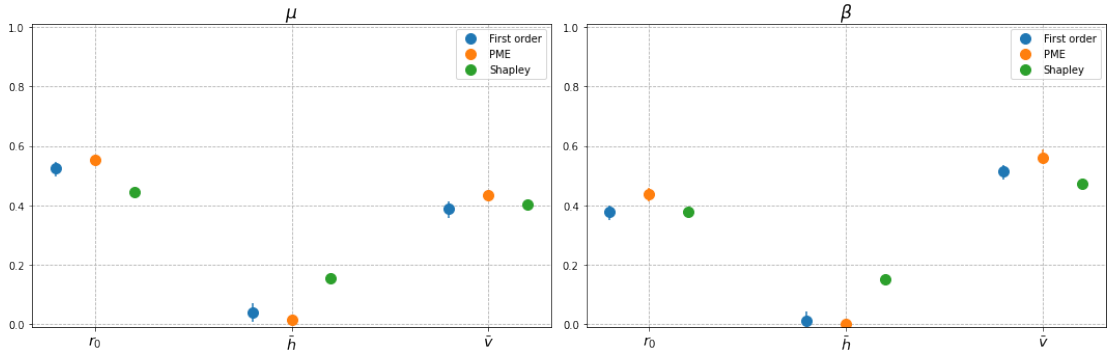

(a) AO case 2: 15 $N_{corr}$; 1.3$kHz$

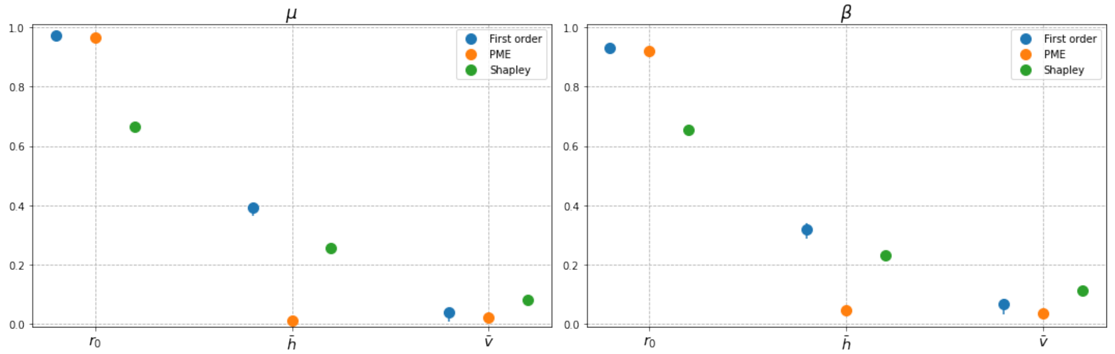

(b) AO case 3: 6 $N_{corr}$; 3kHz

Figure 4.29.: Sensitivity analysis on the prediction of $\mu$ and $\beta$ depending on the AO cases.

The result of the sensitivity analysis in figure 4.29 is particularly illustrative about the phenomena that take place in the prediction process.

With AO number two, where the sampling frequency is the lowest and thus where the temporal error has the strongest impact, we measure a contribution of $\bar{v}$ in the output variance significantly larger for the 3 indices than in our base case, shown in figure 4.13. This is the expected behaviour with a temporal error that depends mostly on the value of $\bar{v}$.

The second plot shows the opposite phenomenon. As the temporal error becomes negligible, the impact of $\bar{v}$ on the prediction accuracy becomes negligible as well, and the 3 associated sensitivity indices are very small. The machine learning model uses mostly $r_0$ to describe the output variance and relies on the value of $\bar{h}$ to describe small variation in the results giving $\bar{h}$ a stronger influence that it had in the other cases for the first order Sobol' and Shapley indices. On the other hand, its PME indice is almost null, which underlines the interest to analyze both Shapley and PME indices: Shapley indices can give an estimation of the influence of the variable, and PME indices identify possible exogeneous variables.

## 4.4. Results on the half-correlation time

The next step of our study is to be able to estimate the auto-correlation time of the received optical power using the same moments. Knowledge on the temporal behavior of the received optical power is fundamental, as the duration of the fading in the received signal will dictate the use of numerical mitigation techniques and the latency in the telecommunication protocol.

Once again, it should be noted that analytical expressions exist to describe the auto-covariance of $L_\phi$ [Can+18] and of $\rho_I$ [Rob+08][SYF14]. The ultimate goal is to estimate those auto-covariance functions using a small number of instruments but, in order to simplify the problem, we first look at the half-correlation time of $L_\phi$ and $\rho_I$ time series independently. A simplistic way to predict the auto-covariance could then be to fit an exponential decay law matching the estimated half-correlation time.

### 4.4.1. Metamodel construction

The approach is exactly the same as for the prediction of the PDF: half-correlation times were computed using SAOST and we use $r_0$, $\bar{h}$ and $\bar{v}$ as inputs of our metamodels. Once more, best results were obtained using GP regression with a Matérn 5/2 kernel.

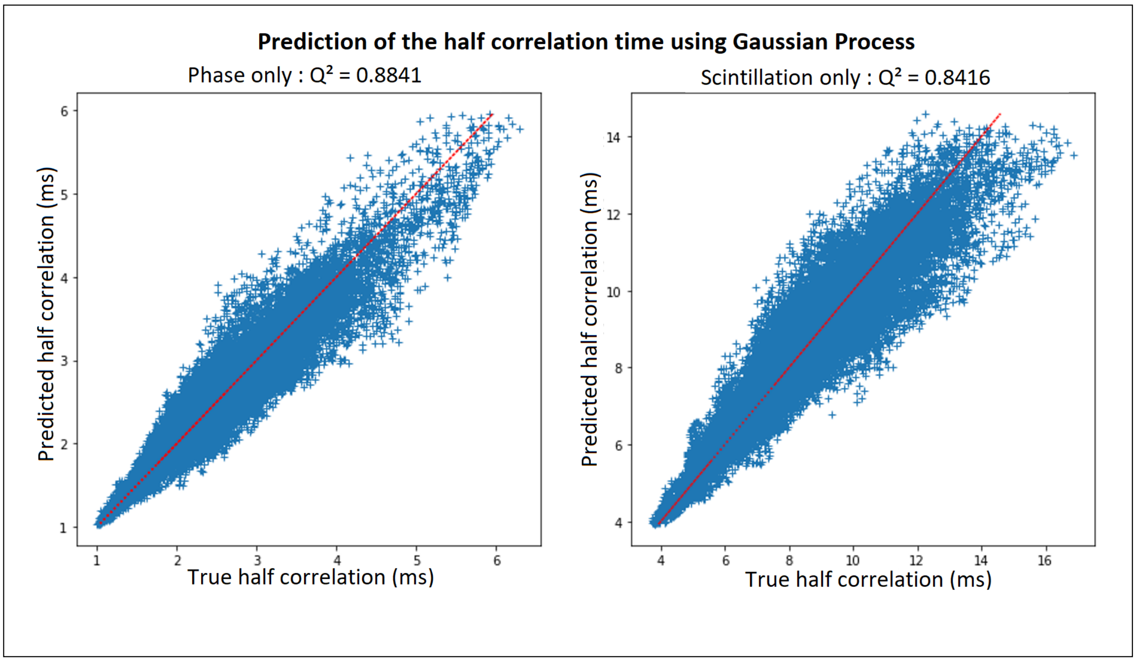

Figure 4.30.: Prediction of the half-correlation time using GP on inputs $r_0$, $\bar{h}$ and $\bar{v}$; x axis shows the real value and y the predicted one. On the left the half-correlation neglecting scintillation effects and on the right neglecting phase effects.

Figure 4.30 shows that the prediction using $r_0$, $\bar{h}$ and $\bar{v}$ is able to recreate the trend, but that it lacks precision with a high variance on the distribution of the error. The chosen input moments do not account well enough for the temporal aspect of the turbulence, and it is then necessary to consider an additional measurement.

One way to recover the missing temporal information on the atmospheric layer is through measurement of the power spectral density of the scintillation on a small pupil instrument. To simulate the measurement of such an instrument, we used the expression given in [SYF14] and calculated the power spectral density of the scintillation for a 5 cm pupil at a wavelength of 1500 nm. Simulation was done on one hundred points spaced evenly on a log scale from $10^{-4}$ Hz up to $10^{3}$ Hz.

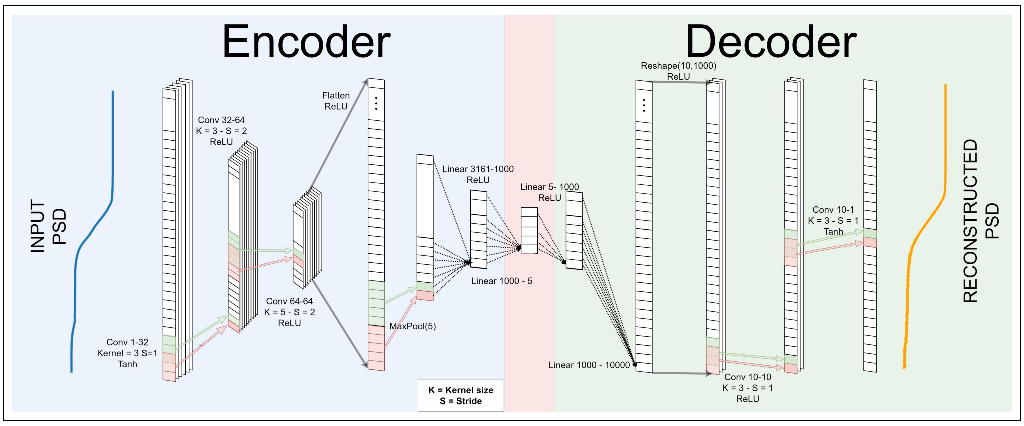

Figure 4.31.: Architecture of the autoencoder used to encode the power spectral density.

In order to add information associated to the scintillation spectrum in our model, we wish to reduce the data dimension while keeping the maximum of information. Indeed, there is a lot of information redundancy in the 100 points used to simulate the power spectrum density, but these points have to be decimated in a non-linear way if we want to keep the relevant information no matter the profile.

To do so, we used a convolutional autoencoder, a kind of neural network extensively used for data reduction. The underlying concept is simple, the architecture consists of two parts, an encoder and a decoder. The encoder learns an encoding of the data and is validated and refined by attempting to regenerate the inputs from the latent space with the decoder. In our case, the input data is of dimension 100 and the encoded data of dimension 5, (the architecture can be found in Figure 4.31). Increasing the dimension of the latent space above 5 did not resulted in significant reconstruction improvement. In figure 4.32, we can see an example of reconstruction on two randomly picked power spectral density from our database. The real PSD (Power spectral density) computed from [SYF14] is represented in blue, while the output of the decoder applied on the encoding of the PSD in the 5 dimension latent space is in orange. We can see that most of the information is conserved in the latent space.

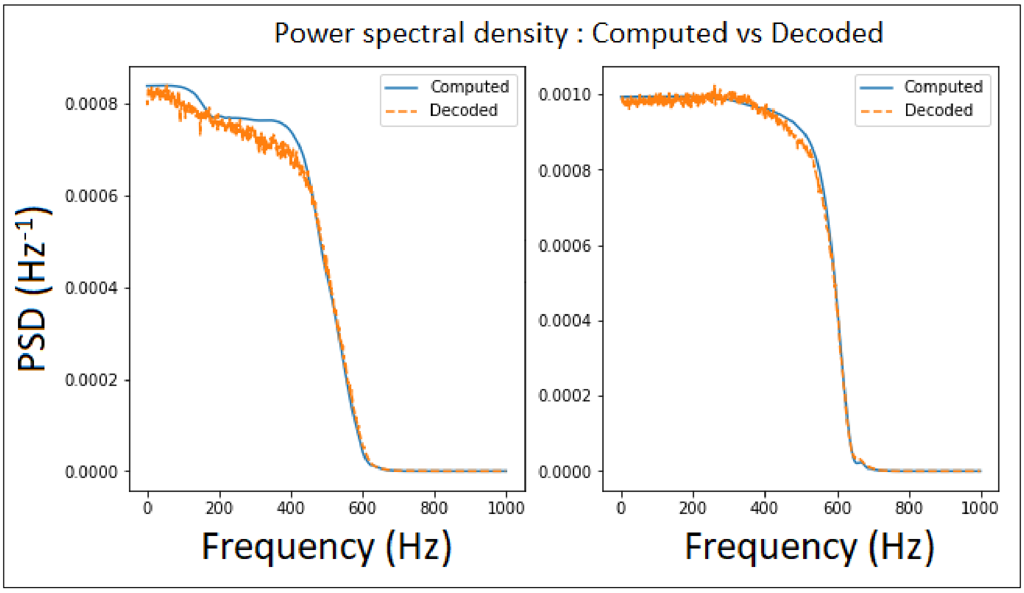

Figure 4.32.: Comparison of the computed PSD and the one reconstructed using the autoencoder.

We then built a new GP, this time with 8 inputs: the 3 previous moments and the 5 encoded values of PSD.

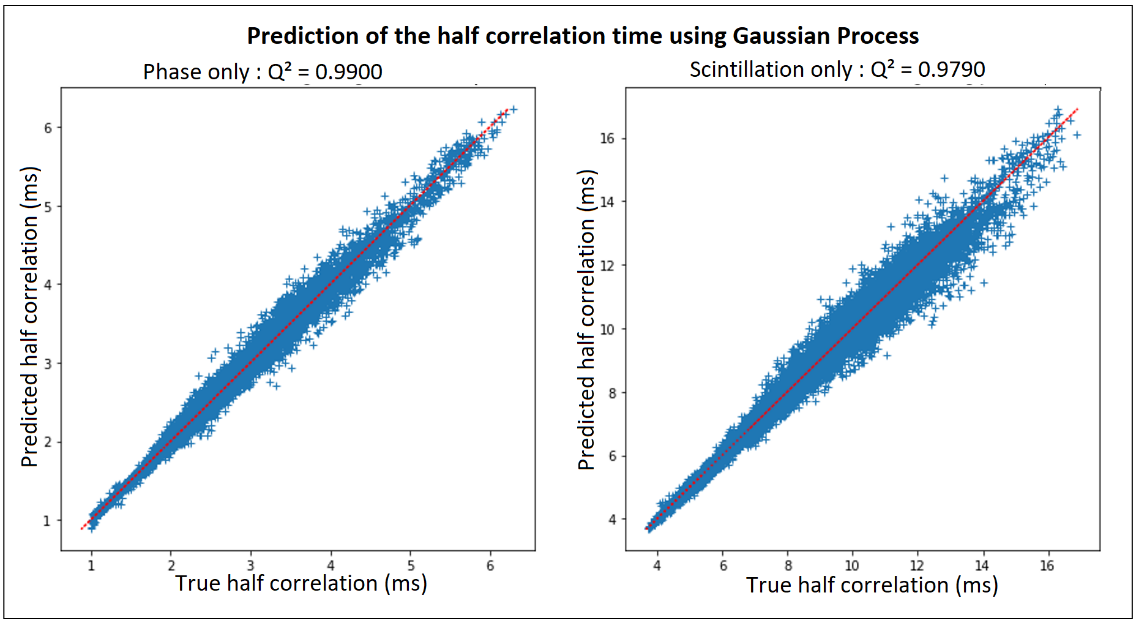

Figure 4.33.: Prediction of the half-correlation time using GP on inputs $r_0$, $\bar{h}$ and $\bar{v}$ and information on the PSD of scintillation for a 5cm pupil. The same other parameters as in figure 4.30.

As anticipated, with the added temporal information, we obtained much more satisfactory results than the ones described in figure 4.30 (see $Q^2$ figure 4.33: 0.99 and

0.98 against $Q^2$ figure 4.30: 0.88 and 0.84).

## 4.4.2. Sensitivity analysis

Using the same tools as the ones described in section 4.1.2, we conducted a sensitivity analysis and calculated first order Sobol' indices as well as Shapley and PME indices for each of the models described in 4.2.1.

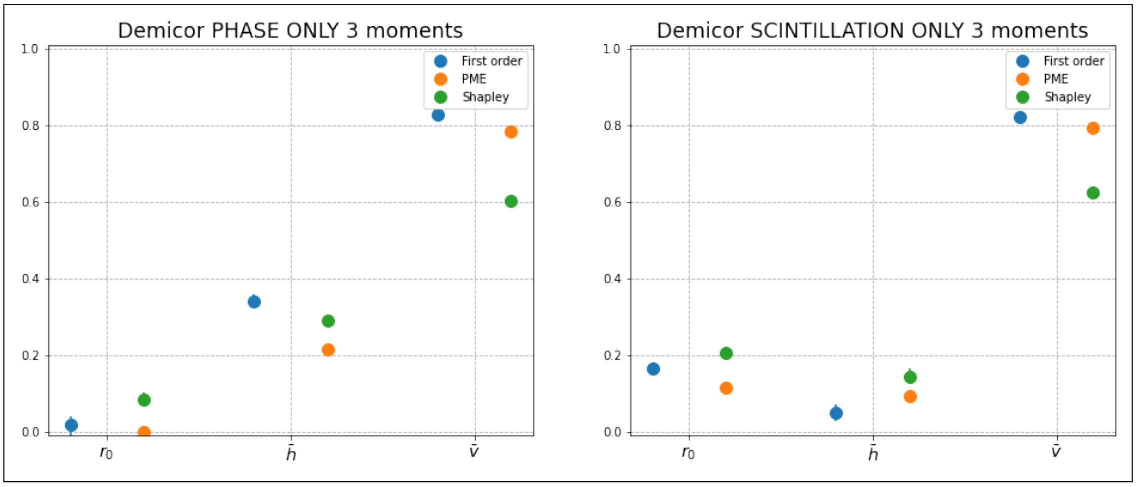

Figure 4.34.: Sensitivity analysis of the model described in Figure 4.30.

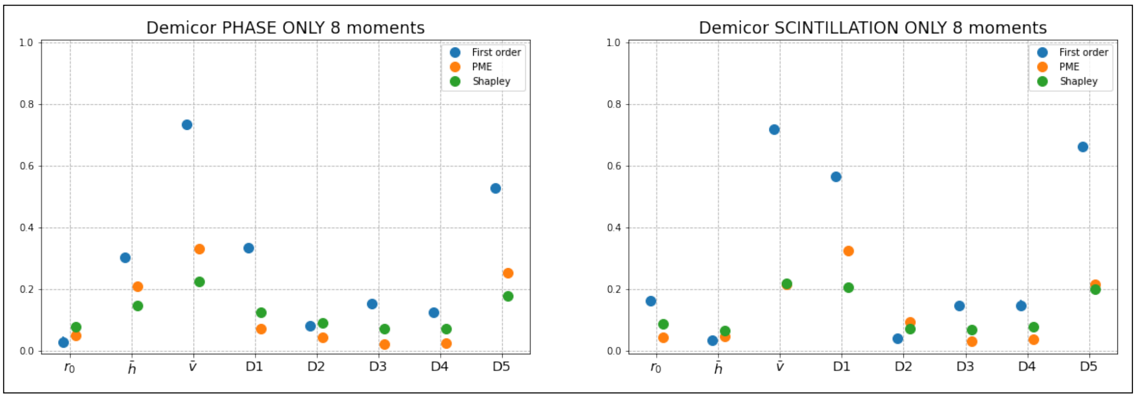

Figure 4.35.: Sensitivity analysis of the model described in Figure 4.33.

The results of the metamodel taking only $r_0$, $\bar{h}$, and $\bar{v}$ as inputs can be seen in Figure 4.34, while sensitivity analysis results computed on the model with the PSD added to the inputs are shown in Figure 4.35. In both cases, we can clearly see that the most influential variable is $\bar{v}$, which is not surprising given the fact that the correlation time depends on the displacement speed of the turbulent layer.

When adding the 5 moments of PSD (D1 to D5 in Figure 4.35), we obtain some interesting values. It can be noted that, while D1 and D5 have a lot of influence on the metamodel outputs, D2 seems to have very little. It would be interesting to look further into the characteristics of the autoencoder to better understand what features of the PSD each encoded value represents most, and thus what part of the PSD function is important in the description of the demi-correlation time of the ROP. This study is not trivial and will not be conducted here.

### 4.4.3. Influence of the AO design

Using the same two AO cases as in 4.3.5, we can try to assess the impact of the AO parameters on the prediction of the half-correlation of the coupled flux time series. In section 4.3.5 we explain how the scintillation behaviour is not impacted by the choice of the AO dimensioning. We will thus study exclusively the half-correlation of the coupling rate taking only the phase effects in consideration.

In Figure 4.36 we can visualise the values taken by this half-correlation of the coupling rate depending on the AO case. In both cases, the half-correlation time is almost the same with however a longer distribution tail and higher maximum values for AO case 2 (9 ms against 7 ms). As a reminder AO case 2 has a loop frequency of 1.3 kHz against 3 kHz for AO case 3. This result make sense as a faster response times and higher-speed actuators allow to correct for changes in the atmosphere more effectively, thus resulting in a shorter half-correlation time.

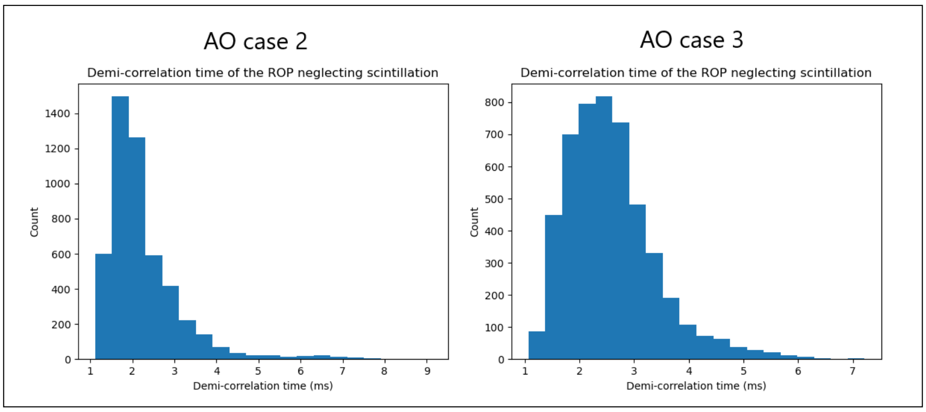

Figure 4.36.: Half-correlation of the coupling rate neglecting the scintillation for the 2 other cases of AO

Figure 4.37 shows the prediction accuracy of the model using only $r_0$, $\bar{h}$ and $\bar{v}$ as inputs as well as the accuracy using the model enriched with the knowledge on the PSD of the scintillation using the transformer considering the second AO case (15 radial orders and 1.3 kHz). Figure 4.38 shows the same thing for the third case of AO case (6 radial orders and 3 kHz).

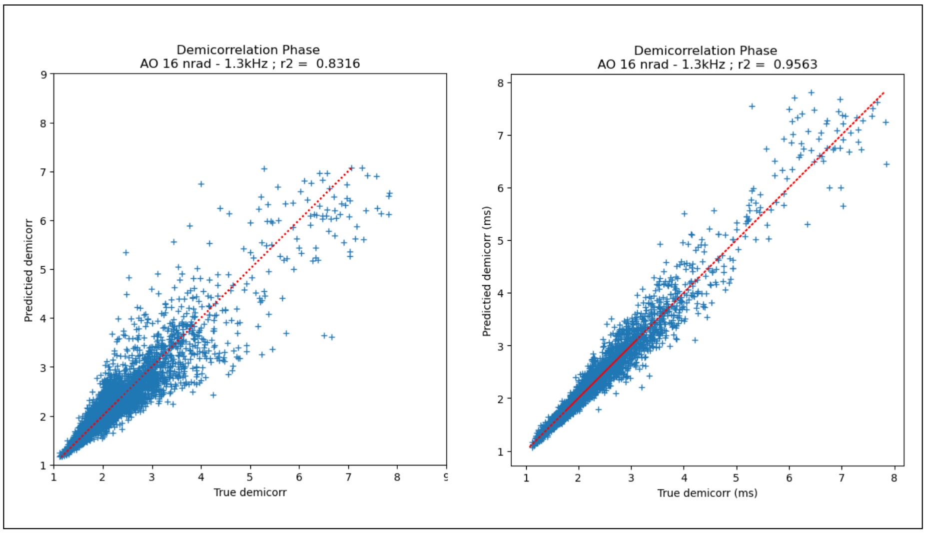

Figure 4.37.: Assessment of the half-correlation using 3 moments (left) and the 3 moments plus the 5 parameters of the PSD (right) for AO case 2

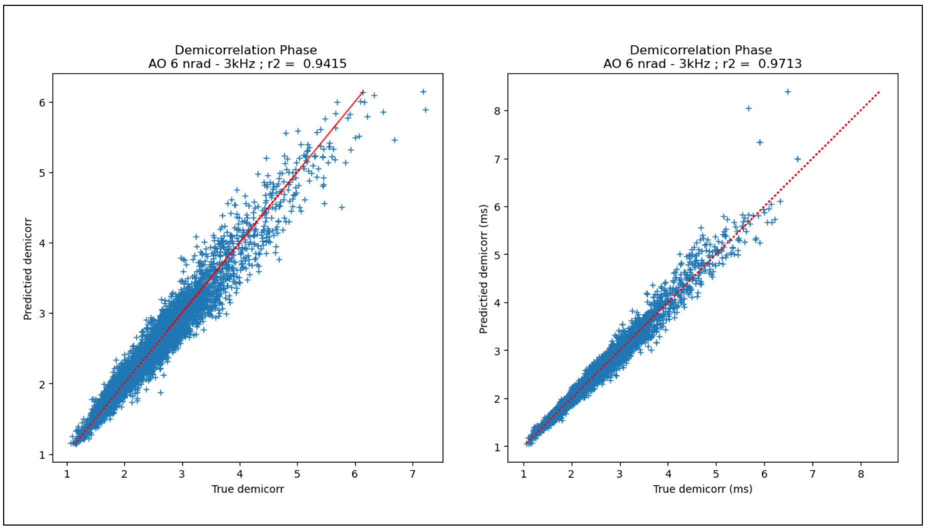

Figure 4.38.: Assessment of the half-correlation using 3 moments (left) and the 3 moments plus the 5 parameters of the PSD (right) for AO case 3

It seems that the quicker the AO system, the more accurate the prediction of the half-correlation time will be in spite of the lower number of corrected radial orders. This is true with or without the addition of the temporal information of the scintillation, also when considering our standard AO case of 10 kHz.

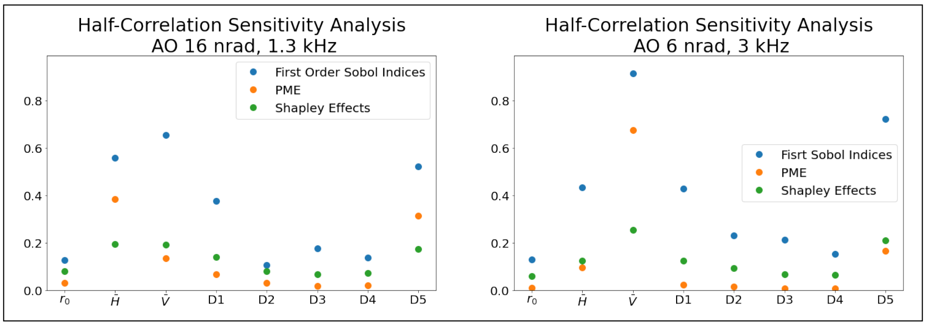

Figure 4.39.: Sensitivity analysis of the half-correlation assessment using 3 moments plus the 5 parameters of the PSD (right) for AO case 2 (left) and 3 (right)

The sensitivity analysis performed in figure 4.39 shows that the model used to predict the half-correlation time depends for the most part on $\bar{v}$ in the quick AO case while in the slower AO case, $\bar{v}$ and $\bar{h}$ both have a significant contribution. $D_1$ and $D_5$ are also influential in this case. We know that $\bar{h} \propto \left(\int_0^\infty v(z)^{\frac{5}{3}} C_n^2(z)dz\right)^{\frac{3}{5}}$ and $\bar{v} \propto \left(\int_0^\infty z^{\frac{5}{3}} C_n^2(z)dz\right)^{\frac{3}{5}}$. This translates in the fact that $\bar{h}$ is weighted mainly by the upper layers (where $z$ is large) while $\bar{v}$ is weighted by the lower and intermediates layers where the $C_n^2$ takes large values.

Looking at the error distribution of Figure 4.26, we can see that the autocorrelation function depends on two different phenomena depending on the studied AO case. In the case (2) at 1.3 kHz, the temporal error is the main source of error and the main contributor to the autocorrelation in the corrected signal. This error, and thus the autocorrelation of the corrected signal, is impacted both by $\bar{h}$ (for the angular decorrelation) and $\bar{v}$ (for the temporal decorrelation) wich translate in the sensitivity analysis of Figure 4.39.

On the other hand, for AO case (3), the fitting error clearly prevails. It is the time signature of the lowest order uncorrected modes (wich are the most energetic) that gives the signal its correlation. Since the fitting error depends neither on the layer height nor on the $C_n^2$ profile, the time signature of the residual (and therefore its correlation) depends only on the velocity of the layers that contribute most to these lowest orders, described almost solely by $\bar{v}$.

## 4.5. Discussions

In this chapter, we studied the possibility to assess downlink GEO to ground optical link ROP statistics by applying a machine learning methodology. We demonstrate that, assuming several simplification hypotheses on the AO system performance model, a set of a small number of integrated turbulence parameters appears sufficient to precisely assess ROP statistics. Moreover, exploiting the temporal power spectrum of the scintillation recorded by a small diameter receiver eases the evaluation of the ROP correlation time.

The results presented rely on the representativeness of the numerical model describing the influence of the propagation channel, it assumes a Rytov regime and a decorrelation of phase and amplitude perturbations.

The first hypothesis, regarding compatibility with the Rytov regime, has been verified with the data used in this study, but its validity at lower altitudes or under more severe turbulence conditions could be compromised. A study should be carried out to evaluate the difference between the performance evaluation provided by our metamodel and that obtained by an end-to-end model in cases of very severe turbulence, which would deepen our understanding of the limitations of the approach.

The second hypothesis, concerning the decorrelation of phase and amplitude perturbations, is widely accepted in the community, as it is justified by the fact that the phenomena causing these perturbations are generated at different distances from the receiver, and are therefore uncorrelated. The simulations mentioned in the previous paragraph would also contribute to strengthen the understanding of the limitations implied by this assumption.

# 5. Predicting the Link Availability

## Contents

5.1. Methods for the generation of stochastic processes with arbitrary marginal distributions . . . . . 93
  - 5.1.1. System . . . . . 97
  - 5.1.2. AnySim . . . . . 97
  - 5.1.3. Extended ARMA: ARRC . . . . . 104
    - 5.1.3.1. ARRC(5) & ARRC(4) . . . . . 104
    - 5.1.3.2. ARRC(1) . . . . . 109

5.2. Results . . . . . 112
  - 5.2.1. Impact of the half-correlation time . . . . . 112
  - 5.2.2. Comparison between **AnySim** and ARRC(1) . . . . . 114
  - 5.2.3. Sensitivity analysis . . . . . 117

The goal of Chapter 4 was to provide models to assess the statistics of a ROP time series using a small set of easily measurable moments. However, the statistic of ROP is not sufficient to manage successfully the handover between ground stations and the necessity arises of obtaining, using the same moments, information on the link power margin.

The link availability and the link power margin are calculated on the interleaved time series of ROP. The process, described in Chapter 2, consists of a non-linear transformation of the time series of ROP to the time series of MI. The interleaver is then modelled as a moving average on this MI time series. Given the non-linearity of the transformations that take place in the description of the power margin, we believe that it is not possible to obtain the power margin based solely on the ROP statistics obtained from the models of Chapter 4. This problem can be addressed using series generation methods. By generating a series stochastically equivalent to the initial ROP series from the predicted statistics, we shall be able to take into account the impact of interleaving and of the corrector code.

Although generating Gaussian processes is relatively easy due to their well-defined properties, the generation of stochastic processes with arbitrary marginal distributions presents a significant challenge. Our study falls within the broad field of the need to generate non-Gaussian stochastic processes, with the aim of generating two types of correlated process, one being a Gumbel-type PDF and the other being lognormal. The following section explores the difficulty in achieving this objective and proposes potential solutions to address this gap.

## 5.1. Methods for the generation of stochastic processes with arbitrary marginal distributions

Gaussian processes are widely used due to their simplicity and analytical tractability. Their generation involves specifying a mean function and a covariance function. Using techniques such as Cholesky decomposition or spectral methods, it is relatively straightforward to generate samples from a Gaussian process [AM88]. This simplicity arises from the inherent properties of Gaussian processes, which enable easy characterisation of their statistical behaviour.

During Cholesky decomposition, a multivariate normal distribution is generated with zero mean and a covariance matrix that depends on the covariance function of the process. The Cholesky decomposition is then used to transform the multivariate normal distribution into a Gaussian process.

Spectral representation, on the other hand, involves representation of the process as a sum of sinusoidal functions with random coefficients. Random coefficients are generated from a multivariate normal distribution with zero mean and a covariance matrix that depends on the spectral density of the process.

In contrast to Gaussian processes, generating stochastic processes with arbitrary marginal distributions is a complex task. Non-Gaussian processes often have complex statistical properties, such as highly skewed or heavy-tailed distributions, which require more sophisticated simulation techniques. Additionally, non-Gaussian processes may have prescribed covariance and marginal distribution functions that need to be satisfied during the simulation process, which further complicates the generation process. The marginal distributions of individual data points are not only determined by their own characteristics, but are also influenced by interactions and dependencies with other points in the process.

Despite the significance of generating stochastic processes with arbitrary marginal distributions, there are limited methods available to accomplish this task. Unlike the straightforward techniques used for Gaussian process generation, reproducing desired marginal distributions with the adequate autocorrelation function requires more sophisticated approaches that consider both the marginal characteristics and the dependencies between data points.

Traditionally, transformation methods are used. Also called translation-based simulation approaches, these methods for generating non-Gaussian processes assume a compatible relationship between the prescribed covariance function and the prescribed marginal distribution function. These approaches involve generating a Gaussian process and then transforming it into a non-Gaussian process by applying a non-linear transformation that preserves the covariance function. The non-linear transformation is chosen on the basis of the prescribed marginal distribution function [Cho03; Gri98; Gri07; XZ19]. However, this method is not applicable to reproduce higher-order statistics of the object function in the simulated sample functions [Cho03]. Due to its nature, it may also not be applicable when the target covariance and marginal distribution functions are specified independently, leading to difficulties in finding suitable translation functions that simultaneously satisfy both requirements.

Other methods exist. [PL98] presents a method for generating baseband and narrowband non-Gaussian processes with any specified marginal probability density function using stochastic differential equations. [ZC14] uses non-linear filters to generate non-Gaussian stochastic processes that match the spectral density and probability density.

In this work, we focus on two specific methods, one transformation method, **AnySim**, developed by [Tso18]. The other one, a discrete-time models for stationary time series generation, **ARRC** (Auto Regressive with Random Coefficients) is presented in [Pic10].

**AnySim** aims at the preservation of the marginal distribution and correlation structure of the process. The main strength comes from the fact that it is the only available complete package [TKM20] that allows for the simulation of non-Gaussian univariate and multivariate processes, stationary or cyclostationary (with varying periodicity), at different time scales. It can also be used for disaggregation of coarser-level sequences to finer-level sequences as well as for the generation of random fields with target spatiotemporal correlation structure. Further details will be given in section 5.1.2.

The second model, **ARRC**, was obtained from a collaboration with B. Picinbono and was developed as an extension of his model [Pic10]. This model offers fewer functions than **AnySim** and is limited to discrete-time modelling for stationary time series data. On the other hand, the fact that it uses only recursive generation and not transformation methods makes it a particularly computationally inexpensive and therefore fast model. Where **ARRC**'s complexity is in $o(n)$, **AnySim**'s is in $o(n^3)$ because of the necessary matrix inversions in transformation methods.

As a reminder to the reader, the ARMA (Autoregressive–moving-average model) model is a mathematical representation used to describe the behaviour of a stochastic process or signal over time. It combines two components: the autoregressive (AR) component, which captures the linear dependence of the signal on its own past values, and the moving average (MA) component, which represents the linear dependence on past error terms or residuals. By specifying the appropriate parameters for the AR and MA components, an ARMA model can be used to simulate or analyse various types of signal; however, the traditional ARMA model assumes Gaussian distribution, which makes it unsuitable for our application.

In [Pic10] a method for the generation of ARMA signals, with arbitrary specified symmetric marginal distribution functions, is presented. This is achieved by starting with a sequence of independent and identically distributed (IID) random variables with uniform distribution, and then transforming them to obtain a sequence of IID random variables with the desired marginal distribution function. The resulting ARMA signal will then have the desired marginal distribution function, and its autocovariance function can be computed using the algorithm presented in the article. However, this method was limited to the case of a probability function of symmetric density, which is not our case. On top of that, the auto-regressive coefficients associated with our stochastic process do not verify the necessary assumptions in equation 4 of the article, as it will be discussed in section 5.1.3. This limitation led us to develop a more complete version of the model in collaboration with B. Picinbono.

Each method will be described and explained using two sets of profiles that have been chosen to represent two different correction conditions. The first embodies a case of favourable correction conditions for the standard AO correction used before. It corresponds to a couple of $C_n^2$ and wind profiles for which the average coupled flux is higher than 95% of the entire population of profiles. They will be designated as the "Good correction" set in what follows. The second set of profiles aims to represent less favourable turbulence conditions, with an average coupled flux only higher than 5% of all cases. The profiles pertaining to this population correspond to the "Poor correction" set in what follows. The following figures (5.1, 5.2, 5.3) show the two sets of profiles, as well as how they statistically compare to the rest of the database.

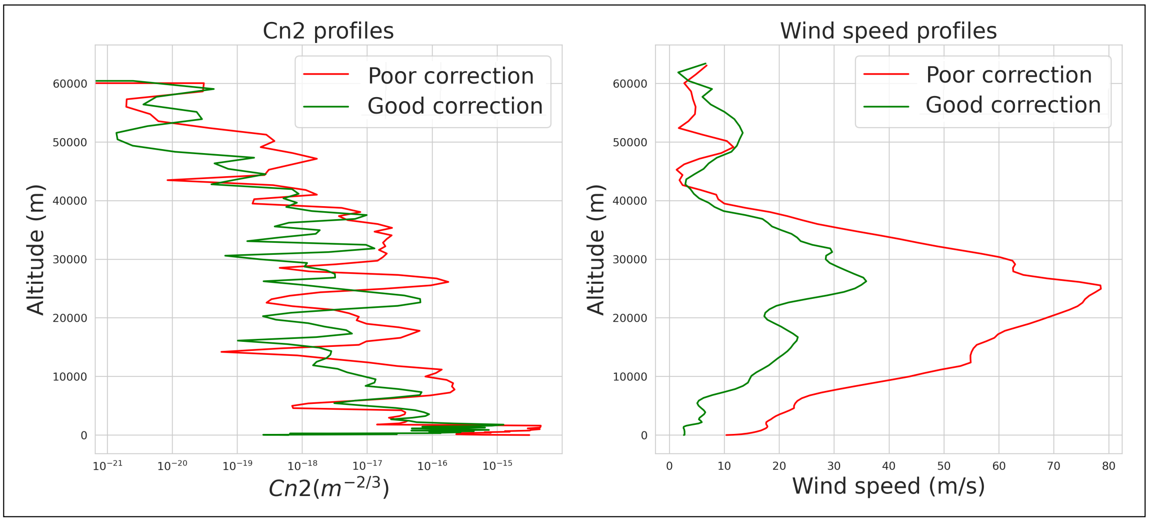

Figure 5.1.: The two sets of profiles, one in green for a good case of correction and one in red for a poor correction case.

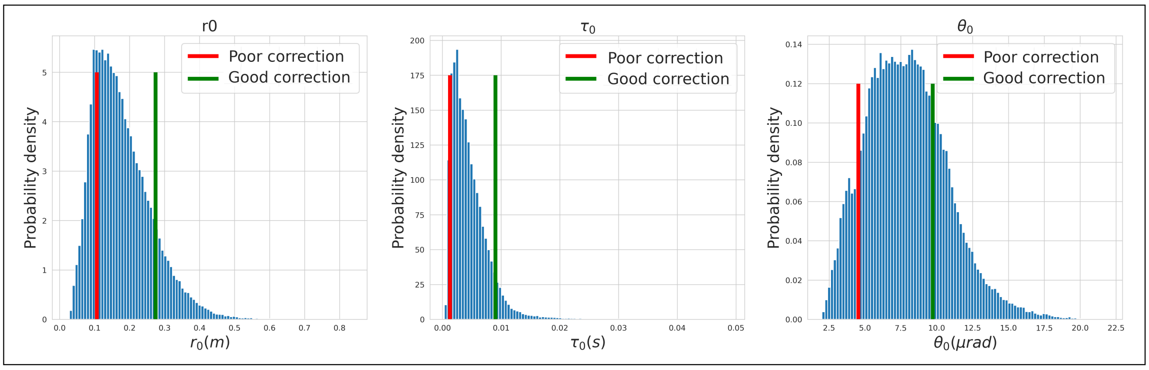

Figure 5.2.: The integrated parameters of the two previous sets of profiles (same colours) compared to the whole database.

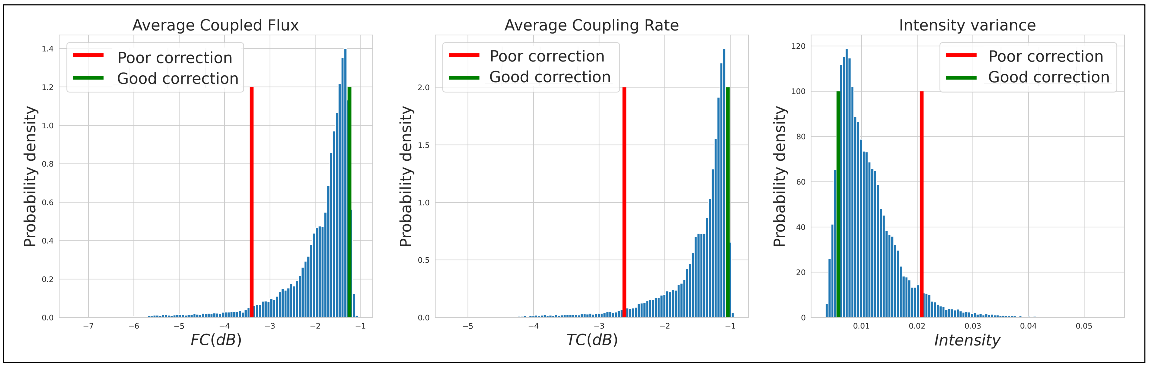

Figure 5.3.: The values of coupling efficiency of the two previous sets of profiles (same colours) compared to the whole database for our standard case of AO.

### 5.1.1. System

We remind the reader that the process for the power margin is explain in Section 2.3.3.1.

As long as the relation between the time series of ROP and the time series of MI is a monotonically non-decreasing function, the method will be the same. In order to simplify the description and give practical examples, we rely on the relation between the ROP and the MI provided by Airbus [Pou+23] and visible in Figure 5.4. The downlink budget excluding turbulence is $-38.33\ dB$ and is detailed in Chapter 2.

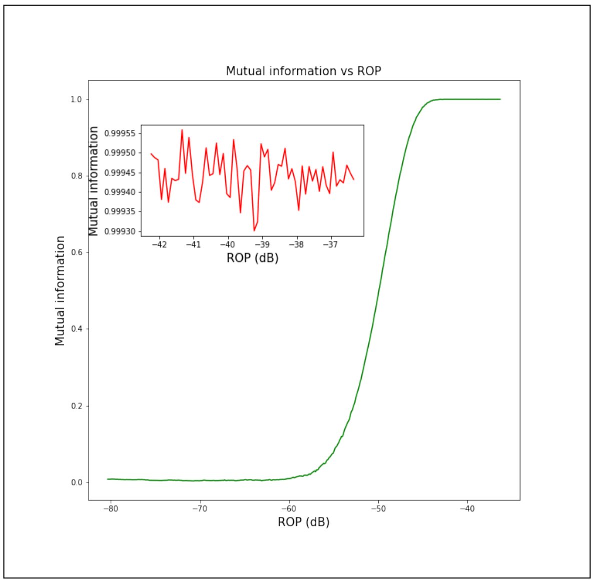

Figure 5.4.: Mutual Information vs received optical power, in red a zoom on the saturation zone

### 5.1.2. AnySim

As explained in the introductory paragraph, **AnySim** presents many advantages for the stochastic simulation of random variables, stochastic processes and random fields, with any marginal distribution and dependence structure. This powerful toolbox has been extensively validated in various publications, including [TKM20; Kos20; Kos+19; Tso18; KM18] where the flexibility of the tool is demonstrated on various applications such as rainfall, runoff, temperature, wind speed, and more.

In our work, we use only a small part of **AnySim** capabilities, as our goal is to generate a stationary non-Gaussian univariate process. For this specific application, **AnySim** uses the *Autoregressive To Anything* (ARTA) model developed in 1996 by [CN96]. The ARTA model is a sophisticated stochastic simulation approach that combines principles from autoregressive linear models and the concept of Nataf's joint distribution model (NDM)[Nat62] to simulate correlated non-Gaussian time series with arbitrary marginal distributions. The core idea behind the ARTA model is to transform an auxiliary Gaussian autoregressive process with zero mean and unit variance, into a target domain that adheres to desired marginal distributions and correlation structures. This transformation involves the use of inverse cumulative distribution functions (ICDFs), enabling the generation of time series that retain the prescribed statistical characteristics. The model's effectiveness lies in its ability to provide realistic representations of stochastic processes while maintaining the specified correlation and marginal features.

The advantage of using **AnySim** here is that it provides a complete and simple working framework in the only available well supported and fully tested library.

The generation method is quite straightforward. First, the type of process to be simulated is identified (in this case a univariate stationary non-Gaussian process) and the appropriate target marginal distributions as well as the target correlation structure are assigned using only the relevant integrated parameters coupled with the machine learning models developed in Chapter 4. Regarding the half-correlation, we used the metamodel which exploits the temporal spectrum of scintillation. ARTA, the stochastic generation model, is then used to simulate the auxiliary Gaussian process[CN96; TKM20].

It is implemented through two key R-functions: *EstARTAp* and *SimARTAp*:
*EstARTAp* is used to estimate the parameters of the auxiliary (Gaussian) autoregressive model of order $p$ using the nonparametric density matching (NDM) method.
*SimARTAp* is used to generate synthetic data according to a target stationary process. It takes the estimated parameters from *EstARTAp* and uses them to simulate the autoregressive process. The simulated Gaussian data is then transformed into the desired non-Gaussian process using the Nataf transformation method. This transformation is a mathematical procedure that maps the simulated Gaussian data to the desired non-Gaussian distribution. It ensures that the statistical properties of the simulated data, such as their marginal distribution and autocorrelation, match those of the target process [Nat62].

Following this methodology, we were able to generate time series of coupled flux and of scintillation. The autocorrelation model that we used is one of the default ones implemented in **AnySim** called CAS. CAS stands for the Cauchy-type two-parameter correlation structure. It is a correlation structure introduced by Koutsoyiannis [Kou00] that is designed to capture a wide range of processes and is used to simulate spatial and temporal dependencies in various applications.

The CAS correlation structure is defined by the following equation:

$$\rho_\tau^{\mathrm{CAS}}(\beta, \kappa) = (1 + \kappa\beta\tau)^{-1/\beta}, \tau \geq 0 \tag{5.1}$$

In this equation, $\beta$ and $\kappa$ are model parameters, and $\tau$ represents the time lag. The CAS correlation structure can model both short-range dependence (SRD) and long-range dependence (LRD) depending on the values of its parameters. When $\beta = 0$, it represents SRD, while $\beta > 0$ represents LRD.

In our case, it is quite clear that we have a SRD as the correlation function becomes zero after a few milliseconds or a few tens of milliseconds. We thus use $\beta = 0$ and the correlation structure becomes:

$$\rho_{\tau}^{\mathrm{CAS}}(\beta,\kappa) = (1+\kappa\tau)^{-1}, \tau \geq 0 \tag{5.2}$$

also known as the exponential correlation structure, which is commonly used for simulating processes with rapid fluctuations and high variability, such as precipitation and temperature.
$\tau$ can be easily calculated using the half-correlation time predicted by the Gaussian processes of Chapter 4. A more complex correlation structure could have been chosen but, as it would have been defined by more than one parameter, it would therefore have required the creation of other metamodels. Given the large error in predicting the half-correlation time (section 4.4), we can question the relevance of trying to predict other, more complex parameters. In section 5.2.1, we will show that the error made on the determination of the correlation time has a low impact on the description of the power margin.

One can see an example of the generation of coupled flux time series using **AnySim** on the predicted value of distribution and half-correlation time on Figure 5.5. Visually we observe the same order of magnitude and approximately the same fading duration in both cases (Observed and Generated cases). This is validated by the graphs of Figure 5.6, where the distribution of coupling efficiency (the term "coupling rate" used in the title is used interchangeably in this chapter) given by SAOST (named in the following as target values) and the one obtained after **AnySim** generation are compared as well

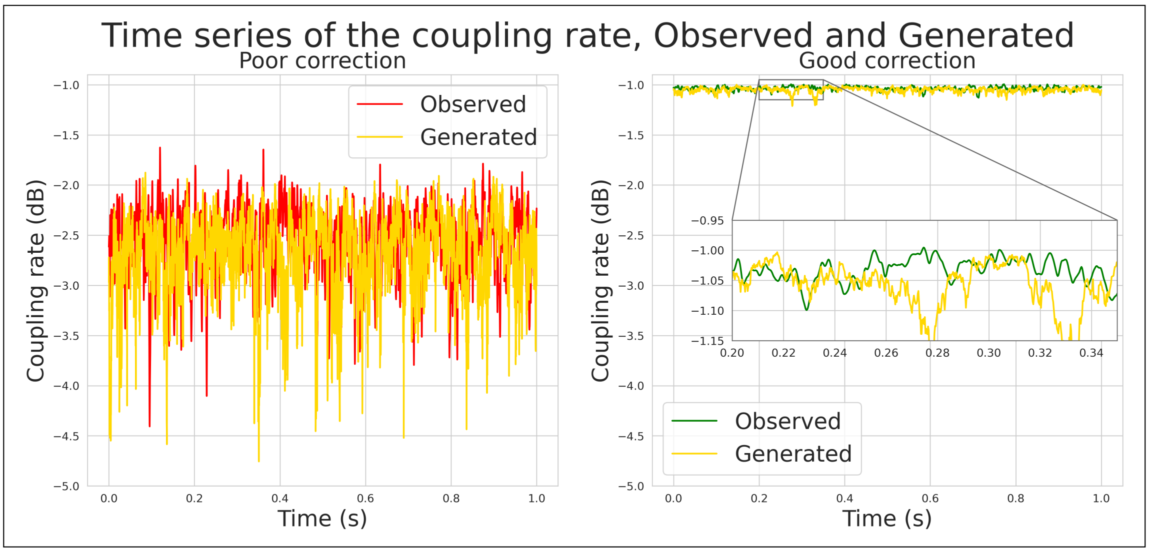

Figure 5.5.: Generated time series of coupling efficiency using **AnySim** compared to the targets for the two profiles described in Figure 5.1.

as the autocorrelation functions. One can see that the distribution function are not perfectly matching, with a mean coupled flux that is a bit underestimated by **AnySim** compared to the SAOST case. This is not due to the time series generation process, but to the fact that the prediction uses only the moments (ML model). As illustrated by the red dashed distribution in Figure 5.6, the error is due to the error on the predicted value of the distribution ($\mu$ and $\beta$ ) using algorithms of Chapter 4. For poor correction, the predicted values of $\mu$ and $\beta$ are respectively -2.52 and 0.33 versus -2.44 and 0.31 for the real values. In the case of a good correction we have a predicted $\mu$ of -1.04 that differs from the real value of -1.03 and a predicted $\beta$ equal to the real value of 0.02.

Regarding the autocorrelation function, the half-correlation time is well approximated in both cases, but the target (SAOST) function has a faster decay. The impact of the error on the autocorrelation function on the prediction of the power margin will be detailed in section 4.30, but we anticipate it to be very low due to the presence of a convolutional interleaver in the detection chain.

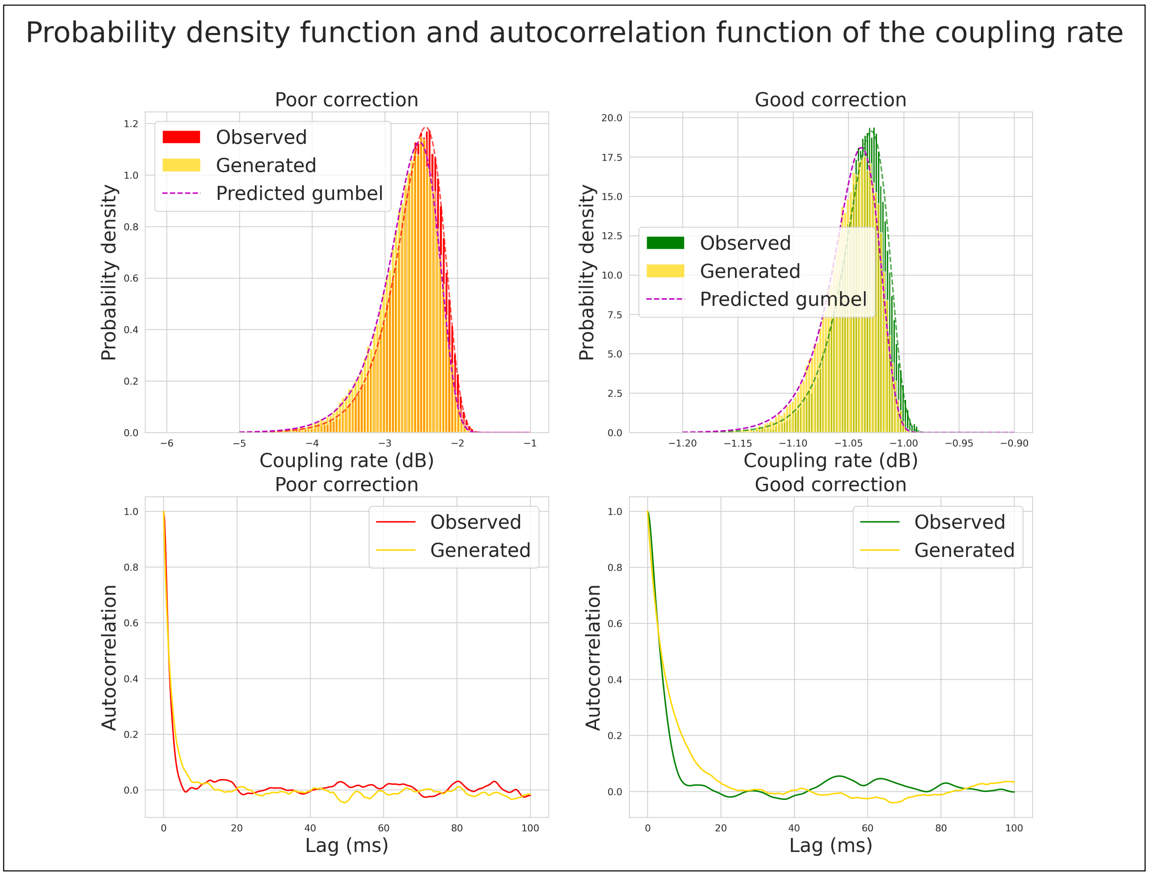

Figure 5.6.: Generated distribution and autocorrelation of coupled flux using **AnySim** compared to the target.

Figures 5.7 and 5.8 show the scintillation time series and their associated statistics. The overlay of observed and generated distributions indicate a very good match.

However, the error is large on the prediction of the autocorrelation function, especially for the case of good correction. The error on the half-correlation time remains low with a target value of 10.5 $ms$ against a predicted value of 11.4 $ms$. From Figure 5.6 and 5.8, one can see that the case chosen for its high average coupled flux is a case with both very good AO correction and with a low scintillation impact. The small variations in phase and intensity are also slower than in the case of poorer correction. This is consistent with the much more favourable wind profile of the "Good correction" case.

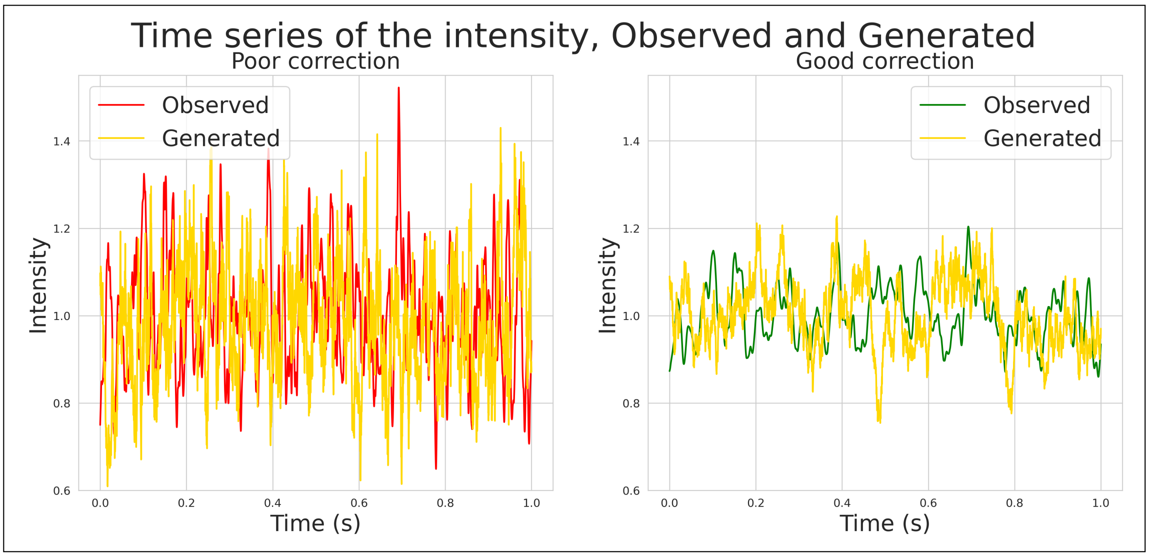

Figure 5.7.: Generated time series of scintillation using **AnySim** compared to the target series

The generation of the coupled flux time series illustrated by Figure 5.9 and 5.10 is done by multiplying the generated time series of coupling efficiency with the generated time series of scintillation 4.3. The impact of the scintillation is clearly visible, especially on the autocorrelation function due to the limited contribution of the coupling efficiency (thanks to the AO correction).

From these two time series of coupled flux, mutual information time series were computed. From these MI time series the power margins were calculated as a function of the interleaver size. We assume a 9/10 FEC overhead for the system presented earlier, corresponding to the required mutual information of 0.94 (2.3.3.1). With an interleaver size varying from 0 to 150 ms, Figure 5.11 shows the estimated power margin using **AnySim** and machine learning metamodels against the power margin obtained directly through SAOST.

With no interleaver or an interleaver close to 0, the error made on the power margin gets close to 1 dB. The error is the biggest for the case of poor correction. Because of the tail of the distribution and the finite nature of the series studied, the better the correction and the longer the interleaver, the greater the probability of having a small error in estimating the minimum of the time series.

For both considered cases, the error gets extremely small and well under the system

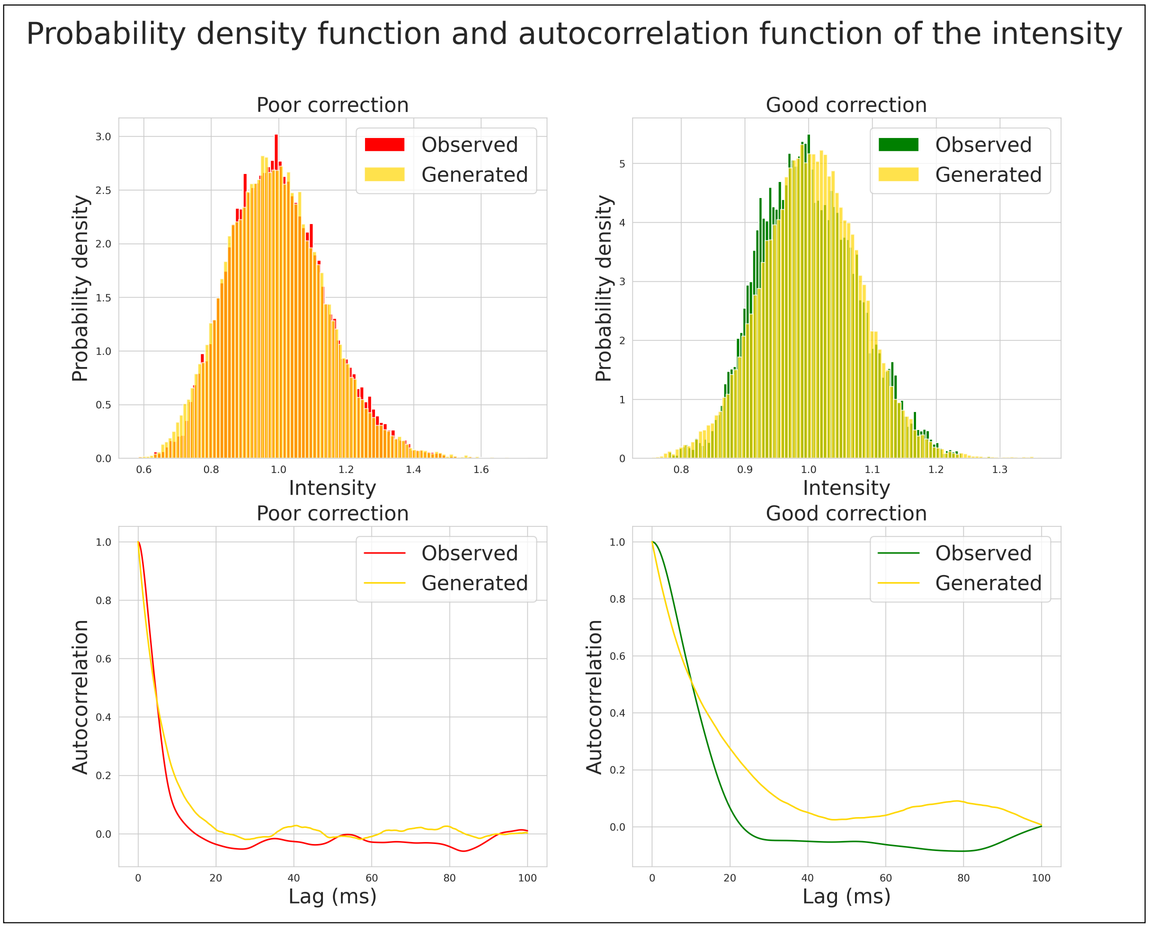

Figure 5.8.: Generated distribution and autocorrelation of scintillation using **AnySim** compared to the target series.

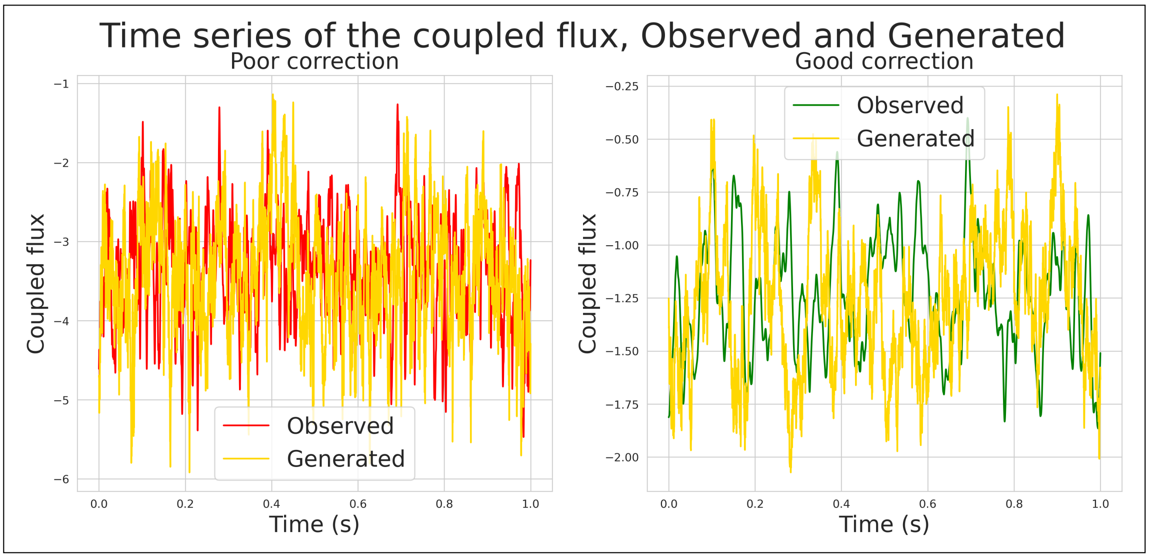

Figure 5.9.: Generated time series of coupled flux using **AnySim** compared to the target series

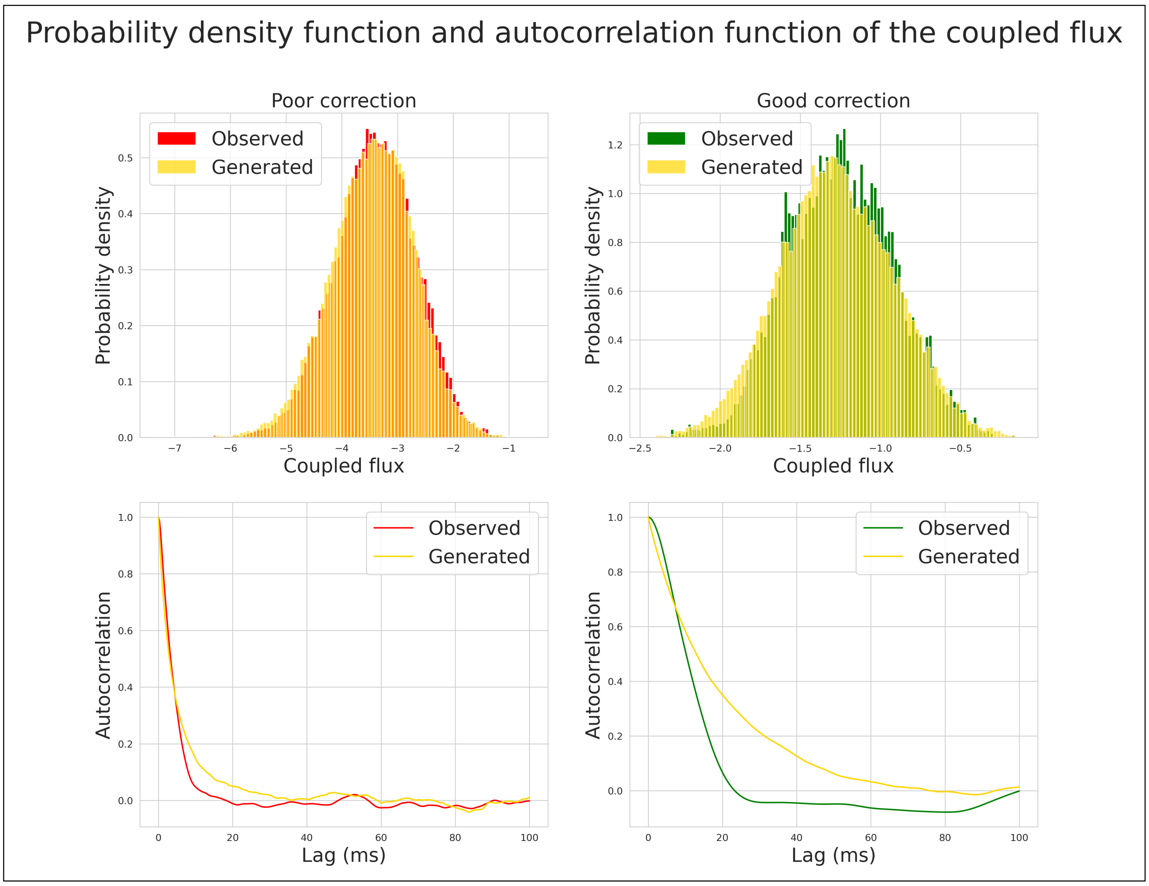

Figure 5.10.: Generated distribution and autocorrelation of scintillation using **AnySim** compared to the target series.

margin (commonly a few dB, here 2 dB ) when the interleaver gets above 100 ms, which is typically the range of interest.

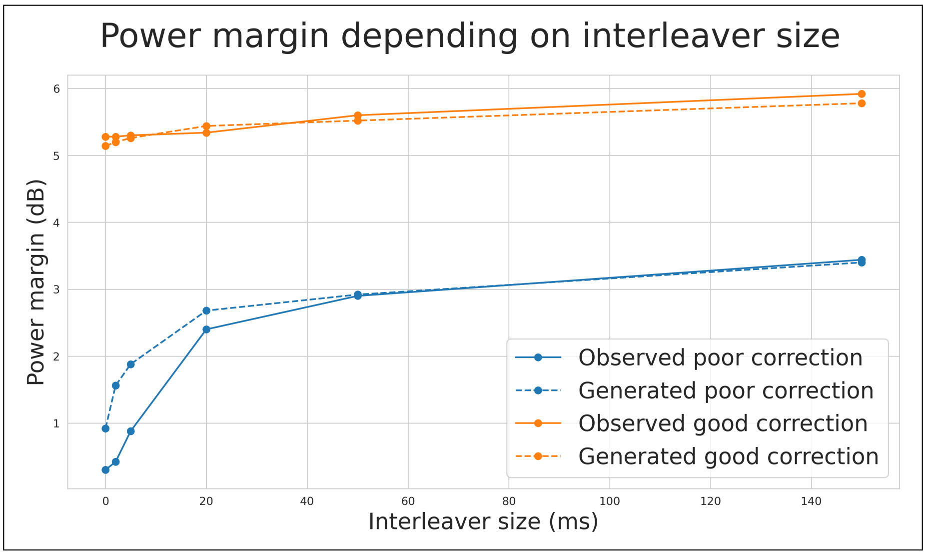

Figure 5.11.: Estimated power margin using **AnySim** and machine learning metamodels compared to target one.

### 5.1.3. Extended ARMA: ARRC

As introduced in the beginning of this chapter, B. Picinbono showed [Pic10] the possibility of introducing random coefficients into the defining recurrent equations of widely used ARMA models, thus generating random signals with the spectral properties of ARMA signals and an arbitrary marginal distribution. The new model is called the ARMA with Random Coefficients (ARMARC) model.

In the following, we chose to study an ARRC (auto regressive with random coefficients) model, the autoregressive part of the ARMARC model, as well as the value of the coefficients. An AR model alone can capture the linear dependence of a signal on its own past values, which shall be sufficient to translate correctly the autocorrelation function. The MARC (moving average with random coefficients) model can always be implemented later if needed.

#### 5.1.3.1. ARRC(5) & ARRC(4)

We base the first part of this section on the study of the coupling efficiency of the poor AO correction case. In the course of the article [Pic10], several assumptions were made. The first concerned the probability law of the white noise generator used in the model studied, assuming that its probability density function was a symmetrical (or even) function. This symmetry is convenient as it leads to the nullity of all odd moments associated with this PDF, and the same explicit or implicit assumption is used in most published work as a way to simplify the calculations. However, this symmetry condition is not valid for the representation of the coupled flux into the SMF. Through analysis it appears that, as long as the regression vector **a** contains only positive components $a_i$, the symmetry condition is sufficient but not necessary. Focusing on this case, we first need to determine the order of the ARRC model, as well as the values of the coefficients. Multiple methods are proposed in literature, but the most widely used is to compute the partial autocorrelation function (Partial Autocorrelation Function (PACF)). The Box-Jenkins method [And77] indicates that the order of the AR process can be determined by identifying the last significant spike in the PACF plot. The lag corresponding to this spike represents the order of the AR process. A significant spike is often set at $\pm 2/\sqrt{n}$, where $n$ is the number of data points (in our case $n = 20000$). According to Figure 5.12, the case of poor correction would correspond to an AR(5) process.

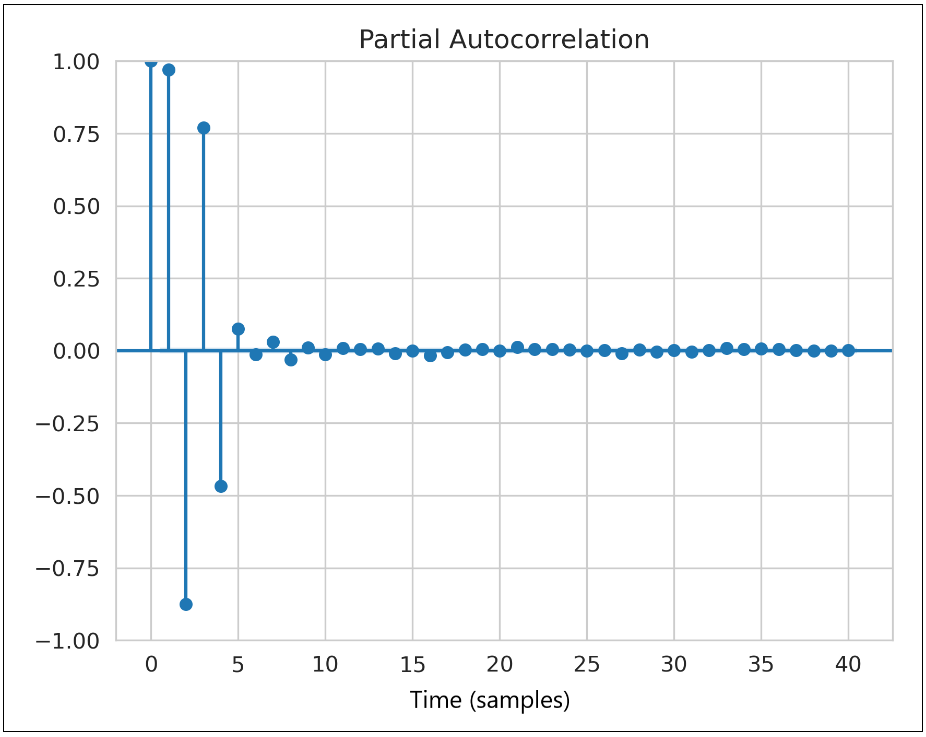

Figure 5.12.: Partial autocorrelation function of the target (SAOST) time series for the poor correction case.

The Yule-Walker equations are a set of equations that can be used to estimate the coefficients of an AR process[Yul27; Wal31]. After determining the order of the process and making sure the process is stationary (which is the case by construction), we find the 5 coefficients of the AR process given in Table 5.1. When determining the appropriate order for an AR process, it is important to consider the significance of

Table 5.1.: AR(5) coefficients calculated on the of the target (SAOST) time series for the poor correction case.

| Coefficient | $a_1$ | $a_2$ | $a_3$ | $a_4$ | $a_5$ |
|---|---|---|---|---|---|
| Value | 2.889 | -3.488 | 2.188 | -0.682 | 0.075 |

the coefficients. In this case, the last coefficient is negligible compared to the rest, which suggests that these lag have minimal impact on the current value of the time series, even though it appeared to be non-negligible in the PACF. In these cases, it is appropriate to consider a lower-order AR process. The coefficient of the associated AR(4) process determined using Yule-Walker equations are given in Table 5.2.

Table 5.2.: AR(4) coefficients calculated on the of the target (SAOST) time series for the poor correction case.

| Coefficient | $a_1$ | $a_2$ | $a_3$ | $a_4$ |
|---|---|---|---|---|
| Value | 2.853 | -3.342 | 1.937 | -0.468 |

According to [Pic10], multiple conditions are required to ensure the validity of the ARRC(4) process. First, in order to obtain a signal $X_k$ with finite variance (stability problem), the vector $a$ must belong to a domain called stability domain, ensuring that the roots of $D(z)$, where $D(z) = z^r - \left(a_1 z^{r-1} + a_2 z^{r-2} + \ldots + a_r\right)$, are located inside the unit circle. This is verified in our case where the roots of $D(z)$ can be visualised in Figure 5.13.

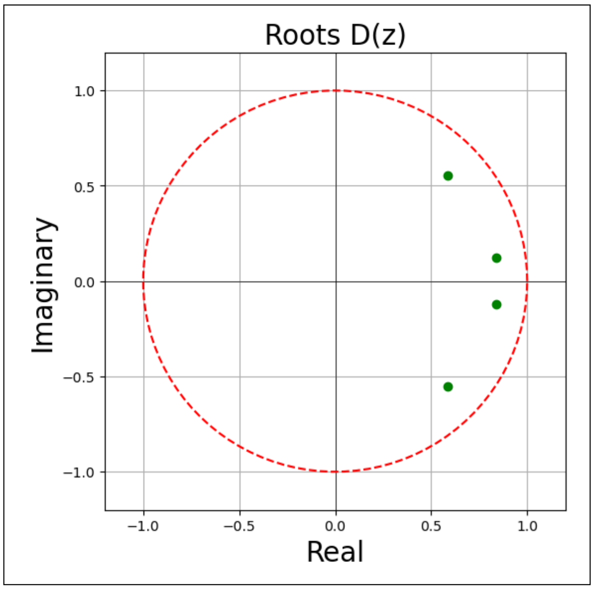

Figure 5.13.: The roots of $D(z)$ with the coefficients calculated in Table 5.2.

The second condition given in [Pic10] is that $S = \sum_{i=1}^{4} |a_i| < 1$. It is not respected here, as $S = 8.60$. A method developed within the collaboration is exposed here. If the sum $S$ of the modulus of $a_1$, $a_2$, $a_3$ and $a_4$ exceeds 1, it is possible to perform a similar partition as the one proposed in the equation 4 of the article using a larger interval. It is sufficient to choose an interval [0, D] with 1 < D < S and partition it into five parts with measures $|a_1|$, $|a_2|$, $|a_3|$, $|a_4|$, $D - |a_1| - |a_2| - |a_3| - |a_4|$ .

The recursive process to generate the ARRC signal is then defined in the following way:

$$X_k = \epsilon_1 A_1 X_{k-1} + \epsilon_2 A_2 X_{k-2} + \epsilon_3 A_3 X_{k-3} + \epsilon_4 A_4 X_{k-4} + A_5 W_k \tag{5.3}$$

$A_i$ are Bernoulli random variables (i.e. with two possible values: 0 and 1) that take the value 1 with probabilities proportional to $|a_1|$, $|a_2|$, $|a_3|$, $|a_4|$, $D - |a_1| - |a_2| - |a_3| - |a_4|$ respectively, for i equal to 1, 2, 3, 4, or 5. $\epsilon_i = \frac{a_i}{|a_i|}$ is the sign of the coefficient $i$.

It is then straightforward to follow the demonstration from [Pic10] and verify that the generator noise **W** and the signal **X** have the same marginal probability distribution, at least if the distribution of **W** is symmetric, as in [Pic10]. The non-symmetric case is more complex to analyse, and currently, no satisfying results are being reported.

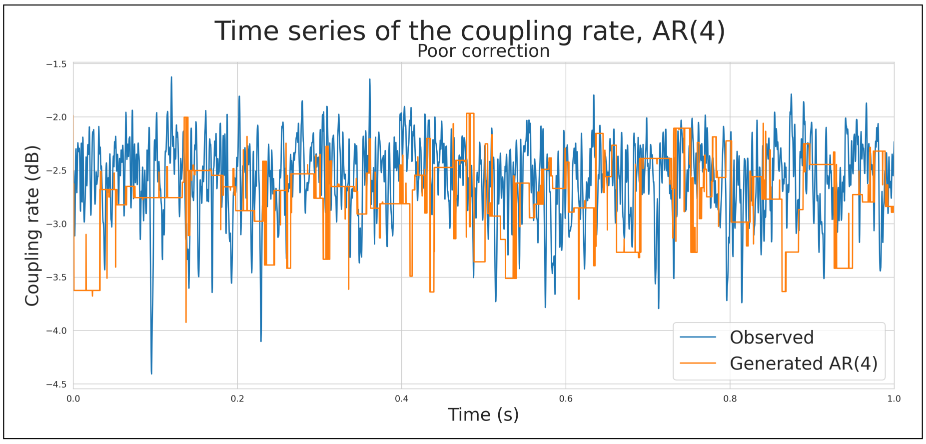

Figure 5.14.: Time series of coupling efficiency generated using ARRC(4) method compared to the target series for the poor correction case.

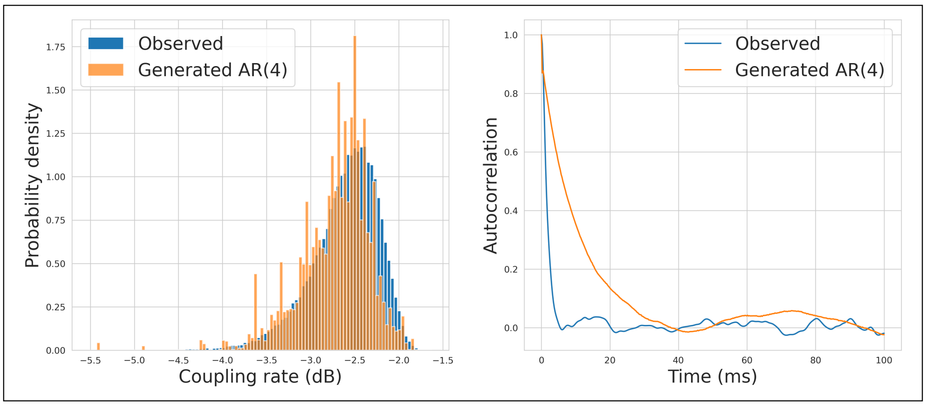

Figure 5.15.: Statistics of the time series of coupling efficiency generated using ARRC(4) method compared to the target series for the poor correction case.

The series generated according to this method can be found in Figure 5.14 with the associated statistics in Figure 5.15. As one can see, we make an overly large error on the prediction of the autocorrelation function.

This might be due to the fact that the symmetry of the probability density function seems necessary when the regression vector **a** contains components $a_i$ that are not all of the same sign. In this situation, we can introduce two vectors $\mathbf{a}^+$ and $\mathbf{a}^-$ to isolate the positive and negative parts. Thus, the components of $\mathbf{a}^+$ are $a_i$ if $a_i \geq 0$ and 0 otherwise, and the same applies to $\mathbf{a}^-$. It was verified that, in this case, the PDFs of the generated time series are those of the model generating noise **W**.

However, the way to combine $\mathbf{a}^+$ and $\mathbf{a}^-$ opens up several options that can lead to laborious calculations. This question of how well the ARRC(4) process could reproduce the statistics of the coupling efficiency remains open at this stage. However interesting this ARRC method initially seemed, especially regarding computational costs, we were led to to the same approximation as in the previous section (5.1.2). This approximation considers a decreasing exponential autocorrelation function defined by the sole parameter of the half-decorrelation time. The resulting change in the description of the autocorrelation causes variation in the generation model. In fact, whatever the series, if it has an exponential autocorrelation function it can be described by an ARRC(1) process.

#### 5.1.3.2. ARRC(1)

ARRC(1) means a time series $\mathbf{X} = (X_0, X_1, X_2, ...)$ where $X_k$ would depend only on $X_{k-1}$ and thus an autocorrelation function which would be equivalent to a decreasing exponential function. Using equation 5.3 at order one:

$$X_n = B_n X_{n-1} + (1 - B_n) W_n \tag{5.4}$$

where $W_n$ is the white noise with the same marginal distribution as $\rho_\phi$, $B_n$ is a Bernoulli random variable that takes the value 1 with probability $a$ and 0 with probability $1 - a$, $a$ being the ARRC(1) coefficient.

From the induction of equation 5.4 assuming $X_1 = W_1$, one can deduce that the stationary distribution $X$ and $W_n$ have the same marginal distribution. Let us write $\gamma(k, a)$ the auto covariance function at lag $k$.

$$\begin{aligned} \gamma(k,a) =& \mathbb{E}\left((X_n - \mu)(X_{n-k} - \mu)\right) \\ =& \mathbb{E}(X_n X_{n-k}) - \mu^2 \end{aligned} \tag{5.5}$$

where $\mu$ is the mathematical expectation of the stochastic process.

$$\gamma(0, a) = \mathbb{E}(X_n^2) - \mu^2 = \sigma^2 \tag{5.6}$$

where $\sigma^2$ is the variance of the stochastic process. We can calculate:

$$\begin{aligned} \gamma(1,a) =& \mathbb{E}(X_n X_{n-1}) - \mu^2 \\ =& \mathbb{E}\left[aX_{n-1} + (1-a)W_n)X_{n-1}\right] - \mu^2 \\ =& a\mathbb{E}(X_{n-1}^2) + (1-a)\mathbb{E}(X_{n-1}W_n) - \mu^2 \\ =& a\left(\mathbb{E}(X_{n-1}^2) - \mu^2\right) \\ =& \sigma^2 a \end{aligned} \tag{5.7}$$

using the fact that $W_n$ and $X_n$ are independent, $W_n$ being a white noise.

Using a standard mathematical induction, one can show that:

$$\gamma(k, a) = \sigma^2 a^{|k|} \tag{5.8}$$

Leading to

$$a = e^{\frac{ln(0.5)}{\tau_{half-correlation}}} \tag{5.9}$$

with $\tau_{half-correlation}$ the half-correlation time, that can be easily determined using the machine learning metamodels of the previous chapter.

Using this ARRC(1) model with the analytical expression of $a$, we generated the time series of Figure 5.4 corresponding to the statistics of Figure 5.17.

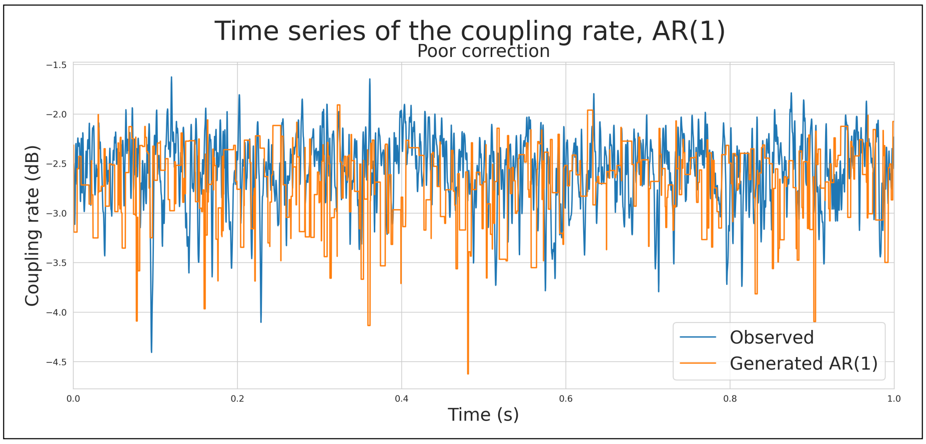

Figure 5.16.: Time series of coupling efficiency generated using ARRC(1) method compared to the target series for the poor correction case.

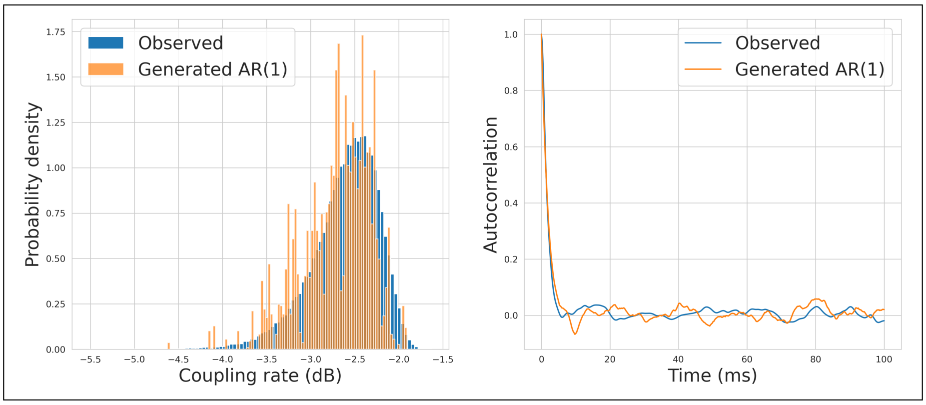

Figure 5.17.: Statistics of the time series of coupling efficiency generated using ARRC(1) method compared to the target series for the poor correction case.

The marginal distribution is still accurate, even though it would need far more points to converge due to the structure of the generation method. To mimic the target (SAOST) series, only 4 000 points where used leading in a 10 seconds simulation.
The autocorrelation function fits better than in the ARRC(4) case.

Using ARRC(1) to generate series of $\rho_\phi$ and $\rho_I$ and knowing $\sigma_\chi^2$, we can easily generate time series of $f_{smf}$. Using the same formalism as in the last section, we plotted the statistics of $f_{smf}$ generated from ARRC(1) and the machine learning metamodels for both, the poor and the good case of correction in Figure 5.18. Once again, the marginal distribution did not converge but seems to accurately match the one of the initial signal and the fit of the autocorrelation function is more convincing than in **AnySim** cases.

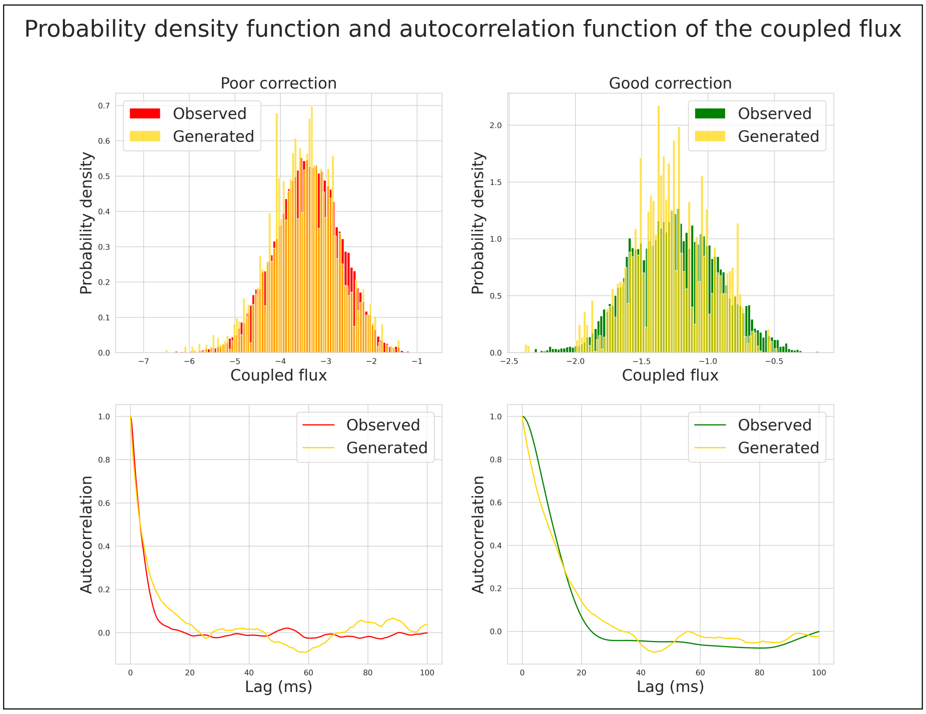

Figure 5.18.: Generated distribution and autocorrelation of scintillation using ARRC(1) compared to the target one.

Figure 5.19 shows the power margin depending on the interleaver size calculated with ARRC(1) and compared to the ground truth (SAOST).

Results are similar to the ones given in Figure 5.11 for **AnySim**.

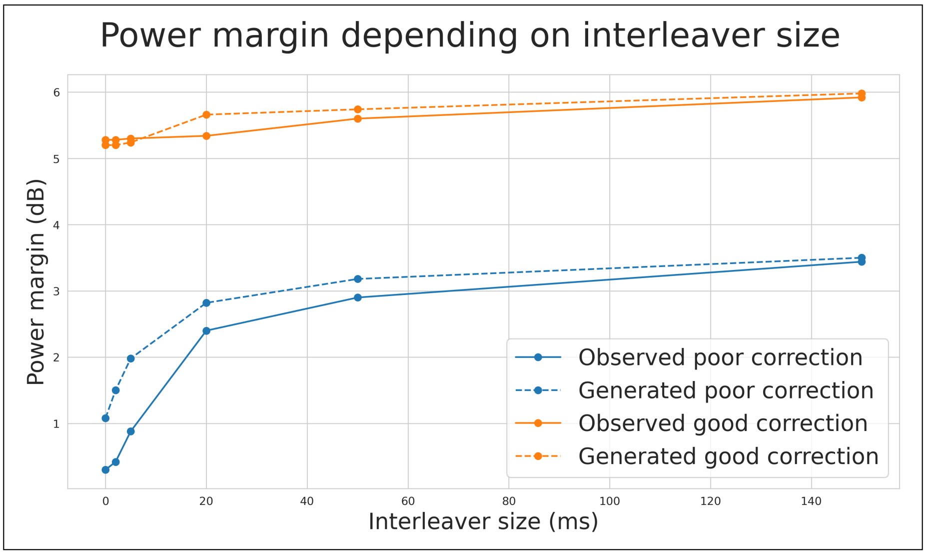

Figure 5.19.: Power margin depending on the interleaver size calculated with ARRC(1) compared to the ground truth.

Two alternative approaches have been proposed for generating ROP time series from the evaluation of moments. These methods make it possible to evaluate power margins with a very small error (below 1 dB) under a wide variety of conditions. This makes it possible to control performance without requiring highly precise information about the state of the channel in the medium term and thus is a crucial step in the development of future operational systems. However, the use of only two profiles is not sufficient to compare the accuracy in the determination of the power margin to each of the model. This comparison will be carried out in depth in the next section by showing the error on the power margin estimation for every time series of the database.

## 5.2. Results

In the following, two cases are studied, our system requirements with an interleaver size of 100 $ms$ are constant. In one case, we look at a **MODCOD** 9/10 with a required mutual information of 0.94, and in the other a **MODCOD** 3/10 with a required mutual information of 0.12.

The two methods are compared on all times series in our database. The time series are generated using the distributions provided by the machine learning models using the moments as input.

### 5.2.1. Impact of the half-correlation time

The generation of random time series of 5 seconds with a 4 $kHz$ sampling, i.e. 20.000 occurrences to ensure good statistical convergence, is very memory intensive. In this small section, we limited our simulation to 5.000 pairs of profiles randomly selected in our database. The generation of random time series was performed two times with **AnySim**, once using the half-correlation time computed using only $r_0$, $\bar{h}$, $\bar{v}$ and $\sigma^2_\chi$ and once with the scintillation PSD added to the prediction of the half-correlation time. The following results of power margin are given using our system requirement with an interleaver size of 100 $ms$ coupled to a **MODCOD** 9/10 with a required mutual information of 0.94 and a **MODCOD** 3/10 with a required mutual information of 0.12.

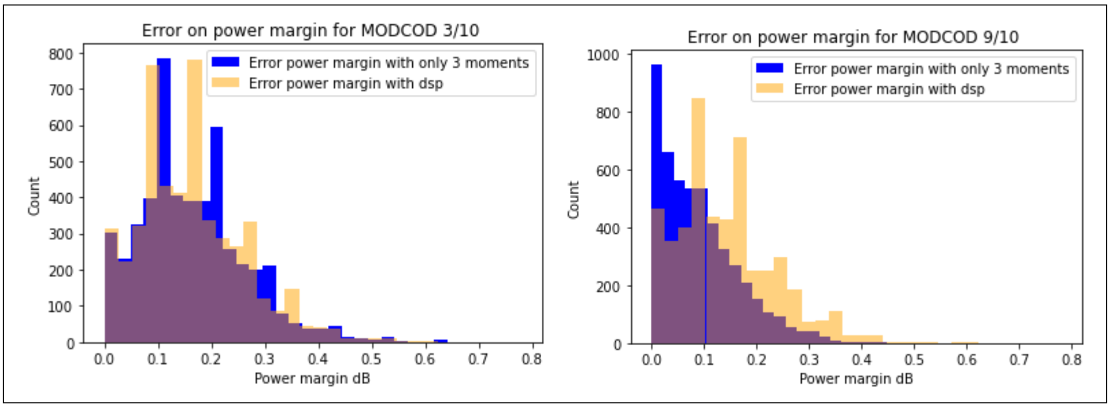

Figure 5.20.: Distribution of power margin error using **AnySim** for MODCOD 3/10 (top) and 9/10 (bottom) - interleaver 100ms. In blue using the model with $r_0$, $\bar{h}$, $\bar{v}$ and $\sigma^2_\chi$ in yellow when the PSD of scintillation is added.

In Figure 5.20 we can compare the probability density function of the power margin error with or without the use of the PSD in the models. The power margin error is calculated as the absolute value of the difference in the power margin error given by SAOST and given after the generation of time series using **AnySim**. When the temporal PSD of scintillation is added to the input (yellow in Figure 5.20), no significant improvement is observed, we even have a maximal error a bit higher in both **MODCOD** cases, which might be attributed to the convergence error of the estimation due to the limited length of the considered time series. In this specific case of a 100 ms interleaver, significantly larger than the half-correlation time (ranging in the $10^{th}$ of milliseconds), a better prediction of the half-correlation does not translate into better prediction of the power margin.This confirms the relevance of the interleaving process.

The same results have been obtained using ARRC(1), where the use of the scintillation PSD does not improve the evaluation of the power margin. This means that, in the system considered here, the use of an additional instrument to measure the scintillation spectrum would only bring about extra complexity without visible improvements. In the following, we don't take into account such instrument and results of power margin are calculated exclusively with $r_0$, $\bar{h}$, $\bar{v}$ and $\sigma^2_\chi$.

### 5.2.2. Comparison between AnySim and ARRC(1)

Running both models on each **MODCOD** case for the entire database shows the difference in terms of complexity in the models. We generated the 37059 times series of 10 seconds each sampled at 4 $kHz$ using the AO parameters of our main system, ie. 10 corrected radial order and an AO frequency of 2 $kHz$. While it takes few minutes to generate this series using ARRC(1), ARCA requires more than 24 hours to run for each case of **MODCOD**, using a single processor.

The algorithm used to determine the power margin from the generated time series detailed in Chapter 3 takes about 8 hours on a single core CPU for each model and **MODCOD** case. However, moving the operations on a standard GPU with 8 Gb of VRAM enabled us to reduce this time to only a few minutes. The computation of the power margin was done with a resolution of 0.1 dB, hence the large bars on the histograms of Figure 5.23.

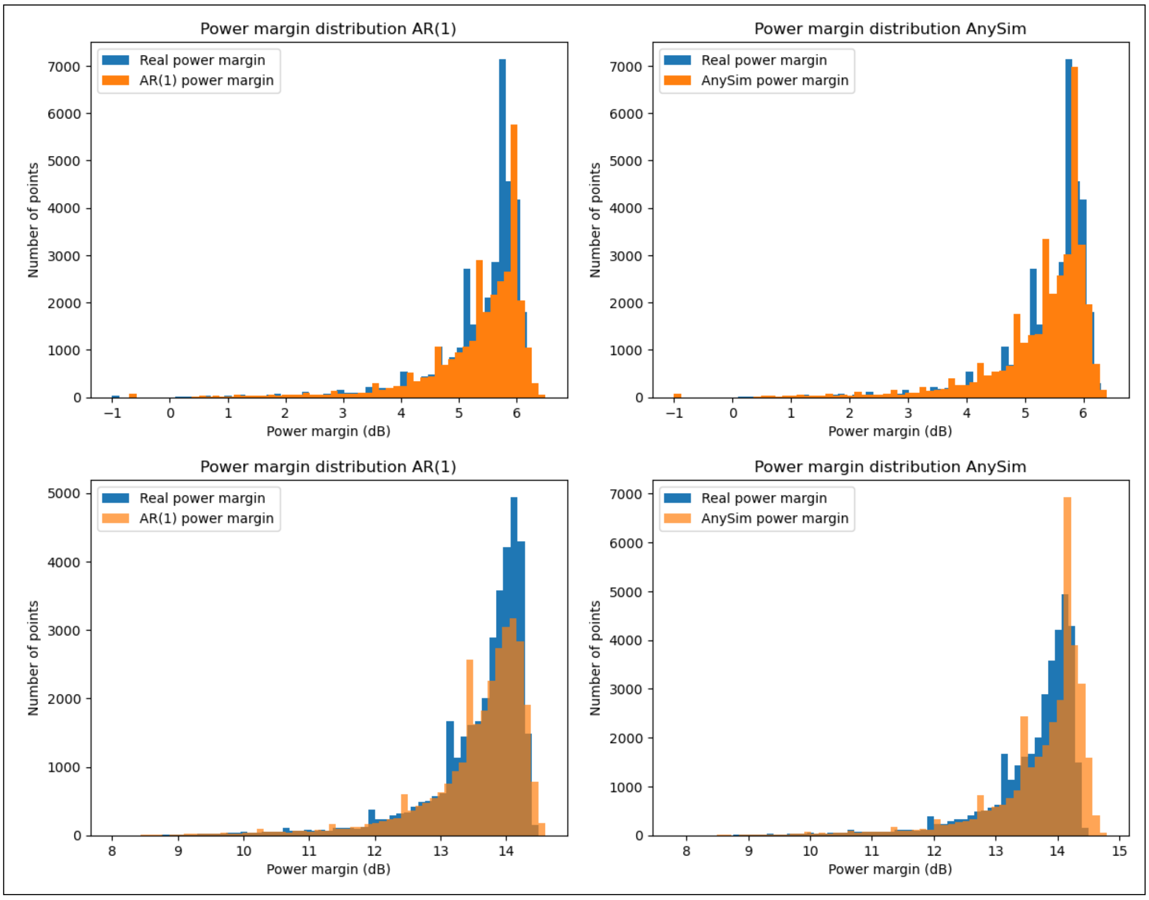

Figure 5.21.: Distribution of the estimated power margin with time series generation versus the distribution of the target power margin.
**Upper left:** ARRC(1) MODCOD 9/10; **Upper right:** **AnySim** MODCOD 9/10; **Lower left:** ARRC(1) MODCOD 3/10; **Lower right:** **AnySim** MODCOD 3/10

From Figure 5.22 one can see that the score is approximately the same with **AnySim** showing a better score in the case of low redundancy in the correction code (high **MODCOD**) and ARRC(1) a better score in the other case. Based on this Figure, it is hard to tell if a model should be privileged regarding accuracy only. When taking computation time into account, **ARRC** is the clear winner.

The number of false-positive and false-negative on the link availability are particularly interesting as they are representative of the accuracy of our availability model. Focusing on the higher **MODCOD** case (in the **MODCOD** 3/10 case we don't encounter link outage), one can see that for both models there is a non-negligible amount of false negatives on the availability of the link ( $-1$ in ordinate associated to a positive value in abscissa). There are 32 cases in the database where the link is not available when our model detects 74 occurences of these interruptions (both for ARRC(1) and AnySim) leading to a total of 42 false negatives. This means that 0.11% ($\frac{42}{37059-32}$) of the time, we could have had a viable link, but our model returned information about an unavailable ground station. This unfortunate result must be put into perspective with the fact that in these 0.11% of cases, the power margin is less than 1dB, which, in an operational case where large margins are taken, would have led us to choose another station anyways.

There appear to be no false-positives. The lack of false positive is very good for an industrial use of the models. It would be harmful to handover the link to a station thinking think is available but is not in reality causing an unexpected shortage.

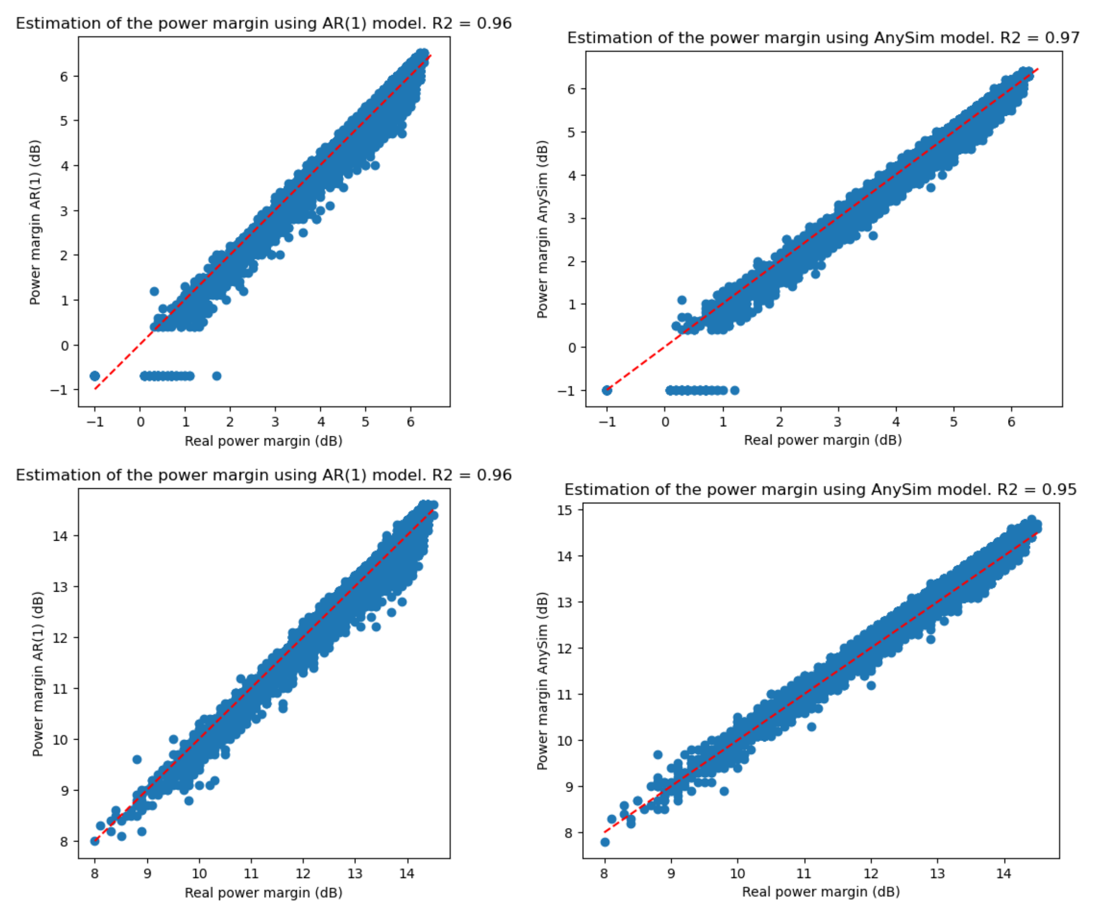

Figure 5.22.: Generated vs real power margin with $R^2$ score for each case
Upper left: ARRC(1) MODCOD 9/10; Upper right: **AnySim** MODCOD 9/10; Lower left: ARRC(1) MODCOD 3/10; Lower right: **AnySim** MODCOD 3/10

Figure 4.26 shows the distribution of the error made by each of the models on the two **MODCOD** scenario with the given 100 *ms* interleaver. It can be seen that both models behave very similarly, however, with a longer distribution tail on the error made by ARRC(1). This is probably due to the fact that with the ARRC method, the probability density does not converge with 4000 points (Figure 5.17). A larger number of points could be considered, but this would imply a more computationally expensive estimation of the power margin. A compromise has to be found and this number of points is satisfactory in view of the 2dB system margins.

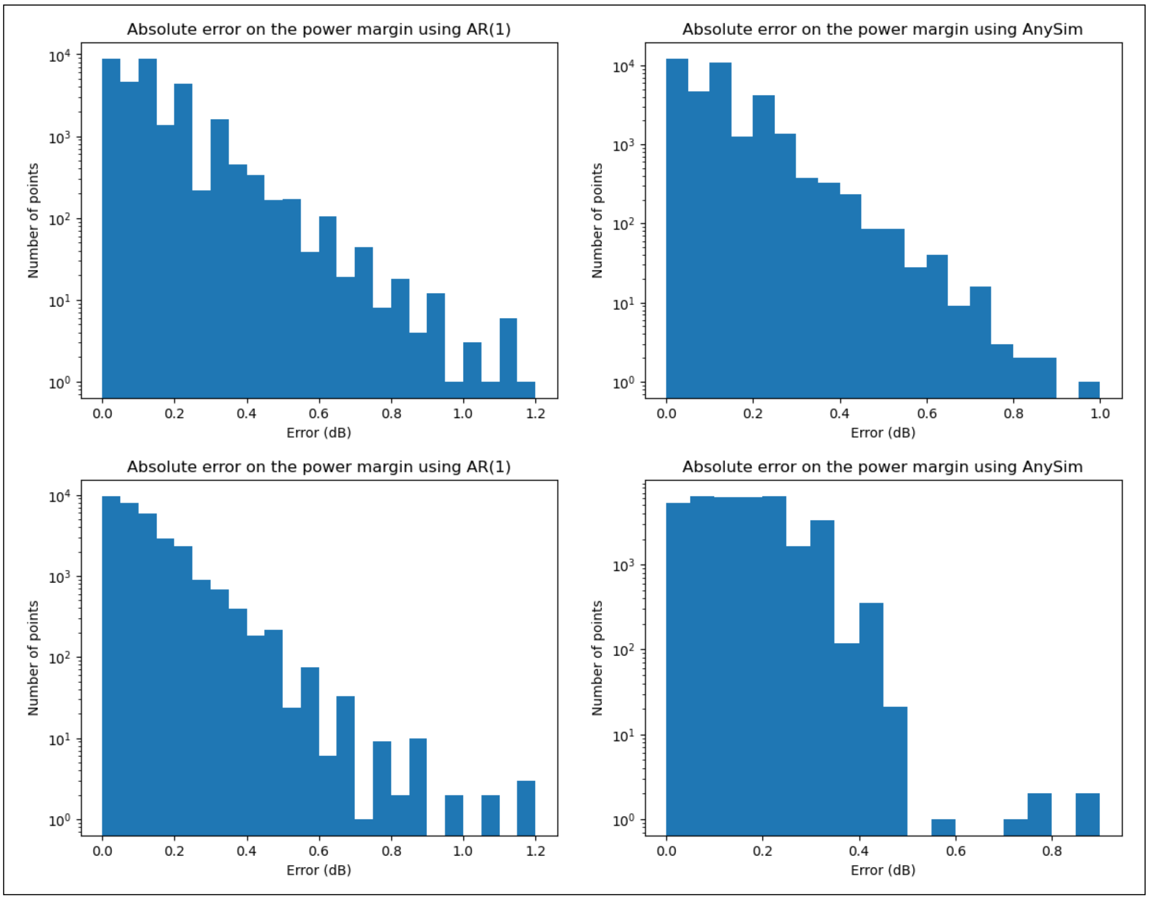

Figure 5.23.: Distribution of the absolute error on the power margin. Upper left: ARRC(1) MODCOD 9/10; Upper right: **AnySim** MODCOD 9/10; Lower left: ARRC(1) MODCOD 3/10; Lower right: **AnySim** MODCOD 3/10

## 5.2.3. Sensitivity analysis

A sensitivity analysis was performed to find which of the inputs has the biggest impact on the power margin estimation.

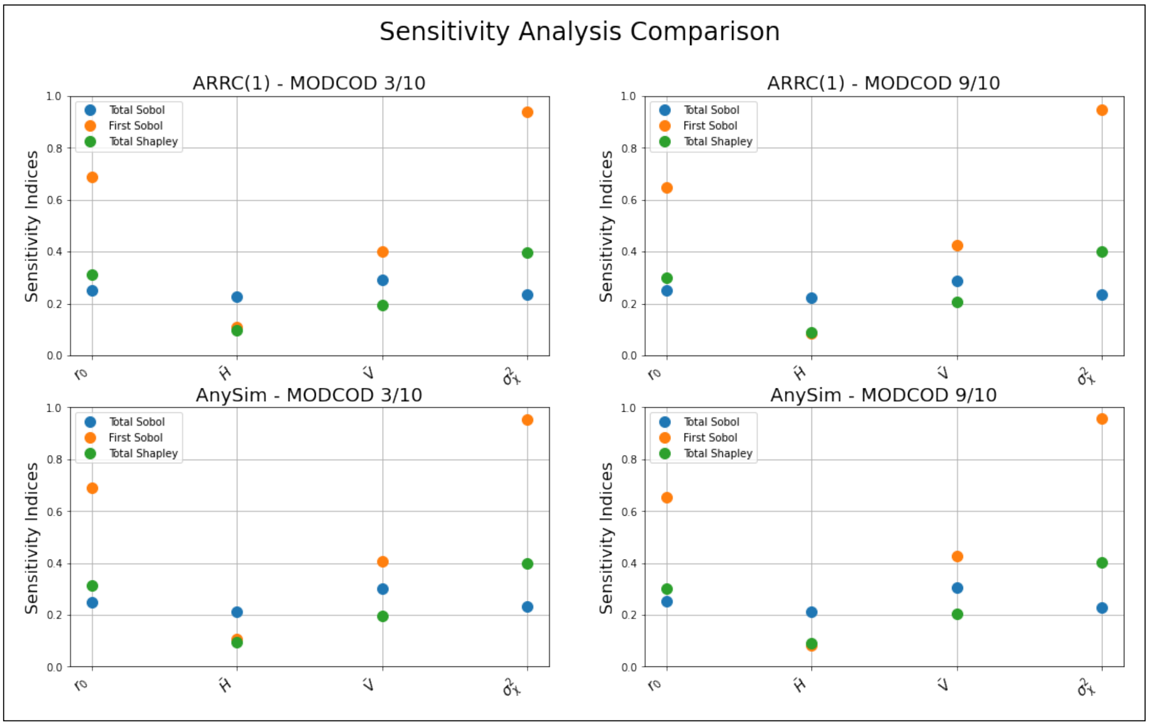

Figure 5.24.: Sensitivity analysis for each of the studied cases

In Figure 5.24 it can be seen that, regardless of the case, $\sigma_\chi^2$ has the greatest impact on the predicted value of the power margin, accounting for more than 40% of the variance according to Shapley values. This result was expected as the value of $\sigma_\chi^2$ intervenes directly in the definition of the optical power received with the $\exp\left(-\sigma_\chi^2\right)$ factor of $f_{smf}$. The total Sobol' indices presented here do not account for effects due to the correlations among variables, which explains why they are quite low.

$r_0$ has also a strong impact, it intervenes in every contributor of the adaptive optics error budget considered here.

If a trade-off has to be made in the instrument that will be chosen for this application, the priority should be given to an accurate measurement of $\sigma_\chi^2$ and $r_0$. $\bar{h}$, which has the least impact here, could on the other hand be approximately measured, or, even set to a constant average value. However, this is only true for this specific case of a downlink GEO case with our 10 radial orders, 2 kHz, AO system. $\bar{h}$ will probably have a much bigger impact on the uplink case, as the anisoplanatic error will become an important term in the error budget. For a LEO downlink case the temporal error will become the predominant error term due to a big slew rate, then the impact of $\bar{v}$ should appear significantly bigger.

Throughout this chapter, two approaches have been developed to take account of the impact of interleaving in the process of making data transmission more reliable. These two approaches make it possible to generate ROP time series from the metamodels developed in Chapter 4. The errors obtained on the power margin are of the order of a dB in the wide variety of cases studied. These approaches make it possible to obtain a representative performance evaluation of a set of profiles in a few milliseconds using ARRC to a few seconds using **AnySim**.

# 6. Instrumental Considerations

## Contents

6.1. Impact of deviation in the line of sight . . . . . . . . . . . . . . . . . . . . . 121
6.2. Error on the moments . . . . . . . . . . . . . . . . . . . . . . . . . . . . . 122
6.3. Error on the associated power margin . . . . . . . . . . . . . . . . . . . . . 124

All the study presented in chapter 4 and 5 is based on the sole knowledge of $r_0$, $\bar{h}$, $\bar{v}$ and $\sigma^2_\chi$.

So far, we considered error-free measurements of these moments while in practice there are numerous sources of error on their measurements [Boo17]. On top of neglecting measurement noise, we only considered, in the simulation of the moments measurement, an instrument with an infinitely small spectral width. These errors are to be taken into account for the deployment of the models in operational conditions, but have not been studied in the scope of this PhD due to time constraints. Nonetheless, we were able to study the impact of a deviation between the line of sight of the instrument and the one of the telescope.

## 6.1. Impact of deviation in the line of sight

Instruments such as the one produced by Miratlas will typically measure the moments using an array of sensors at a the elevation angle of a bright star during night and the sun during daytime. On the other hand, the typical mission scenario for the GEO satellite and the Tenerife site where the ESA OGS is located implies an elevation of 30°. The difference between the line of sight of the OGS and the one of the instrument is, to our understanding, the main source of error on the moments in these conditions. An expeditious study was conducted to estimate this error and it's impact on the power margin estimation.
So far, integrated parameters were given using the Durham University database. There, profiles were taken at a zenith angle and stretched to simulate a measure at 30°. In the following, we create composite profiles to calculate the integrated parameters as seen by the ground station. This is done by projecting section of profiles on the line of sight, as illustrated by figure 6.1.

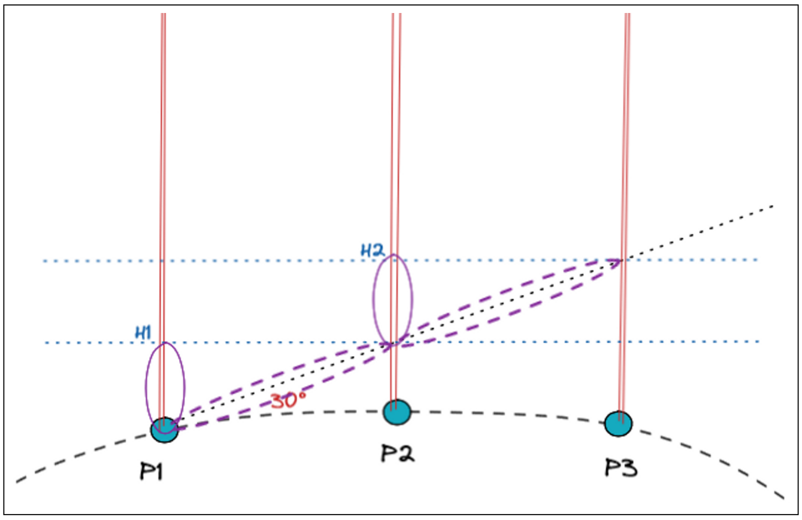

Figure 6.1.: Method for the creation of composite profiles

| | $r_0$ | | | $\sigma_\chi^2$ | | | $\bar{v}$ | | | $\bar{h}$ | | |
|---|---|---|---|---|---|---|---|---|---|---|---|---|
| angle | mean | std | max | mean | std | max | mean | std | max | mean | std | max |
| 10° | 0.849 | 1.281 | 16.483 | 4.519 | 5.380 | 89.031 | 2.250 | 2.792 | 29.658 | 3.926 | 4.201 | 47.664 |
| 20° | 0.375 | 0.735 | 12.530 | 2.132 | 2.460 | 33.269 | 1.023 | 1.258 | 11.521 | 1.916 | 1.989 | 19.282 |
| 30° | 0.295 | 0.727 | 11.220 | 1.711 | 2.192 | 32.297 | 0.845 | 1.075 | 9.191 | 1.544 | 1.781 | 18.623 |

Table 6.1.: Error in % made on the moments for different elevations

The distance between two profiles $P_n$ and $P_{n+1}$ in metres is calculated from the coordinates and written $d(P_n, P_{n+1})$. For each profile, a section $[H_{n-1}, H_n]$ corresponding to the intersection with the line of sight is selected with

$$H_n = H_{n-1} + d(P_n, P_{n-1}) * \tan(elevation). \tag{6.1}$$

The final profile is the concatenation of the multiple projected portions $\frac{P_n[H_{n-1}, H_n]}{sin(elevation)}$.

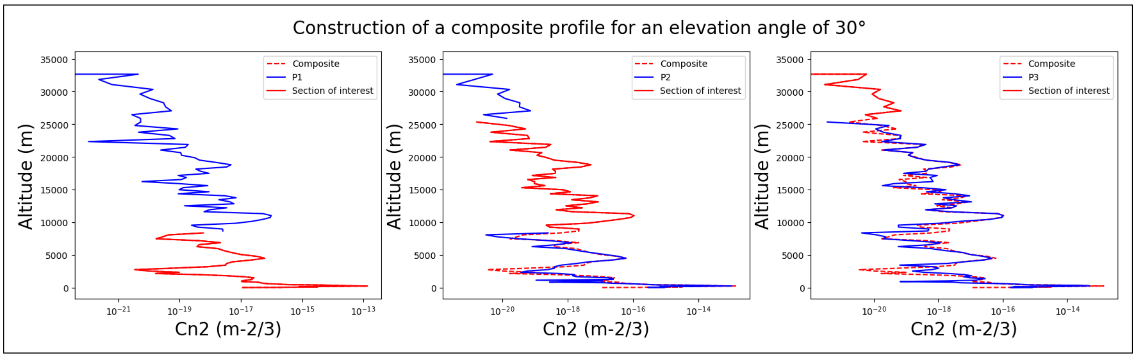

Figure 6.2.: Composite profile creation for a 30° elevation

Figure 6.2 illustrates, for the first date, the creation of a composite $C_n^2$ profile (the methodology is similar for wind profiles) for a 30° elevation. In this case, only 3 profiles are being used due to the 0.3° spatial resolution of the database, while an elevation of 20° brings into play 5 profiles and one of 10° 8 profiles.

## 6.2. Error on the moments

For each case, the composite profile is created using a starting point in the center of the ECMWF simulation at the exact point of ESA's OGS. The composite profile is created assuming a line of sight that would be orientated towards the east. There is one composite profile per time sample, that is, 923 profiles. The statistics of relative error on the moments coming from these profiles compared to a measurement done at the zenith angle are given in table 6.1 in %. The distribution of the error on each of the integrated parameters for the different elevation angles is visible in figure 6.3.

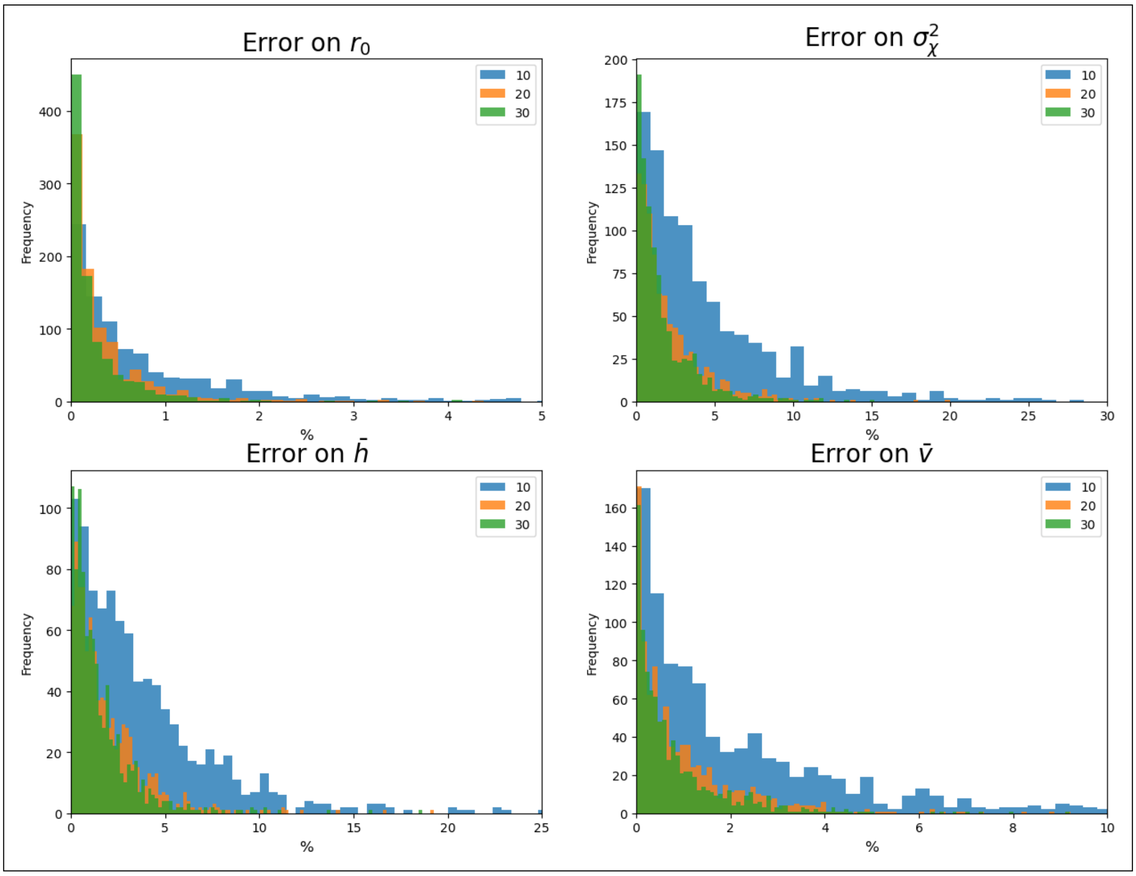

Figure 6.3.: Distribution of the error on each of the moments for different elevations (in °)

The farther the turbulence layer, the higher the impact from a difference in elevation. While the instrument and the telescope see mostly the same ground layer, they see distant layers that are far apart and potentially fully uncorrelated. This explains why the error is the largest for $\sigma_\chi^2$ and smallest for $r_0$. As explained in chapter 4, while $r_0$ accounts mostly for the ground layer, the intensity variance caused by atmospheric turbulence is mostly impacted by distant layers.
Due to the construction method, no matter the elevation, the ground layer is the same as we don't benefit from sufficiently fine spatial sampling. This may represent a strong limitation in the method by underestimating the error at the lowest order moments (typically $r_0$). Further investigation should be conducted using a database with much smaller spatial sampling, or, using two instruments with different lines of sight. Such work is being conducted at Durham University and initial results are presented in [Wes+23].

The goal being to present a methodology and giving a first estimation of the propagation of error on the moments in the determination of the power margin, we consider the orders of magnitude to be sufficient and proceed with the values of figure 6.3.

| Elevation | False Positive | False Negative | True Positive | True Negative | Sensitivity | Specificity | Precision |
|---|---|---|---|---|---|---|---|
| 10° | 5.31 | 4.01 | 34.99 | 55.69 | 89.72 | 91.30 | 86.83 |
| 20° | 0.87 | 0.54 | 94.04 | 4.55 | 99.43 | 84.00 | 99.09 |
| 30° | 0.11 | 0.00 | 99.57 | 0.33 | 100.00 | 75.00 | 99.89 |

Table 6.2.: Main elements of the confusion matrix given in % at different elevations

## 6.3. Error on the associated power margin

In the computation of the moments of 6.1, the moments obtained along the true line of sight are compared to the moments obtained by a transformation of a measurement at the zenith angle. Considering the measurement along the line of sight as the truth regarding the availability of link power, table 6.2 gives a good idea of what can be expected using an instrument that would have a zenith line of sight combined with our models. In the event that the link is available, the outcome is considered positive and negative if the link is interrupted. A false positive event describes the case of a link being determined as available using the moments measured at a zenith angle but that is not considering the true line of sight. The opposite case is called a false negative.

The sensitivity (True Positive Rate or Recall) measures the proportion of actual positive cases that are correctly identified by the model.

$$\text{Sensitivity} = \frac{\text{True Positives}}{\text{True Positives} + \text{False Negatives}}$$

The specificity (True Negative Rate) measures the proportion of actual negative cases that are correctly identified by the model.

$$\text{Specificity} = \frac{\text{True Negatives}}{\text{True Negatives} + \text{False Positives}}$$

The precision (Positive Predictive Value) measures the proportion of positive cases predicted that are correctly identified.

$$\text{Precision} = \frac{\text{True Positives}}{\text{True Positives} + \text{False Positives}}$$

From table 6.2, we can confidently say that, as expected, when the difference between the real line of sight and the instruments line of sight increases, the sensitivity increases. We even obtain a 100% sensitivity at a 60° difference (30°) elevation as all actual positive cases are identified correctly. The same argument however is not valid for the specificity, which appears to be decreasing when our model should be gaining in accuracy. This is due to the fact that, at a 10° elevation, the link is not available in 65% of the cases (600 cases out of the 923) with this number dropping to 0.43% (4 cases) at a 30° elevation. The 49 false positive values of the 10° case consequently impact less the specificity than the one in the 30° case.

Suppose a system blindly following our assessment and establishing a link whenever it is said to be available by our model. It would result in a failure every-time we encounter a false positive. This rate of failure can be given as the number of false positive over the total number of positive assessed values. In other words, the system would work successfully at a rate that is no other than the precision given in table 6.2. This precision is insufficient in the case of a 10° elevation in an operational situation, yet, for a 30° elevation the scenario of a different line of sight between the instrument and the satellite can be considered with an availability guaranteed in 99.9% of the time.

The result has to be put in perspective with the vastly resilient AO system considered which allows for some discrepancy in the moments and a study database with very little set of profiles that lead to link downtime.

Focusing now on the link power margin (only true positive cases are considered where a power margin can be calculated), the distribution of absolute error is visible in Figure 6.4.

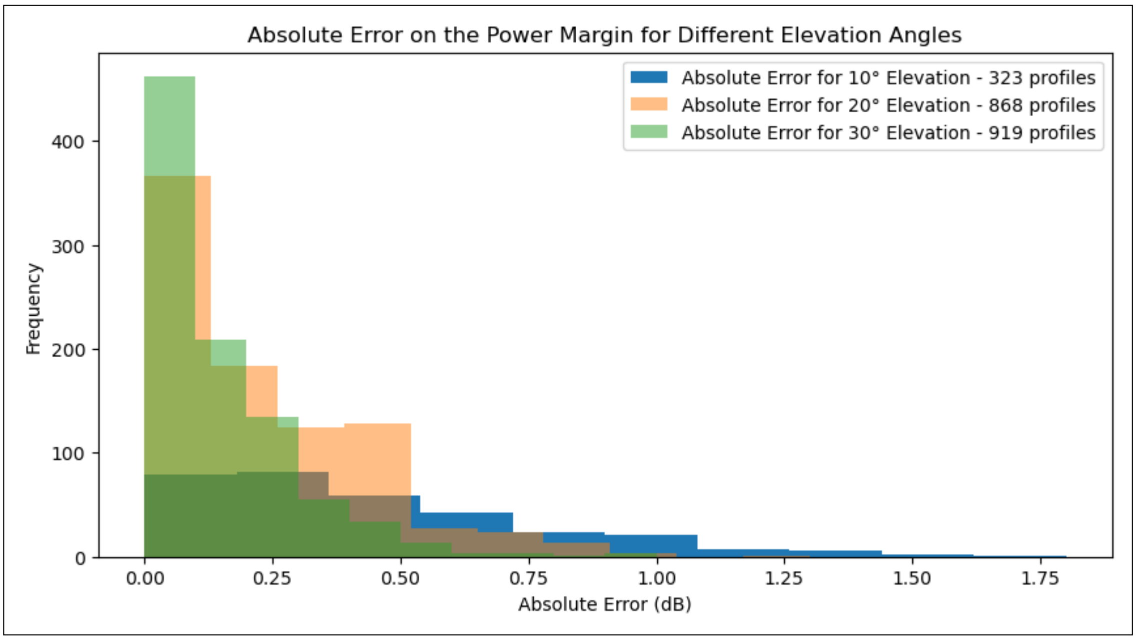

Figure 6.4.: Absolute error on the power margin for the true positive cases for the different elevation angles

The absolute error on the power margin is kept relatively low especially for the case of interest in our study of a 30° elevation with a maximum error of $1dB$, which is about the same as the error made by our machine learning model with series generation. As explained in the previous section, the error on some of the low order moments is underestimated using this description with composite profile, but overall our resilient AO combined with the low error shown here reassures us about the ability to determine the availability of the link using unsophisticated instruments.

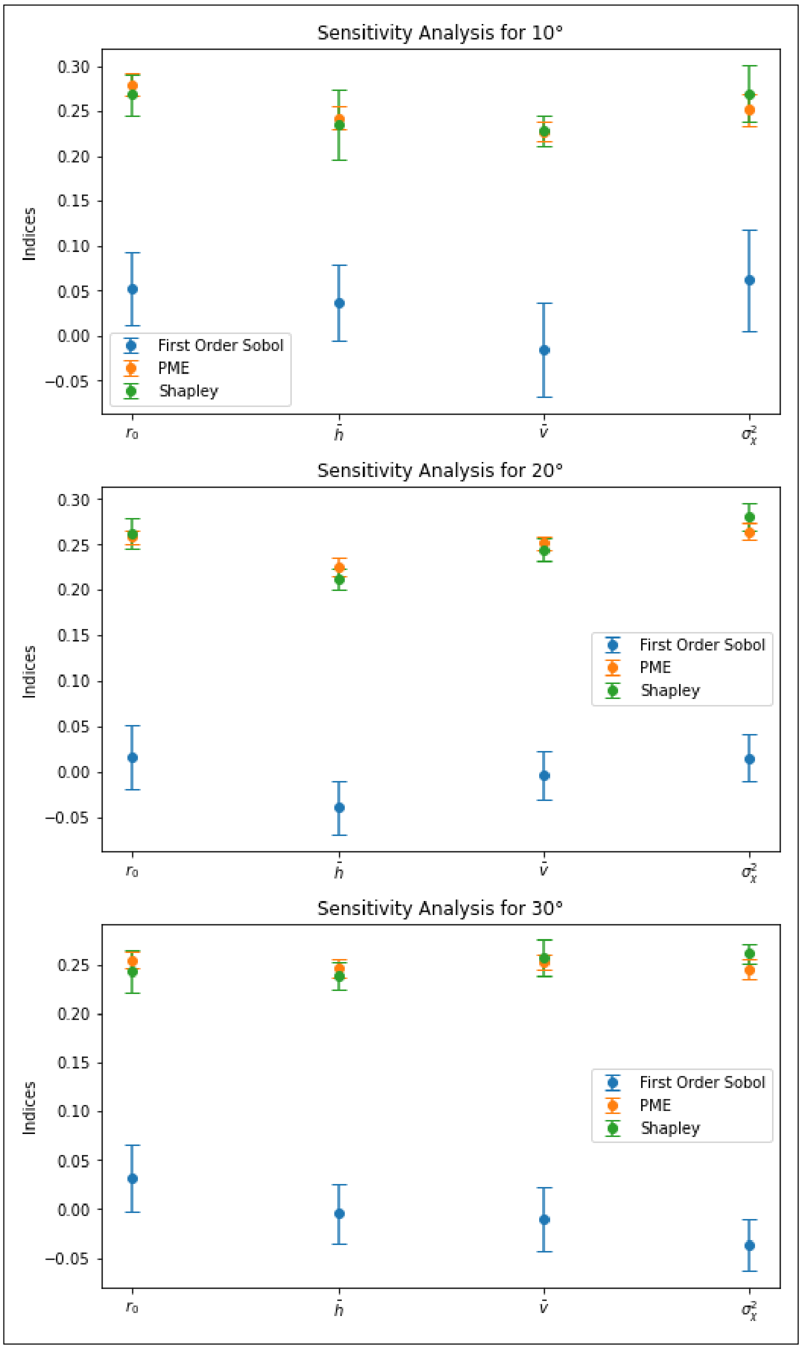

Figure 6.5.: Sensitivity analysis on the absolute error on the power margin as a function of the relative error on the moments for different elevations

Figure 6.5 shows 3 sensitivity analyses for the 3 elevation angles considered. These sensitivity analyses provide the sensitivity of the absolute link power margin error to the relative error made on the description of each of the moments. The vertical bars correspond to ± the variance of the sensitivity indices. No single variable appears to dominate the others, regardless of the elevation angle. This means that an error of $x$% on one or another variable will not significantly impact the results. The main factor that will impact the error on the power margin is thus the amplitude of the relative error on the moments that is, according to figure 4.26, predominant for $\sigma_\chi^2$ and $\bar{h}$. If one wants to lower the error on the power margin, the focus should be on measuring these two quantities along the line of sight prior to the rest.

It should be pointed out one final time that this conclusion is based on a discrete database and a partial representation of the spatial correlation of turbulence profiles (especially at ground level). The results need to be fleshed out on a larger number of data from measurements or from a finer simulation database of ground layer turbulence structures (e.g. Large Eddy Simulation (LES) simulations).

# 7. From Minutes to Hours Availability Forecasting

## Contents

7.1. Database construction . . . 129

  7.1.1. Geographical location . . . 129

  7.1.2. WRF simulations . . . 130

  7.1.3. $C_n^2$ modelling . . . 130

    7.1.3.1. Dewan's approach . . . 130

    7.1.3.2. Turbulent Kinetic Energy approach . . . 132

7.2. Comparison to on site measurements . . . 135

7.3. Use of machine learning for temporal prediction . . . 141

  7.3.1. Method . . . 141

  7.3.2. Results . . . 143

  7.3.3. Arima . . . 143

  7.3.4. Deep neural network for temporal prediction . . . 144

7.4. Introduction of covariates in the deep learning models . . . 148

7.5. Results . . . 150

7.6. Potential improvements in temporal prediction of moments . . . 151

In chapter 4 and 5, I demonstrated the possibility to assess the availability of a free space optical link using a small set of integrated parameters. The forecasting capacity of the turbulence profiles are already exploited on astronomical observatories to plan nighttime observations[OS18]. It raises the perspective of a real forecasting capacity of AO corrected FSO systems if the daytime forecasting challenge is addressed. We investigate the potential use of ML approaches to face this challenge.

## 7.1. Database construction

In chapter 4 and 5, I presented a way to assess the availability of a free-space optical link using a small set of integrated parameters. For this purpose, we used a database of atmospheric profiles provided by Durham university. The general circulation model used (ECMWF) has a spatial resolution of 0.3° along latitude and longitude (a spatial resolution of $\approx 30km$ around Tenerife) and provides an hourly forecast. This was appropriate to build the required database to feed the statistical analysis.

In the following section, we aim at predicting the temporal evolution of the small set of integrated parameters identified earlier in a near future, typically a few hours. The database used so far is evidently not appropriate for this application, as the temporal sampling is of one hour.

To overcome this need for a much more temporal-resolved database, we worked with WRF where the temporal resolution can be as low as 5 minutes. There are several possibilities to assess the $C_n^2$ profiles from WRF database, the main challenge being to properly parameterise the WRF output to ensure the relevance of the calculated quantities, particularly in the boundary layer. We choose to investigate two approaches that are summed up in what follows. The first approach, based on the state of the art opened literature and Dewan's strategy to explicit the dependence of $C_n^2$ to the outer scale profile, will be called "Dewan's approach", this strategy has been implemented at ONERA, in collaboration with the Electromagnetism and Radar department that provided WRF outputs; the second one, based on the exploitation of the turbulent kinetic energy (TKE) will be denoted the "TKE approach", this strategy has been implemented by F. Quatresooz (Louvain University) and the results were provided to ONERA in the framework of a scientific collaboration.

### 7.1.1. Geographical location

$C_n^2$ profile estimation from WRF outputs has been performed using the two strategies previously cited. To estimate the reliability of the results, we selected a location and a time period for which we had access to local integrated parameter measurements. Four temporal periods were selected, April, July, August and October of 2021 to cover different seasons. Simulations were done for the Teide observatory (28.30228, -16.51032) at altitude 2390 m where an instrument measuring integrated parameters has been installed by Miratlas.

### 7.1.2. WRF simulations

The Weather Research and Forecasting (WRF) model is a prominent numerical weather prediction system that is used to simulate atmospheric processes. Operating on a grid-based framework, WRF employs sophisticated numerical methods to characterize interactions within the atmosphere. Simulations involve data initialisation, integration of governing equations, and post-processing. Key parameters include grid resolution, time step, initial and boundary conditions, physics parameterizations (microphysics, convection, radiation, etc.), land surface and ocean models, nested domains for localised refinement, and output settings. The versatility of WRF requires skillful parameter selection to achieve accurate results, making it indispensable for weather research and prediction.

In the data provided by the University of Louvain [Qua+23b], the WRF configuration makes use of the following physical schemes: WSM6 [HL06] for microphysics, Tiedtke [ZWH11] for cumulus physics (only in domain d01), Dudhia [Dud89] and RRTM [Mla+97] for short-wave and long-wave radiations, revised MM5 [Jim+12] for the surface layer, and MYNN 2.5 [NN09] for planetary boundary layer physics. Three nested domains, detailed in Table 7.1, enable one to reach a horizontal resolution of 1 km, while 80 levels are used vertically. These levels are distributed between the ground and the upper pressure of the atmosphere, set to 5000 Pa, with a smaller level spacing close to the ground. For each day, simulations start at 18h00 the day before, ensuring a lead time of 6 hours. Then, outputs are saved every 5 minutes above the location of interest, for the full day (i.e., from 00h00 to 00h00 the next day). Atmospheric parameters outputs simulated with WRF at ONERA and in Louvain are plotted on figure 7.1. Wind profiles are plotted on figure 7.2. These plots illustrate the very comparable parametrisation of WRF for the two approaches for 4 random occurrences. These profiles are very similar and comfort the accuracy of our WRF database.

| Domain | Grid resolution (km) | Number of grid points | Domain size (km) | Number of vertical levels |
|---|---|---|---|---|
| d01 | 9 | 112 × 112 | 1008 × 1008 | 80 |
| d02 | 3 | 112 × 112 | 336 × 336 | 80 |
| d03 | 1 | 112 × 112 | 112 × 112 | 80 |

Table 7.1.: Grid parameters from WRF simulations.

### 7.1.3. $C_n^2$ modelling

#### 7.1.3.1. Dewan's approach

In order to assess the $C_n^2$ profile from atmospheric turbulent parameters this approach consists in exploiting traditional Tatarskii modelisation [Tat71] f equation 1.17 with the outer scale profile calculated following Dewan's description [Dew+93] that we remind is defined as:

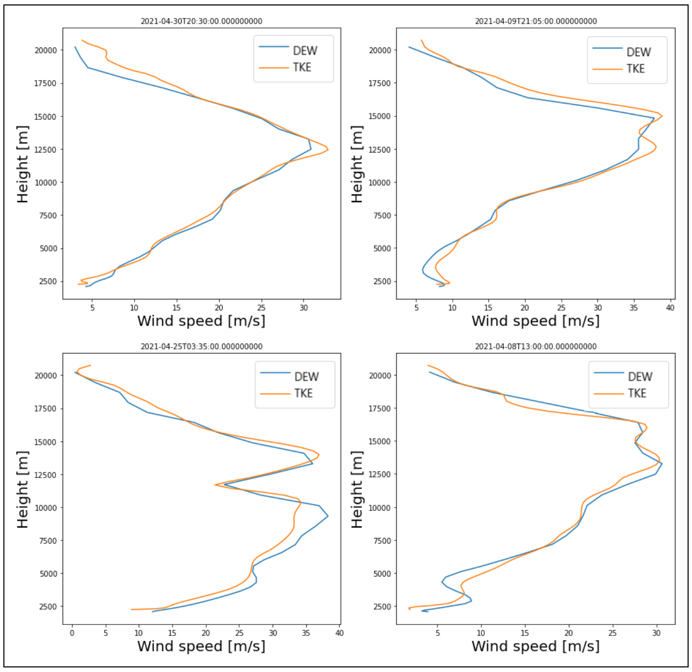

Figure 7.1.: Comparison between the temperature profile extracted from the dataset using TKE (orange) and from the one using Dewan's (blue) for 4 random occurences

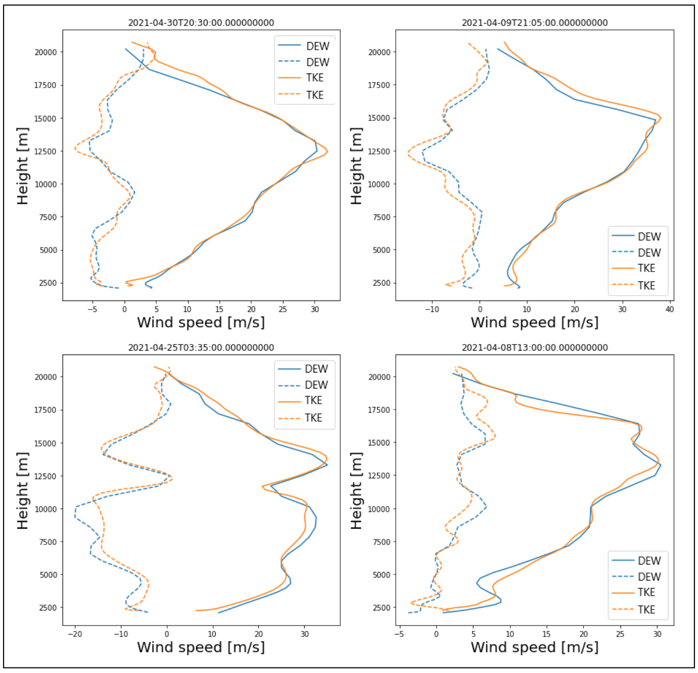

Figure 7.2.: Comparison between the wind profiles extracted from from the dataset using TKE (orange) and from the one using Dewan's (blue) for 4 random occurrences. Full line zonal and dashed line meridional

$$\begin{aligned} L_0^{4/3} &= 10^{1.64+42.0S} (\text{Troposphere}) \\ L_0^{4/3} &= 10^{0.506+50.0S} (\text{Stratosphere}) \end{aligned} \tag{7.1}$$

where S the wind shear is $S = \sqrt{\frac{dV_x^2}{dz} + \frac{dV_y^2}{dz}}$.

#### 7.1.3.2. Turbulent Kinetic Energy approach

A recent alternative has been proposed by Florian Quatresooz [Qua+23a]. The idea consists in exploiting $C_n^2$ model, Astro-Meso-Nh, presented in [MVB99]. This model is also based on the Gladstone's relationship linking the refractive index structure parameter to the temperature structure parameter introduced in equation 1.15. The chosen $C_T^2$ model is the one of Masciadri given in equation 1.16. The outer scale depends on the turbulent kinetic energy $e$ rather than the wind shear. The model is given by:

$$L = \sqrt{\frac{2e}{\frac{g}{\theta_v}\frac{\partial\theta_v}{\partial z}}} \tag{7.2}$$

where $e$ is the Turbulent Kinetic Energy (TKE), $g$ is the gravity of Earth and $\theta_v$ is the virtual potential temperature obtained from $\theta_v = \theta(1 + 0.61r)$ for unsaturated air with mixing ratio $r$ of water vapor.

TKE is a fundamental concept in fluid dynamics that quantifies the mean kinetic energy associated with the chaotic motion of fluid particles in turbulent flows. It characterises the energy contained within eddies, expressed as the root-mean-square velocity fluctuations.

The use of a TKE-based model offers a more comprehensive framework for describing the $C_n^2$. Unlike the Dewan approach that solely rely on wind shear, the TKE-based model takes into account the intricate interplay between velocity fluctuations, temperature variations, and turbulent eddies. By capturing the intricate details of turbulence dynamics, it should be more appropriate to describe optical turbulence near the ground in the boundary layer.

As seen in Figure 7.3, depending on the method used, the $C_n^2$ profiles differ strongly by multiple orders of magnitude.

As our study focuses mainly on integrated parameters, we compared them for the two models in figure 7.4. Each graph represents the average and the confidence interval of the given integrated parameter depending on the time of the day for the first 14 days of April 2021. The orange curves are obtained from the TKE modelisation and the blue ones from Dewan's. All calculations have been done for a zenith angle at 550 $nm$. The most consequential difference between the two models. Where the Dewan's approach gives equivalent moments at all times of day, with no variability from day to day, the data obtained using the TKE represents the expected diurnal cycle

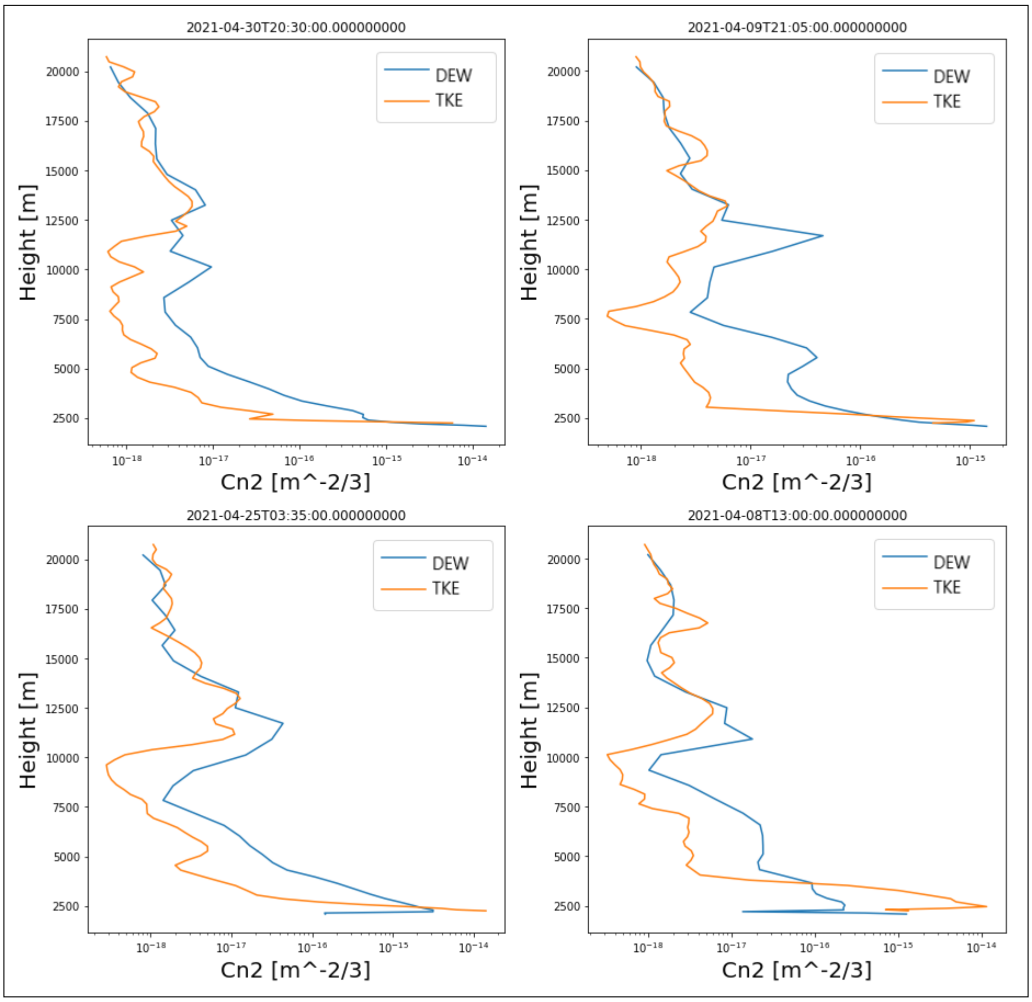

Figure 7.3.: Comparison between zenital $C_n^2$ profile extracted from TKE and from Dewan approach for 4 random occurences

extremely well, with a wide range of values whatever the parameter observed.

The diurnal cycle is a well-known cycle caused by differences in air and soil heating between night and day [SS13], and even at different times of day. The greater the temperature difference between the ground and air or between different air masses, the greater the force of the turbulence. This is particularly visible on the orange curves where the values of $r_0$, $\tau_0$ and $\theta_0$ are at their minimum around 2pm (i.e. 12pm solar time) and where the value of $\sigma_\chi^2$, the variance of log-amplitude, is at its maximum at the same time.

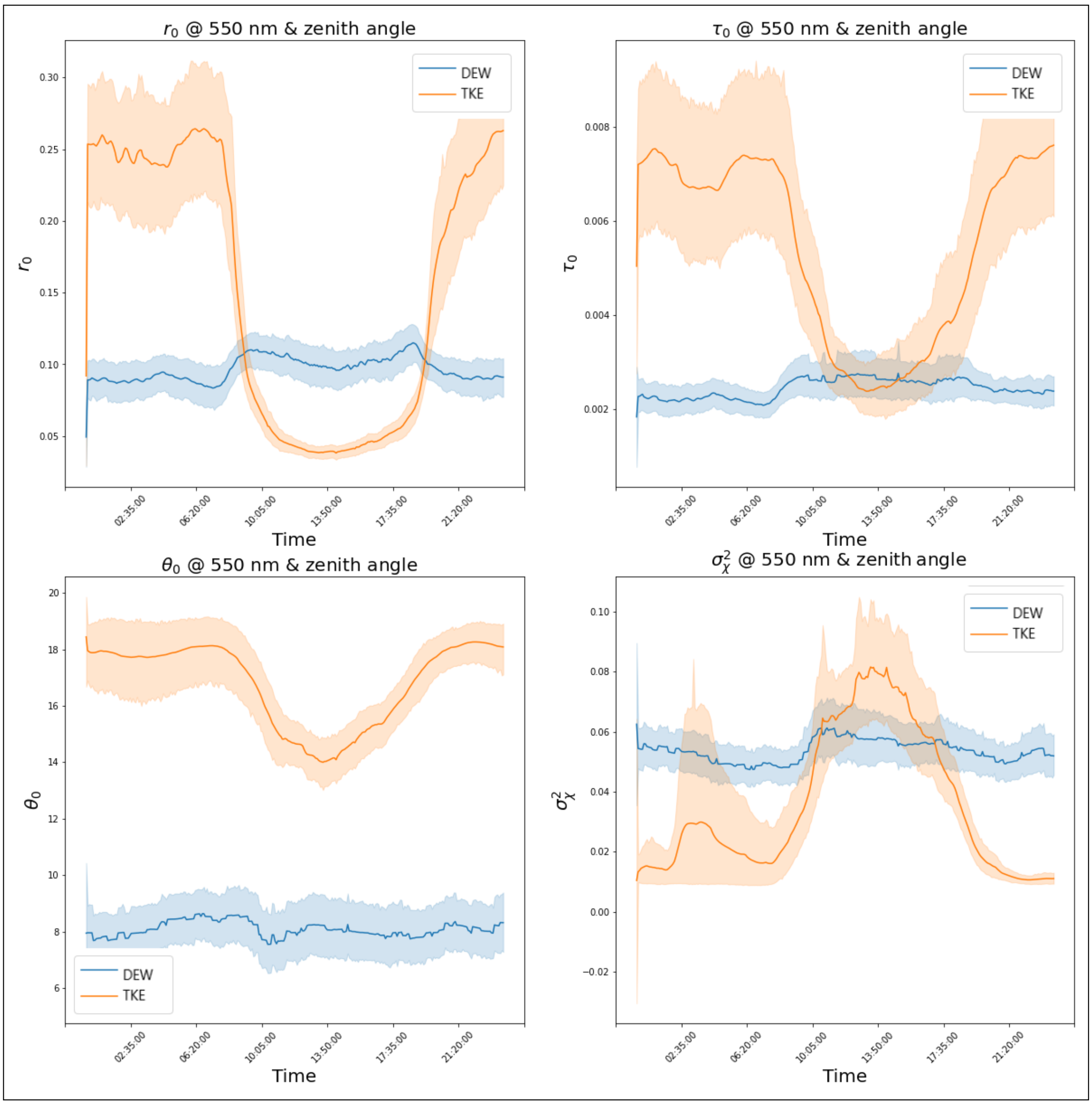

Figure 7.4.: Comparison between the averaged moments profile extracted from the TKE approach (orange) and from Dewan's (bleu) for an zenith angle measurement at 550 nm

The lack of variability in the moment calculated with the wind shear based model gives us low confidence in its ability to reproduce real world conditions, especially when the TKE based model is reproducing the highly expected temporal cycle. In the following, all the prediction work is thus based on $C_n^2$ profiles generated for the TKE outer scale model with WRF data from the University of Louvain.

Thorough validation and calibration against real on-site measurements where conducted in the next section to assess the reliability of the model on the model for practical applications.

## 7.2. Comparison to on site measurements

On-site measurements were provided by Miratlas through an instrument deployed at the Teide observatory. Miratlas designs, manufactures and operates the Integrated Sky Monitor (ISM), a device monitoring the optical atmospheric conditions in a compact, rugged, and carrier grade package. The ISM array of sensors visible in Figure 7.5, provides all-sky images both in the visible and thermal range along with measurements of the Fried parameter by day and night, incoming integrated solar energy, sky brightness in the visible as well as in the telecom bands, integrated water vapor and other relevant meteorological parameters. At Teide, the instrument is positioned on a 7 metre high tower to limit the sensitivity to the most intense ground phenomena. During year 2021, $r_0$ was measured only during day time due to a failure of the night time instrument.

However, since the systems dedicated to Free Space Optics will have to cover all the turbulence conditions likely to be encountered, they are designed for demanding turbulence conditions, which almost always occur during the day. In this respect, the database supplied by Miratlas provides representative measurements, as it covers daytime conditions.

Figure 7.5.: Miratlas Integrated Sky Monitor.

First step of validation of Louvain's WRF data has been to look at the meteorological parameters on the ground level.

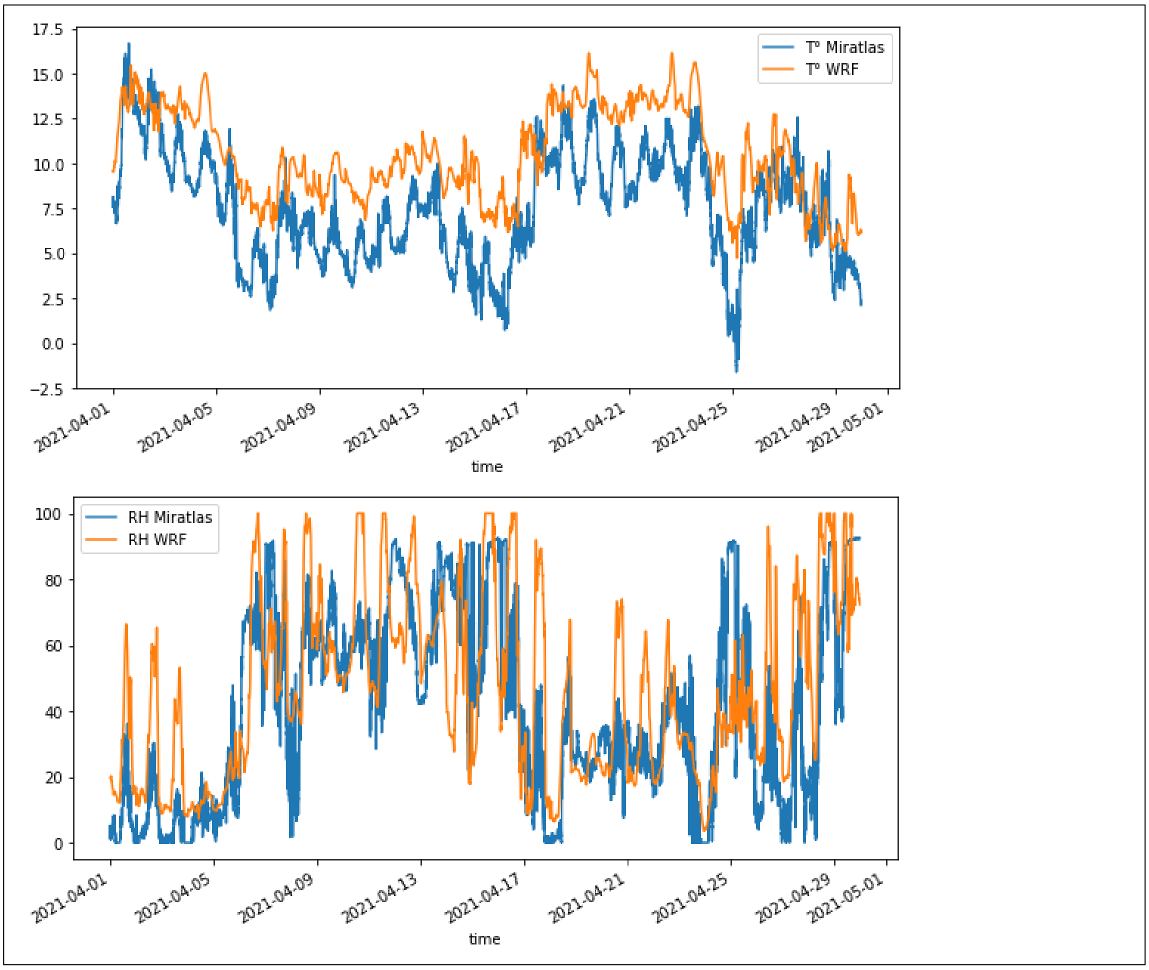

Figure 7.6.: Comparison of the temperature and humidity on the ground level obtained through WRF (orange) and measured through the local meteorological station (blue)

As we can see on figure 7.6, we are confident in Louvain's WRF simulation. The trend is well represented, here through the month of April, but similar comparisons are obtained for the other months. Nevertheless, a systematic error appears on the simulation of the ground layer temperature using WRF, this could be due either to the height of the first layer not being extremely accurate or due to the fact that the nature of the ground is not accounted for in our simulations.

The high frequency variation in temperature or relative humidity over short time scales is not accurately described, this is even more visible when comparing the $r_0$ values in April as we did in Figure 7.7. Miratlas' Fried parameter is measured only during day time but it is enough to see that WRF at best gives an average value of the Fried parameter over a couple of hours but does not translate the high frequency variability.

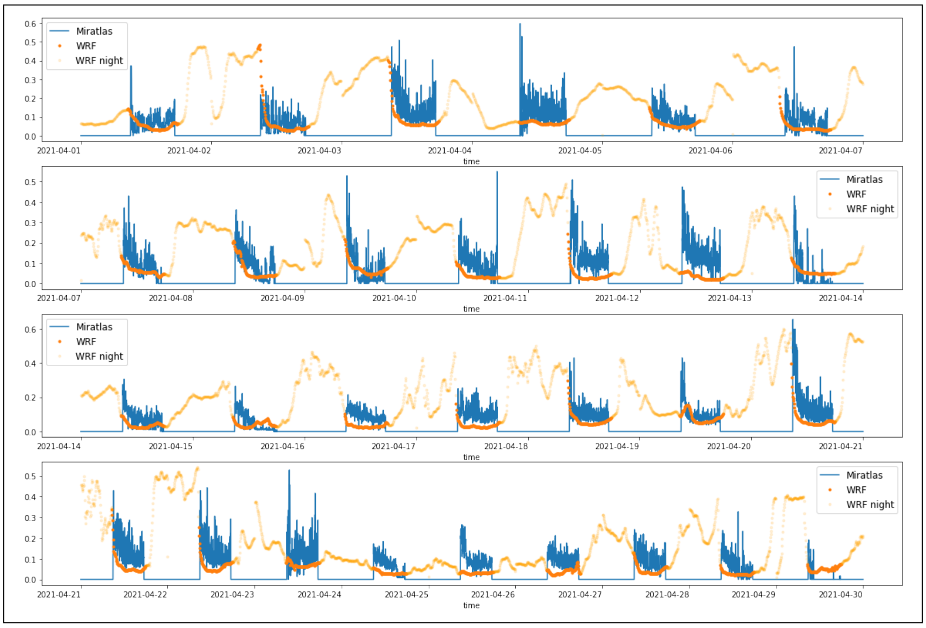

Figure 7.7.: Comparison of the $r_0$ obtained through WRF (orange) and measured through the local meteorological station (blue)

The reasons are numerous:

- WRF simulations are conducted on a grid with a large spatial resolution compared to the local variations in atmospheric parameters. This is particularity true for fine-scale processes such as optical turbulence parameters that have, close to the ground, an outer scale of a few metres.
- WRF uses parametrisation schemes to simulate the processes at unresolved scales like turbulence and boundary layer interactions, which are the processes contributing to large-scale variability. Nonetheless, these parametrisation schemes are only statistical models.
- The region being simulated presents complex terrain and heterogeneous land, which leads to challenges in accurately representing local atmospheric conditions that cannot be solved using only WRF.
- The 5 minutes temporal resolution of WRF involves temporal averaging, which smooths out high-frequency variability, while the local measurement consists of the acquisition of a point every minute without any averaging being done.

Figure 7.8 shows the same comparison but with Miratlas' $r_0$ averaged over 20 minutes, 20 minutes being a characteristic time for programming the handover from one ground station to another. With this figure, the similarity between the two data sets starts to emerge. Nonetheless, it remains clear that the WRF simulation only translates the general trend over a few hours.

Figure 7.8.: Comparison of the $r_0$ obtained through WRF (orange) and the average value over 20 minutes of $r_0$ measured through the local meteorological station (blue)

Although we might assume WRF will be suitable to predict the trend of the $r_0$ and the other moments, having a clear understanding of the high frequency variation observed in the on site measurements is important to put into perspective the validity of our approach.

In figure 7.9 we intend to characterise those small variations. For doing so, we subtract a 20 min moving average from the raw data. The time series obtained is shown for the first 6 days of April. This "noise" is not constant over time and not white. Through Figure 7.10, we can see however that it is strongly uncorrelated and has a more or less Gaussian distribution. We also see that the variation of $r_0$ to the average values is usually less than 10 centimetres with a maximum value of 40 centimetres. This is a variation of up to 200% of the average $r_0$ value.

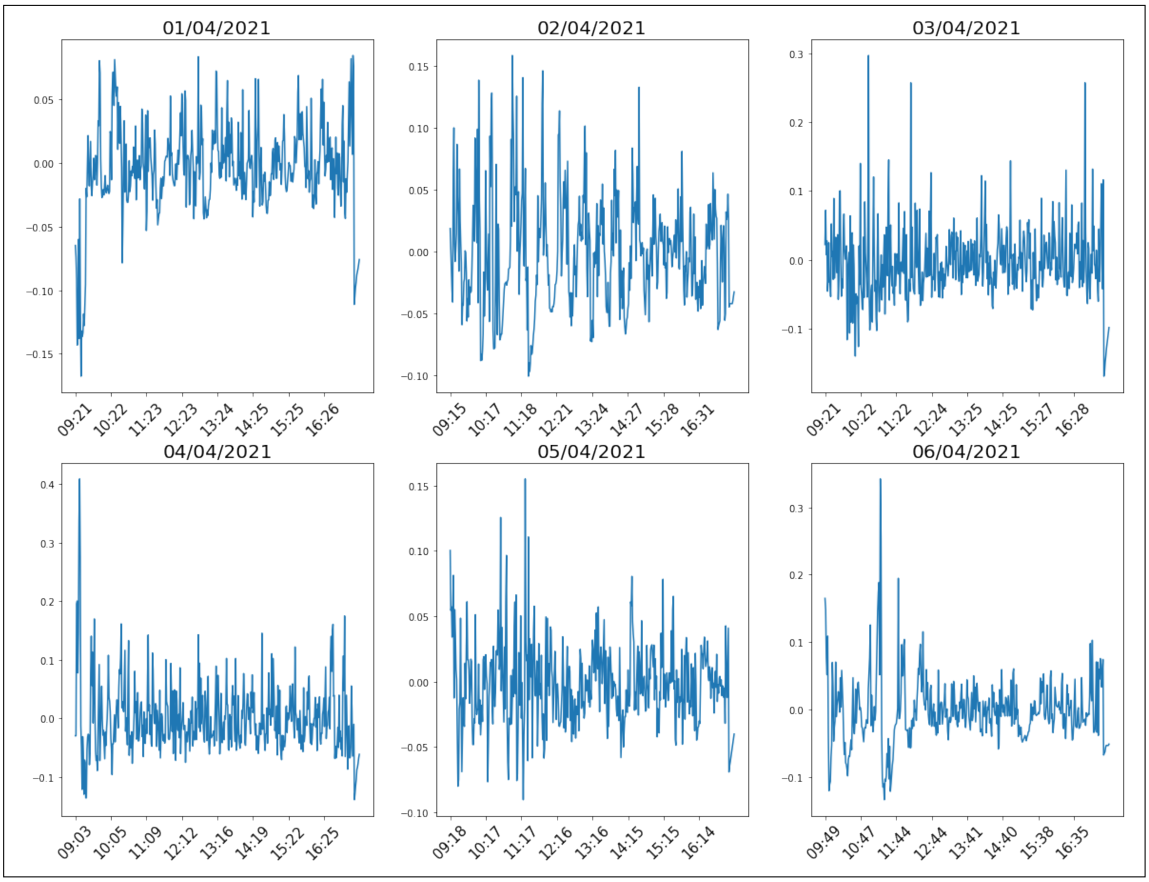

Figure 7.9.: $r_0$ Miratlas after subtraction of a 20 min width sliding average (Trend)

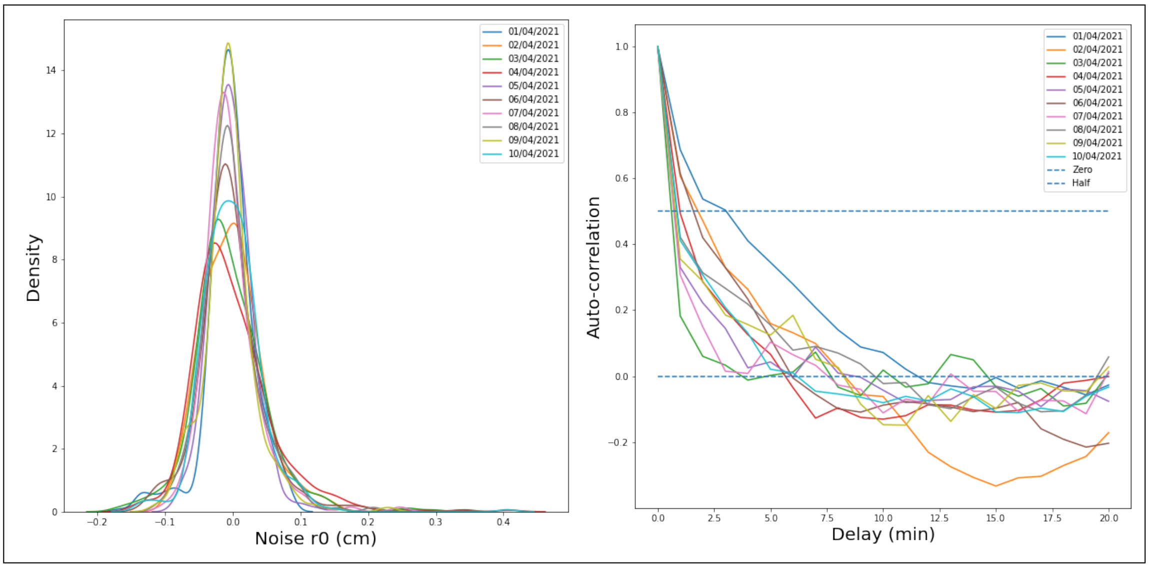

Figure 7.10.: Distribution and autocorrelation of the noise in the $r_0$ Miratlas without the trend (20 minutes averaged)

Even so, these greatest variations are towards a bigger $r_0$ which means a reduction in the turbulence strength and a better link availability. We are only interested in the negative variation of $r_0$ as they are the ones that will compromise our estimate of the availability of the link. These variations can be up to 20 centimetres and will most certainly impact the link in a way that will not be anticipated using WRF and the deep learning model for temporal prediction.

This is an elementary characterisation, and the approach should be systematised by studying both the impact of a sliding window of variable size and the temporal frequency content of the $r_0$ measurements in order to identify the duration for which the fluctuations in the Fried parameter measured are fully uncorrelated.

Also, one should note that if the amplitude of the variations remain under control and the AO (or system) is sized with a sufficient margin, a high level of short-term accuracy might not be necessary. Nonetheless, a reliable prediction of short term behaviour would benefit the optimization and the operation of the AO (either its sizing in the design phase, or its operation in the operational phase).

The macroscopic analysis we carried out was only using data from the Tenerife observatory, an astronomical site. However, future ground stations will be set up in peri-urban environments (close to network nodes). As far as short-term prediction is concerned, it will be for the most part only linked to the characteristics of the siting site. The adjustment to short-term turbulence conditions should therefore preferably be carried out on representative data, such as that which will be produced by the FEELINGS ground station before the end of 2023, located 30 km south of Toulouse, on the ONERA site at Fauga-MAuzac.

This work will be the subject of a follow-up to the thesis currently being prepared (post-doc proposed).

WRF simulations are able to capture the larger-scale trends and patterns in the atmospheric data. They give us an idea of the evolution of each layer of the atmosphere for kilometres around the observation point. Due to their nature, they are not exceptionally site-dependent and shall easily be generalised to all ground stations.

These considerations led us to continue the prediction work on WRF data only, for exploratory purposes and with the aim of developing interesting models for forecasting over mid-term time periods.

## 7.3. Use of machine learning for temporal prediction

*The work presented in the following has, for the most part, been conducted by Alex Poiron, an intern who under my supervision spent 6 months at ONERA.*

### 7.3.1. Method

The first trial for the prediction of the integrated parameters of turbulence has been carried out with simple machine learning models to understand what it takes to predict the $r_0$ on different time scales. Based on recent papers [Raf+22][BM19][Li+23][MMT20][CLB21][THH18][DDB20][Liu+21] on this exact topic, we were first led to test a basic ARIMA model detailed in 3.3.1 .
In [Li+23] an enhanced model was proposed based on the use of variational mode decomposition (VMD). Mode decomposition techniques such as Seasonal Decomposition of Time Series (STL) or Empirical Mode Decomposition (EMD) can typically be used to decompose a time series into its underlying components, such as trend, seasonal, and residual components. This decomposition often helps to better understand the underlying patterns and fluctuations present in time series, which is useful for identifying seasonality, trends, or other non-stationary behaviours that might influence the choice of ARIMA parameters.

The VMD emerges as an innovative signal decomposition technique, contrasting with EMD. It introduces a distinct paradigm for signal decomposition augmenting EMD's capabilities and addressing its limitations [DZ14]. While EMD recursively identifies extrema and envelopes to isolate signal modes, VMD adopts a variational approach, enforcing specific bandwidth attributes. This optimization-based method refines modes iteratively through Wiener filtering and spectral center frequency updates via an ADMM (Alternating Direction Method of Multipliers) algorithm. VMD's emphasis on prescribed frequency traits leads to enhanced tone detection, separation, and noise robustness relative to EMD.

Later on, two models using deep neural network temporal prediction are also used, N-BEATS and N-HITS presented in 3.3.3.1 and 3.3.3.2.

In the following, to evaluate the performance of our prediction models, two metrics are used: MAE and RMSE.

The MAE measures the average absolute difference between the predicted values and the actual values. It is defined by the formula:

$$\mathrm{MAE} = \frac{1}{n}\sum_{i=1}^{n}\left|y_i - \hat{y}_i\right| \tag{7.3}$$

where:

$n$ : number of data points
$y_i$ : actual value of the target variable for the $i$-th data point
$\hat{y}_i$ : predicted value of the target variable for the $i$-th data point

The MAE is advantageous because of its simplicity and easy interpretability. It provides a straightforward measure of the average prediction error and is less sensitive to outliers compared to RMSE. This makes MAE particularly suitable when outliers are present in the data.

The RMSE on the other hand is a widely used metric that calculates the square root of the average of the squared differences between the predicted values and the actual values:

$$\mathrm{RMSE} = \sqrt{\frac{1}{n}\sum_{i=1}^{n}\left(y_i - \hat{y}_i\right)^2} \tag{7.4}$$

The RMSE is advantageous because it penalises larger errors more heavily than smaller errors. It thus provide a better indication of the model's performance when dealing with larger deviations between predicted and actual values. Nonetheless, it is more sensitive to outliers compared to MAE.

The training process is always the same. Each month is separated into 2 times 15 days, the first being used as a training set for the models, and the second being used as validation set. It was determined that the prediction gives the best results for an input time series of the model of 5 to 7 days. All parameters were fine tuned using Optuna, a framework for hyperparameter optimization in machine learning. It acts as a grid search on the hyperparameters of the models by iteratively trying different values and keeping the ones that perform the best.

## 7.3.2. Results

## 7.3.3. Arima

Taking the example of a model trained on 12 days of data and validated on the next 2 days, we obtain the results shown in Figure 7.11. The first mode of the diurnal cycle is represented, but soon the prediction converges towards a mean value.

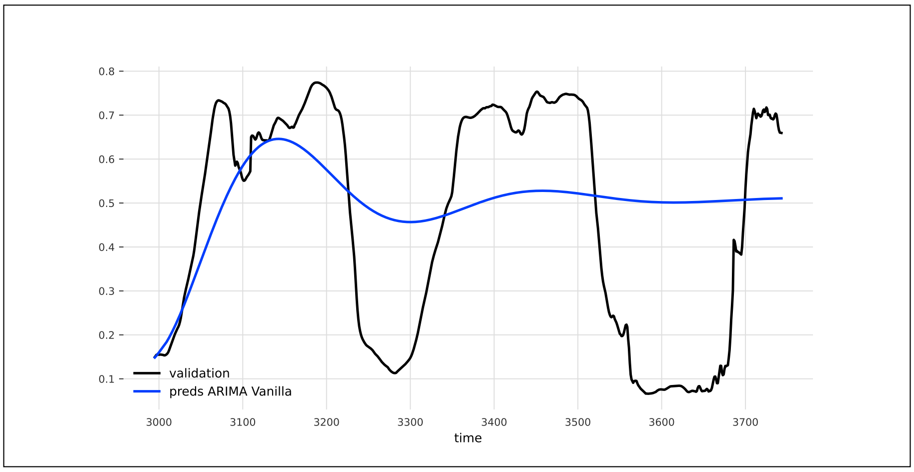

Figure 7.11.: Prediction of an ARIMA model for $r_0$ prediction, trained on the first 12 days of April WRF data and validated on the next 2 days

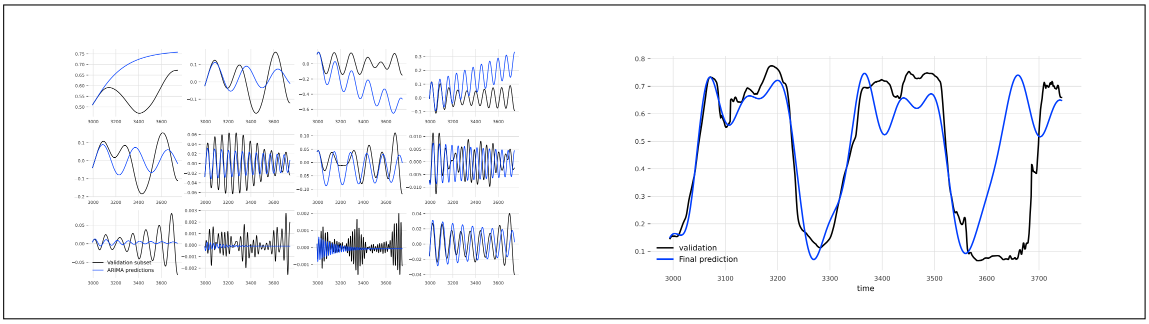

Figure 7.12.: ARIMA model on each mode of the decomposition proposed by [Li+23] for $r_0$ prediction trained on the first 12 days of April WRF data and validated on the next 2 days

Results obtained with VMD decomposition on the same test example presented on figure 7.12 show a huge improvement in ability to predict the forthcoming $r_0$ up to two days ahead, due to the very periodic scheme of this dataset. The results of the VMD and the prediction of each of the modes can be seen on the left figure. The number of modes on which to base the prediction is chosen as the number of modes that share a correlation coefficient with the original time series of more than 0.2. Doing this, we make sure all the relevant modes are being accounted for while limiting the computation to only those modes. On the example of figure 7.12, this corresponds to 5 modes.

Figure 7.13 shows the two metrics as a function of time in the prediction of $r_0$ using ARIMA + VMD for 10 independent predictions in the month of April. The black bars show the best and worst score obtained over the 10 predictions. The value of the score is contained below 0.05 with both metrics for about 20 points (i.e. 100 minutes) but then quickly diverges towards larger values with a large variability depending on the case.

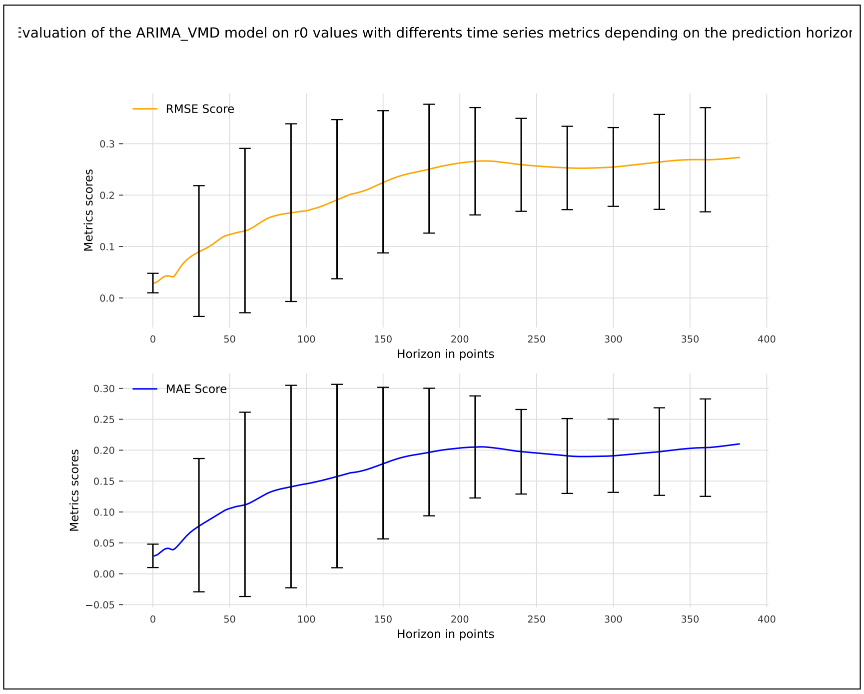

Figure 7.13.: Scores on the prediction of $r_0$ as a function of time with associated error (April)

This result and the same result for the prediction of the other moments will be the baseline of upcoming prediction methods. What has been done here will also be done for different months, giving us an indication of the versatility of our models in front of different atmospheric conditions.

### 7.3.4. Deep neural network for temporal prediction

While being able to reproduce the results of [Li+23] purely on WRF data already brings our work to the state of the art in optical turbulence prediction, we explored the general state of the art in time series forecasting with the use of deep neural network specialised for this task that are N-BEATS and N-HITS presented in 3.3.3.1 and 3.3.3.2.

The best results were obtained with N-BEATS while Neural Hierarchical Interpolation for Time Series Forecasting (N-HITS) is usually more suitable for long trends and requires a more complex parametrisation. Figures 7.14 and 7.15 show four relevant examples of the kind of probabilistic prediction obtained using N-BEATS. For each of these cases, we have applied quantile regression with quantiles corresponding to a 95% confidence interval. Conformal predictions methods are quite new for uncertainty quantification and it would be interesting to compare the associated confidence intervals with our quantile regression ones, all information are to be found in Section 3.3.3.3.

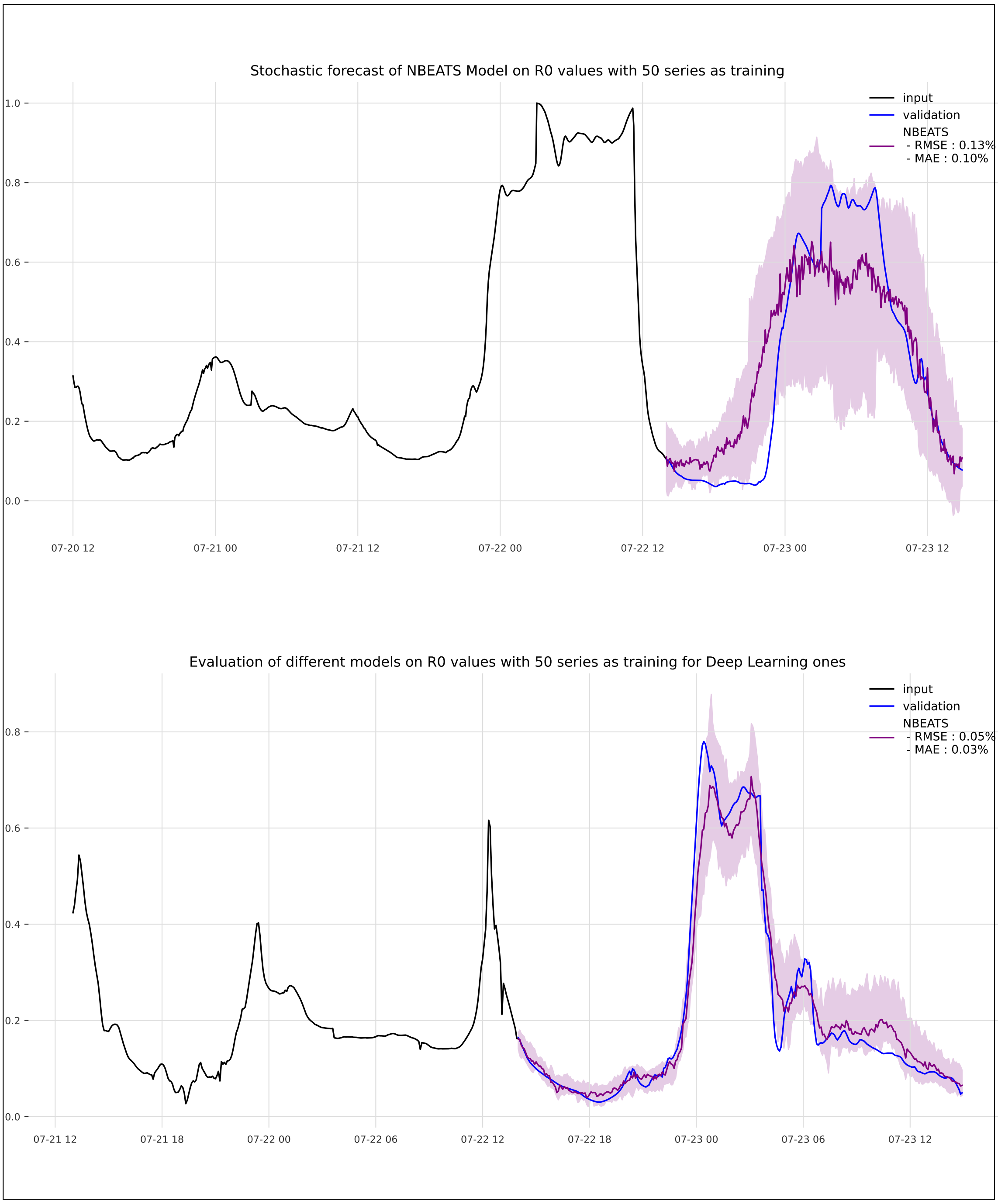

Figure 7.14.: Two examples of prediction of $r_0$ over one day using N-BEATS for July

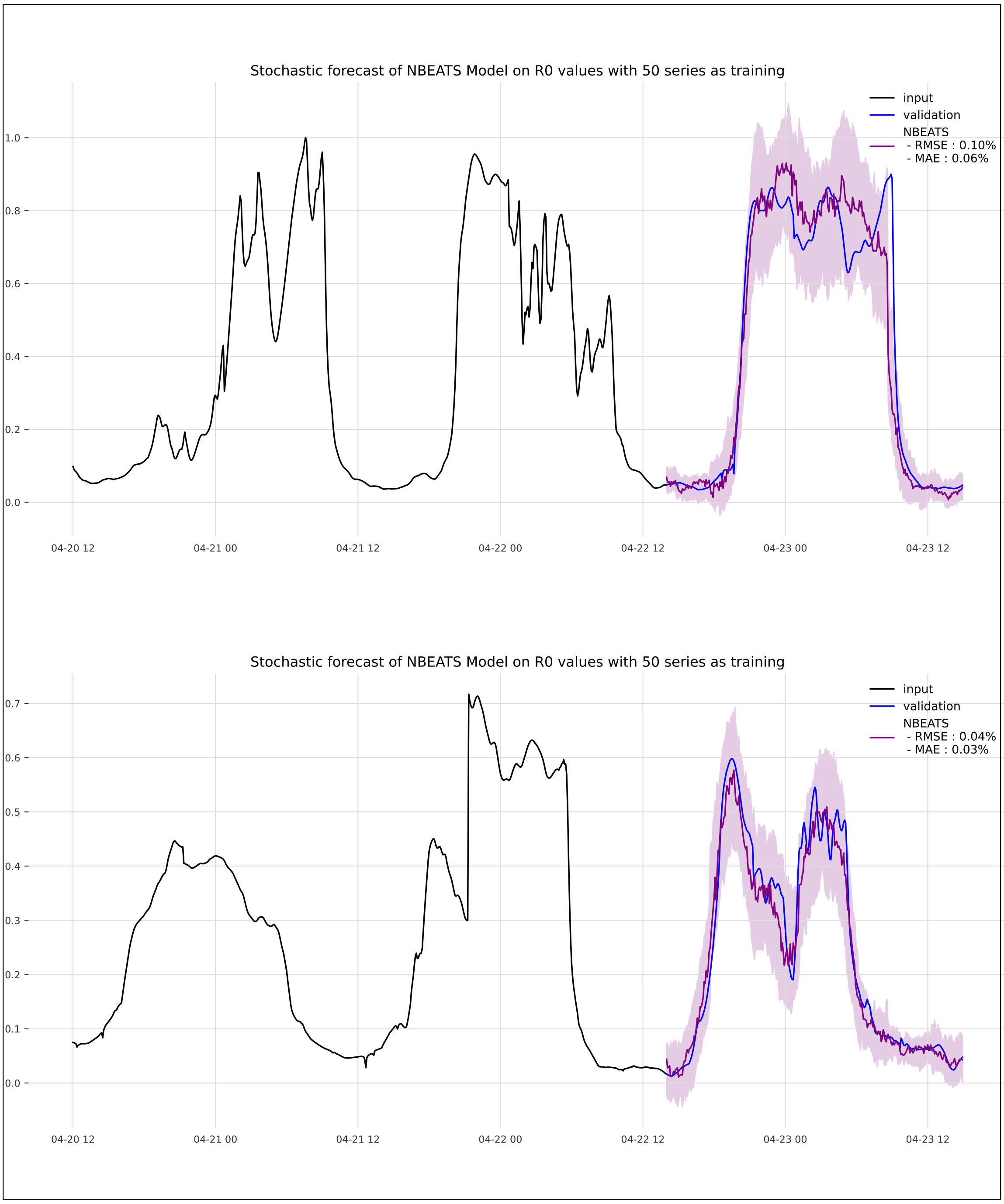

Figure 7.15.: Two examples of prediction of $r_0$ over one day using N-BEATS for April

The model visually gives impressive prediction but is still basic as it only uses moments from the past 7 days to predict the upcoming ones. This results in good trend prediction, but the model would not be able to anticipate unexpected variation due for example to high ground turbulence (sudden change in temperature or wind speed).

## 7.4. Introduction of covariates in the deep learning models

One way to improve the prediction efficiency is through the use of past covariate. Past covariates are time series that are known at the time of prediction and can be used to improve the accuracy of deep learning models. For example, adding the measurement of temperature or wind speed to the input time series of $r_0$ would allow the model to learn the relationship between the past meteorological condition and the future $r_0$, which could improve the precision of the meteorological conditions and the predictions.

There are a few reasons why using past covariates can improve the accuracy of deep learning models for time series prediction. First, past covariates can help capture the underlying trends and seasonality of the time series. Second, they help reduce the noise in the time series. This is important because noise can make it difficult for deep learning models to learn the underlying patterns in the data. Using past covariates, the model can filter out some of the noise and focus on the more important patterns. Third, past covariates can help to prevent overfitting, a phenomenon that occurs when a model learns the training data too well and is unable to generalise to new data. By using past covariates, the model is forced to learn the underlying patterns in the data.

Looking at correlations between the moment of interests and the meteorological data available in WRF simulations, we selected two covariates. Temperature at a ground level, that can be easily measured by any meteorological station, and the ground TKE, as it is directly related to the intensity of the turbulence close to the ground, as illustrated by the impact of the TKE on the ground $C_n^2$. Instruments can also be used for this purpose; for example, an ultrasonic anemometer combined with an infrared gas analyser can determine wind speed, as well as fluctuations in wind speed that contribute to TKE [FV92]; it also allows one to measure the exchange of mass, momentum, and energy between the Earth's surface and the atmosphere providing information about turbulent fluxes and thus TKE.

The use of these covariates significantly improves the score with metrics decreasing by 5 to 15% depending on the case (lower is better). All metrics are visible in the next section.

We can visually interpret the improvement using figure 7.16 and 7.17 where we show how the addition of covariates impact the prediction for two different dates . Figure 7.16 shows that the addition of the TKE as a covariate does improve the model with a prediction that sticks to reality for a much longer period. Yet, it does not impact, in the presented case, the confidence interval. The addition of the temperature, on the other hand, for the considered prediction in October, has a big impact on the confidence interval, making our prediction much more probable and thus accurate.

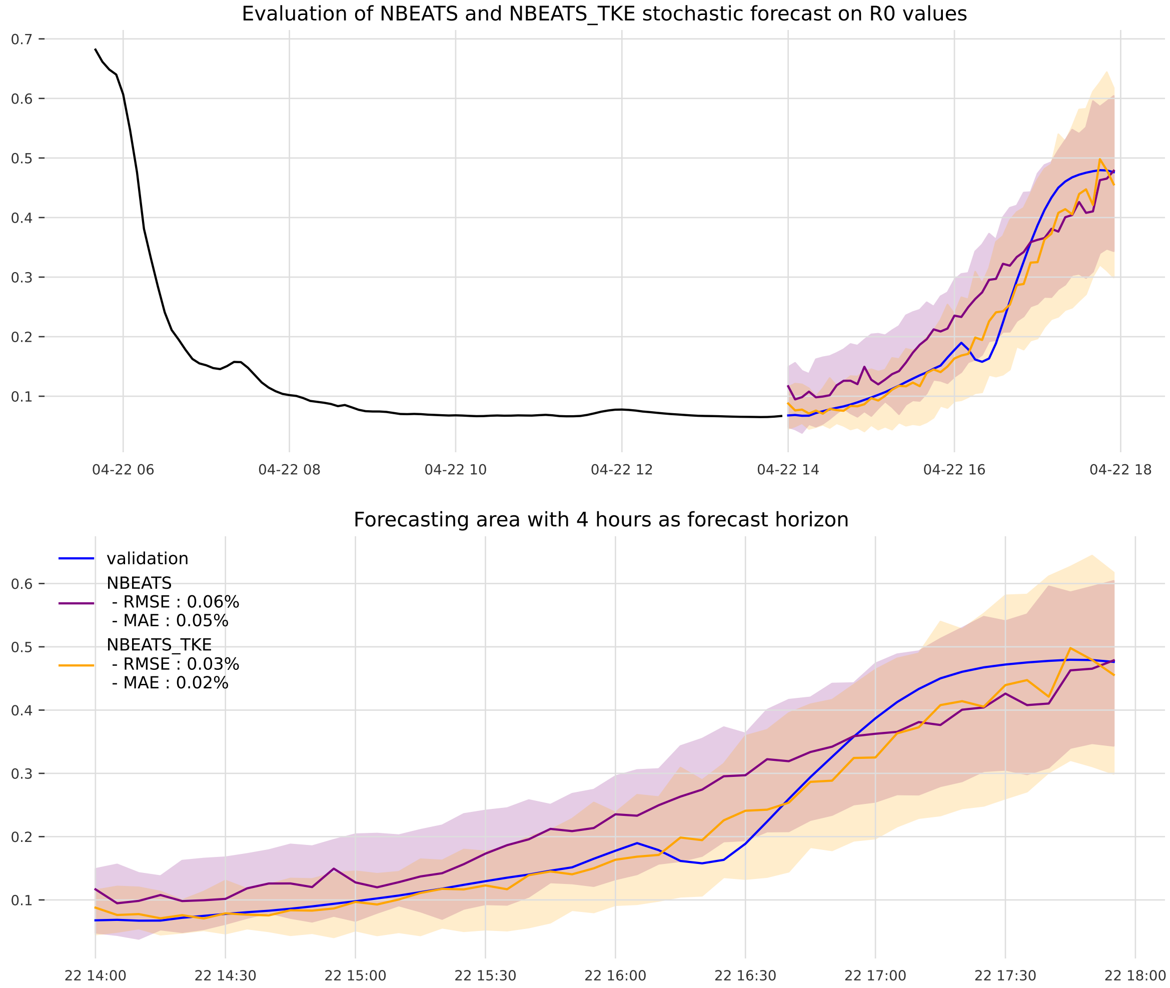

Figure 7.16.: Comparison of N-BEATS with (yellow) and without (purple) TKE as a past covariate for a prediction of a few hours the $22^{nd}$ of April.

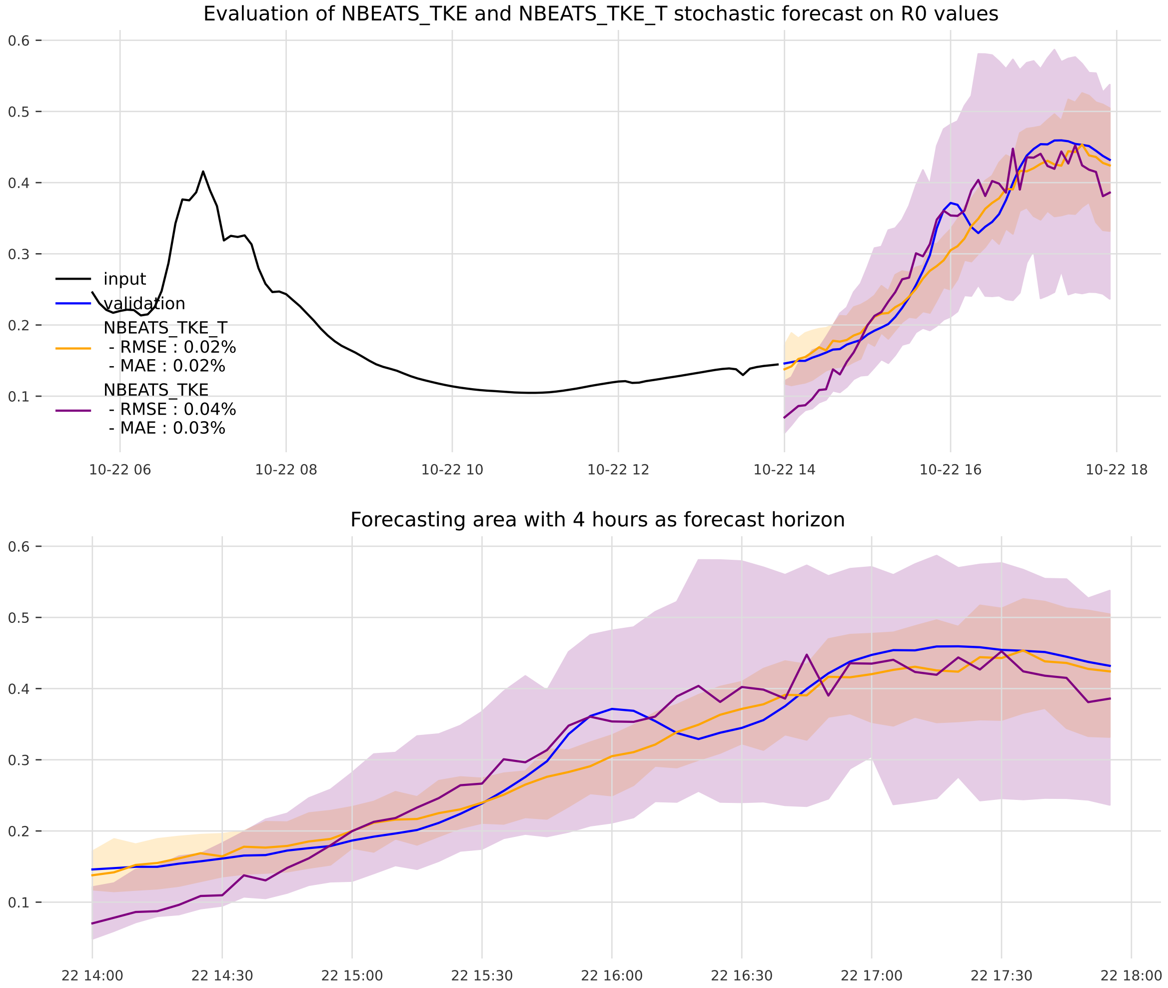
Evaluation of NBEATS_TKE and NBEATS_TKE_T stochastic forecast on R0 values

Forecasting area with 4 hours as forecast horizon

Figure 7.17.: Comparison of N-BEATS with TKE (purple) as a past covariate and with T° + TKE (yellow) as past covariates for a prediction of a few hours the $22^{nd}$ of October.

## 7.5. Results

- We ran training of the model for each of the 4 months using 50 input time series per month. These 50 time series are obtained by randomly selecting 7 day series in the 15 first days of the month, enabling the model to see different starting and ending times even if a lot of series share common days.

| Moments | $r_0$ | $\tau_0$ | $\theta_0$ |
|---|---|---|---|
| $ARIMA_{VMD}$ | 0.100/0.087 | 0.128/0.117 | 0.119/0.109 |
| $NHITS$ | 0.096/0.081 | 0.128/0.118 | 0.127/0.120 |
| $NBEATS$ | 0.071/0.061 | 0.075/0.068 | 0.083/0.076 |
| $NBEATS_{TKE}$ | 0.069/0.059 | 0.073/0.066 | 0.076/0.069 |
| $NBEATS_{TKE_T}$ | 0.061/0.049 | 0.070/0.063 | |

Table 7.2.: Prediction score for the different models and different moments of interest. The left score is the RMSE and the right one the MAE

- Each model was evaluated for 10 test series on the last 15 days of each month, which is a total of 40 test series. Each test series is composed of eight days, seven input days, and one day to parse the goodness of the models output.
- These two steps were done using two different seeds, allowing for a score less dependent on the choice of the training sets while keeping the same training and testing data for each of the models allowing for a better comparison. This brings the number of conducted tests to 80 per models .
- Final MAE and RMSE scores were obtained as an average value of the scores obtained on each of the 80 tests.

From all scores presented in Table 7.2, it is clear that the latest temporal prediction model N-HITS does not behave better than the ARIMA based method in our case and the reasons remain unclear. It could be that the more complex architecture of N-BEATS, even though it is slower, allows us to learn more complex patterns in the data, which can lead to better predictions. The ability of N-HITS to capture long-term dependency much better than N-BEATS is probably not as relevant in our case, since there is little long-term dependency in moments due to the nature of atmospheric phenomena.
In spite of this, N-BEATS outperforms the current state-of-the-art ARIMA + VMD model no matter the moment considered. The prediction score can slightly be improved with the addition of the TKE as a past covariate and even further adding the temperature measured near the ground as well.

## 7.6. Potential improvements in temporal prediction of moments

Despite the promising results presented in the previous section, there remain several avenues to enhance and refine the temporal prediction of time series of integrated parameters using deep learning models.

This work has allowed us to assess the feasibility of a prediction model. Despite this, a high amount of exploration still on the direct integration of other relevant parameters has to be conducted, rather than using specific weather values as supplementary information and incorporating additional parameters that are inherently related to the moments of the turbulence. Another notable direction for improvement is the exploration of deep learning models' performance when using future co-variables. The models discussed in this work predominantly focused on past covariate information, potentially overlooking valuable insights from future data. Using future covariates, possibly through the application of methods such as the **NBEATSxx** [Oli+21] model, could enable more accurate and forward-looking predictions. This future covariate could be estimated using the mesoscale meteorological model around the site.

Doing so implies the creation of a composite model, combining widely used meteorological model with deep neural networks, designed for the prediction of parameters specific to optical turbulence and trained to account for the site specificity such as the topography and the ground station architecture.

A composite model that combines the strengths of both the WRF predictions for trends and another model for capturing high-speed variability in the measured on site data could also be envisaged.

Even so, it seems complex to predict high-frequency variations precisely because of the number of phenomena that affect them and the pseudo-random nature that results. It should be possible to construct a statistical model capable of predicting the amplitude and correlation of high frequency integrated parameter variations based on ground data or simulations capable of taking account of topography and turbulent phenomena close to the ground, such as LES [BC15] simulations.

Robust uncertainty estimation is important for making informed decisions based on model predictions, thus incorporating measures of uncertainty from both models will be necessary. This will help provide a sense of the reliability and confidence associated with the composite predictions.

It should also be kept in mind that near-ground turbulence can change rapidly due to a change in vegetation, or anything else impacting ground topography. The composite model should be designed to adjust in near-real time to capture these changes. Regular updates based on new on-site measurements and new WRF data will improve accuracy.

This perspective is of great interest for the future of optical communication systems and should be pushed forward. It entails a model capable of forecasting long-term availability of an optical link with an associated probability that could be tuned for a given location and ground station.

# Conclusion

## Highlights and conclusions

This thesis embarked on a journey to address the ever-growing demand for efficient and high-capacity data transmission between satellites and ground stations. The limitations of traditional RF technologies have emphasised the need for innovative solutions, especially in the face of escalating demands for space-to-ground communication.

The need to inject the signal in a single-mode optical fibre for amplification and coherent detection emphasises the sensitivity of the link to atmospheric turbulence. Scintillation and wavefront distortions emerge as significant hurdles that need to be overcome for seamless communication. Although wavefront distortions can be partially corrected using adaptive optics, this comes at the cost of increased complexity and expense. Managing scintillation and residual power fluctuations requires effective data processing, including the application of suitable error correction codes and interleaving techniques.

Adverse weather conditions such as cloud blocking and challenging turbulence can disrupt even the most advanced systems, jeopardizing the promise of low-latency communication channels. To mitigate these challenges, the implementation of site diversity, which involves dynamic routing of information through optical ground stations less affected by environmental factors, offers a promising solution. Such a dynamic routing will rely on the ability to anticipate several minutes to tens of minutes in advance the compatibility of the propagation channel with very high data rates optical links. The question of cloud blocking being already answered, we focus in this manuscript on the impact of atmospheric turbulence on the performance evaluation of an optical link and on the possibility of anticipating it.

According to the open literature, AO performance evaluation usually requires the access to high vertical resolution turbulence and wind profile to meet application related specific requirements. For astronomy, ESO conducts high vertical resolution site testing campaigns to accurately qualify astronomical sites. For optical links, ESA is currently founding an ambitious site characterisation project (ANATOLIA) to gather statistics of vertical high-resolution turbulence profiles on different sites.

At the beginning of this work, the need for high vertical resolution both turbulence and wind profiles to describe accurately the performance of an AO corrected optical link was unclear. It is with this in mind that we have embarked on an exploratory process to try to determine the possibility of a link power margin assessment using a small number of integrated parameters that can be measured easily and at minimal costs.

In the chapter 4, we focused on assessing the statistics of the received optical power into a SMF after AO correction.

Focusing on the GEO-downlink and assuming several fully justified simplification hypotheses on the AO model, we constructed a metamodel to predict both the probability density function (PDF) and the half-correlation time of the received optical power using machine learning techniques, particularly Gaussian process (GP) regression. The metamodel incorporated a set of four critical atmospheric parameters, the Fried parameter ($r_0$), an average wind speed ($\bar{v}$), an average altitude of turbulence layers ($\bar{h}$) and the log-amplitude variance ($\sigma_\chi^2$).

The results showed that these four parameters appear sufficient to accurately assess ROP probability density function.

Taking into account the temporal characteristics of the downlink received signal, we demonstrated that adding the temporal power spectrum of the scintillation recorded by a small diameter receiver to the other parameters enables the evaluation of the ROP correlation time. This result will be of particular interest to optimise the specificities of the interleaving process, such as the length of the interleaver.

The key atmospheric parameters to be included in the simulation were identified through a sensitivity analysis that demonstrates the complementary of each quantity. This approach, conducted on the downlink, could easily be generalised to the uplink with potentially different conclusions, due to the significant impact of point ahead angle anisoplanatism that is expected on the uplink.

Exploring the impact of different AO system configurations on the precision of the meta-models demonstrated the flexibility of the models to a wider range of scenarios.

The use of a FEC and an interleaver in the detection chain introduces non-linearities, making access to the power margin a complex problem which we have solved using two different tools for generating non-Gaussian processes.

First, we introduced AnySim, an approach that offers a systematic way to generate non-Gaussian time series while preserving the desired statistical properties, particularly the autocorrelation function.

Next, we explored ARRC, a method based on autoregressive conditional random processes. This approach has been developed together with Bernard Picinbono for our application and gives highly promising results, while allowing to generate series at unrivalled computing speed, providing a valuable alternative to more complex approaches.

With standard low budget AO parameters, we demonstrated, using both methods, a prediction of the power margin with an absolute error of less than one dB on all the database (May 2021 Tenerife). The model seems robust to possible interruptions as it does not display any false positives on the availability prediction.

Machine learning tools can make a decisive contribution, on the condition that they are approached rationally through an understanding of physical phenomena. The tools created here are intelligible thanks to the use of Gaussian processes, autoregressive processes, and the numerous sensitivity analyses carried out. The methodology, thanks to the adaptability of the machine learning tools exploited within the study, could be transposed to the exploitation of real measured quantities when the necessary inputs will be available. Ultimately, all the work was carried out with a view to mitigating uncertainty in the results.

The last part of this work, more exploratory, focused on the ability to predict the value of moments and therefore availability over long periods of time using cutting-edge deep learning models. We presented a comprehensive set of results, comparing different models, including ARIMA-based methods, NHITS and NBEAT. The results clearly indicated that NBEATS outperformed the current state-of-the-art ARIMA + VMD model across all moments of interest.

We later introduced the concept of covariates, which are additional time series that are known at the time of prediction and can enhance the accuracy of our models. Specifically, we discussed the inclusion of temperature and the ground turbulent kinetic energy (TKE) that can be obtained through ground meteorological stations.

Incorporation of covariates proved to be beneficial, leading to significant improvements in prediction accuracy. These covariates helped capture the underlying trends, reduce noise, and prevent overfitting, ultimately enhancing our models' ability to make accurate predictions. We demonstrated this improvement through visual representations as well as prediction accuracy scores.

# Limitations and next steps

Our earlier simulations assumed flawless measurements of the turbulence parameters. Later, a propagation of a measurement error has been studied. We assumed a characterisation instrument that would have a different aiming angle than the satellite. This led to the conclusion that, while all moments are equally impacting the error made on the power margin, a difference in line of sight bellow 60° limit the maximum error to 1 dB, thus well within the system margin.

However, significant focus should still be put on studying the potential errors introduced by instrumental measurements bias and noise. Comparison between measurements yield by characterisation instruments such as the one proposed by Miratlas, and measurements conducted through the WFS on a real optical link is essential. This in the goal to complement the angle-of-sight error approach that has been carried out discretely on a large-mesh grid, and to establish and quantify all the phenomena that will most likely impact integrated parameters measurements.

We can also observe that sensitivity analysis using Sobol or Shapley indices does not take into account the tails of distributions. However, it is these rare events that cause link interruption, and special attention should be devoted to understanding them. In this regard, techniques such as the one presented in [MAG21] would likely be more suitable.

It is also to be noted that all results are based on an experimentally validated pseudo-analytical model (SAOST). This implies a range of validity and underlying hypotheses. The most restrictive are undoubtedly the phase-amplitude independence assumption, the log-amplitude representation limited to small perturbations, and the purely monochromatic description of the processes at play. Furthermore, the model only contains what's inside, and hard-coded parameters such as the ground outer scale become variables in real-life conditions. Investigating the impact of the outer scale on the conclusions raised here shall be considered a priority.

All these concerns about the limitations inherent in these hypotheses would really benefit from field measurement campaigns. ONERA is currently developing a ground station for GEO-feeder demonstration (FEELINGS [Cyr+22]). Its primary objective is to validate models of optical propagation through the atmosphere, out of which the one developed in this work. The 60 cm telescope will be commissioned at the Fauga-Mauzac site, and will be accompanied by a Miratlas station for measuring integrated parameters. Simultaneous measurement of these integrated parameters, of the optical power injected during link operation, and of the $C_n^2$ profiles reconstructed from the WFS data [Véd08] will allow for the building of a comprehensive database without model bias. This database will be compared both with simulated profiles and with SAOST output to justify the statistics established in this thesis. Finally, it will enable the metamodels to be retrained, either from scratch or with the help of transfer learning techniques, in order to adapt them to the actual site and operating conditions.

Finally, the initial results obtained with the state-of-the-art machine learning models for the prediction of parameters integrated over long periods of time need to be significantly expanded. Despite the promising results, we acknowledged that several avenues for improvement exist. Future work will involve exploring the use of different and future covariates. Predictive capacity primarily focused on the Fried parameter, and other parameters should be studied. Finally, given that the variability of the surface layer is not finely represented by WRF, one should study the impact of high-frequency variations in Fried parameter during real-world demonstrations. It would then be advisable to supplement the study with the creation of composite models to account for these variations. Studies on improving the data obtained through WRF predictions should be considered, using for example the work done in [Raf+22] where "site learning" methods are proposed to account for local measurements in the turbulence model, thus taking into account the specificity of a given site.

# A. $C_n^2$ profile decimation method suited to the study of turbulence

## A.1. Database

Models understanding and comparison was done using profiles measured using radiosonde operated by the GGCOS Reference Upper-Air Network (GRUAN) [Tho+13].

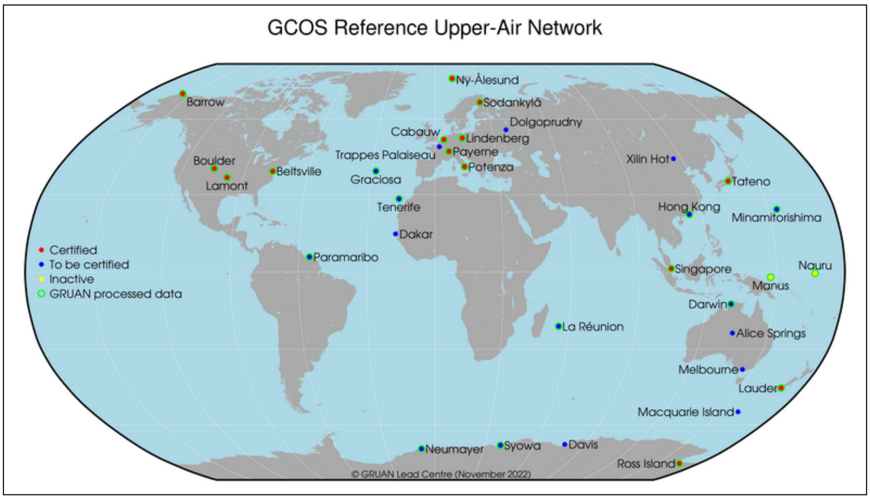

Figure A.1.: GRUAN is envisaged as a global network of eventually 30-40 radiosonding stations.

GRUAN is described as follow on their website :

> The Global Climate Observing System (GCOS) Reference Upper-Air Network (GRUAN) is an international reference observing network of sites measuring essential climate variables above Earth's surface, designed to fill an important gap in the current global observing system. GRUAN measurements are providing long-term, high-quality climate data records from the surface, through the troposphere, and into the stratosphere. These are being used to determine trends, constrain and calibrate data from more spatially-comprehensive observing systems (including satellites and current radiosonde networks), and provide appropriate data for studying atmospheric processes. GRUAN is envisaged as a global network of eventually 30-40 sites that, to the extent possible, builds on existing observational networks and capabilities.

Data for the site of Tenerife, a site of interest for the rest of this work, was obtained directly from their website. This dataset contains two balloon release a day, one at midday, the other at midnight. The balloons measure the air pressure as well as the associated geopotential height, the air temperature, the relative humidity, and the zonal and the meridional wind speed. Over its course from ground to about 33 kilometres above ground where it explodes, the balloon makes a measurement every given time period providing extremely resolved profiles of between six and seven thousand point depending on the conditions and the ascension speed.

While a SAOST simulation using a 100 layers profile takes about 3 minutes, the same study using a 6000 layers profile will take up to two days. Through our need to generate large databases came the need to be able to decimate profiles while preserving moments, which, we understood, are the defining parameters of system link availability.

## A.2. Gauss-Legendre quadrature

This optimal decimation is done using the Gauss-Legendre quadrature, a method presented in an optimal approach to reduce the number of observations. This approach has been originally developed to reduce the size of maximum likelihood problems developed in [Mus93; PM23].

Let $Y_h$ be the measures of the $C_n^2$ at a given height h. We have a sample $Y_{h_1}, \cdots, Y_{h_n}$. We assume that the $Y_{t_h}$ are uncorrelated, Gaussian, and have the same standard deviation $\sigma$. Of course, this strong assumption is not satisfied in our case, where we have non-stationarities (jumps) and correlations in the $C_n^2$ profile. However, we still use this method relying on the associated mathematical arguments.

The measures result from a non-linear function of a hidden state (modelling of $C_n^2$ introduced in Chapter 1). The goal is to reduce the size of the sample with minimal loss of information, particularly preserving moments.

Let $1 \leq m \leq n$ be the new number of observations. The new set of observations denoted by $\left(\tilde{Y}_1, \cdots, \tilde{Y}_m\right)$ will be given as a linear combination of the original set of observations $\left(Y_{t_1}, \cdots, Y_{t_n}\right)$,

$$\tilde{Y}_i = \frac{1}{\|\Phi_i\|^2} \sum_{h=h_1}^{h_n} \Phi_i(h) Y_h, \tag{A.1}$$

with $\|\Phi_i\|^2 = \sum_{h=h_1}^{h_n} \Phi_i^2(h)$ where $\Phi_i$ is the Lagrange polynomial of degree $m-1$.

For any $1 \leq i \leq m$, let us introduce $\Phi_i$ the Lagrange polynomial of degree $m-1$ such that

$$\Phi_i(h) = \begin{cases} 1 & \text{if} \quad h = H_i \\ 0 & \text{if} \quad h = H_j \neq T_i. \end{cases} \tag{A.2}$$

where $H_1 \leq \cdots \leq H_m$ are the roots of the Legendre polynomial $\Psi_m$ of degree $m$. One can prove that for any $i \neq j$ with $1 \leq i, j \leq m$, $H_i$ is a real such that:

$$h_1 \leq H_i \leq h_n \quad \text{and} \quad H_i \neq H_j. \tag{A.3}$$

If $m = n$, then $H_i = h_i$, for any $1 \leq i \leq m = n$.
We have :

$$\left\langle \Psi_m, h^j \right\rangle = 0 \tag{A.4}$$

for any integer $0 \leq j \leq m-1$ with the scalar product :

$$\langle f, g \rangle = \sum_{h=h_1}^{h_n} f(h) g(h) \tag{A.5}$$

In [MO05] and [VO09], it is shown that the $\tilde{Y}_i$ are independent Gaussians of reduced standard deviation $\frac{\sigma}{\|\Phi_i\|_2}$. Moreover, the information contained in these new measurements is close to that contained in the initial measurements. In particular, if we work with this reduced sample $(m << n)$, we preserve the moments.

A robust and optimal method for finding Legendre polynomials roots is described in [GW69]. The eigenvalues of the Jacobi matrix give the zeros assuming known polynomial recursion coefficients; the paper also shows how to compute these coefficients from a QR decomposition of a Hankel matrix. Analytic recursive expressions are provided that greatly facilitate the implementation of this approach.

## A.3. Results

We extracted from GRUAN database all radiosonding data for the station of Tenerife over the whole year 2020. With two releases a day, it corresponds to 730 set of radiosonding data. From this data were generated 730 sets of $C_n^2$ and wind profile using Dewan's model of equation1.18, each having six to seven thousand layers.

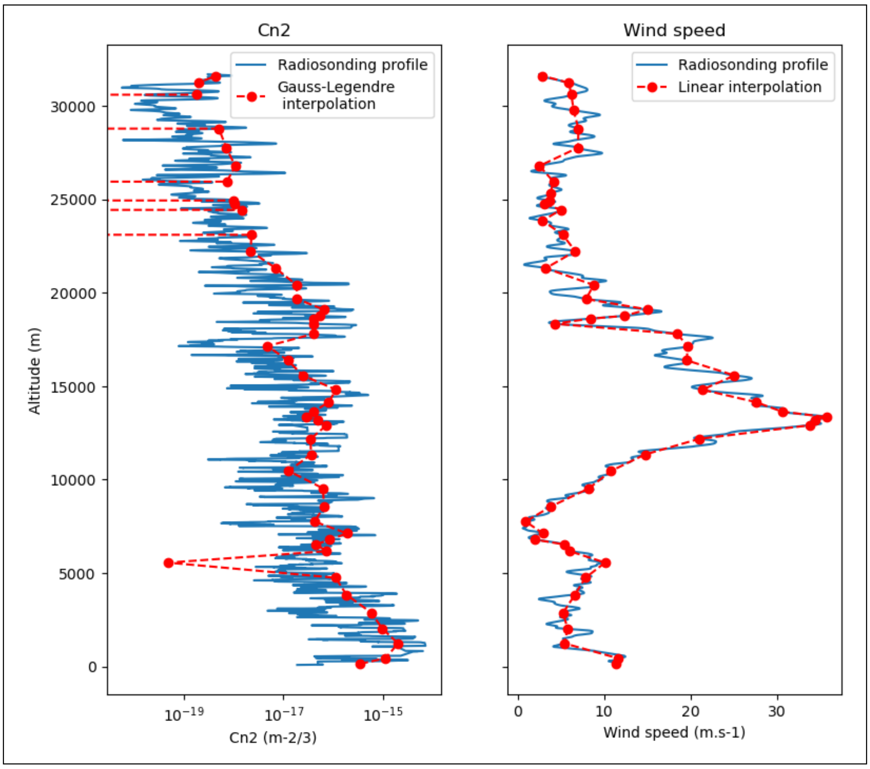

Figure A.2.: Gauss-Legendre interpolation of the $C_n^2$ profile and associated wind profile

The Gauss-Legendre decimation method was applied on each of the $C_n^2$ profile with a generation of 50 output points. Doing the same decimation on the wind profile does not guarantee to find the same 50 sampling heights.

Wind profiles have a more stationary nature than $C_n^2$, variations occur over wider altitude range. We thus kept the sample points returned by the Gauss-Legendre method on the associated $C_n^2$ profile and took the wind profile on these points with a simple linear interpolation between them.

This process can be seen in on Figure A.2 for the first profile of the set (01/01/2020 - 11:00). In blue are the original $C_n^2$ and average wind profiles. In yellow is the $C_n^2$ profile obtained through Gauss-Legendre interpolation preserving the moments. In red is the decimated wind profile with the sampling (red dots) of the Gauss-Legendre interpolation calculated on the $C_n^2$.

Figure A.3 shows the difference in distribution over the whole database between the moments computed from the 50 layers interpolated profiles compared to moments computed from the 6000+ layers profiles.

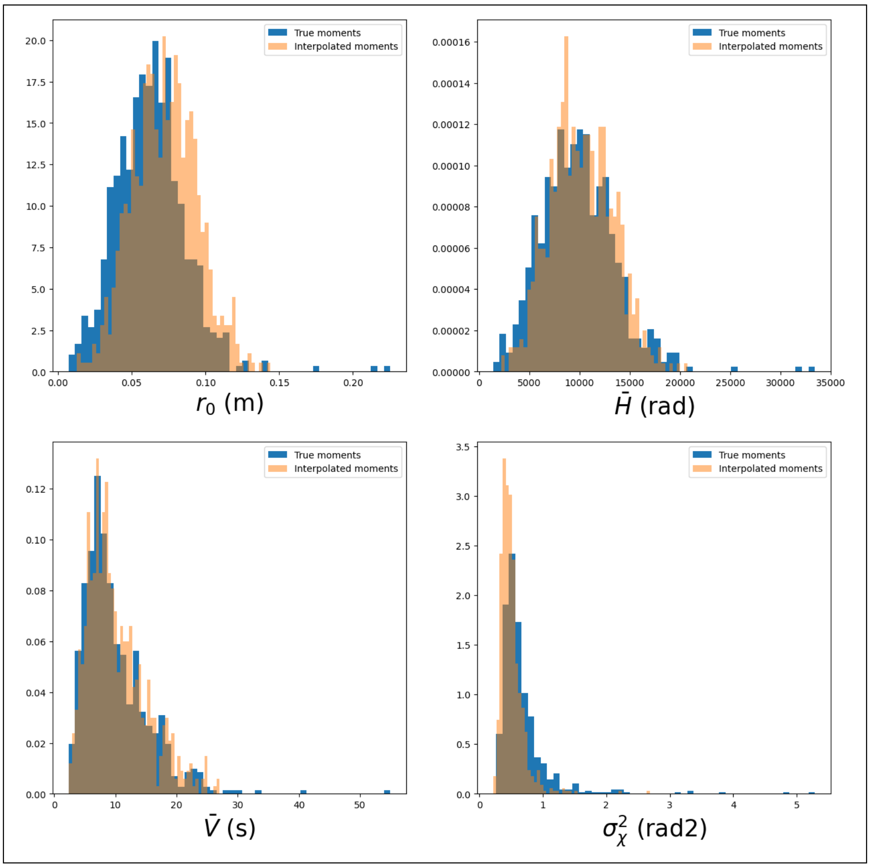

Figure A.3.: Moments from the 50 layers interpolated profiles compared to moments from the 6000+ layers profiles

While we can see that the method is not perfect because the distribution of the moments is not reproduced exactly, this method is still an excellent way of obtaining profiles with a very small number of layers, while retaining the main turbulence statistics for the entire database. This enables accurate statistical site studies.

# B. Statistical description without the use of moments

Another way that was explored to estimate the link power margin is to skip the time series generation step and to use a fully statistical approach to describe the impact of the conversion to mutual information and of the interleaver.

This was done as AIRBUS wanted to explore a way to determine link availability without knowledge of the moments and knowing only the statistics of the flux (mean, variance, half-correlation time) measured on a time series of 900ms. The question raised by this problem is how accurately the minimum of a 10 seconds interleaved time series of mutual information can be estimated using only those informations measured on a short time scale.

Using the mutual information law introduced at the beginning of chapter 5 in figure 5.4, two regimes are to be taken into account. The first is the case of strong turbulence (with an injection of optical power from $\approx -55$ up to $\approx -45dBm$), where the relation between ROP and mutual information is nearly linear, and the second is the case of weak turbulence (with a ROP always $> -45dBm$), where a threshold effect occurs and mutual information is almost constant no matter the value of ROP.

These two regimes, illustrated by figure B.1, have to be studied independently as the autocorrelation function has a very different behaviour in each case.

In a case of weak turbulence, the value of the mutual information saturates to a value superior to 0.999, being constant no matter the time, and we end up with a fully decorrelated signal time series (figure B.2). On the other end, in the case of low values of ROP, the variations of MI are synchronised with the variations of ROP, the autocorrelation functions are very close in shape and values (but not exactly the same, as the relation is not truly linear and a threshold effect still exists for the highest values of ROP).

In other words, we see that the autocorrelation function will impact the determination of the link availability in the case of a poorly corrected signal but not in the case of a "good correction" where the MI is constant $\approx 1$.

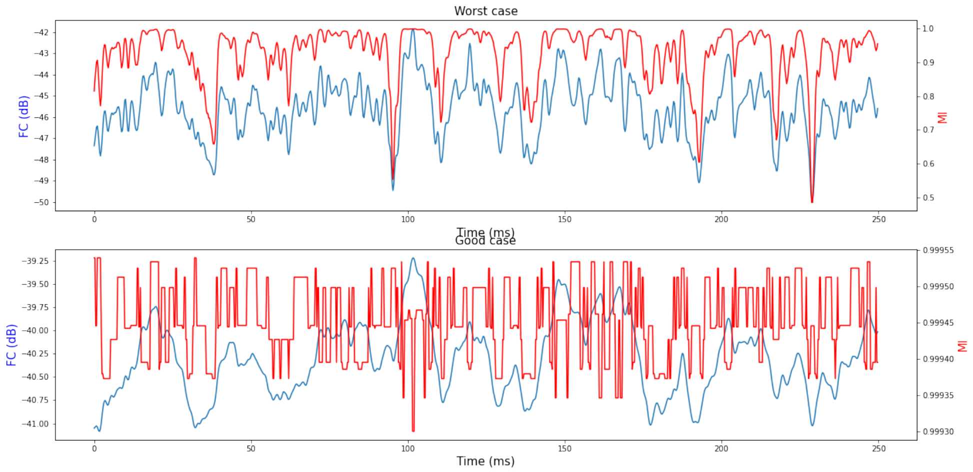

Figure B.1.: Temporal serie of ROP (blue) vs MI (red) on an average case of turbulence (top) and a case of weak turbulence (bottom).

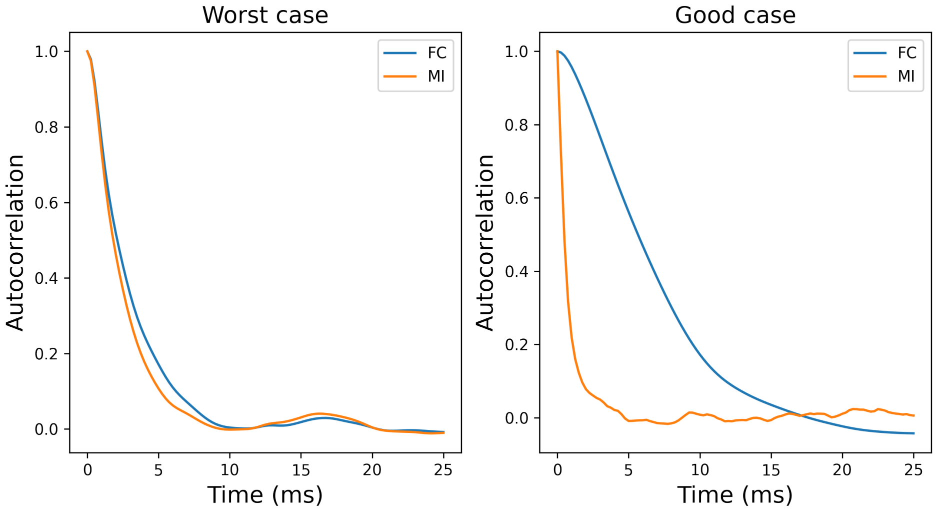

Figure B.2.: Autocorrelation of ROP (blue) vs MI (orange) on an average case of turbulence (left) and a case of weak turbulence (right).

# B.1. Impact of the half-correlation on the minimum of an interleaved MI time series for a poorly corrected signal

## B.1.1. Autocorrelation fit

In the following, we are led to study the time series shown in the previous section that correspond to the worst time series (in terms of ROP) of our database, where the saturation regime of MI is not reached.

To simplify the study, an approximation is made, that is, considering the autocorrelation function of the MI time series as a decreasing exponential function: $\exp(-kx)$, $x$ being the time delay. This does not impact the general methodology, and the validity of this approximation will be discussed later on.

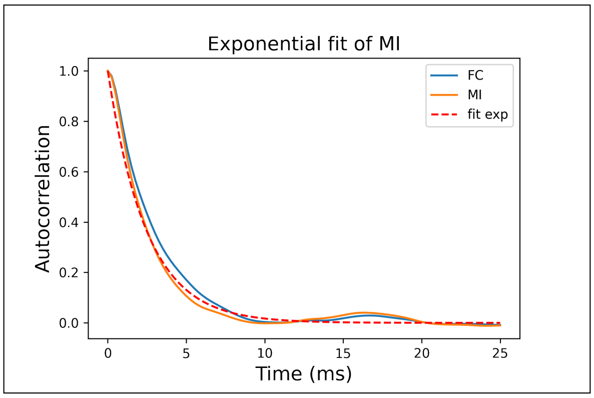

Figure B.3.: Exponential approximation of the autocorrelation of MI.

# B.2. Comparison with uncorrelated time series

The first study we conducted was to compare the impact of the interleaver on correlated and uncorrelated time series. Uncorrelated time series were obtained as a random permutation of the correlated time series of MI. Thus, they share the same exact distribution but in a fully uncorrelated order.

Figure B.4 shows in both normal and log scale the value of the minimum of the interleaved time series for both the correlated and uncorrelated cases, as a function of the length of the interleaver. This is given for the example case of an average ROP visible in the top section of figure B.1.

As can be seen, for a given interleaver size, the correlation affects the minimum level of the interleaved series of MI

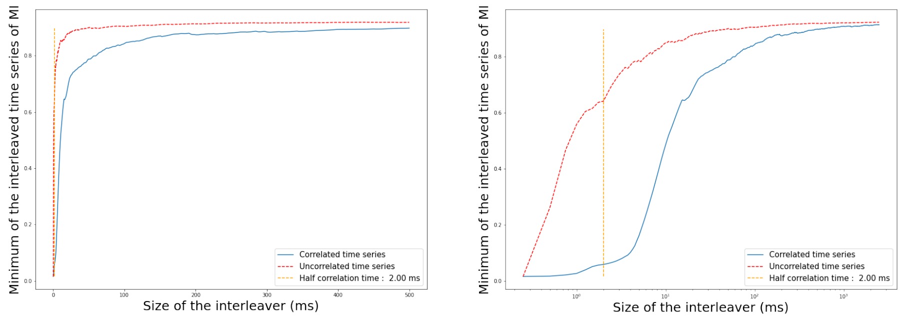

Figure B.4.: Minimum of MI time series vs interleaver size (in log scale on the right). In blue for the correlated time series and in red for an uncorrelated time series with the same distribution.

This can be put in equations, assuming that the minimal value of the given time series can be approximately described as the lower bound of a confidence interval of the values taken by the MI. Under this hypothesis, the confidence interval can be written as $Pr(\mu - \alpha\sigma \leq X \leq \mu + \alpha\sigma) \approx 100\%$ where $\mu$ is the mean of the MI time series and $\sigma$ its standard deviation. $\alpha$ is a positive real value that depends on the law of $X$ and, in the Gaussian case, it is common to take $\alpha = 3$ for a confidence interval of 99.7% or $\alpha = 5$ for 99.999994%.

$\mu$ is a constant for any interleaver size or correlation function, but the latest is not true for $\sigma$. For a size $n$ interleaver $\sigma^2(X_{inter}) = Var(X_{inter}) = Var\left(\frac{\sum_{i=0}^{n} X_i}{n}\right)$ where $X_i$ is the random variable associated with the stochastic process associated to the temporal series of MI at a delay $i$.

$$Var(X_{inter}) = \frac{\sum_{i=0}^{n} Var(X_i)}{n^2} = \frac{Var(X)}{n} \tag{B.1}$$

in the uncorrelated case.

In the case of correlated random variables with an exponential correlation function, the analytic expression of the variance is the following :

$$Var(X_{inter}) = \frac{\sum_{i=0}^{n} Var(X_i)}{n^2} + \frac{2}{n} \sum_{1 \leq i < j \leq n} cov(X_i, X_j) = \frac{Var(X)}{n} + \frac{2}{n} Var(X) \sum_{1 \leq i < j \leq n} e^{-k(j-i)} \tag{B.2}$$

With :

$$
\begin{aligned}
\sum_{1\leq i<j\leq n} e^{-k(j-i)} &= \sum_{j=2}^{n} e^{-kj} \sum_{j=1}^{j-1} e^{ki} \\
&= \sum_{j=2}^{n} e^{-kj} \frac{e^{kj}-e^{k}}{e^{k}-1} \\
&= \sum_{j=2}^{n} \frac{1-e^{-k(j-1)}}{e^{k}-1} \\
&= \frac{1}{e^{k}-1}\left((n-1)-\sum_{j=1}^{n-1} e^{-kj}\right) \\
&= \frac{(n-1)e^{k}+e^{-k(n-1)}-n}{(e^{k}-1)^{2}}
\end{aligned}
$$

Figure B.5 shows for both cases the evolution of the variance with the interleaving time, calculated from the time series and evaluated from the above equations. Our model of exponential correlation structure seems to overestimate the variance for larger values of $n$ on this set of profiles. The reason for that was not further investigated, since the figure B.5 is only shown for illustration purposes of the method.

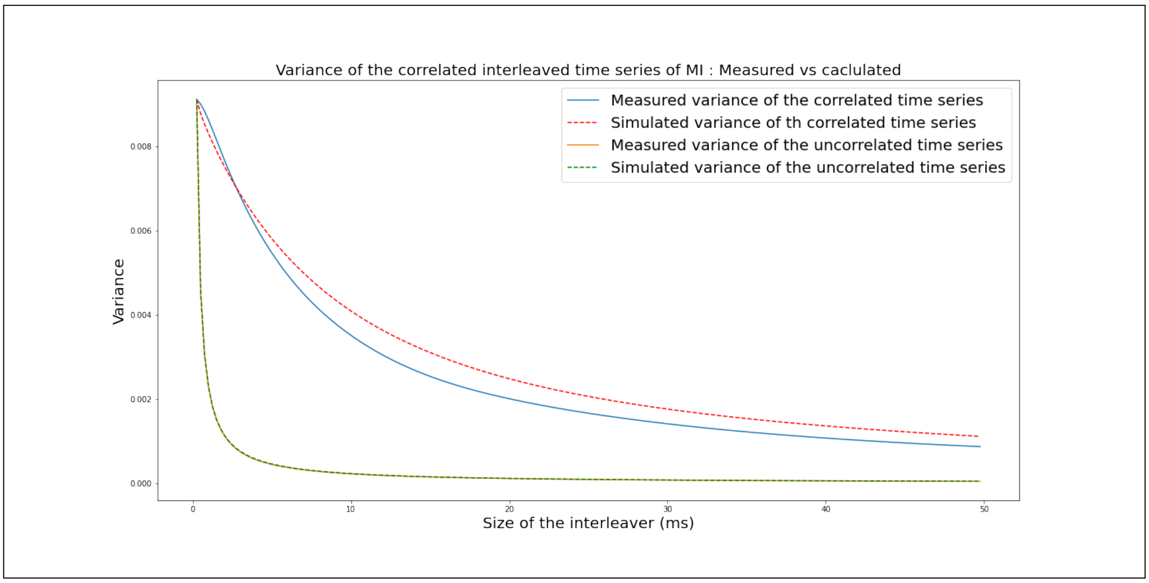

Figure B.5.: Evolution of the variance with the interleaving time, computed from the time series and evaluated from the above equations. 1ms = 4points so for 100ms, n=400

## B.3. Results

The fitting of the curves obtained in figure B.4 with law in $\mu - \alpha\sigma(n)$, is presented in figure B.6.

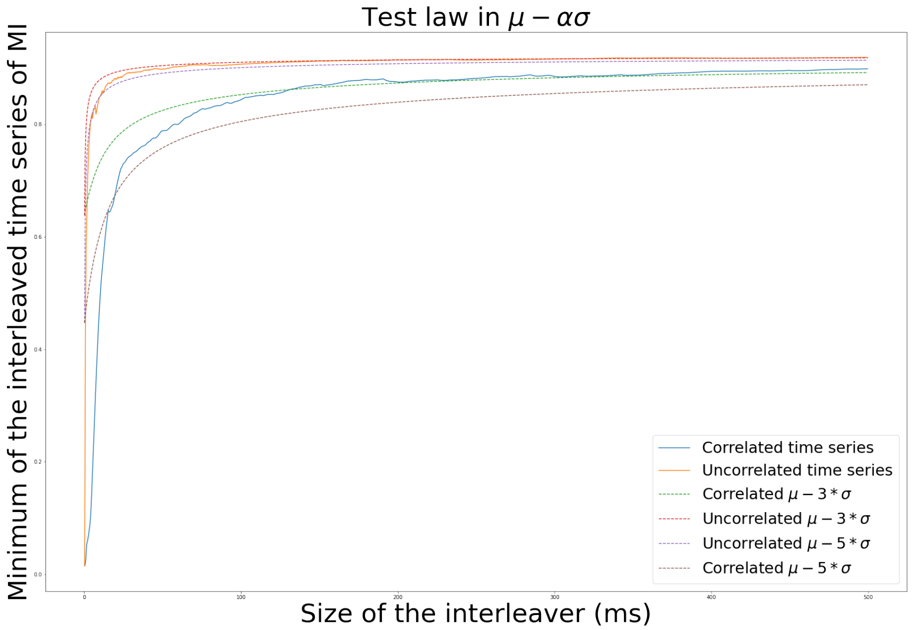

Figure B.6.: Law of the min vs $\mu - 3\sigma$ and $\mu - 5\sigma$. 1ms = 4points so for 100ms n=400

For this one particular time serie, the fitting law in $\mu - \alpha * \sigma$ is accurate for large values of the interleaver (from 100ms ==> n=400). A low $\sigma$ and a soft tailed distribution (large interleavers) makes it easy to determine the minimum value using a confidence interval, but these conditions are not met in the case of an heavy tailed distribution and deep fading associated with a small interleaver size.

### B.3.1. Results on the database using a 900ms time series as input

Figure B.7 shows the comparison between the prediction using the statistical method with statistics from a 900 ms times series compared to the minimum value of mutual information of an interleaved time series computed from a 10 seconds simulation. Choosing 0.94 as the value of required mutual information (as previously for a MODCOD 9/10), one can see that not every series where the availability of the link is not guaranteed is identified as so (right panel of figure B.7). On the 52 series where the link is not available, the statistics method gives a false positive in 13 cases, meaning

25% of the time. Error on the prediction of the exact value is shown in figure B.8 and is up to 3% on the selected cases.

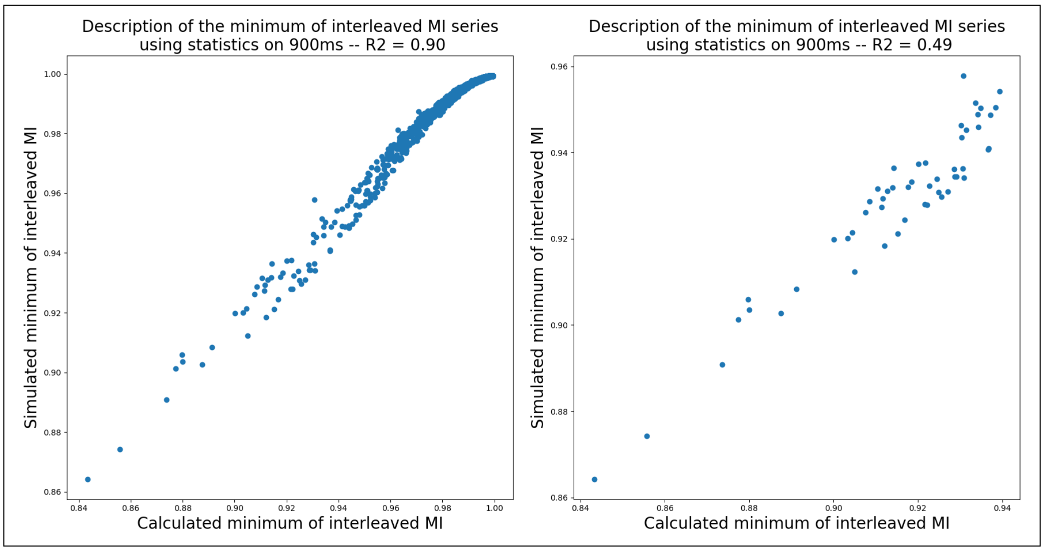

Figure B.7.: Assessment of the minimum of the interleaved series of MI using the statistical method.

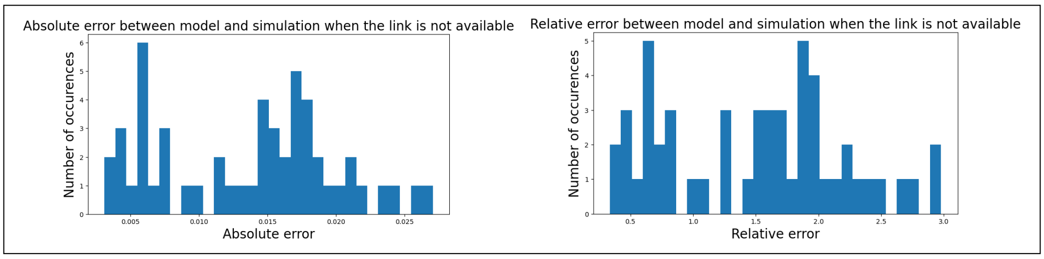

Figure B.8.: Absolute and relative error(in %) on the assessment of the minimum of the interleaved MI series (when the link is not available (min<0.94))

### B.3.2. Impact of the half correlation time on the prediction

We saw that the autocorrelation has very little impact for good correction, and for bad correction the impact of the autocorrelation can be calculated. The error on the half-correlation time can be reported as an error on the standard deviation as $k = \frac{-log(0.5)}{halfcorrelation}$, this error decrease as a factor of $n$.

Lets consider our series of MI. The series are made of 40000 points for 10 seconds. The half correlation time is 9 points ie. 2.25 ms. $k = -log(0.5)/9 = 0.077$. The variance is 0.009 and the mean is 0.924. Taking a 50 ms interleaver, i.e., n = 200, we have the variance of the interleaved series $Var(k = -\ln(0.5)/9, n = 200) = 0.0011$, $\mu - 3\sigma = 0.82$.

Now let us assume that we did a 100% mistake on the half correlation time with $k = -\ln(0.5)/18$, $Var(k = -\ln(0.5)/9, n = 200) = 0.0021$, $\mu - 3\sigma = 0.79$. In this precise case a error of 100% on the autocorrelation time results in a 5% error on the value of $\mu - 3\sigma$. If we were to consider a 100 ms interleaver, this error would only be of 3%.

## B.4. Limitations

One should notice that this method can be used to determine the link availability with little knowledge on the $f_{smf}$. However, due to the non linearity of the MI transformation and the interleaving process and due to the lack of information about the distribution of $f_{smf}$, the limits of this statistical description quickly appear, with the impossibility to asses the power margin. This method is only useful to assess the minimum value of mutual information associated to an interleaved series of $f_{smf}$ with an associated error much larger than what was obtained through time series generation.

# Publications

Received: 17 February 2023 | Revised: 2 August 2023 | Accepted: 16 August 2023
DOI: 10.1002/sat.1497

ORIGINAL PAPER

WILEY

# Assessment of adaptive optics-corrected optical links statistics from integrated turbulence parameters through a Gaussian process metamodel

**Emile Klotz**[1] | **Sidonie Lefebvre**[1] | **Nicolas Vedrenne**[1] | **Christian Musso**[1] | **Sylvain Poulenard**[2] | **Thierry Fusco**[1,3]

[1]DOTA, ONERA, Paris-Saclay University, Paris, France
[2]Airbus Defence and Space, Toulouse, France
[3]Laboratoire d'Astrophysique de Marseille, Aix Marseille Univ, CNRS, CNES, Marseille, France

**Correspondence**
Emile Klotz, DOTA, ONERA, Paris-Saclay University Fr-91120, France.
Email: emile.klotz@onera.fr

**Funding information**
This research was done in the framework of Emile Klotz's PhD thesis partially founded by Airbus Defence and Space.

**Summary**

With the development of free space optical links (FSO) for space-ground communications comes the need to mitigate the effects of the atmospheric turbulence to guarantee a lossless connection. By having a network of addressable ground stations, we want to guarantee to always target a point where the link is available. Assuming atmospheric transmission is managed thanks to site diversity, we focus only on the influence of atmospheric turbulence on the signal injected into a single mode fiber on the downlink. The use of adaptive optics (AO) is assumed to avoid turbulence-induced signal disruptions and enable a sufficiently high level of received signal for data transmission. Up to now, AO performance adequate assessment required the knowledge of high-resolution $C_n^2$ and wind profiles. With the advent of integrated atmospheric parameters measurement instruments, we investigate here the possibility to estimate AO-corrected performance from a limited number of integrated parameters. In this paper, we propose to use a Gaussian process metamodel to assess the statistics of the received optical power after an AO correction. Taking as input only four integrated parameters of the turbulence profile and associated wind profile, which can be measured with simple instruments, the estimation error on the value of the 1% quantile of the received optical power is inferior to 0.7dB. We also demonstrate the possibility to estimate the half correlation time of the received optical power using the same integrated parameters.

KEYWORDS
adaptive optics, FSO, machine learning

## 1 | INTRODUCTION

To match the growing need for data transmission between the ground and space that is driven by the development of space data highways[1] and upcoming mega communication constellations,[2] optical links become an increasingly credible alternative to radiofrequency links. Offering a favorable size, weight and power, and frequency allocation free and intrinsically secured very high data rate transmission, the implementation of optical communication between space and the ground is the subject of sustained developments. Many projects are ongoing to establish such a link between a GEO satellite and a fixed Earth ground station for missions such as Internet delivery and/or data repatriation from point to point on earth. However, the development of these atmospheric optical links remains conditioned by their availability, which is highly dependent on the atmospheric channel: absorption, scattering, and turbulence. Cloud masking issues can be managed thanks to site diversity,[3] and we focus here on atmospheric turbulence influence.

With the wish for very high bandwidth comes the necessity to inject the signal into a single mode optical fiber (SMF) to be amplified and/or to enable coherent detection. Deep fluctuations in the injected signal happen due to atmospheric turbulence that causes amplitude variations, that is, scintillation and wavefront distortions. A significant telescope aperture enables averaging of the scintillation effects as the size of the speckles becomes small in comparison with the receiving aperture. Phase-related fadings in the received signal can be reduced with the use of adaptive optics (AO) systems to correct the distorted wavefront and maximize the coupling efficiency in the SMF.[4,5] AO and pupil averaging, because of technological and cost limitation, does not perfectly correct for turbulent channel errors. To maximize the retrieved information, digital mitigation techniques can be used such as forward error correction on an interleaved signal[6] in addition to the physical mitigation technics. Forward error coding will operate efficiently if the error probability (hence fading probability) remains reasonable on the interleaved signal. The size of the interleaving window depends on temporal characteristics of the received optical power (ROP) such as the typical coherence time.[7] Those techniques will have a big impact on the bandwidth and on the latency of the whole system and thus must be adequately scaled according to the ROP. Knowing what would be the ROP distribution and ROP coherence time on any site and at any moment would give us precious information on how to adapt the system in real time. However, this statistic highly depends on turbulence conditions knowledge along the line of sight and on the AO system. Considering the significant variability of turbulence conditions with the location of ground stations, several initiatives have recently been taken to gather local measurements of the most relevant atmospheric parameters with respect to AO-corrected optical links. Some of these initiatives deploy high vertical spatial resolution measurements,[8] whereas others focus on integrated turbulence parameters.[9]

Knowledge of the turbulence and wind profiles at kilometer vertical resolution along the line of sight guarantees to precisely assess fading statistics,[10] hence an accurate optical link performance evaluation. High-resolution atmospheric turbulence characterization can be performed thanks to rather complex instrumentation such as Moon Limb Profiler by nighttime[11] or Sun Limb Profiler.[11] Such instruments are being deployed to demonstrate high-resolution turbulence characterization capacity on several sites over Europe.[12] They will provide high-resolution $C_n^2$ profile characterization along the line of sight between the ground and the direction of the target used, which might be different from the optical links direction, the impact of this difference of line of sight on the optical links availability being hardly documented. Initiatives to systematically document integrated turbulence parameters sometimes with really simple instrumentation are also emerging.[13] Considering the importance of integrated turbulence parameters in the assessment of AO-corrected error budgets, indications exist in favor of a link performance which would depend only on a few integrated parameters, but such a relation between corrected optical link performance and integrated turbulence parameters has never been clearly established so far. The exact expression of the correction residuals involves a complex combination of moments of the $C_n^2$ profile and wind, whose weightings depend on the number of corrected modes and the tractability of analytical expressions raises real challenges for a clear-cut demonstration that integrated parameters are sufficient to characterize optical link availability. Machine learning methods associated to physical performance models might provide crucial indications to answer this question.

It is the major prospect of this paper: investigating the possibility to assess AO-corrected optical link availability from integrated turbulence parameters by machine learning and to identify the compulsory parameters to be monitored, thanks to a sensitivity analysis.

Over the past 10 years, some studies have taken advantage of machine learning for atmospheric turbulence estimation or temporal prediction. Most focus on assessing $C_n^2$ near the land surface, such as Wang and Basu[14,15] which propose to use a multilayer perceptron (MLP) trained, respectively, on seven measured meteorological input variables: wind speed, temperature and temperature gradient, soil temperature, relative humidity, net radiation and sol water content, or only five input variables: wind speed, relative humidity, pressure, wind shear, and potential temperature gradient. In Su et al,[16] only four meteorological variables are used: temperature of the surface, temperature, wind speed, and relative humidity measured at 0.5 and 2 m. Prediction results are overall accurate but associated with a particular scenario. In addition to these MLP metamodels, Jellen et al[17] compared three other metamodels: polynomial regression, random forest, and boosted regression trees with six input variables: air temperature, air-water temperature difference, pressure, relative humidity, wind speed, and solar radiation. Best results were obtained with random forest, but the predictions were not always accurate. Some deep neural networks have also been used more recently: in Lamprecht et al,[18] a ResNet residual network is proposed to retrieve the refractive index structure parameter from the height above sea level and the corresponding wind speed, instead of relying on analytical formulae. The performances are promising, but it would require to collect training data from many different places on earth in order to deliver accurate results. A recent PhD work aimed at forecasting future daytime $C_n^2$ conditions from prior meteorological data: wind speed, pressure, temperature, relative humidity and solar irradiance, and $C_n^2$ measurements.[19] Neural networks (MLP and recurrent neural network) are used to create a low-altitude model capable of forecasting $C_n^2$ up to 4 h later using 16 h of prior measurements. The forecasting quality is not always sufficient, best in the middle of the day, moderate in the morning, and generally worst in the evening.

Finally, some recent approaches[20] use deep neural network to infer the atmospheric turbulence refractive index structure parameter $C_n^2$ from short exposure images of turbulence-induced laser beam intensity scintillations.

Other studies focus instead on integrated turbulence parameters temporal prediction. Among these, we can cite Milli etal.,[21] where turbulence nowcasting, that is, the ability to forecast the turbulence conditions over the next 2 h, is investigated at Paranal Observatory. MLP performed best among the three metamodels tested: random forest, MLP, and long short-term memory (LSTM) deep network trained on 1 or 2 h history of meteorological and integrated turbulence parameters such as seeing, coherence time, temperature, pressure, wind speed, and direction. In Giordano et al,[22] a random forest metamodel is trained to predict the seeing over the next 2 h on a large atmospheric database measured by the Calern Atmospheric Turbulence Station, including ground meteorological conditions, vertical profiles of the $C_n^2$, and integrated parameters characterizing the optical turbulence: seeing, isoplanatic angle, and coherence time.

As far as free space optical links (FSO) are concerned, machine and deep learning methodology mostly focus on compensating the effects of atmospheric turbulence on the performance of the whole single input single output (or SISO) and multiple input multiple output (or MIMO) FSO system[23] or on predicting parameters of the FSO channel,[24] such as optical signal-to-noise ratio. Closer to the methodology we propose in this paper, two publications aimed at predicting the RSSI (received signal strength indicator) of the FSO. In Tóth et al,[25] pressure, air temperature, particle concentration, visibility, relative humidity, and wind speed at different past time horizons are used as input variables for the metamodels. Best results were obtained with random forest and enabled to retrieve some atmosphere behavioral patterns influencing RSSI. Lionis et al[26] compared different metamodels: k-nearest neighbors, tree-based methods-decision trees, random forest, gradient boosting, and MLP trained on seven local atmospheric parameters: wind speed, pressure, temperature, humidity, dew point, solar flux, and air-sea temperature difference. Best determination coefficient $R_2$ is 0.949 and is obtained with the MLP metamodel.

Here, we focus on the injected power statistics assessment, and we consider input variables associated to the turbulence profile and to the wind profile in a perspective to identify a minimum of compulsory parameters. Using machine learning on a database of turbulence profiles over Tenerife and a physical AO modeling tool, we propose a metamodel to estimate the probability density function (PDF) of the injected power into the single mode fiber of the receiver of the optical ground station. We further develop this metamodel to be able to assess the autocorrelation function of the injected power. For our method to be suitable for a massive deployment of ground stations around the world, we wish to use exclusively data provided by simple and easily deployable instruments.

Section 2 describes our atmospheric channel model and the profiles database, Section 3 presents the methodology, including metamodel construction and sensitivity analysis, and Section 4 discusses the numerical results.

## 2 | ATMOSPHERIC CHANNEL MODELING

The metric of free space optical communication availability in the case of a coded channel is given by Shannon's noisy-channel coding theorem[27] that states that for successful decoding with arbitrarily small error probability, the capacity of a communication channel must be greater than the rate of the code used (the proportion in bits of the datastream that is useful, i.e., nonredundant). Unfortunately, due to slow-fading or other random factors, the channel capacity can fall below the code rate, hence compromising error-free decoding. In other words, the probability of interruption of the turbulent channel is $P_{outage}(R_0) = P(C(SNR) < R_0)$, where $C$ is the channel capacity defined by Shannon[27] as the maximal data rate that can be achieved with the given channel, $SNR$ is the electrical signal-to-noise ratio, and $R_0$ is the coding rate of the forward error correction code.

The capacity and, on a wider scale, the SNR are strongly dependent on the reception system. The challenge of accounting for all the intricate phenomena arising from different types of receiving chains is beyond the scope of this article. We present here a proof-of-concept study in a straightforward scenario, and we focus our attention on the received power into a SMF (the ROP) statistics. Looking at the ROP statistics will allow us to take into account the interleaving and the coding while avoiding strong hypothesis on the noise statistic, which allows a more exhaustive approach. In the very simplistic case of a noise that would be independent of the signal, we can show that there exists a bijection between the channel capacity fluctuations and the fluctuations of the ROP.[28]

In order to train our metamodel to estimate the ROP statistics, we first need access to a database of ROP and associated turbulence measurements. All those data are obtained thanks to simulations that we want to be as representative as possible of the most significant phenomena that affect AO performance in the limit of tractability of the model, in the prospect to build a methodology and identify the most adapted ML tools to extract relevant informations from the data. A necessary adaptation of the inputs used in the metamodel will be needed when switching to experimental data. In this section, we describe the AO correction modeling, the database, and the system hypotheses.

### 2.1 | Modeling of the ROP after AO correction

In this work, we study separately the impact of the scintillation on the ROP and the impact of the distorted phase. We call $\rho_\phi$ the coupling efficiency neglecting the impact of scintillation and $\rho_I$ the term of scintillation. Correlated time series of $\rho_\phi$ and $\rho_I$ are obtained by modeling the fluctuation of the coupled flux in a SMF with a pseudo-analytic AO modeling tool called SAOST (simplified adaptive optics simulation tool).[10,29,30] This model neglects the influence of noncommon path aberrations between the wavefront sensor and the injection path and assumes a perfect wavefront sensor (not sensitive to scintillation), a Zernike description of the correction phase, and an infinitely fast deformable mirror (the delay in the loop mostly comes from integration time of the wavefront sensor and calculation of the control voltages sent to the mirror). Comparison between SAOST and end-to-end models can be found in Canuet.[31] Experimental validation has been conducted in relevant condition for a GEO feeder link and can be found in Bonnefois et al.[32]

In case of moderate turbulence strength, terms of interaction between the scintillation, mostly caused by distant turbulence, and the phase effects, related to close to ground phenomena, can be neglected, and thus, SAOST works under the assumption of independence between $\rho_\phi$ and $\rho_I$. Let $f_{SMF}=\rho_\phi * \rho_I$ be the coupling efficiency in a SMF after propagation through atmosphere and AO correction. Analytical expressions of $f_{SMF}$ and its distribution under the hypothesis of independence are described in more details in Canuet et al.[10] Scintillation influence is simulated assuming the small perturbation approximation in the Rytov regime. In practice, this constrains the validity of the approach to limited Rytov variance (typically when the point source log-amplitude variance $\sigma^2_\chi < 0.3$) which corresponds to the experimental limit of validity of the small perturbation approximation for horizontal propagation as first identified in Gracheva and Gurvich.[33] This strong limitation in the case of horizontal propagation is, to our understanding, not restrictive when dealing with vertical propagation where $\sigma^2_\chi$ takes low values. In the database presented in the following part containing 37,059 profiles, less than 0.05% have a $\sigma^2_\chi \geq 0.3$.

We adopt in this paper the same approach as in SAOST, that is, to consider independently the effects due to the phase error and those due to the scintillation; the benefit of this dissociation is to be able to interpret our results more easily.

### 2.1.1 | Residual phase error model

The residual phase error is computed in SAOST using a Monte Carlo approach. Following the algorithm described in Roddier,[34] random occurrences of Zernike coefficients are sampled to describe the corrected phase. The temporal correlation of the ROP time series is obtained by filtering the raw Zernike coefficients by a temporal power spectral model[35] in the Fourier domain. Some hypothesis have to be made on the turbulence condition of which we can cite von Kármán statistics for the index of refraction fluctuations spectrum assuming a fixed outer scale. More details and comparisons with an end-to-end simulation can be found in Canuet.[31]

### 2.1.2 | Scintillation impact

The temporal impact of scintillation on the coupling efficiency can be approximated by the product[10]

$$\rho_I = \exp\left(-\sigma^2_\chi\right)\exp(2\chi_{AP}(t)) \tag{1}$$

in the weak fluctuation regime of the scintillation index $\chi(r,t)$ where $\sigma^2_\chi$ is the variance of the punctual log-amplitude and $\chi_{AP}(t)$ is the log-amplitude averaged on the receiver aperture.

Under weak irradiance fluctuation hypothesis, we have $\chi_{AP}(t)\sim\mathcal{N}\left(-\sigma^2_{\chi_{AP}},\sigma^2_{\chi_{AP}}\right)$. We can then write the normalized irradiance distribution, $\exp(2\chi_{AP}(t))$, as the following log-normal distribution[36,37]:

$$f_{\rho_I}(x)=\frac{1}{2x\sigma_{\chi_{AP}}\sqrt{2\pi}}\exp\left[-\frac{\left[\ln(x)+2\sigma^2_{\chi_{AP}}\right]^2}{2\left(2\sigma_{\chi_{AP}}\right)^2}\right], x>0 \tag{2}$$

## 2.2 | System hypothesis and training database

### 2.2.1 | AO and simulation parameters

In the following, all the generations of power attenuation's time series will be done with the same parameters of AO. We assume an AO system that corrects the first 10 radial orders with a frequency of 2kHz. The simulation is done with a time sampling of 4kHz for a duration of 10 s which gives us 40.000 points per time series. Our telescope is taken with a pupil of 60cm. These choices are being made as they assume a relatively simple and cost effective hardware for this type of application.

### 2.2.2 | Atmospheric conditions database

As we want to describe the ROP statistics using a set of integrated parameters from the $C_n^2$ and wind profile, the best approach is to build a large database of such profiles.

It should be noted that knowledge of the $C_n^2$ and wind profiles at kilometer vertical resolutions guarantees an accurate optical link performance evaluation using simulation tools such as end-to-end modeling of the atmospheric propagation and the correction by AO. Unfortunately, it is challenging to determine the profile of $C_n^2$ with altitude even with complex and expensive instruments such as SLODAR (slope detection and ranging), SCIDAR (scintillation detection and ranging) and SODAR (sonic detection and ranging).[38–40] In addition to this, these profiles present the risk to be affected by measurement noise (hence, influencing the metamodel). To our knowledge, there is no experimental database available that would be representative of the various atmospheric conditions, which leads us to use a database from an atmospheric reanalysis model. Indeed, data provided by numerical models present the advantage to precisely control underlying hypothesis and input parameters at the expense of a more questionable relevance. As the first goal of this work being to demonstrate the possibility to rely on a metamodel for performance assessment in relevant conditions, the possibility to cover a large scope of atmospheric conditions justifies in itself to exploit data obtained from a numerical model.

There exist models based on empirical measurements, some nonparametric such as Greenwood's,[41] H-V Night,[42] and AFGL AMOS[43] and some parametric such as the famous Hufnagel–Valley model,[44] its enhanced version the Hufnagel–Andrews–Phillips[45] model, or the Sadot–Kopeika[46] model. All those models are suitable to describe the average value of the turbulence over a given site and are useful for site selection, but they will not give an instantaneous and accurate turbulence profile description. Overall, these models have been developed for specific sites at given time of the year, and it is not clear to what extent they would be suitable to other sites or meteorological conditions.

As our work aims at characterizing the statistics of the instantaneous ROP and, especially, the distribution's tail to describe the probability of interruption, we need to work with a theoretical model that would describe any small variation in the turbulence induced by different meteorological conditions and would work for any location and any hour of the day.

Such a description is achieved using Gladstone's formula and Tatarskii's[36] theory with a model for the outer scale such as Dewan's[47] or HMNSP99.[48] In this approach, the $C_n^2$ profile is calculated from precise vertical profiles of meteorological parameters (temperature, pressure, relative humidity, wind speed, and wind direction).

Our database of profiles was provided by Durham University. Wind and $C_n^2$ profiles were obtained through a global turbulence model capable of converting meteorological data from a general circulation model, into three-dimensional optical turbulence maps. This model based on Tatarskii's is developed in Osborn and Sarazin[49] and was confronted successfully to on site measurements in Paranal. It was improved to include a separate boundary layer and enable stronger turbulence strength near the ground to be modeled.[50]

The general circulation model used is ERA5[51] from the European Centre for Medium range Weather Forecasts (ECMWF). This model, from which the turbulence is calculated, has a spatial resolution of $0.3^\circ$ along latitude and longitude and provides a forecast for every hour. We chose a grid of 11 by 11 points around Tenerife's island (with a spatial resolution of $\approx$ 30 km), which is a site of interest for a potential future ground station, and focused on the first 19 days of March 2018. It leaves us with 121 simultaneous measurements for each hour, with some missing values. On the overall 19 days considered, we thus have 37,059 profiles on 113 pressure levels each. Historical data are freely available on ECMWF website.

These 37,059 $C_n^2$ and wind profiles cover a large set of condition. In the following, we consider that these profiles are representative of field data and could be obtained with instruments directly measuring turbulence along the line of sight.

## 3 | MACHINE LEARNING METHODOLOGY

As described in Sections 2.1, we consider the residual phase error and the scintillation as two independent phenomenons and the quantity of interest, the coupled flux in a single mode fiber, as the product of both.

In Sections 2.1.2, we presented our scintillation simulation model, which is based on a parametric expression of the distribution that depends only on the two parameters $\sigma_\chi^2$ and $\sigma_{\chi_{AP}}^2$ (Equation (1)). However, the latter is not easily measurable, as it would require an instrument with the same pupil size as our telescope. Our first goal is therefore to be able to assess $\sigma_{\chi_{AP}}^2$ with machine learning using a small number of easily measurable parameters. Our second goal is to describe the PDF of $\rho_\phi$ with the minimum amount of variables and be able to determine those variables from the same small number of measurable parameters.

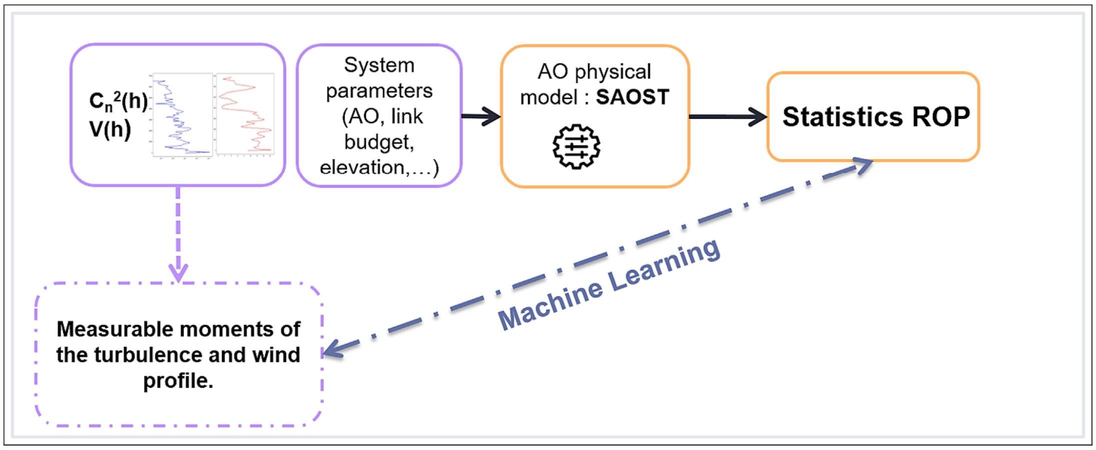

**FIGURE 1** Schematic description of the method proposed in this paper.

Figure 1 sums up the methodology; the upper boxes with full lines represent the current state of modeling the statistic of ROP. It requires the use of $C_n^2$ and wind profiles coupled with a physical model of light propagation through the atmosphere and wavefront correction with an AO loop. What we aimed at is represented by the dashed box and arrows as we want to shortcut the heavy process of profiles measurement and simulation thanks to machine learning on a small number of integrated parameters easily measurable.

### 3.1 | Residual phase error distribution description

A usual and effective way to predict a distribution using machine learning is to parameterize this distribution and then use a metamodel to predict each parameter.

Here, we were led to study

$$L_\phi(t) = 10\log_{10}(\rho_\phi(t)) \tag{3}$$

the loss in power induced by the phase fluctuation in dB as it gives a bigger weight to the low values of $\rho_\phi(t)$ that are the critical values for our application.

Studying the distribution of $\rho_\phi(t)$ on our 37 k profiles, we highlighted that it has an exponential decay, which is consistent with the closed form of the distribution already proposed by Canuet.[31] We can show that the logarithm of an exponential distribution is a Gumbel distribution, and we verified experimentally that the distribution that best fit the distribution of our loss $L_\phi(t)$, in perspective with the Bayesian information criterion and sum of square error, is a Gumbel distribution of the following form:

$$\frac{1}{\beta}e^{-(z+e^{-z})} \tag{4}$$

where $z = \frac{x-\mu}{\beta}$.

This result is particularly interesting as, with the Gumbel distribution being a good enough approximation of the density probability of power attenuation, we can describe the PDF with only two parameters, $\mu$ and $\beta$, that contain all the information on the statistic of power attenuation.

The quality of the fit can be seen by looking at the relative error measured between the quantiles of the experimental distribution and those of the theoretical distribution. We show in Table 1 the statistics of relative error made on some relevant quantiles. The statistics are given for the whole database. For example, the relative error on the 0.01 quantile is, in average, of 0.57% and is below 1.92% in 99% of the cases. Such small relative errors emphasize to which extent our fit is appropriate. It is to be noticed that, the number of data of our simulations being finite, the error on the smallest quantiles can be due to a lack of data to precisely estimate the latest, as much as a nonability of the Gumbel distribution to

**TABLE 1** Relative errors on quantiles with the Gumbel fit over the 37,059 power attenuation's series.

| | Quantile | | | | |
|---|---|---|---|---|---|
| **Relative error** | **0.001** | **0.003** | **0.01** | **0.03** | **0.1** |
| Mean | 1.43% | 0.91% | 0.57% | 0.37% | 0.19% |
| 1% | 0.02% | 0.01% | 0.01% | 0.01% | 0.01% |
| 50% | 1.17% | 0.75% | 0.48% | 0.33% | 0.17% |
| 99% | 5.36% | 3.28% | 1.92% | 1.14% | 0.54% |

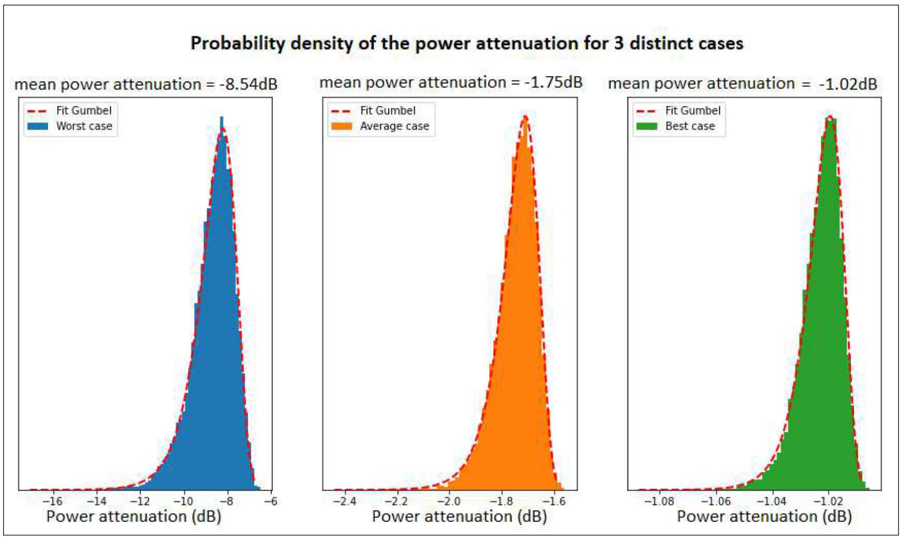

**FIGURE 2** Gumbel fit on the distribution of $L_\phi$ in three cases: First one in blue corresponds to the minimum of coupling efficiency, second one in orange is an average coupling efficiency, and the last one in green is obtained for the profile with the highest coupling efficiency.

describe precisely the smallest quantiles. Further work in this regard was not conducted as the quality of the approximation is good enough for our application.

Figure 2 aims at visually demonstrating the goodness of the fit in the diversity of conditions encountered. We selected three sets of $C_n^2$ and wind profiles from the whole database, one corresponding to the average value of mean power attenuation over the 37,059 profiles (orange), one to the worst value of mean power attenuation (blue), and the last one to the best value of mean power attenuation (green).

## 3.2 | Gaussian process (GP) metamodel

Different machine learning techniques have been tested of which we can cite gradient boosting, MLP, support vector machine regression, and GPs.[52] Best results were obtained for a GP, and we only describe this metamodel here.

A GP writes the output of interest as the sum of a regression part, a constant term in this study, and a centered stochastic process $Z$:

$$\gamma(\mathbf{x}) = \beta_0 + Z(\mathbf{x}) \tag{5}$$

The stochastic part $Z(\mathbf{x})$ is a Gaussian-centered process fully characterized by its covariance function $Cov(Z(\mathbf{x}), Z(\mathbf{u})) = \sigma^2 R(\mathbf{x}, \mathbf{u})$ with $\sigma^2$ the variance of $Z$ and $R$ the correlation function, or kernel, that accounts for spatial correlation effects.

In this study, we focus on a stationary process $Z$, which means that, for new points, the prediction consists of a linear combination of the observed values, with weights that depend on the distance between the new input point and the training data. The assumption is that the closer the inputs are, the more correlated the outputs are. The kernel we chose is a Matérn 5/2 kernel, an extension of the radial basis function kernel, one of the most commonly used forms of kernel. The Matérn kernel computes the similarity of two given points **x** and **x**′ in dimension $d$ as follows:

$$R(\mathbf{x}-\mathbf{x}') = 1+\sqrt{5}\sum_{j=1}^{d}\frac{\left(x_j-x_j'\right)}{\theta_j}+ \\ \frac{5}{3}\sum_{j=1}^{d}\frac{\left(x_j-x_j'\right)^2}{\theta_j^2}\exp\left(-\sqrt{5}\sum_{j=1}^{d}\frac{\left(x_j-x_j'\right)}{\theta_j}\right) \tag{6}$$

where the $\theta_j$ are the hyperparameters and should be optimized in addition to $\beta_0$.

One of the advantages of GPs is that an estimate of the uncertainty associated with the prediction is available.

In order to evaluate the predictive ability of the metamodel, we rely on the predictivity coefficient $Q_2$, which stands for the percentage of the output variance explained by the metamodel. It is the same as the determination coefficient $R_2$ but computed on $n$ test data $Y_i$ instead of training ones:

$$Q_2 = 1-\frac{\sum_{i=1}^{n}\left(Y_i-\widehat{Y}_i\right)^2}{\sum_{i=1}^{n}\left(Y_i-\overline{Y}\right)^2} \tag{7}$$

where $\overline{Y}$ is the mean of the test data and $\widehat{Y}_i$ stands for the output of the metamodel for the same input values as $Y_i$. $Q_2$ is between 0 and 1 and should be close to 1 for an accurate metamodel prediction.

## 3.3 | Choice of relevant inputs

We have based our choice of integrated parameters on the integrated parameters regularly used to describe the error budget of an AO. The first chosen parameter is Fried's parameter, an essential parameter when one is interested in the effects of turbulence. Fried's parameter $r_0$ is defined as the typical diameter of a telescope whose resolution would be limited by atmospheric turbulence. In the case of a plane wave, considering a Kolmogorov spectrum, we have along the line of sight:

$$r_0 = \left[0.42\left(\frac{2\pi}{\lambda}\right)^2\int_0^\infty C_n^2(z)dz\right]^{-\frac{3}{5}} \tag{8}$$

where $\lambda$ is the wavelength (1.55 μm). Experimentally, Fried's parameter can be estimated either from the amplitude jitter of a star at the focal plane of an imager or more robustly thanks to differential imaging such as performed with a DIMM.[53]

The second parameter, denoted $\overline{h}$,[54] is a measure of the height dispersion of atmospheric layers, homogeneous to an altitude:

$$\overline{h} = \left[\frac{\int_0^\infty z^{\frac{5}{3}}C_n^2(z)dz}{\int_0^\infty C_n^2(z)dz}\right]^{\frac{3}{5}} \tag{9}$$

It provides an assessment of the physical origin for the angular decorrelation of the phase perturbations (the influence of distant turbulence layers) while being independent from the turbulence strength. It is useful to characterize and compare different profiles. $\overline{h}$ is related to Fried's parameter and the isoplanatic path $\theta_0$ by[55]:

$$\theta_0 = 0.314\frac{r_0}{\overline{h}} \tag{10}$$

The estimation of $\overline{h}$ can therefore be performed thanks to a measurement of $\theta_0$, which is derived, for instance, from limited aperture averaged scintillation by nighttime[56] or thanks to a Shabar measurement by daytime.[57] The last parameter, denoted $\overline{v}$, describes an average wind speed over the turbulent layers[59] and similar to $\overline{h}$ is given as follows:

$$\overline{v} = \left[ \frac{\int_0^\infty v(z)^{\frac{5}{3}} C_n^2(z) dz}{\int_0^\infty C_n^2(z) dz} \right]^{\frac{3}{5}}, \tag{11}$$

where $v$ is the modulus of the transverse wind velocity. It is related to the turbulence coherence time $\tau$ according to the following:

$$\tau = 0.314 \frac{r_0}{\overline{v}} \tag{12}$$

The turbulence coherence time can be extracted, for instance, from the temporal analysis of the jitter of a bright enough point source image. This evaluation can then be exploited to provide an estimation of $\overline{v}$.

$r_0$, $\overline{h}$, and $\overline{v}$ are quantities that characterize the phase of the wave and $\sigma_\chi^2$ the intensity fluctuations. The link between phase and intensity perturbations involves diffraction, which is not accounted for in the calculation of the integrated parameters, hence the need to be able to measure $\sigma_\chi^2$

The Rytov approximation discussed in Section 2.1 assumes that the refractive index fluctuations are small compared with the mean refractive index, allowing for linearization of the wave propagation equation. This approximation is valid for weak turbulence, where the fluctuations are small and the wavefronts do not experience significant bending. Under this regime, $\sigma_\chi^2$ can be approximated in the following way:

$$\sigma_\chi^2 = 0.563 \left( \frac{2\pi}{\lambda} \right)^{\frac{7}{6}} \int_0^\infty z^{\frac{5}{6}} C_n^2(z) dz \tag{13}$$

According to,[33,58] $\sigma_\chi^2$ value is precise when it is less than 0.3, which is in accordance with the studied database.

Based on this considerations, the point source log-amplitude variance $\sigma_\chi^2$ is supposed to be measured from the scintillation of a bright point source with a small diameter instrument.

Thus, the PDF of the scintillation only depends on the unknown parameter $\sigma_{\chi_{AP}}^2$.

## 3.4 | Sensitivity analysis

In this study, we rely on Sobol's indices,[60] also known as variance-based sensitivity analysis. The variance of the output of interest $Y$ is decomposed into fractions, which can be attributed to each of the moments we use here as input variables for our metamodel. The values of Sobol's indices enable to rank input variables according to their importance in the uncertainty of the output. The first-order Sobol index $S_i$ characterizes the contribution of a given input $X_i$ to the output variance, and the total Sobol index $S_{T_i}$ measures the contribution to the output variance of the studied input $X_i$, including all variance caused by its interactions of any order with all other input variables. They are estimated thanks to a Monte Carlo method and can be written as follows:

$$S_i = \frac{Var(E[Y|X_i])}{Var(Y)} \tag{14}$$

and

$$S_{T_i} = 1 - \frac{Var(E[Y|X_{\sim i}])}{Var(Y)} \tag{15}$$

where $E$ stands for the esperance of the random variables and $X_{\sim i}$ all $X$ except $X_i$. First-order indices vary between 0 and 1, and the difference between 1 and their sum characterizes the global influence of interaction effects. If the total index associated to an input variable is close to zero, this input has a negligible impact on the output variability and can be set at a constant value. On the contrary, Sobol's indices close to one indicate that the input variable is influent.

Sobol' indices are very often used to determine the sensitivity of a simulation code to a specific input but works under the assumption of independence between input variables; their interpretation becomes hazardous in the case of correlated inputs. In our case, $r_0$, $\overline{h}$, and $\overline{v}$ are strongly correlated being all moments of the same profiles. To deal with correlated inputs, methods have been developed around Shapley values, which come from the field of cooperative games theory.[61,62] The associated Shapley indices are designed as a simple and easy way to interpret effects of the interactions and dependences contributions between the inputs involved on the total output variance.

# 4 | NUMERICAL RESULTS

## 4.1 | Probability density assessment

### 4.1.1 | Metamodel construction

Our database is split in two datasets: one training set containing 15% of the profiles randomly selected and a test set containing the remaining 85%. This arbitrary choice corresponds to 5558 randomly selected profiles. Less profiles would be enough to learn the few parameters of this GP as long as they cover the variability of the encountered cases.

The complexity of GP algorithms is $O(n^3)$ due to the need to invert an $n \times n$ matrix; a 15% training set is a good trade-off between prediction accuracy and learning time with 20 min of single core time on a modern processor for the training process.

The input vector of Equation (5) is $\mathbf{x} = (r_0, \overline{h}, \overline{v})$.

Figure 3 shows the estimated value against the one obtained with our metamodel. The coefficient of determination $Q^2$ is superior to 0.99 in every case and shows how observed outcomes are predicted by the model. We find 0.9994 for the prediction of $\mu$, 0.9992 for $\beta$ and 0.9969 for $\sigma_{\chi_{AP}}$.

As we are able to predict $\mu$, $\beta$, and $\sigma_{\chi_{AP}}$ from the moments, the next step is to reconstruct the probability density of the ROP using the parametric descriptions of $L_\phi(t)$ (Equation (3)) and $\rho_I$ (Equation (1)). An example is given in Figure 4 where, for one randomly selected profile, we can see, from left to right, the statistical reconstruction of $L_\phi(t)$, $\rho_I$, and the ROP.

In order to characterize the relevance of our estimation on the ROP's statistic, we can compute the absolute error made on the mean and standard deviation of the reconstructed PDF of the ROP. We also look at the absolute error on the 1% quantile of the ROP (see red dashed line in Figure 4) as we want a faithful reproduction of the tail of the distribution. Statistics on the absolute error associated to our 37 k profiles can be seen in Figure 5.

On all profiles, the prediction error on the value of the 1% quantile is inferior to 0.7 dB which is compatible with current assumptions done in commonly used link budgets (margins are typically 3dB).

Once again, we have to put into perspective this value with the fact that the temporal series of ROP generated with SAOST are finite, and thus, part of the error is due to the nonperfect convergence of the random variable. The weight of this error due to convergence in the overall error has yet to be determined.

### 4.1.2 | Sensitivity analysis

After finding satisfactory results with our metamodel, we want to describe the impact of each input variable on each output. To do so, we are using sensitivity indices: first and total order Sobol indices as well as Shapley indices, which were presented in Sections 3.4. Sensitivity indices were estimated using "Sensitivity: Global Sensitivity Analysis of Model Outputs",[63] an open source, GPL-2 licensed, R[64] library developed for the treatment of uncertainties.

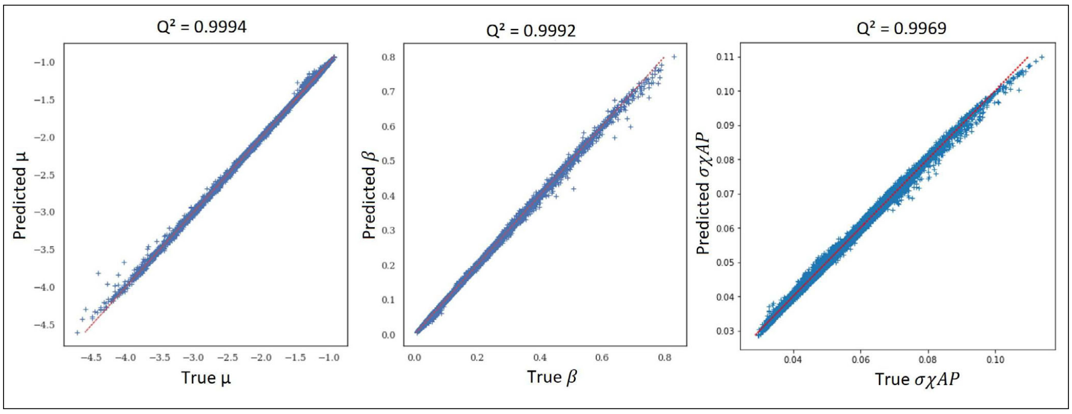

**FIGURE 3** Predicted values with a Gaussian process using $r_0$, $\overline{h}$, and $\overline{v}$ versus real values of $\mu$, $\beta$, and $\sigma_{\chi_{AP}}$ on the test data.

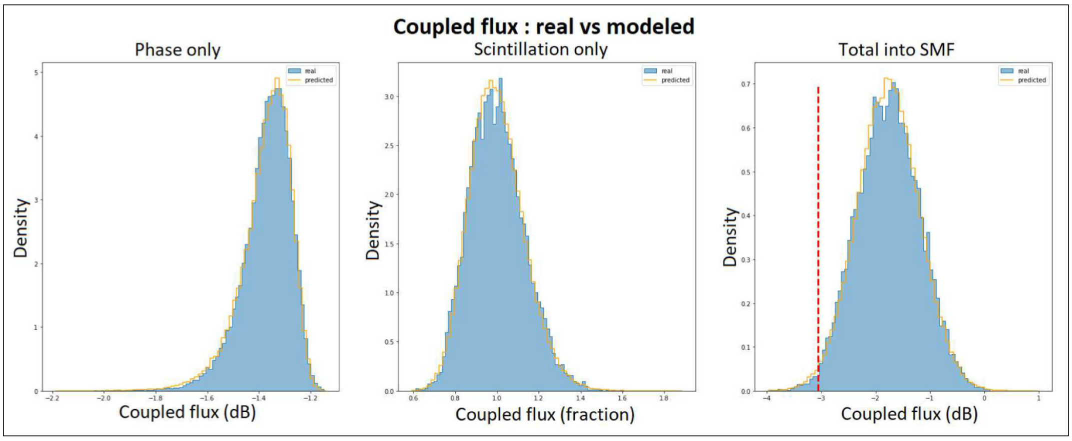

**FIGURE 4** Probability density function (PDF) computed from simplified adaptive optics simulation tool (SAOST) time series and PDF computed from our metamodel with, from left to right: $L_\phi(t)$, $\rho_I$, and the received optical power.

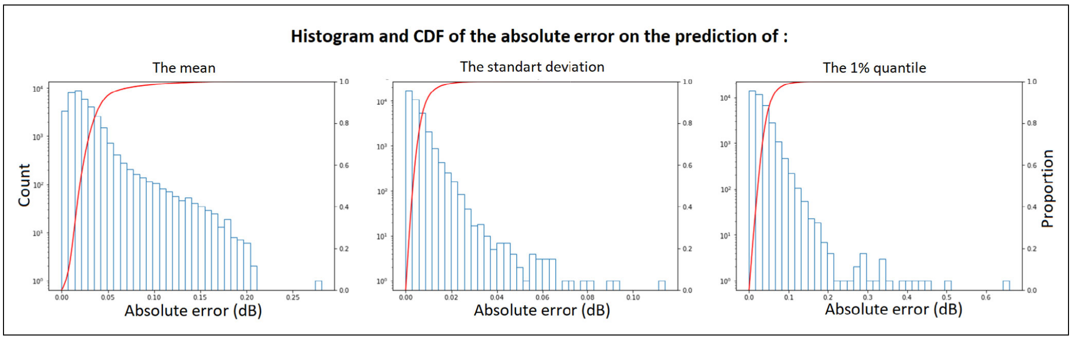

**FIGURE 5** Histogram and CDF of the absolute error on prediction of the mean, the standard deviation, and the 1% quantile.

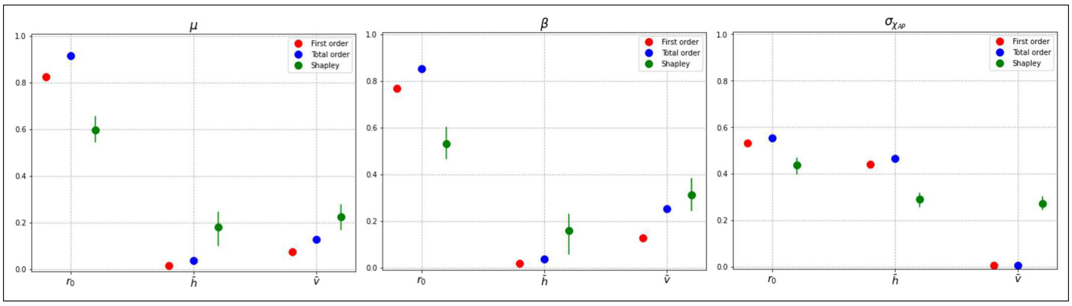

**FIGURE 6** Sensitivity analysis on $\mu$, $\beta$, and $\sigma_{chi}$. **Red:** first Sobol indices; **blue:** total Sobol indices; **green:** Shapley indices.

In Figure 6, we notice that the variability of $\bar{h}$ has little impact on $\mu$ and $\beta$. We thus can wonder if we would be able to predict the value taken by $\mu$ and $\beta$ with the same accuracy if we were to fix the value of $\bar{h}$. Doing so and using the same GP structure as the one described in Sections 3.2, we obtain a prediction score of 0.9988 for $\mu$ and 0.9984 for $\beta$. The slight decrease in $Q^2$ is due to a bigger error on the small values of $\mu$ and the large values of $\beta$, that is, the cases were the residual phase error after AO correction is the highest. Even if $\overline{h}$ is not essential to adequately describe the residual phase error, the additional information it provides on the structure of the profile allows better treatment of cases of strong turbulence where the correction by AO is the worse.

Same analysis can be conducted for the prediction of $\sigma_{\chi_{AP}}$ where, according to Figure 6, the impact of $\overline{v}$ seems very low: Its total Sobol index is almost equal to zero, and its Shapley index is larger but also accounts for its correlation with the two other input variables. Removing $\overline{v}$ from the input parameters of our metamodel leads us to a prediction score of 0.9955, very close to the 0.9969 obtained with $\overline{v}$. This result was to be expected as expressions of the variance of log-amplitude averaged on a pupil that can be found in the literature are independent of the wind speed profile.[65]

## 4.2 | Autocorrelation assessment

The next step of our study is to be able to estimate the autocorrelation time of the ROP using the same moments. Knowledge on the temporal behavior of the ROP is fundamental as the duration of the fading in the received signal will dictate the use of numerical mitigation techniques and the latency in the telecommunication protocol.

Once again, it should be noted that analytical expressions exist to describe the auto-covariance of $L_\phi$[10] and of $\rho_I$.[66,67] The ultimate goal is to estimate those autocovariance functions using a small number of instruments but, in order to simplify the problem, we first look at the half-correlation time of $L_\phi$ and $\rho_I$ time series independently. A simplistic way to predict the autocovariance could then be to fit an exponential decay law matching the estimated half correlation time.

### 4.2.1 | Metamodel construction

The approach is exactly the same as for the prediction of the PDF: Half-correlation times were computed using SAOST, and we use $r_0$, $\overline{h}$, and $\overline{v}$ as inputs of our metamodels. Once more, best results were obtained using GP regression with a Matérn 5/2 kernel.

Figure 7 shows that the prediction using $r_0$, $\overline{h}$, and $\overline{v}$ is able to recreate the trend but that it lacks precision with a high variance on the distribution of the error. The chosen input moments do not account well enough for the temporal aspect of the turbulence, and it is then necessary to consider an additional measurement.

One way to recover the missing temporal information on the atmospheric layer is through measurement of the power spectral density (PSD) of the scintillation on a small pupil instrument. To simulate the measurement of such an instrument, we used the expression given in Shen et al[67] and calculated the PSD of the scintillation for a 5cm pupil at a wavelength of 1500nm. Simulation was done on 100 points spaced evenly on a log scale from $1e^{-4}$Hz up to 1000Hz.

In order to add information associated to the scintillation spectrum in our model, we wish to reduce the data dimension while keeping the maximum of information. Indeed, there is a lot of information redundancy in the 100 points used to simulate the power spectrum density, but these points have to be decimated in a nonlinear way if we want to keep the relevant information no matter the profile.

Trials were done using the cutoff frequency, slope, and magnitude of the PSD, but these added input did not result in significant improvements of the prediction score. This is due the fact that it is sometimes hard to extract and define this parameters due to multiple regimes in the PSD of the scintillation.

To extract relevant features of the PSD without analyzing each case manually, we used a convolutional autoencoder, a kind of neural network extensively used for data reduction. The underlying concept is simple; the architecture consists of two parts, an encoder and a decoder.[68] The encoder learns an encoding of the data and is validated and refined by attempting to regenerate the inputs from the latent space with the decoder. In our case, the input data are of dimension 100 and the encoded data of dimension 5, as shown on Figure 8. A value of 5 was shown to be the minimal value that enables accurate reconstruction of the PSD whatever the profiles might be; increasing the dimension of the latent space above 5 did not result in significant reconstruction improvement. In Figure 9, we can see an example of reconstruction on two randomly picked PSDs from our database. The real PSD computed from Shen et al[67] is represented in blue, while the output of the decoder applied on the encoding of the PSD in the 5 dimension latent space is in orange. We can see that most of the information is conserved in the latent space.

We built a new GP; this time with eight inputs: the three previous moments and the five encoded values of the PSD.

As anticipated, with the added temporal information, we obtained much more satisfactory results than the one described in Figure 7 (see $Q^2$ in Figure 10: 0.99 and 0.98 against $Q^2$ in Figure 7: 0.88 and 0.84)

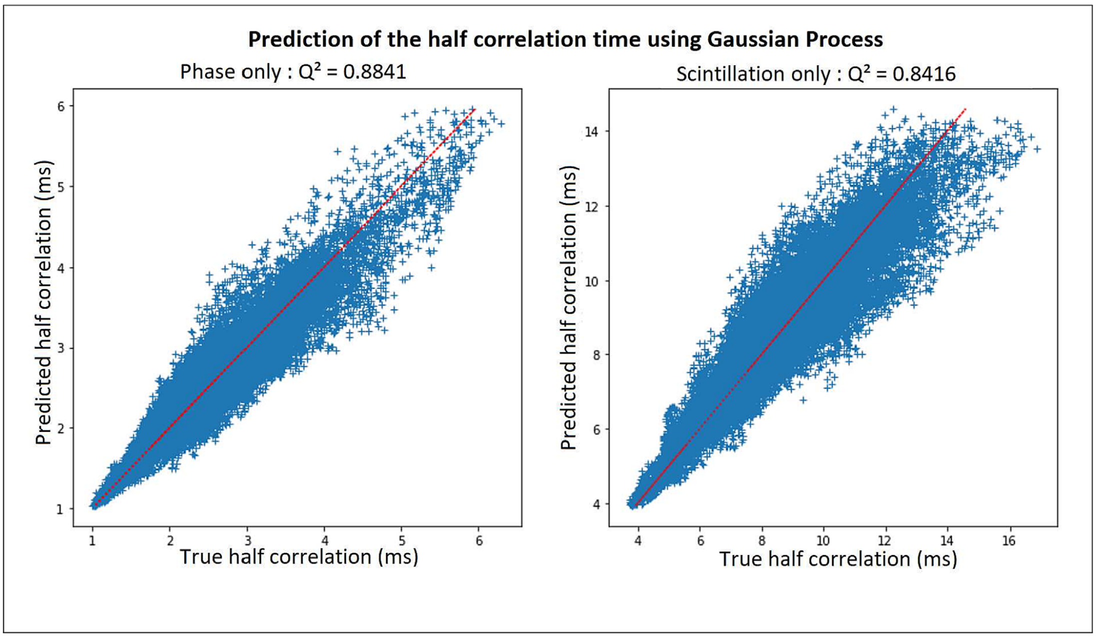

**FIGURE 7** Prediction of the half-correlation time using Gaussian process (GP) on inputs $r_0$, $\overline{h}$, and $\overline{v}$; $x$-axis shows the real value and $y$-axis the predicted one. **On the left** are the half-correlation neglecting scintillation effects and **on the right** are neglecting phase effects.

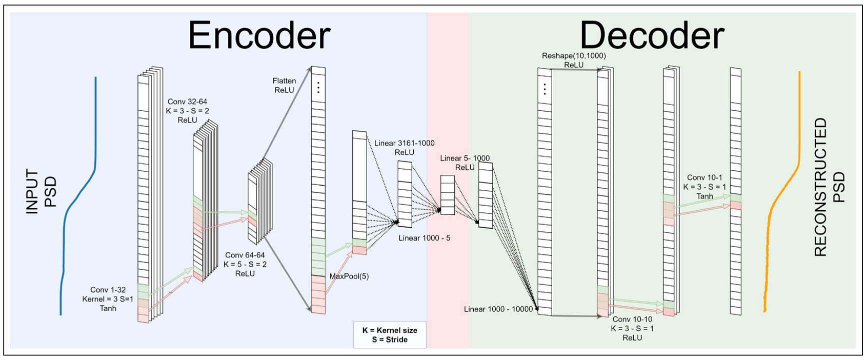

**FIGURE 8** Architecture of the autoencoder used to encode the power spectral density (PSD)

### 4.2.2 | Sensitivity analysis

Using the same tools as the ones described in Section 4.1.2, we conducted a sensitivity analysis and calculated first and total Sobol indices as well as Shapley indices for each of the models described in Section 4.2.1.

Results for the metamodel taking only $r_0$, $\overline{h}$, and $\overline{v}$ as inputs can be seen in Figure 11, while sensitivity analysis results computed on the model with the PSD added in the inputs are shown in Figure 12. In both cases, we can clearly see that the most influential variable is $\overline{v}$, which is not surprising given the fact that the correlation time depends on the displacement speed of the turbulent layer.

When the five moments of the PSD are added (D1 to D5 in Figure 12), we obtain some interesting values. It can be noted that while D1 and D5 have a lot of influence on the metamodel outputs, D2 seems to have very little. It would be interesting to look further into the

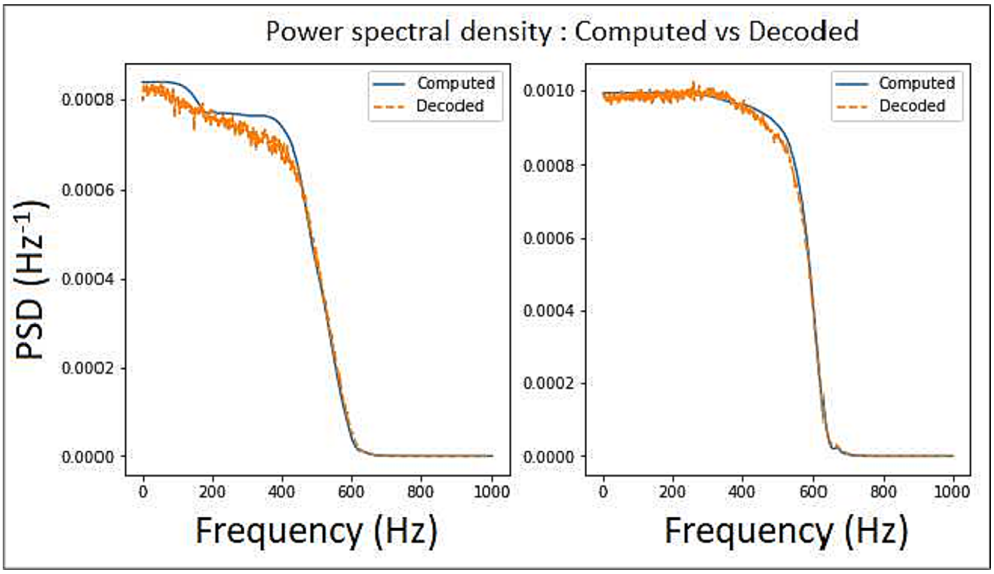

**FIGURE 9** Comparison of real and reconstructed power spectral density (PSD)

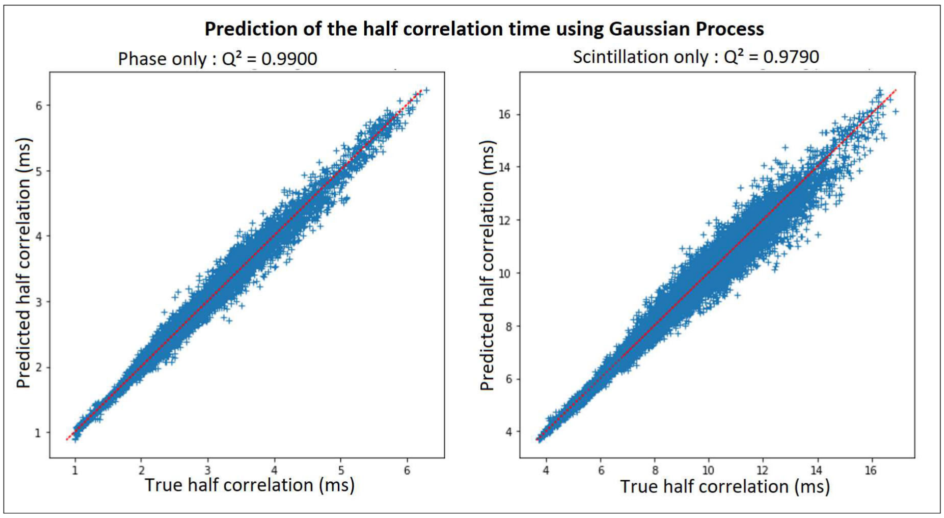

**FIGURE 10** Prediction of the half-correlation time using Gaussian process on inputs $r_0$, $\overline{h}$, and $\overline{v}$ and information on the power spectral density (PSD) of scintillation for a 5 cm pupil. Same other parameters as in Figure 7

weights of the autoencoder to better understand what features of the PSD does each of the encoded value represent most and thus what part of the PSD function is important in the description of the demicorrelation time of the ROP. This study is not trivial and will not be conducted in the context of this article.

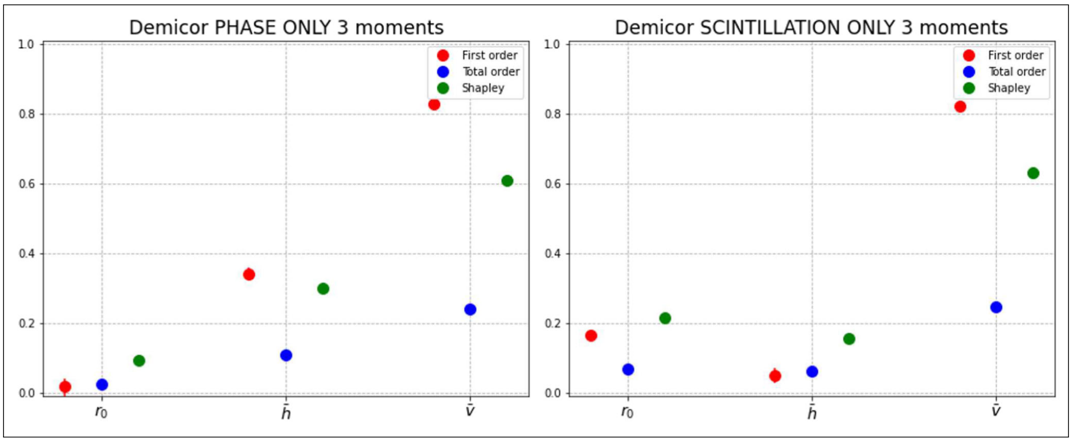

**FIGURE 11** Sensitivity analysis of the model described in Figure 7. **Red:** first Sobol indices; **blue:** total Sobol indices; **green:** Shapley indices.

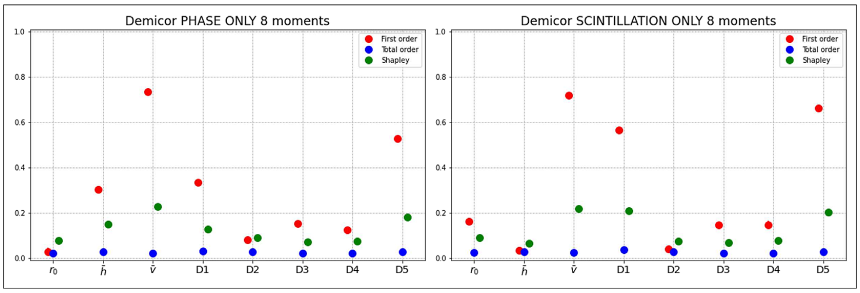

**FIGURE 12** Sensitivity analysis of the model described in Figure 10. **Red:** first Sobol indices; **blue:** total Sobol indices; **green:** Shapley indices.

## 5 | DISCUSSIONS

The results presented in this study rely on the representativeness of the numerical model describing the influence of the propagation channel, but this model has three main limitations: (1) it assumes that we are in a Rytov regime, (2) it assumes a decorrelation of phase and amplitude disturbances, and (3) it ignores the potential influence of uncorrected static aberrations, assumes a perfect wavefront sensor and a perfect deformable mirror, and neglects the noises affecting the detection chain.

The first hypothesis, regarding compatibility with the Rytov regime, has been verified with the data used in this study, but its validity at lower altitudes or under more severe turbulence conditions could be compromised. A study should be carried out to evaluate the difference between the performance evaluation provided by our metamodel and that obtained by an end-to-end model in cases of very severe turbulence, which would deepen our understanding of the limitations of the approach.

The second hypothesis, concerning the decorrelation of phase and amplitude perturbations, is widely accepted in the community, as it is justified by the fact that the phenomena causing these perturbations are generated at different distances from the receiver, and are therefore decorrelated. The simulations mentioned in the previous paragraph would also contribute to strengthen the understanding of the limitations implied by this assumption.

Concerning the third hypothesis, on the influence of the various assumptions made to simulate the ROP, these assumptions were intentionally made to ease the understanding of limitations raised by AO before the proposed methodology being applied on data obtained by a real system. In order to validate the methodology experimentally, a proper approach could be to select experimental data so that they respect the underlying hypothesis of the physical model used to build the methodology. The possibility to extend the approach to more complex cases (where the assumptions made are no longer valid) would still have to be investigated and would probably necessitate to increase the number of parameters in the metamodel.

## 6 | CONCLUSION

We studied here the possibility to assess downlink GEO to ground optical link ROP statistics by applying a machine learning methodology. We demonstrate that, assuming several simplification hypotheses on the AO system performance model, a set of a very small number of integrated turbulence parameters appears sufficient to precisely assess ROP statistics. Moreover, exploiting the temporal power spectrum of the scintillation recorded by a small diameter receiver eases the evaluation of the ROP correlation time. An experimental validation of such a methodology could be conducted on real data, first by restricting the cases of application to those where the assumptions made to build the metamodel are satisfied. Further investigations are being conducted to extend the method to the uplink case and to evaluate the impact, in terms of performance assessment, of a deviation of the instrument aiming angle to the link line of sight.

### ACKNOWLEDGMENTS

Atmospheric data were kindly provided by Durham University, whose model is commercially exploited by Miratlas.

### CONFLICT OF INTEREST STATEMENT

Nicolas Védrenne : Miratlas (I); other authors declare no conflicts of interest.

### REFERENCES

1. Hauschildt H, Elia C, Moeller HL, et al. HydRON: high thRoughput optical network. In: 2019 IEEE International Conference on Space Optical Systems and Applications (ICSOS); 2019:1-6. https://doi.org/10.1109/ICSOS45490.2019.8978985
2. Toyoshima M. Recent trends in space laser communications for small satellites and constellations. *J Light Technol*; 39(3):693-699. https://doi.org/10.1109/JLT.2020.3009505
3. Lacoste F, Guérin A, Laurens A, Azema G, Periard C, Grimal D. FSO ground network optimization and analysis considering the influence of clouds. In: Proceedings of the 5th European Conference on Antennas and Propagation (EUCAP); 2011:2746-2750.
4. Wright MW, Morris JF, Kovalik JM, Andrews KS, Abrahamson MJ, Biswas A. Adaptive optics correction into single mode fiber for a low earth orbiting space to ground optical communication link using the OPALS downlink. *Opt Express.* 2015;23(26):33705-33712. https://doi.org/10.1364/OE.23.033705
5. Fischer E, Berkefeld T, Feriencik M, et al. Development, integration and test of a transportable adaptive optical ground station. In: IEEE International Conference on Space Optical Systems and Applications (ICSOS); 2015:1-6. https://doi.org/10.1109/ICSOS.2015.7425071
6. Clark Jr GC, Cain JB. *Error-Correction Coding for Digital Communications*: Springer Science & Business Media; 2013.
7. Poulenard S, Gadat B, Barthe L, Garzón-Bohórquez R. Protection schemes for optical communication between optical ground station and a satellite. In: COAT-2019-workshop (Communications and Observations through Atmospheric Turbulence: characterization and mitigation) ONERA; 2019. https://doi.org/10.34693/COAT2019-S5-002
8. Chabé J, Aristidi E, Ziad A, et al. PML: a generalized monitor of atmospheric turbulence profile with high vertical resolution. *Appl Optics*. 2020;59(25):7574. https://doi.org/10.1364/AO.384504
9. Jabet F. C-DIMM: an autonomous, outdoor and fixed seeing monitor for astronomy, atmospheric studies and free space optical communications. In: Stein K, Gladysz S, eds. *Environmental Effects on Light Propagation and Adaptive Systems IV*. Online Only, Spain: SPIE; 2021:3. https://doi.org/10.1117/12.2599211
10. Canuet L, Védrenne N, Conan J-M, Petit C, Artaud G, Rissons A, Lacan J. Statistical properties of single-mode fiber coupling of satellite-to-ground laser links partially corrected by adaptive optics. *J Opt Soc Am A*. 2018;35(1):148-162. https://doi.org/10.1364/JOSAA.35.000148
11. Aristidi E, Ziad A, Fanteï-Caujolle Y, Chabé J, Giordano C, Renaud C, Lanteri H. Monitoring daytime and nighttime optical turbulence profiles with the PML instrument. https://doi.org/10.48550/ARXIV.2002.04947; 2020.
12. Ziad A, Giordano C, Aresta A, et al. ANAtOLIA: a new mobile site-testing station for astronomy and optical communications. In: Schreiber L, Schmidt D, Vernet E, eds. *Adaptive Optics Systems VIII*, Vol. 12185: SPIE; 2022:121855Z.
13. Miratlas. https://www.miratlas.com/products_services.html
14. Wang Y, Basu S. Estimation of optical turbulence in the atmospheric surface layer from routine meteorological observations an artificial neural network approach. In: Proceedings of SPIE, Vol. 9224; 2014. https://doi.org/10.1117/12.2063168
15. Wang Y, Basu S. Using an artificial neural network approach to estimate surface-layer optical turbulence at Mauna Loa, Hawaii. *Opt Lett*. 2016;41(10):2334-2337. https://doi.org/10.1364/OL.41.002334
16. Su C, Wu X, Luo T, Wu S, Qing C. Adaptive niche-genetic algorithm based on backpropagation neural network for atmospheric turbulence forecasting. *Appl Opt*. 2020;59(12):3699-3705. https://doi.org/10.1364/AO.388959
17. Jellen C, Oakley M, Nelson C, Burkhardt J, Brownell C. Machine-learning informed macro-meteorological models for the near-maritime environment. *Appl Opt*. 2021;60(11):2938-2951. https://doi.org/10.1364/AO.416680
18. Lamprecht C, Bekhrad P, Ivanov H, Leitgeb E. Modelling the refractive index structure parameter: A ResNet approach. In: 2020 International Conference on Broadband Communications for Next Generation Networks and Multimedia Applications (CoBCom); 2020:1-4. https://doi.org/10.1109/CoBCom49975.2020.9174186
19. Grose M. Forecasting atmospheric turbulence conditions from prior environmental parameters using artificial neural networks: an ensemble study. *Ph. D. Thesis*; 2021.
20. Vorontsov AM, Vorontsov MA, Filimonov GA, Polnau E. Atmospheric turbulence study with deep machine learning of intensity scintillation patterns. *Appl Sci*. 2020;10(22):8136. https://doi.org/10.3390/app10228136
21. Milli J, Gonzalez R, Fluxa PR, et al. Nowcasting the turbulence at the paranal observatory. https://doi.org/10.48550/ARXIV.1910.13767; 2019.

22. Giordano C, Rafalimanana A, Ziad A, Aristidi E, Chabé J, Fanteï-Caujolle Y, Renaud C. Statistical learning as a new approach for optical turbulence forecasting. In: SPIE Astronomical Telescopes + Instrumentation, Adaptive Optics Systems VII, Vol. 11448 SPIE; 2020:114484E. https://doi.org/10.1117/12.2562316
23. Amirabadi MA, Kahaei MH, Nezamalhosseni SA. Low complexity deep learning algorithms for compensating atmospheric turbulence in the free space optical communication system. *IET Optoelectron*. 2022;16(3):93-105. https://doi.org/10.1049/ote2.12060
24. Esmail MA, Saif WS, Ragheb AM, Alshebeili SA. Free space optic channel monitoring using machine learning. *Opt Express*. 2021;29(7):10967-10981. https://doi.org/10.1364/OE.416777
25. Tóth J, Ovseník L', Turán J, Michaeli L, Márton M. Classification prediction analysis of RSSI parameter in hard switching process for FSO/RF systems. *Measurement*. 2018;116:602-610. https://doi.org/10.1016/j.measurement.2017.11.044
26. Lionis A, Peppas K, Nistazakis HE, Tsigopoulos A, Cohn K, Zagouras A. Using machine learning algorithms for accurate received optical power prediction of an FSO link over a maritime environment. *Photonics*. 2021;8(6). https://doi.org/10.3390/photonics8060212
27. Shannon CE. A mathematical theory of communication. *Bell Syst Tech J*. 1948;27(3):379-423. https://doi.org/10.1002/j.1538-7305.1948.tb01338.x
28. Farid AA, Hranilovic S. Outage capacity optimization for free-space optical links with pointing errors. *J Lightwave Technol*. 2007;25(7):1702-1710. https://doi.org/10.1109/JLT.2007.899174
29. Conan J-M, Montmerle-Bonnefois A, Védrenne N, et al. Adaptive optics for GEO-feeder links: from performance analysis via reciprocity based models to experimental demonstration. In: COAT-2019 - workshop (Communications and Observations through Atmospheric Turbulence: characterization and mitigation) ONERA; 2019; Châtillon, France. https://doi.org/10.34693/COAT2019-S5-003
30. Vedrenne N, Conan J-M, Petit C, Michau V. Adaptive optics for high data rate satellite to ground laser link. In: Proc. SPIE 9739, Free-Space Laser Communication and Atmospheric Propagation XXVIII, 97390E 9739; 2016. https://doi.org/10.1117/12.2218213
31. Canuet L. Reliability of satellite-to-ground optical communication. *Ph.D. Thesis*; 2018.
32. Bonnefois AM, Velluet M-T, Cissé M, et al. Feasibility demonstration of AO pre-compensation for GEO feeder links in a relevant environment. *Opt Express*. 2022;30(26):47179-47198. https://doi.org/10.1364/OE.470705
33. Gracheva ME, Gurvich AS. Strong fluctuations in the intensity of light propagated through the atmosphere close to the earth. *Sov Radiophysics*. 1965; 8(4):511-515.
34. Roddier NA. Atmospheric wavefront simulation using Zernike polynomials. *Opt Eng*. 1990;29(10):1174-1180. https://doi.org/10.1117/12.55712
35. Conan J-M, Rousset G, Madec P-Y. Wave-front temporal spectra in high-resolution imaging through turbulence. *JOSA*. 1995;12(7):1559-1570. https://doi.org/10.1364/JOSAA.12.001559
36. Tatarskii VI. The effects of the turbulent atmosphere on wave propagation; 1971.
37. Vetelino FS, Young C, Andrews L, Recolons J. Aperture averaging effects on the probability density of irradiance fluctuations in moderate-to-strong turbulence. *Appl Opt*. 2007;46(11):2099-2108. https://doi.org/10.1364/AO.46.002099
38. Wilson RW. SLODAR: measuring optical turbulence altitude with a Shack–Hartmann wavefront sensor. *Mon Not R Astron Soc*. 2002;337(1):103-108. https://doi.org/10.1046/j.1365-8711.2002.05847.x
39. Osborn J, Wilson RW, Sarazin M, et al. Optical turbulence profiling with Stereo-SCIDAR for VLT and ELT. *Mon Not R Astron Soc*. 2018;478(1):825-834. https://doi.org/10.1093/mnras/sty1070
40. Miller JE, Eaton FD, Stokes SS. Correlation of weather parameters with sodar-derived Cn2 profiles. In: Thompson WE, Merritt PH, eds. *Laser Weapons Technology II*, Vol. 4376: SPIE; 2001:116-123.
41. Greenwood DP. Bandwidth specification for adaptive optics systems* *J Opt Soc Am*. 1977;67(3):390. https://doi.org/10.1364/JOSA.67.000390
42. Good RE, Beland RR, Murphy EA, Brown JH, Dewan EM. Atmospheric models of optical turbulence. In: Modeling of the Atmosphere; 1988; Orlando, FL, United States:165. https://doi.org/10.1117/12.975626
43. Parenti RR, Sasiela RJ. Laser-guide-star systems for astronomical applications. *J Opt Soc Am*. 1994;11(1):288. https://doi.org/10.1364/JOSAA.11.000288
44. Hufnagel RE. Propagation through atmospheric turbulence. *The Infrared Handbook*: USGPO; 1974.
45. Andrews LC, Phillips RL, Wayne D, Leclerc T, Sauer P, Crabbs R, Kiriazes J. Near-ground vertical profile of refractive-index fluctuations. In: Wasiczko Thomas LM, Gilbreath GC, eds. *In Atmospheric Propagation*. Orlando, Florida, USA; 2009:732402. https://doi.org/10.1117/12.820369
46. Sadot D, Kopeika NS. Forecasting optical turbulence strength on the basis of macroscale meteorology and aerosols: models and validation. *Opt Eng*. 1992;31(2):200-212.
47. Dewan EM, Good RE, Beland RR, Brown JH. A model for CSUBN(2) (optical turbulence) profiles using radiosonde data; 1993.
48. Ruggiero FH, DeBenedictis DA. Forecasting optical turbulence from mesoscale numerical weather prediction models. In: DoD High Performance Modernization Program Users Group Conference; 2002:10-14.
49. Osborn J, Sarazin M. Atmospheric turbulence forecasting with a general circulation model for Cerro Paranal. *Mon Not R Astron Soc*. 2018;480(1):1278-1299. https://doi.org/10.1093/mnras/sty1898
50. Osborn J, Communal J-E, Jabet F. Global atmospheric turbulence forecasting for free-space optical communications; 2023.
51. Copernicus Climate Change Service. ERA5-Land hourly data from 2001 to present. Type: dataset. https://doi.org/10.24381/CDS.E2161BAC; 2019.
52. Rasmussen CE, Williams CKI. *Gaussian Processes for Machine Learning*: MIT press Cambridge, MA; 2005.
53. Tokovinin A. From differential image motion to seeing. In: Publications of the Astronomical Society of the Pacific, Vol. 114; 2002:1156-1166. https://doi.org/10.1086/342683
54. Roddier F. V the effects of atmospheric turbulence in optical astronomy. *Progress in Optics*: Elsevier; 1981:281-376.
55. Fried DL. Anisoplanatism in adaptive optics. *J Opt Soc Am*. 1982;72(1):52-61. https://doi.org/10.1364/JOSA.72.000052
56. Loos GC, Hogge CB. Turbulence of the upper atmosphere and isoplanatism. *Appl Opt*. 1979;18(15):2654-2661. https://doi.org/10.1364/AO.18.002654
57. Beckers JM. A seeing monitor for solar and other extended object observations. *Exp Astron*. 2001;12(1):1-20.
58. Roddier F, Gilli JM, Lund G. On the origin of speckle boiling and its effects in stellar speckle interferometry. *J Opt*. 1982;13(5):263-271. https://doi.org/10.1088/0150-536x/13/5/002
59. Fante RL, Electromagnetic beam propagation in turbulent media. *Proc IEEE*. 1975;63(12):1669-1692. https://doi.org/10.1109/PROC.1975.10035

60. Sobol IM. Global sensitivity indices for nonlinear mathematical models and their monte carlo estimates. *Math Comput Simul*. 2001;55(1):271-280. The Second IMACS Seminar on Monte Carlo Methods. https://doi.org/10.1016/S0378-4754(00)00270-6
61. Song E, Nelson BL, Staum J. Shapley effects for global sensitivity analysis: theory and computation. *SIAM/ASA J Uncertain Quantif*. 2016;4(1):1060-1083. https://doi.org/10.1137/15M1048070
62. Iooss B, Prieur C. Shapley effects for sensitivity analysis with correlated inputs: comparisons with Sobol' indices, numerical estimation and applications. *Int J Uncertain Quantif*. 2019;9(5):493-514. https://doi.org/10.1615/Int.J.UncertaintyQuantification.2019028372
63. Iooss B, Veiga SD, Janon A, et al. sensitivity: global sensitivity analysis of model outputs. https://CRAN.R-project.org/package=sensitivity; 2021.
64. R Core Team. R: a language and environment for statistical computing. In: R Foundation for Statistical Computing; 2022; Vienna, Austria. https://www.R-project.org/
65. Ziad A, Conan R, Tokovinin A, Martin F, Borgnino J. From the grating scale monitor to the generalized seeing monitor. *Appl Opt*. 2000;39(30):5415-5425. https://doi.org/10.1364/AO.39.005415
66. Robert C, Conan J-M, Michau V, Renard J-B, Robert C, Dalaudier F. Retrieving parameters of the anisotropic refractive index fluctuations spectrum in the stratosphere from balloon-borne observations of stellar scintillation. *J Opt Soc Am A*. 2008;25(2):379-393. https://doi.org/10.1364/JOSAA.25.000379
67. Shen H, Yu L, Fan C. Temporal spectrum of atmospheric scintillation and the effects of aperture averaging and time averaging. *Opt Commun*. 2014;330:160-164. https://doi.org/10.1016/j.optcom.2014.05.039
68. Hinton GE, Salakhutdinov RR. Reducing the dimensionality of data with neural networks. *Science*. 2006;313(5786):504-507. https://doi.org/10.1126/science.1127647

## AUTHOR BIOGRAPHIES

**Emile Klotz** is a last year PhD student in the Optics Department at ONERA (The French Aerospace Lab). He graduated with a Master's degree at *Institut d'Optique Théorique et Appliquée*. His main research interests are optics applied to space telecommunications and the integration of machine learning techniques into physical modelling.

**Sidonie Lefebvre** received her Ph.D. degree from Ecole Centrale Paris in 2006. She is currently working as a Research Scientist in statistics at ONERA Palaiseau (France), in the Optics and Associated Techniques Department. Her research interests are centered on the design and modeling of computer experiments, uncertainty quantification and sensitivity analysis, and target detection.

**Nicolas Vedrenne** joined ONERA in 2004. He defended his Phd on optical propagation and correction through strong turbulence in 2008. He developed and applied his skills on adaptive optics for different fields of applications for more than 15 years in the High Angular Resolution team: initiator of the SCO-SLIDAR method, a Cn2 profil measurement method from Shack-Hartmann data, he led several on site demonstrations of AO systems for optical links, and he was the project leader for FEEDELIO (field demonstration of precompensation by AO for ESA). N. Védrenne is since 2018 the Principal Investigator of FEELINGS, ONERA's ground station demonstrator for optical links and the head of the High Angular Resolution unit of ONERA.

**Christian Musso** received a PHD in Applied Mathematics in 1993 and a habilitation to supervise research in 2017 (Habilitation à Diriger des Recherches). He was hired by the French naval direction in 1986 where he supervises optimal maneuvers algorithms in Target Motion Analysis. Since 1991, he works at ONERA, The French Aerospace Lab. He is interested in signal processing applied to radar and infrared images. His research focuses on nonlinear filtering and optimization using Monte Carlo methods.

**Sylvain Poulenard** obtained his PhD in 2015 entitled "Laser link, an alternative to radio-frequency feeder link for high throughput satellite?". He works for Airbus Defence and Space since then and is now the system engineer responsible for the TELEO Demonstrator, an experimental optical communications payload designed to facilitate very high capacity optical feeder link communications to GEO satellite.

**Thierry Fusco** is a senior research director at ONERA and the science deputy director of the Optics Department. He has 25 years of expertise in adaptive optics and post-processing for astronomy. After his PhD in 2000 on the mitigation of partial correction and anisoplanatism in AO, he was the VLT-SPHERE AO scientist (extreme AO system for direct detection and characterization of extrasolar planet) from 2004 to 2015, and he is now the AO scientist of HARMONI (which gathers both a classical and laser tomographic AO system) the first light integral field spectrograph instrument for the European ELT. Thiery Fusco received the Fabry de Gramont award from the French Otpical Society in 2009, the Scientific Excellence Award from the French Aeronautics and Astronautics Association in 2020, and the "Grand Prix Charles Defforey" from the French Science Academy in 2020. He published more than 200 papers in scientific journals, and he has an H-index larger than 50.

**How to cite this article:** Klotz E, Lefebvre S, Vedrenne N, Musso C, Poulenard S, Fusco T. Assessment of adaptive optics-corrected optical links statistics from integrated turbulence parameters through a Gaussian process metamodel. *Int J Satell Commun Network*. 2023;1-19. doi:10.1002/sat.1497

# Bibliography

[AA12] A. Alkholidi and K. Altowij. “Effect of Clear Atmospheric Turbulence on Quality of Free Space Optical Communications in Western Asia”. In: *Optical Communications Systems*. Ed. by N. Das. Section: 2. Rijeka: IntechOpen, 2012. DOI: 10.5772/35186. URL: https://doi.org/10.5772/35186.

[AKN22] M. A. Amirabadi, M. H. Kahaei, and S. A. Nezamalhosseni. “Low complexity deep learning algorithms for compensating atmospheric turbulence in the free space optical communication system”. In: *IET Optoelectronics* 16.3 (2022), pp. 93–105. DOI: https://doi.org/10.1049/ote2.12060.

[AM88] J. W. Abdul-Sada and M. K. Mahmood. “Generation of gaussian pseudorandom process with specific correlation properties”. en. In: *International Journal of Systems Science* 19.11 (Jan. 1988), pp. 2163–2168. ISSN: 0020-7721, 1464-5319. DOI: 10.1080/00207728808964109. URL: http://www.tandfonline.com/doi/abs/10.1080/00207728808964109 (visited on 06/12/2023).

[And+12a] L. C. Andrews et al. “Creating a Cn2 profile as a function of altitude using scintillation measurements along a slant path”. In: *High Energy/Average Power Lasers and Intense Beam Applications VI; Atmospheric and Oceanic Propagation of Electromagnetic Waves VI*. Vol. 8238. International Society for Optics and Photonics, 2012, 82380F.

[And+12b] L. Andrews et al. *Channel characterization for free-space optical communications*. Tech. rep. FLORIDA SPACE INST CAPE CANAVERAL FL, 2012.

[And77] O. Anderson. “The Box-Jenkins approach to time series analysis”. In: *RAIRO-Operations Research* 11.1 (1977). Publisher: EDP Sciences, pp. 3–29.

[Ara+96] K. Araki et al. “Performance evaluation of laser communication equipment onboard the ETS-VI satellite”. In: *Proceedings of SPIE, Free-Space Laser Communication Technologies VIII*. San Jose, 1996.

[Ari+20] E. Aristidi et al. *Monitoring daytime and nighttime optical turbulence profiles with the PML instrument*. 2020. DOI: 10.48550/ARXIV.2002.04947.

[Art+19] G. Artaud et al. “Impact of molecular absorption on the design of free space optical communications”. In: *International Conference on Space Optics — ICSO 2018*. Ed. by N. Karafolas, Z. Sodnik, and B. Cugny. Chania, Greece: SPIE, July 2019, p. 50. ISBN: 978-1-5106-3077-2 978-1-5106-3078-9. DOI: 10.1117/12.2535970. URL: https://www.spiedigitallibrary.org/conference-proceedings-of-spie/11180/2535970/Impact-of-molecular-absorption-on-the-design-of-free-space/10.1117/12.2535970.full (visited on 09/15/2023).

[Bab53] H. W. Babcock. “THE POSSIBILITY OF COMPENSATING ASTRONOMICAL SEEING”. In: *Publications of the Astronomical Society of the Pacific* 65.386 (Oct. 1953). Publisher: The Astronomical Society of the Pacific, p. 229. DOI: 10.1086/126606.

[Bar20] S. Barnhart. “Design and Development of a Coherent Detection Rayleigh Doppler Lidar System for Use as an Alternative Velocimetry Technique in Wind Tunnels”. en. In: (2020). Publisher: Unpublished. DOI: 10.13140/RG.2.2.32670.15688. URL: http://rgdoi.net/10.13140/RG.2.2.32670.15688 (visited on 08/29/2023).

[Bar93] A. Barron. “Universal approximation bounds for superpositions of a sigmoidal function”. In: *IEEE Transactions on Information Theory* 39.3 (May 1993), pp. 930–945. ISSN: 0018-9448, 1557-9654. DOI: 10.1109/18.256500. URL: https://ieeexplore.ieee.org/document/256500/ (visited on 09/07/2023).

[Bas+20] S. Basu et al. “Mesoscale modelling of optical turbulence in the atmosphere: the need for ultrahigh vertical grid resolution”. en. In: *Monthly Notices of the Royal Astronomical Society* 497.2 (Sept. 2020), pp. 2302–2308. ISSN: 0035-8711, 1365-2966. DOI: 10.1093/mnras/staa2010. URL: https://academic.oup.com/mnras/article/497/2/2302/5870696 (visited on 02/08/2021).

[Bas15] S. Basu. “A simple approach for estimating the refractive index structure parameter (Cn2) profile in the atmosphere”. en. In: *Optics Letters* 40.17 (Sept. 2015), p. 4130. ISSN: 0146-9592, 1539-4794. DOI: 10.1364/OL.40.004130. URL: https://opg.optica.org/abstract.cfm?URI=ol-40-17-4130 (visited on 09/06/2023).

[BC15] C. Bailly and G. Comte-Bellot. “Direct and Large Eddy Simulation of Turbulent Flows”. In: *Turbulence*. Cham: Springer International Publishing, 2015, pp. 211–244. ISBN: 978-3-319-16160-0. DOI: 10.1007/978-3-319-16160-0_8. URL: https://doi.org/10.1007/978-3-319-16160-0_8.

[Bec01] J. M. Beckers. “A Seeing Monitor for Solar and Other Extended Object Observations”. In: *Experimental Astronomy* 12.1 (Jan. 2001), pp. 1–20.

[Bee52] Beer. “Bestimmung der Absorption des rothen Lichts in farbigen Flüssigkeiten”. de. In: *Annalen der Physik und Chemie* 162.5 (1852), pp. 78–88. ISSN: 00033804, 15213889. DOI: 10.1002/andp.18521620505. URL: https://onlinelibrary.wiley.com/doi/10.1002/andp.18521620505 (visited on 09/04/2023).

[Bel80] A. G. Bell. “On the Production and Reproduction of Speech by Light”. In: *American Journal of Science* 20.118 (Oct. 1880), pp. 305–324.

[Ber+23] P. Berceau et al. “Space optical instrument for GEO-Ground laser communications”. In: *International Conference on Space Optics — ICSO 2022*. Ed. by K. Minoglou, N. Karafolas, and B. Cugny. Dubrovnik, Croatia: SPIE, July 2023, p. 110. ISBN: 978-1-5106-6803-4 978-1-5106-6804-1. DOI: 10.1117/12.2690326. URL: https://www.spiedigitallibrary.org/conference-proceedings-of-spie/12777/2690326/Space-optical-instrument-for-GEO-Ground-laser-communications/10.1117/12.2690326.full (visited on 07/19/2023).

[BM19] P. Bauweraerts and J. Meyers. “On the Feasibility of Using Large-Eddy Simulations for Real-Time Turbulent-Flow Forecasting in the Atmospheric Boundary Layer”. en. In: *Boundary-Layer Meteorology* 171.2 (May 2019), pp. 213–235. ISSN: 0006-8314, 1573-1472. DOI: 10.1007/s10546-019-00428-5. URL: http://link.springer.com/10.1007/s10546-019-00428-5 (visited on 03/14/2023).

[Bon+22] A. M. Bonnefois et al. “Feasibility demonstration of AO pre-compensation for GEO feeder links in a relevant environment”. In: *Opt. Express* 30.26 (Dec. 2022). Publisher: Optica Publishing Group, pp. 47179–47198. DOI: 10.1364/OE.470705. URL: https://opg.optica.org/oe/abstract.cfm?URI=oe-30-26-47179.

[Boo17] C. G. Book. “Real-time weather and atmospheric characterization data”. In: *Informational Report, CCSDS* (2017).

[Bor+09] D. M. Boroson et al. “The Lunar Laser Communications Demonstration (LLCD)”. In: *2009 Third IEEE International Conference on Space Mission Challenges for Information Technology*. Pasadena, CA, USA: IEEE, July 2009, pp. 23–28. ISBN: 978-0-7695-3637-8. DOI: 10.1109/SMC-IT.2009.57. URL: http://ieeexplore.ieee.org/document/5226852/ (visited on 08/28/2023).

[Buh03] M. D. Buhmann. *Radial Basis Functions: Theory and Implementations*. 1st ed. Cambridge University Press, July 2003. ISBN: 978-0-521-63338-3 978-0-521-10133-2 978-0-511-54324-1. DOI: 10.1017/CBO9780511543241.

[Can+18] L. Canuet et al. “Statistical properties of single-mode fiber coupling of satellite-to-ground laser links partially corrected by adaptive optics”. In: *J. Opt. Soc. Am. A* 35.1 (Jan. 2018). Publisher: OSA, pp. 148–162. DOI: 10.1364/JOSAA.35.000148.

[Can18a] L. Canuet. “Fiabilisation des transmissions optiques satellite-sol”. PhD Thesis. 2018. URL: http://www.theses.fr/2018ESAE0005/document.

[Can18b] L. Canuet. “Reliability of satellite-to-ground optical communication”. PhD Thesis. 2018.

[Caz+17] V. Cazaubiel et al. “LOLA: a 40.000 km optical link between an aircraft and a geostationary satellite”. In: *International Conference on Space Optics — ICSO 2006*. Ed. by E. Armandillo, J. Costeraste, and N. Karafolas. Noordwijk, Netherlands: SPIE, Nov. 2017, p. 129. ISBN: 978-1-5106-1623-3 978-1-5106-1624-0. DOI: 10.1117/12.2308161. URL: https://www.spiedigitallibrary.org/conference-proceedings-of-spie/10567/2308161/LOLA--a-40000-km-optical-link-between-an-aircraft/10.1117/12.2308161.full (visited on 09/15/2023).

[Cha+20] J. Chabé et al. “PML: a generalized monitor of atmospheric turbulence profile with high vertical resolution”. en. In: *Applied Optics* 59.25 (Sept. 2020), p. 7574. ISSN: 1559-128X, 2155-3165. DOI: 10.1364/AO.384504.

[Cha+22] C. Challu et al. “N-HiTS: Neural Hierarchical Interpolation for Time Series Forecasting”. In: (2022). Publisher: arXiv Version Number: 6. DOI: 10.48550/ARXIV.2201.12886. URL: https://arxiv.org/abs/2201.12886 (visited on 08/07/2023).

[Cho03] H. Choi. “Translation method: a historical review and its application to simulation of non-Gaussian stationary processes”. In: *Wind and Structures* 6.5 (Oct. 2003), pp. 357–386. DOI: 10.12989/WAS.2003.6.5.357. URL: https://doi.org/10.12989/WAS.2003.6.5.357 (visited on 06/12/2023).

[CLB21] T. Cherubini, R. Lyman, and S. Businger. “Forecasting seeing for the Maunakea observatories with machine learning”. en. In: *Monthly Notices of the Royal Astronomical Society* 509.1 (Nov. 2021), pp. 232–245. ISSN: 0035-8711, 1365-2966. DOI: 10.1093/mnras/stab2916. URL: https://academic.oup.com/mnras/article/509/1/232/6391506 (visited on 03/14/2023).

[CN96] M. C. Cario and B. L. Nelson. “Autoregressive to anything: Time-series input processes for simulation”. en. In: *Operations Research Letters* 19.2 (Aug. 1996), pp. 51–58. ISSN: 01676377. DOI: 10.1016/0167-6377(96)00017-X. URL: https://linkinghub.elsevier.com/retrieve/pii/016763779600017X (visited on 06/22/2023).

[Con+19] J.-M. Conan et al. “Adaptive Optics for GEO-Feeder Links: from Performance Analysis via Reciprocity Based Models to Experimental Demonstration”. In: *COAT-2019 - workshop (Communications and Observations through Atmospheric Turbulence: characterization and mitigation)*. Châtillon, France: ONERA, Dec. 2019. DOI: 10.34693/COAT2019-S5-003.

[Con94] J.-M. Conan. “Etude de la correction partielle en optique adaptative”. In: 1994.

[CRM95] J.-M. Conan, G. Rousset, and P.-Y. Madec. “Wave-front temporal spectra in high-resolution imaging through turbulence”. In: *J. Opt. Soc. Am. A* 12.7 (July 1995). Publisher: Optica Publishing Group, pp. 1559–1570. DOI: 10.1364/JOSAA.12.001559.

[Cyr+22] P. Cyril et al. “FEELINGS : the ONERA’s optical ground station for Geo Feeder links demonstration”. In: *2022 IEEE International Conference on Space Optical Systems and Applications (ICSOS)*. Kyoto City, Japan: IEEE, Mar. 2022, pp. 255–260. ISBN: 978-1-66543-439-3. DOI: 10.1109/ICSOS53063.2022.9749705. URL: https://ieeexplore.ieee.org/document/9749705/ (visited on 09/09/2023).

[DDB20] H. S. Dhiman, D. Deb, and V. E. Balas. “Hybrid machine intelligent wind speed forecasting models”. en. In: *Supervised Machine Learning in Wind Forecasting and Ramp Event Prediction*. Elsevier, 2020, pp. 75–99. ISBN: 978-0-12-821353-7. DOI: 10.1016/B978-0-12-821353-7.00017-X. URL: https://linkinghub.elsevier.com/retrieve/pii/B978012821353700017X (visited on 04/05/2023).

[Dew+93] E. M. Dewan et al. “A Model for Csubn(2) (Optical Turbulence) Profiles Using Radiosonde Data”. In: 1993.

[Dud89] J. Dudhia. “Numerical Study of Convection Observed during the Winter Monsoon Experiment Using a Mesoscale Two-Dimensional Model”. In: *Journal of Atmospheric Sciences* 46.20 (1989). Place: Boston MA, USA Publisher: American Meteorological Society, pp. 3077–3107. DOI: https://doi.org/10.1175/1520-0469(1989)046<3077:NSOCOD>2.0.CO;2. URL: https://journals.ametsoc.org/view/journals/atsc/46/20/1520-0469_1989_046_3077_nsocod_2_0_co_2.xml.

[DZ14] K. Dragomiretskiy and D. Zosso. “Variational Mode Decomposition”. In: *IEEE Transactions on Signal Processing* 62.3 (Feb. 2014), pp. 531–544. ISSN: 1053-587X, 1941-0476. DOI: 10.1109/TSP.2013.2288675. URL: http://ieeexplore.ieee.org/document/6655981/ (visited on 08/25/2023).

[Erd+21] E. Erdogan et al. “Site Diversity in Downlink Optical Satellite Networks Through Ground Station Selection”. In: *IEEE Access* 9 (2021), pp. 31179–31190. ISSN: 2169-3536. DOI: 10.1109/ACCESS.2021.3059641. URL: https://ieeexplore.ieee.org/document/9354784/ (visited on 08/29/2023).

[Esm+21] M. A. Esmail et al. “Free space optic channel monitoring using machine learning”. In: *Opt. Express* 29.7 (Mar. 2021). Publisher: Optica Publishing Group, pp. 10967–10981. DOI: 10.1364/OE.416777.

[Fan75] R. Fante. “Electromagnetic beam propagation in turbulent media”. In: *Proceedings of the IEEE* 63.12 (1975), pp. 1669–1692. DOI: `10.1109/PROC.1975.10035`.

[FHL91] G. Fletcher, T. Hicks, and B. Laurent. “The SILEX optical interorbit link experiment”. en. In: *Electronics & Communications Engineering Journal* 3.6 (1991), p. 273. ISSN: 09540695. DOI: `10.1049/ecej:19910045`. URL: `https://digital-library.theiet.org/content/journals/10.1049/ecej_19910045` (visited on 08/28/2023).

[FM15] C. Fuchs and F. Moll. “Ground Station Network Optimization for Space-to-Ground Optical Communication Links”. en. In: *Journal of Optical Communications and Networking* 7.12 (Dec. 2015), p. 1148. ISSN: 1943-0620, 1943-0639. DOI: `10.1364/JOCN.7.001148`. URL: `https://opg.optica.org/abstract.cfm?URI=jocn-7-12-1148` (visited on 08/29/2023).

[Fri66] D. L. Fried. “Optical Resolution Through a Randomly Inhomogeneous Medium for Very Long and Very Short Exposures”. In: *J. Opt. Soc. Am.* 56.10 (Oct. 1966). Publisher: Optica Publishing Group, pp. 1372–1379. DOI: `10.1364/JOSA.56.001372`.

[FTO22] O. J. D. Farley, M. J. Townson, and J. Osborn. “FAST: Fourier domain adaptive optics simulation tool for bidirectional ground-space optical links through atmospheric turbulence”. en. In: *Optics Express* 30.13 (June 2022), p. 23050. ISSN: 1094-4087. DOI: `10.1364/OE.458659`. URL: `https://opg.optica.org/abstract.cfm?URI=oe-30-13-23050` (visited on 09/16/2023).

[Fuc+17] C. Fuchs et al. “Optimization and throughput estimation of optical ground networks for LEO-downlinks, GEO-feeder links and GEO-relays”. In: *Free-Space Laser Communication and Atmospheric Propagation XXIX*. Ed. by H. Hemmati and D. M. Boroson. Vol. 10096. Backup Publisher: International Society for Optics and Photonics. SPIE, 2017, pp. 298–307. DOI: `10.1117/12.2254795`.

[Fus+04] T. Fusco et al. “NAOS on-line characterization of turbulence parameters and adaptive optics performance”. In: *Journal of Optics A: Pure and Applied Optics* 6.6 (June 2004), pp. 585–596. ISSN: 1464-4258, 1741-3567. DOI: `10.1088/1464-4258/6/6/014`. URL: `https://iopscience.iop.org/article/10.1088/1464-4258/6/6/014` (visited on 08/24/2023).

[Fus+06] T. Fusco et al. “High-order adaptive optics requirements for direct detection of extrasolar planets: Application to the SPHERE instrument”. In: *Opt. Express* 14.17 (Aug. 2006). Publisher: Optica Publishing Group, pp. 7515–7534. DOI: `10.1364/OE.14.007515`.

[FV92] P. Frenzen and C. A. Vogel. "The turbulent kinetic energy budget in the atmospheric surface layer: A review and an experimental reexamination in the field". en. In: *Boundary-Layer Meteorology* 60.1-2 (July 1992), pp. 49–76. ISSN: 0006-8314, 1573-1472. DOI: 10.1007/BF00122061. URL: http://link.springer.com/10.1007/BF00122061 (visited on 08/22/2023).

[Gar+09] B. García-Lorenzo et al. "Adaptive optics parameters connection to wind speed at the Teide Observatory". en. In: *Monthly Notices of the Royal Astronomical Society* 397.3 (Aug. 2009), pp. 1633–1646. ISSN: 00358711, 13652966. DOI: 10.1111/j.1365-2966.2009.15071.x. URL: https://academic.oup.com/mnras/article-lookup/doi/10.1111/j.1365-2966.2009.15071.x (visited on 08/22/2023).

[GC19] A. Gressier and K. Caillault. "Aerosols' Impact on Optical Satellite Transmission". en. In: *Aerotecnica Missili & Spazio* 98.3 (Sept. 2019), pp. 207–219. ISSN: 0365-7442, 2524-6968. DOI: 10.1007/s42496-019-00018-1. URL: http://link.springer.com/10.1007/s42496-019-00018-1 (visited on 08/29/2023).

[GG65] M. Gracheva and A. Gurvich. "Strong fluctuations in the intensity of light propagated through the atmosphere close to the earth". In: *Soviet Radiophysics* 8.4 (1965). Publisher: Springer, pp. 511–515.

[Gio+20] C. Giordano et al. "Statistical learning as a new approach for optical turbulence forecasting". In: *SPIE Astronomical Telescopes + Instrumentation, Adaptive Optics Systems VII*. Vol. 11448. SPIE, 2020, 114484E. DOI: 10.1117/12.2562316.

[Gon+20] S. Gong et al. "Network Availability Maximization for Free-Space Optical Satellite Communications". In: *IEEE Wireless Communications Letters* 9.3 (Mar. 2020), pp. 411–415. ISSN: 2162-2337, 2162-2345. DOI: 10.1109/LWC.2019.2958804. URL: https://ieeexplore.ieee.org/document/8930623/ (visited on 08/29/2023).

[Gre77] D. P. Greenwood. "Bandwidth specification for adaptive optics systems*". en. In: *Journal of the Optical Society of America* 67.3 (Mar. 1977), p. 390. ISSN: 0030-3941. DOI: 10.1364/JOSA.67.000390.

[Gri07] M. Grigoriu. "Parametric translation models for stationary non-Gaussian processes and fields". en. In: *Journal of Sound and Vibration* 303.3-5 (June 2007), pp. 428–439. ISSN: 0022460X. DOI: 10.1016/j.jsv.2006.07.045. URL: https://linkinghub.elsevier.com/retrieve/pii/S0022460X06006407 (visited on 06/12/2023).

[Gri98] M. Grigoriu. "Simulation of stationary non-Gaussian translation processes". In: *Journal of Engineering Mechanics-asce* 124 (1998), pp. 121–126.

[Gro21] M. Grose. “Forecasting Atmospheric Turbulence Conditions From Prior Environmental Parameters Using Artificial Neural Networks: An Ensemble Study”. PhD Thesis. 2021.

[GW69] G. H. Golub and J. H. Welsch. “Calculation of Gauss quadrature rules”. en. In: *Mathematics of Computation* 23.106 (1969), pp. 221–230. ISSN: 0025-5718, 1088-6842. DOI: `10.1090/S0025-5718-69-99647-1`. URL: `https://www.ams.org/mcom/1969-23-106/S0025-5718-69-99647-1/` (visited on 09/07/2023).

[Har98] J. W. Hardy. *Adaptive optics for astronomical telescopes*. Oxford series in optical and imaging sciences 16. New York: Oxford University Press, 1998. ISBN: 978-0-19-509019-2.

[Hau+19] H. Hauschildt et al. “HydRON: High thRoughput Optical Network”. In: *2019 IEEE International Conference on Space Optical Systems and Applications (ICSOS)*. Oct. 2019, pp. 1–6. DOI: `10.1109/ICSOS45490.2019.8978985`.

[Hei+18] F. F. Heine et al. “The European data relay system and Alphasat to T-AOGS space to ground links, status, and achievements in 2017”. In: *Free-Space Laser Communication and Atmospheric Propagation XXX*. Ed. by H. Hemmati and D. M. Boroson. San Francisco, United States: SPIE, Feb. 2018, p. 29. ISBN: 978-1-5106-1533-5 978-1-5106-1534-2. DOI: `10.1117/12.2290791`. URL: `https://www.spiedigitallibrary.org/conference-proceedings-of-spie/10524/2290791/The-European-data-relay-system-and-Alphasat-to-T-AOGS/10.1117/12.2290791.full` (visited on 09/15/2023).

[Her+22] M. Herin et al. “Proportional marginal effects for global sensitivity analysis”. In: (2022). Publisher: arXiv Version Number: 1. DOI: `10.48550/ARXIV.2210.13065`. URL: `https://arxiv.org/abs/2210.13065` (visited on 09/05/2023).

[HL06] S.-Y. Hong and J.-O. J. Lim. “The WRF Single-Moment 6-Class Microphysics Scheme (WSM6)”. In: *Asia-pacific Journal of Atmospheric Sciences* 42 (2006), pp. 129–151. URL: `https://api.semanticscholar.org/CorpusID:120362377`.

[HS97] S. Hochreiter and J. Schmidhuber. “Long Short-Term Memory”. en. In: *Neural Computation* 9.8 (Nov. 1997), pp. 1735–1780. ISSN: 0899-7667, 1530-888X. DOI: `10.1162/neco.1997.9.8.1735`. URL: `https://direct.mit.edu/neco/article/9/8/1735-1780/6109` (visited on 09/15/2023).

[HSW89] K. Hornik, M. Stinchcombe, and H. White. “Multilayer feedforward networks are universal approximators”. en. In: *Neural Networks* 2.5 (Jan. 1989), pp. 359–366. ISSN: 08936080. DOI: `10.1016/0893-6080(89)`

90020-8. URL: https://linkinghub.elsevier.com/retrieve/pii/0893608089900208 (visited on 09/07/2023).

[HTF09] T. Hastie, R. Tibshirani, and J. H. Friedman. *The elements of statistical learning: data mining, inference, and prediction.* 2nd ed. Springer series in statistics. New York, NY: Springer, 2009. ISBN: 978-0-387-84857-0 978-0-387-84858-7.

[Hu+23] X. Hu et al. "Effect of data spatial vertical resolution on the estimation of vertical profiles of the refractive index structure constant". en. In: *Optics Express* 31.16 (July 2023), p. 25815. ISSN: 1094-4087. DOI: 10.1364/OE.493562. URL: https://opg.optica.org/abstract.cfm?URI=oe-31-16-25815 (visited on 01/22/2024).

[Huf74] R. E. Hufnagel. "Propagation through atmospheric turbulence". In: *The Infrared Handbook.* Section: 6. USGPO, 1974.

[Ioo+21] B. Iooss et al. *sensitivity: Global Sensitivity Analysis of Model Outputs.* 2021. URL: https://CRAN.R-project.org/package=sensitivity.

[IP19] B. Iooss and C. Prieur. "Shapley effects for sensitivity analysis with correlated inputs: comparisons with Sobol' indices, numerical estimation and applications". In: *International Journal for Uncertainty Quantification* 9.5 (2019). Publisher: Begell House Publishers, pp. 493–514. DOI: 10.1615/Int.J.UncertaintyQuantification.2019028372.

[Jab21] F. Jabet. "C-DIMM : an autonomous, outdoor and fixed seeing monitor for astronomy, atmospheric studies and free space optical communications". In: *Environmental Effects on Light Propagation and Adaptive Systems IV.* Ed. by K. Stein and S. Gladysz. Online Only, Spain: SPIE, Sept. 2021, p. 3. ISBN: 978-1-5106-4564-6 978-1-5106-4565-3. DOI: 10.1117/12.2599211.

[JBA22] V. Jensen, F. M. Bianchi, and S. N. Anfinsen. "Ensemble Conformalized Quantile Regression for Probabilistic Time Series Forecasting". In: *IEEE Transactions on Neural Networks and Learning Systems* (2022), pp. 1–12. ISSN: 2162-237X, 2162-2388. DOI: 10.1109/TNNLS.2022.3217694. URL: https://ieeexplore.ieee.org/document/9940232/ (visited on 09/06/2023).

[Jel+21] C. Jellen et al. "Machine-learning informed macro-meteorological models for the near-maritime environment". In: *Appl. Opt.* 60.11 (Apr. 2021). Publisher: Optica Publishing Group, pp. 2938–2951. DOI: 10.1364/AO.416680.

[Jim+12] P. A. Jiménez et al. "A Revised Scheme for the WRF Surface Layer Formulation". en. In: *Monthly Weather Review* 140.3 (Mar. 2012), pp. 898–918. ISSN: 0027-0644, 1520-0493. DOI: 10.1175/MWR-D-11-00056.1. URL: http://journals.ametsoc.org/doi/10.1175/MWR-D-11-00056.1 (visited on 08/05/2023).

[Kai+76] J. Kaimal et al. “Turbulence structure in the convective boundary layer”. In: *Journal of Atmospheric Sciences* 33.11 (1976), pp. 2152–2169.

[KD74] B. J. Klein and J. J. Degnan. “Optical Antenna Gain 1: Transmitting Antennas”. en. In: *Applied Optics* 13.9 (Sept. 1974), p. 2134. ISSN: 0003-6935, 1539-4522. DOI: `10.1364/AO.13.002134`. URL: `https://opg.optica.org/abstract.cfm?URI=ao-13-9-2134` (visited on 09/16/2023).

[Klo+22] E. Klotz et al. “Assessment of adaptive optics corrected optical links availability from integrated turbulence parameters by machine learning”. en. In: *Imaging and Applied Optics Congress 2022 (3D, AOA, COSI, ISA, pcAOP)*. Vancouver, British Columbia: Optica Publishing Group, 2022, JTu5D.4. ISBN: 978-1-957171-09-8. DOI: `10.1364/AOA.2022.JTu5D.4`. URL: `https://opg.optica.org/abstract.cfm?URI=AOA-2022-JTu5D.4` (visited on 09/09/2023).

[Klo+23a] E. Klotz et al. “Assessment of adaptive optics-corrected optical links statistics from integrated turbulence parameters through a Gaussian process metamodel”. en. In: *International Journal of Satellite Communications and Networking* (Sept. 2023), sat.1497. ISSN: 1542-0973, 1542-0981. DOI: `10.1002/sat.1497`. URL: `https://onlinelibrary.wiley.com/doi/10.1002/sat.1497` (visited on 09/09/2023).

[Klo+23b] E. Klotz et al. “Forecasting of turbulence impact on optical link from geostationary satellite”. In: *International Conference on Space Optics — ICSO 2022*. Ed. by K. Minoglou, N. Karafolas, and B. Cugny. Dubrovnik, Croatia: SPIE, July 2023, p. 188. ISBN: 978-1-5106-6803-4 978-1-5106-6804-1. DOI: `10.1117/12.2690991`. URL: `https://www.spiedigitallibrary.org/conference-proceedings-of-spie/12777/2690991/Forecasting-of-turbulence-impact-on-optical-link-from-geostationary-satellite/10.1117/12.2690991.full` (visited on 09/09/2023).

[KM18] P. Kossieris and C. Makropoulos. “Exploring the Statistical and Distributional Properties of Residential Water Demand at Fine Time Scales”. In: *Water* 10 (2018), p. 1481. DOI: `10.3390/w10101481`.

[Kol41] A. Kolmogorov. “The Local Structure of Turbulence in Incompressible Viscous Fluid for Very Large Reynolds’ Numbers”. In: *Akademiia Nauk SSSR Doklady* 30 (Jan. 1941), pp. 301–305.

[Kos+19] P. Kossieris et al. “Simulating Marginal and Dependence Behaviour of Water Demand Processes at Any Fine Time Scale”. In: *Water* 11 (2019), p. 885. DOI: `10.3390/w11050885`.

[Kos20] P. Kossieris. “Multi-scale stochastic analysis and modelling of residential water demand processes”. PhD Thesis. Athens: Department of Water Resources and Environmental Engineering – National Technical University of Athens, Feb. 2020.

[Kou00] D. Koutsoyiannis. “A generalized mathematical framework for stochastic simulation and forecast of hydrologic time series”. en. In: *Water Resources Research* 36.6 (Feb. 2000), pp. 1519–1533. ISSN: 00431397. DOI: 10.1029/2000WR900044. URL: http://doi.wiley.com/10.1029/2000WR900044 (visited on 06/23/2023).

[KS10] F. R. Kschischang and B. P. Smith. “Forward Error Correction (FEC) in Optical Communication”. In: *Conference on Lasers and Electro-Optics 2010*. Journal Abbreviation: Conference on Lasers and Electro-Optics 2010. Optical Society of America, 2010, CThDD1. DOI: 10.1364/CLEO.2010.CThDD1.

[Lam+20] C. Lamprecht et al. “Modelling the Refractive Index Structure Parameter: A ResNet Approach”. In: *2020 International Conference on Broadband Communications for Next Generation Networks and Multimedia Applications (CoBCom)*. 2020, pp. 1–4. DOI: 10.1109/CoBCom49975.2020.9174186.

[LH79] G. C. Loos and C. B. Hogge. “Turbulence of the upper atmosphere and isoplanatism”. In: *Appl. Opt.* 18.15 (Aug. 1979). Publisher: Optica Publishing Group, pp. 2654–2661. DOI: 10.1364/AO.18.002654.

[Li+23] Y. Li et al. “Multistep ahead atmospheric optical turbulence forecasting for free-space optical communication using empirical mode decomposition and LSTM-based sequence-to-sequence learning”. In: *Frontiers in Physics* 11 (Jan. 2023), p. 1070762. ISSN: 2296-424X. DOI: 10.3389/fphy.2023.1070762. URL: https://www.frontiersin.org/articles/10.3389/fphy.2023.1070762/full (visited on 04/05/2023).

[Lin+21] B. Lindemann et al. “A survey on long short-term memory networks for time series prediction”. en. In: *Procedia CIRP* 99 (2021), pp. 650–655. ISSN: 22128271. DOI: 10.1016/j.procir.2021.03.088. URL: https://linkinghub.elsevier.com/retrieve/pii/S2212827121003796 (visited on 09/16/2023).

[Lio+21] A. Lionis et al. “Using Machine Learning Algorithms for Accurate Received Optical Power Prediction of an FSO Link over a Maritime Environment”. In: *Photonics* 8.6 (2021). ISSN: 2304-6732. DOI: 10.3390/photonics8060212.

[Liu+21] H. Liu et al. “Intelligent modeling strategies for forecasting air quality time series: A review”. en. In: *Applied Soft Computing* 102 (Apr. 2021), p. 106957. ISSN: 15684946. DOI: 10.1016/j.asoc.2020.106957. URL: https://linkinghub.elsevier.com/retrieve/pii/S1568494620308954 (visited on 04/05/2023).

[LN89] D. C. Liu and J. Nocedal. “On the limited memory BFGS method for large scale optimization”. en. In: *Mathematical Programming* 45.1-3 (Aug. 1989), pp. 503–528. ISSN: 0025-5610, 1436-4646. DOI: 10.1007/BF01589116. URL: http://link.springer.com/10.1007/BF01589116 (visited on 09/07/2023).

[MAG21] M. Merritt, A. Alexanderian, and P. Gremaud. “Global sensitivity analysis of rare event probabilities”. In: *arXiv preprint arXiv:2110.13974* (2021).

[Mah00] F. Mahé. “Application d’un modèle atmosphérique à l’étude des fluctuations d’indice de réfraction dans la couche limite : influence de la scintillation sur l’analyse de front d’onde”. In: 2000. URL: https://api.semanticscholar.org/CorpusID:127445929.

[MF88] J. M. Martin and S. M. Flatté. “Intensity images and statistics from numerical simulation of wave propagation in 3-D random media”. In: *Appl. Opt.* 27.11 (June 1988). Publisher: Optica Publishing Group, pp. 2111–2126. DOI: 10.1364/AO.27.002111. URL: https://opg.optica.org/ao/abstract.cfm?URI=ao-27-11-2111.

[Mil+19] J. Milli et al. *Nowcasting the turbulence at the Paranal Observatory.* 2019. DOI: 10.48550/ARXIV.1910.13767.

[Mla+97] E. J. Mlawer et al. “Radiative transfer for inhomogeneous atmospheres: RRTM, a validated correlated-k model for the longwave”. en. In: *Journal of Geophysical Research: Atmospheres* 102.D14 (July 1997), pp. 16663–16682. ISSN: 01480227. DOI: 10.1029/97JD00237. URL: http://doi.wiley.com/10.1029/97JD00237 (visited on 08/05/2023).

[MMT20] E. Masciadri, G. Martelloni, and A. Turchi. “Filtering techniques to enhance optical turbulence forecast performances at short time-scales”. en. In: *Monthly Notices of the Royal Astronomical Society* 492.1 (Feb. 2020), pp. 140–152. ISSN: 0035-8711, 1365-2966. DOI: 10.1093/mnras/stz3342. URL: https://academic.oup.com/mnras/article/492/1/140/5647365 (visited on 03/14/2023).

[MO05] C. Musso and N. Oudjane. “Data reduction for particle filters”. In: *ISPA 2005. Proceedings of the 4th International Symposium on Image and Signal Processing and Analysis, 2005.* ISSN: 1845-5921. Zagreb, Croatia: IEEE, 2005, pp. 52–57. ISBN: 978-953-184-089-7. DOI: 10.1109/ISPA.2005.195383. URL: http://ieeexplore.ieee.org/document/1521262/ (visited on 09/07/2023).

[Mon17] L. Montoya Martinez. “Modeling day time turbulence profiles: Application to Teide Observatory”. In: *Proceedings of the Adaptive Optics for Extremely Large Telescopes 5.* Instituto de Astrofísica de Canarias (IAC), 2017. DOI: 10.26698/AO4ELT5.0178. URL: http://research.iac.es/congreso/AO4ELT5/pages/proceeding0178.html (visited on 09/06/2023).

[Mus93] C. Musso. “Méthodes rapides d’estimation en trajectographie par mesures d’azimuts”. Theses. Université Joseph-Fourier - Grenoble I, Oct. 1993. URL: https://theses.hal.science/tel-00343877.

[MVB99] E. Masciadri, J. Vernin, and P. Bougeault. “3D mapping of optical turbulence using an atmospheric numerical model - I. A useful tool for the ground-based astronomy”. In: *Astronomy & Astrophysics Supplement Series* 137 (1999), pp. 185–202. URL: https://api.semanticscholar.org/CorpusID:54774157.

[Nat62] A. Nataf. “Détermination des distributions de probabilités dont les marges sont données, vol. 225 of Comptes Rendus de la Académie des Sciences”. In: (1962).

[Nei08] B. Neichel. “Etudes des galaxies lointaines et optiques adaptatives tomographiques pour les ELTs.” In: (Jan. 2008).

[New04] I. Newton. *Opticks, or, a treatise of the reflections, refractions, inflections & colours of light.* 1704.

[NN09] M. Nakanishi and H. Niino. “Development of an Improved Turbulence Closure Model for the Atmospheric Boundary Layer”. en. In: *Journal of the Meteorological Society of Japan. Ser. II* 87.5 (2009), pp. 895–912. ISSN: 0026-1165, 2186-9057. DOI: 10.2151/jmsj.87.895. URL: http://www.jstage.jst.go.jp/article/jmsj/87/5/87_5_895/_article (visited on 08/05/2023).

[Nol76] R. J. Noll. “Zernike polynomials and atmospheric turbulence\ast”. In: *J. Opt. Soc. Am.* 66.3 (Mar. 1976). Publisher: Optica Publishing Group, pp. 207–211. DOI: 10.1364/JOSA.66.000207.

[Obu+49] A. M. Obukhov et al. “Structure of the temperature field in a turbulent flow”. In: *Izv. Akad. Nauk SSSR, Ser. Geogr. Geofiz* 13.1 (1949), pp. 58–69.

[OCJ23] J. Osborn, J.-E. Communal, and F. Jabet. “Global atmospheric turbulence forecasting for free-space optical communications”. In: Feb. 2023.

[Oh+04] E. Oh et al. “Estimating optical turbulence using the PAMELA model”. In: ed. by J. C. Ricklin and D. G. Voelz. Denver, CO, Oct. 2004, p. 256. DOI: 10.1117/12.561481. URL: http://proceedings.spiedigitallibrary.org/proceeding.aspx?doi=10.1117/12.561481 (visited on 09/06/2023).

[Oli+21] K. G. Olivares et al. “Neural basis expansion analysis with exogenous variables: Forecasting electricity prices with NBEATSx”. In: (2021). Publisher: arXiv Version Number: 6. DOI: 10.48550/ARXIV.2104.05522. URL: https://arxiv.org/abs/2104.05522 (visited on 08/09/2023).

[Ore+19] B. N. Oreshkin et al. “N-BEATS: Neural basis expansion analysis for interpretable time series forecasting”. In: (2019). Publisher: arXiv Version Number: 4. DOI: 10.48550/ARXIV.1905.10437. URL: https://arxiv.org/abs/1905.10437 (visited on 08/07/2023).

[Ort00] K. M. Ortmann. “The proportional value for positive cooperative games”. In: *Mathematical Methods of Operations Research (ZOR)* 51.2 (Apr. 2000), pp. 235–248. ISSN: 1432-2994, 1432-5217. DOI: 10.1007/s001860050086. URL: http://link.springer.com/10.1007/s001860050086 (visited on 09/05/2023).

[OS18] J. Osborn and M. Sarazin. “Atmospheric turbulence forecasting with a general circulation model for Cerro Paranal”. en. In: *Monthly Notices of the Royal Astronomical Society* 480.1 (Oct. 2018), pp. 1278–1299. ISSN: 0035-8711, 1365-2966. DOI: 10.1093/mnras/sty1898.

[Osb+10] J. Osborn et al. “Profiling the surface layer of optical turbulence with SLODAR: Optical turbulence surface layer profiling”. en. In: *Monthly Notices of the Royal Astronomical Society* (May 2010), no–no. ISSN: 00358711, 13652966. DOI: 10.1111/j.1365-2966.2010.16795.x. URL: https://academic.oup.com/mnras/article-lookup/doi/10.1111/j.1365-2966.2010.16795.x (visited on 01/09/2024).

[Osb+18] J. Osborn et al. “Optical turbulence profiling with Stereo-SCIDAR for VLT and ELT”. In: *Monthly Notices of the Royal Astronomical Society* 478.1 (Apr. 2018), pp. 825–834. DOI: 10.1093/mnras/sty1070.

[Owe14] A. B. Owen. “Sobol’ Indices and Shapley Value”. en. In: *SIAM/ASA Journal on Uncertainty Quantification* 2.1 (Jan. 2014), pp. 245–251. ISSN: 2166-2525. DOI: 10.1137/130936233. URL: http://epubs.siam.org/doi/10.1137/130936233 (visited on 09/05/2023).

[PCR15] S. Poulenard, M. Crosnier, and A. Rissons. “Ground Segment Design for Broadband Geostationary Satellite With Optical Feeder Link”. en. In: *Journal of Optical Communications and Networking* 7.4 (Apr. 2015), p. 325. ISSN: 1943-0620, 1943-0639. DOI: 10.1364/JOCN.7.000325. URL: https://opg.optica.org/abstract.cfm?URI=jocn-7-4-325 (visited on 09/15/2023).

[Per+06] N. Perlot et al. “Measurements of the beam-wave fluctuations over a 142 km atmospheric path”. In: San Diego, California, USA, Aug. 2006, 63041O. DOI: 10.1117/12.681207. URL: http://proceedings.spiedigitallibrary.org/proceeding.aspx?doi=10.1117/12.681207 (visited on 08/22/2023).

[Per+23] S. Perera et al. “SHIMM: A Versatile Seeing Monitor for Astronomy”. In: *Monthly Notices of the Royal Astronomical Society* 520.4 (Feb. 2023). arXiv:2303.00153 [astro-ph], pp. 5475–5486. ISSN: 0035-8711, 1365-2966. DOI: 10.1093/mnras/stad339. URL: http://arxiv.org/abs/2303.00153 (visited on 01/09/2024).

[Pic10] B. Picinbono. “ARMA Signals With Specified Symmetric Marginal Probability Distribution”. In: *IEEE Transactions on Signal Processing* 58.3 (2010), pp. 1542–1552. DOI: 10.1109/TSP.2009.2037076.

[PL98] S. Primak and V. Lyandres. “On the generation of the baseband and narrowband non-Gaussian processes”. In: *IEEE Transactions on Signal Processing* 46.5 (May 1998), pp. 1229–1237. ISSN: 1053587X. DOI: 10.1109/78.668786. URL: http://ieeexplore.ieee.org/document/668786/ (visited on 06/12/2023).

[PM23] D. PHAM and C. Musso. “Une méthode rapide et efficace pour la trajectographie passive par mesures de deux azimuts”. In: *13° Colloque sur le traitement du signal et des images, 1991 ; p. 314-317* (Sept. 2023).

[Pou+14] S. Poulenard et al. “High altitude clouds impacts on the design of optical feeder link and optical ground station network for future broadband satellite services”. In: *Free-Space Laser Communication and Atmospheric Propagation XXVI*. Ed. by H. Hemmati and D. M. Boroson. Vol. 8971. Backup Publisher: International Society for Optics and Photonics. SPIE, 2014, pp. 58–67. DOI: 10.1117/12.2038486.

[Pou+23] S. Poulenard et al. “10 Gbauds digital optical link and analog link from/to geostationary satellite”. In: *International Conference on Space Optics — ICSO 2022*. Ed. by K. Minoglou, N. Karafolas, and B. Cugny. Dubrovnik, Croatia: SPIE, July 2023, p. 31. ISBN: 978-1-5106-6803-4 978-1-5106-6804-1. DOI: 10.1117/12.2689021. URL: https://www.spiedigitallibrary.org/conference-proceedings-of-spie/12777/2689021/10-Gbauds-digital-optical-link-and-analog-link-from-to/10.1117/12.2689021.full (visited on 07/19/2023).

[Qua+23a] F. Quatresooz et al. “Challenges for optical turbulence characterization and prediction at optical communication sites”. In: *International Conference on Space Optics — ICSO 2022*. Ed. by K. Minoglou, N. Karafolas, and B. Cugny. Dubrovnik, Croatia: SPIE, July 2023, p. 204. ISBN: 978-1-5106-6803-4 978-1-5106-6804-1. DOI: 10.1117/12.2691034. URL: https://www.spiedigitallibrary.org/conference-proceedings-of-spie/12777/2691034/Challenges-for-optical-turbulence-characterization-and-prediction-at-optical-communication/10.1117/12.2691034.full (visited on 08/05/2023).

[Qua+23b] F. Quatresooz et al. “Continuous daytime and nighttime forecast of atmospheric optical turbulence from numerical weather prediction models”. en. In: *Optics Express* 31.21 (Oct. 2023), p. 33850. ISSN: 1094-4087. DOI: 10.1364/OE.500090. URL: https://opg.optica.org/abstract.cfm?URI=oe-31-21-33850 (visited on 01/30/2024).

[Raf+22] A. Rafalimanana et al. “Optimal Prediction of Atmospheric Turbulence by Means of the Weather Research and Forecasting Model”. In: *Publications of the Astronomical Society of the Pacific* 134.1035 (May 2022), p. 055002. ISSN: 0004-6280, 1538-3873. DOI: 10.1088/1538-3873/ac6536. URL: https://iopscience.iop.org/article/10.1088/1538-3873/ac6536 (visited on 03/14/2023).

[RF23] G. Rousset and T. Fusco. "Optique adaptative : correction des effets de la turbulence atmosphérique sur les images astronomiques". en. In: *Comptes Rendus. Physique* 23.S1 (Aug. 2023), pp. 293–344. ISSN: 1878-1535. DOI: `10.5802/crphys.111`. URL: `https://comptes-rendus.academie-sciences.fr/physique/articles/10.5802/crphys.111/` (visited on 08/22/2023).

[RGL82] F. Roddier, J. M. Gilli, and G. Lund. "On the origin of speckle boiling and its effects in stellar speckle interferometry". In: *Journal of Optics* 13.5 (Sept. 1982). Publisher: IOP Publishing, pp. 263–271. DOI: `10.1088/0150-536x/13/5/002`.

[Ric+17] I. Richter et al. "The TESAT transportable adaptive optical ground station and the operational experiences". In: *International Conference on Space Optics — ICSO 2016*. Ed. by N. Karafolas, B. Cugny, and Z. Sodnik. Biarritz, France: SPIE, Sept. 2017, p. 217. ISBN: 978-1-5106-1613-4 978-1-5106-1614-1. DOI: `10.1117/12.2296195`. URL: `https://spiedigitallibrary.org/conference-proceedings-of-spie/10562/2296195/The-TESAT-transportable-adaptive-optical-ground-station-and-the-operational/10.1117/12.2296195.full` (visited on 09/15/2023).

[Rob+08] C. Robert et al. "Retrieving parameters of the anisotropic refractive index fluctuations spectrum in the stratosphere from balloon-borne observations of stellar scintillation". en. In: *Journal of the Optical Society of America A* 25.2 (Feb. 2008), p. 379. ISSN: 1084-7529, 1520-8532. DOI: `10.1364/JOSAA.25.000379`. URL: `https://opg.optica.org/abstract.cfm?URI=josaa-25-2-379` (visited on 08/22/2023).

[Rod81] F. Roddier. "V The Effects of Atmospheric Turbulence in Optical Astronomy". In: ed. by E. Wolf. Vol. 19. Progress in Optics. ISSN: 0079-6638. Elsevier, 1981, pp. 281–376. DOI: `https://doi.org/10.1016/S0079-6638(08)70204-X`.

[Roy+15] B. Roy et al. "Optical feeder links for high throughput satellites". In: *2015 IEEE International Conference on Space Optical Systems and Applications (ICSOS)*. New Orleans, LA: IEEE, Oct. 2015, pp. 1–6. ISBN: 978-1-5090-0281-8. DOI: `10.1109/ICSOS.2015.7425074`. URL: `https://ieeexplore.ieee.org/document/7425074/` (visited on 09/15/2023).

[RVL98] F. J. Rigaut, J.-P. Veran, and O. Lai. "Analytical model for Shack-Hartmann-based adaptive optics systems". In: ed. by D. Bonaccini and R. K. Tyson. Kona, HI, Sept. 1998, p. 1038. DOI: `10.1117/12.321649`. URL: `http://proceedings.spiedigitallibrary.org/proceeding.aspx?doi=10.1117/12.321649` (visited on 09/12/2023).

[RW05] C. E. Rasmussen and C. K. I. Williams. *Gaussian Processes for Machine Learning*. en. The MIT Press, 2005. ISBN: 978-0-262-25683-4. DOI: `10.7551/mitpress/3206.001.0001`.

[Sau+16] K. Saucke et al. “The Tesat transportable adaptive optical ground station”. In: ed. by H. Hemmati and D. M. Boroson. San Francisco, California, United States, Mar. 2016, p. 973906. DOI: `10.1117/12.2218275`. URL: `http://proceedings.spiedigitallibrary.org/proceeding.aspx?doi=10.1117/12.2218275` (visited on 09/15/2023).

[Ser19] C. C. C. Service. *ERA5-Land hourly data from 2001 to present.* Type: dataset. 2019. DOI: `10.24381/CDS.E2161BAC`. URL: `https://cds.climate.copernicus.eu/doi/10.24381/cds.e2161bac` (visited on 01/18/2023).

[Sha+15] K. M. Shahiduzzaman et al. “Scattering Effect on Terrestrial Free Space Optical Signal in Tropical Weather Condition”. In: 2015. URL: `https://api.semanticscholar.org/CorpusID:36346875`.

[Sha70] R. V. Shack. “Image processing by an optical analog device”. In: *Pattern Recognition* 2.2 (1970). Publisher: Elsevier, pp. 123–126.

[SNS16] E. Song, B. L. Nelson, and J. Staum. “Shapley Effects for Global Sensitivity Analysis: Theory and Computation”. In: *SIAM/ASA Journal on Uncertainty Quantification* 4.1 (2016), pp. 1060–1083. DOI: `10.1137/15M1048070`.

[Sob01] I. M. Sobol. “Global sensitivity indices for nonlinear mathematical models and their Monte Carlo estimates”. In: *Mathematics and Computers in Simulation* 55.1 (2001), pp. 271–280. ISSN: 0378-4754. DOI: `https://doi.org/10.1016/S0378-4754(00)00270-6`.

[Sod+21] Z. Sodnik et al. “Optical feeder-link between ESA’s optical ground station and Alphasat”. In: *International Conference on Space Optics — ICSO 2020*. Ed. by Z. Sodnik, B. Cugny, and N. Karafolas. Online Only, France: SPIE, June 2021, p. 44. ISBN: 978-1-5106-4548-6 978-1-5106-4549-3. DOI: `10.1117/12.2599231`. URL: `https://www.spiedigitallibrary.org/conference-proceedings-of-spie/11852/2599231/Optical-feeder-link-between-ESAs-optical-ground-station-and-Alphasat/10.1117/12.2599231.full` (visited on 09/15/2023).

[Sol+13] D. Soltau et al. “Solar adaptive optics at the Observatorio del Teide, Tenerife”. In: ed. by A. Comeron et al. Dresden, Germany, Oct. 2013, p. 88901D. DOI: `10.1117/12.2032382`. URL: `http://proceedings.spiedigitallibrary.org/proceeding.aspx?doi=10.1117/12.2032382` (visited on 08/22/2023).

[SR88] S. Shaklan and F. Roddier. “Coupling starlight into single-mode fiber optics”. en. In: *Applied Optics* 27.11 (June 1988), p. 2334. ISSN: 0003-6935, 1539-4522. DOI: `10.1364/AO.27.002334`. URL: `https://opg.optica.org/abstract.cfm?URI=ao-27-11-2334` (visited on 09/12/2023).

[SS13] D. Sprung and E. Sucher. "Characterization of optical turbulence at the solar observatory at the Mount Teide, Tenerife". In: ed. by A. Comeron et al. Dresden, Germany, Oct. 2013, p. 889015. DOI: 10.1117/12.2032744. URL: http://proceedings.spiedigitallibrary.org/proceeding.aspx?doi=10.1117/12.2032744 (visited on 08/22/2023).

[Str95] K. Strehl. "Aplanatische und fehlerhafte Abbildung im Fernrohr". In: *Zeitschrift für Instrumentenkunde* 15.7 (1895), pp. 362–370.

[Su+20] C. Su et al. "Adaptive niche-genetic algorithm based on backpropagation neural network for atmospheric turbulence forecasting". In: *Appl. Opt.* 59.12 (Apr. 2020). Publisher: Optica Publishing Group, pp. 3699–3705. DOI: 10.1364/AO.388959.

[SYF14] H. Shen, L. Yu, and C. Fan. "Temporal spectrum of atmospheric scintillation and the effects of aperture averaging and time averaging". In: *Optics Communications* 330 (2014), pp. 160–164. ISSN: 0030-4018. DOI: https://doi.org/10.1016/j.optcom.2014.05.039.

[Tat61] Tatarski. "Wave Propagation in a Turbulent Medium". In: 134.3475 (Aug. 1961), pp. 324–325. DOI: 10.1126/science.134.3475.324.c.

[Tat71] V. I. Tatarskii. *The effects of the turbulent atmosphere on wave propagation.* 1971.

[THH18] C. Tian, Y. Hao, and J. Hu. "A novel wind speed forecasting system based on hybrid data preprocessing and multi-objective optimization". en. In: *Applied Energy* 231 (Dec. 2018), pp. 301–319. ISSN: 03062619. DOI: 10.1016/j.apenergy.2018.09.012. URL: https://linkinghub.elsevier.com/retrieve/pii/S0306261918313199 (visited on 04/05/2023).

[Tho+13] P. W. Thorne et al. "GCOS reference upper air network (GRUAN): Steps towards assuring future climate records". In: Los Angeles, California, USA, 2013, pp. 1042–1047. DOI: 10.1063/1.4821421. URL: https://pubs.aip.org/aip/acp/article/1552/1/1042-1047/878657 (visited on 09/05/2023).

[Thr77] S. A. Thrope. "Turbulence and mixing in a Scottish Loch". en. In: *Philosophical Transactions of the Royal Society of London. Series A, Mathematical and Physical Sciences* 286.1334 (July 1977), pp. 125–181. ISSN: 0080-4614, 2054-0272. DOI: 10.1098/rsta.1977.0112. URL: https://royalsocietypublishing.org/doi/10.1098/rsta.1977.0112 (visited on 09/06/2023).

[TKM20] I. Tsoukalas, P. Kossieris, and C. Makropoulos. "Simulation of non-Gaussian correlated random variables, stochastic processes and random fields: Introducing the anySim R-Package for environmental applications and beyond". In: *Water* 12.6 (2020), p. 1645. DOI: 10.3390/w12061645.

[Tok02] A. Tokovinin. “From Differential Image Motion to Seeing”. In: *Publications of the Astronomical Society of the Pacific* 114.800 (Oct. 2002). Publisher: IOP Publishing, pp. 1156–1166. DOI: 10.1086/342683.

[Tót+18] J. Tóth et al. “Classification prediction analysis of RSSI parameter in hard switching process for FSO/RF systems”. In: *Measurement* 116 (2018), pp. 602–610. ISSN: 0263-2241. DOI: https://doi.org/10.1016/j.measurement.2017.11.044. URL: https://www.sciencedirect.com/science/article/pii/S0263224117307546.

[Toy+12] M. Toyoshima et al. “Results of Kirari optical communication demonstration experiments with NICT optical ground station (KODEN) aiming for future classical and quantum communications in space”. In: *Acta Astronautica* 74 (May 2012), pp. 40–49. DOI: 10.1016/j.actaastro.2011.12.020.

[Toy21] M. Toyoshima. “Recent Trends in Space Laser Communications for Small Satellites and Constellations”. In: *Journal of Lightwave Technology* 39.3 (Feb. 2021), pp. 693–699. ISSN: 0733-8724, 1558-2213. DOI: 10.1109/JLT.2020.3009505. URL: https://ieeexplore.ieee.org/document/9141375/ (visited on 05/13/2022).

[Tso18] I. Tsoukalas. “Modelling and simulation of non-Gaussian stochastic processes for optimization of water-systems under uncertainty”. PhD Thesis. Department of Water Resources and Environmental Engineering, National Technical University of Athens, 2018.

[TV07] H. Trinquet and J. Vernin. “A statistical model to forecast the profile of the index structure constant $${C_N^2}$$”. en. In: *Environmental Fluid Mechanics* 7.5 (Oct. 2007), pp. 397–407. ISSN: 1567-7419, 1573-1510. DOI: 10.1007/s10652-007-9031-x. URL: http://link.springer.com/10.1007/s10652-007-9031-x (visited on 09/06/2023).

[Val80] G. C. Valley. “Isoplanatic degradation of tilt correction and short-term imaging systems”. In: *Applied Optics* 19.4 (1980). Publisher: Optical Society of America, pp. 574–577.

[Véd+16] N. Védrenne et al. “Adaptive optics for high data rate satellite to ground laser link”. In: *Free-Space Laser Communication and Atmospheric Propagation XXVIII*. Ed. by H. Hemmati and D. M. Boroson. Vol. 9739. Backup Publisher: International Society for Optics and Photonics. SPIE, 2016, pp. 119–128. DOI: 10.1117/12.2218213.

[Véd08] N. Védrenne. “Propagation optique et correction en forte turbulence”. PhD Thesis. Nice: École doctorale Sciences fondamentales et appliquées (Nice), 2008.

[Vet+07] F. S. Vetelino et al. "Aperture averaging effects on the probability density of irradiance fluctuations in moderate-to-strong turbulence". In: *Appl. Opt.* 46.11 (Apr. 2007). Publisher: OSA, pp. 2099–2108. DOI: 10.1364/AO.46.002099.

[VO09] C. Villien and E. Ostertag. "A Polynomial Approximation Algorithm for Real-Time Maximum-Likelihood Estimation". In: *IEEE Transactions on Signal Processing* 57.6 (June 2009), pp. 2085–2095. ISSN: 1053-587X, 1941-0476. DOI: 10.1109/TSP.2009.2016875. URL: http://ieeexplore.ieee.org/document/4799114/ (visited on 09/07/2023).

[Vor+20] A. M. Vorontsov et al. "Atmospheric Turbulence Study with Deep Machine Learning of Intensity Scintillation Patterns". In: *Applied Sciences* 10.22 (2020). ISSN: 2076-3417. DOI: 10.3390/app10228136.

[Wal31] G. T. Walker. "On periodicity in series of related terms". en. In: *Proceedings of the Royal Society of London. Series A, Containing Papers of a Mathematical and Physical Character* 131.818 (June 1931), pp. 518–532. ISSN: 0950-1207, 2053-9150. DOI: 10.1098/rspa.1931.0069. URL: https://royalsocietypublishing.org/doi/10.1098/rspa.1931.0069 (visited on 07/17/2023).

[WB16] Y. Wang and S. Basu. "Using an artificial neural network approach to estimate surface-layer optical turbulence at Mauna Loa, Hawaii". In: *Opt. Lett.* 41.10 (May 2016). Publisher: Optica Publishing Group, pp. 2334–2337. DOI: 10.1364/OL.41.002334.

[Wes+23] L. Westerby-Griffin et al. "Atmospheric optical turbulence measurements at varying elevation angles". In: *Free-Space Laser Communications XXXV*. Ed. by H. Hemmati and B. S. Robinson. San Francisco, United States: SPIE, Mar. 2023, p. 56. ISBN: 9781510659315 9781510659322. DOI: 10.1117/12.2649231. URL: https://www.spiedigitallibrary.org/conference-proceedings-of-spie/12413/2649231/Atmospheric-optical-turbulence-measurements-at-varying-elevation-angles/10.1117/12.2649231.full (visited on 01/18/2024).

[WL93] K. E. Wilson and J. R. Lesh. "An overview of the Galileo Optical Experiment (GOPEX)". In: *The Telecommunications and Data Acquisition Report* (Aug. 1993).

[Wu+20] S. Wu et al. "A Simple Method to Estimate the Refractive Index Structure Parameter (${C}_{n}^{2}$) in the Atmosphere". In: *Publications of the Astronomical Society of the Pacific* 132.1014 (Aug. 2020), p. 084501. ISSN: 0004-6280, 1538-3873. DOI: 10.1088/1538-3873/ab9451. URL: https://iopscience.iop.org/article/10.1088/1538-3873/ab9451 (visited on 01/22/2024).

[XX21] C. Xu and Y. Xie. “Conformal prediction interval for dynamic time-series”. In: *Proceedings of the 38th International Conference on Machine Learning*. Ed. by M. Meila and T. Zhang. Vol. 139. Proceedings of Machine Learning Research. PMLR, July 2021, pp. 11559–11569. URL: https://proceedings.mlr.press/v139/xu21h.html.

[XZ19] Q. Xiao and S. Zhou. “Simulating Non-Gaussian Stationary Stochastic Processes by Translation Model”. In: *IEEE Access* 7 (2019), pp. 34555–34569. ISSN: 2169-3536. DOI: 10.1109/ACCESS.2019.2904510. URL: https://ieeexplore.ieee.org/document/8666115/ (visited on 06/12/2023).

[Yul27] G. U. Yule. “On a Method of Investigating Periodicities in Disturbed Series, with Special Reference to Wolfer’s Sunspot Numbers”. In: *Philosophical Transactions of the Royal Society of London. Series A, Containing Papers of a Mathematical or Physical Character* 226 (1927). Publisher: The Royal Society, pp. 267–298. ISSN: 02643952. URL: http://www.jstor.org/stable/91170 (visited on 07/17/2023).

[Zaf+22] M. Zaffran et al. “Adaptive Conformal Predictions for Time Series”. In: (2022). Publisher: arXiv Version Number: 1. DOI: 10.48550/ARXIV.2202.07282. URL: https://arxiv.org/abs/2202.07282 (visited on 09/06/2023).

[ZC14] W. Zhu and G. Cai. “Generation of non-Gaussian stochastic processes using nonlinear filters”. en. In: *Probabilistic Engineering Mechanics* 36 (Apr. 2014), pp. 56–62. ISSN: 02668920. DOI: 10.1016/j.probengmech.2014.03.004.

[Zer38] F. Zernike. “The concept of degree of coherence and its application to optical problems”. In: *Physica* 5.8 (1938), pp. 785–795. ISSN: 0031-8914. DOI: https://doi.org/10.1016/S0031-8914(38)80203-2.

[Zia+00] A. Ziad et al. “From the grating scale monitor to the generalized seeing monitor”. In: *Appl. Opt.* 39.30 (Oct. 2000). Publisher: Optica Publishing Group, pp. 5415–5425. DOI: 10.1364/AO.39.005415.

[Zia+22] A. Ziad et al. “ANAtOLIA: a new mobile site-testing station for astronomy and optical communications”. In: *Adaptive Optics Systems VIII*. Ed. by L. Schreiber, D. Schmidt, and E. Vernet. Vol. 12185. Backup Publisher: International Society for Optics and Photonics. SPIE, 2022, 121855Z. DOI: 10.1117/12.2629825.

[Zia16] A. Ziad. “Review of the outer scale of the atmospheric turbulence”. In: ed. by E. Marchetti, L. M. Close, and J.-P. Véran. Edinburgh, United Kingdom, July 2016, 99091K. DOI: 10.1117/12.2231375. URL: http://proceedings.spiedigitallibrary.org/proceeding.aspx?doi=10.1117/12.2231375 (visited on 09/06/2023).

[ZWH11] C. Zhang, Y. Wang, and K. Hamilton. “Improved Representation of Boundary Layer Clouds over the Southeast Pacific in ARW-WRF Using a Modified Tiedtke Cumulus Parameterization Scheme*”. en. In: *Monthly Weather Review* 139.11 (Nov. 2011), pp. 3489–3513. ISSN: 0027-0644, 1520-0493. DOI: `10.1175/MWR-D-10-05091.1`. URL: `http://journals.ametsoc.org/doi/10.1175/MWR-D-10-05091.1` (visited on 08/05/2023).